

# EXPERIMENTAL STUDIES OF SILK AND SILK COMPOSITES FOR BIOMEDICAL APPLICATION

Robyn Plowright

A thesis submitted in partial fulfilment of the requirements of the

Nottingham Trent University

for the degree of Doctor of Philosophy

July 2017

## **Dedication**

To Marc, for providing me with unconditional love and the support that I needed to complete this.

## **Acknowledgements**

I would like to thank my supervisors both past and present, Prof Carole Perry for giving me this opportunity and providing guidance, support and patience throughout. Dr David Belton, whose passion for science has inspired me daily and whose advice was always appreciated. I would also like to thank my supervisors from my undergraduate studies, Dr Muriel Funck and Dr Gary Hix for giving me the confidence to go into research.

My sincere thanks go to the entire Perry research group for putting up with me over the last three years; Graham Hickman, Marion Limo, Mithun Parambath, Zayd Westcott, Veeranjanyulu Thota, Mathew Nicklin, Ben Hanby, Mohamad Abou Shamat, Monika Michaelis, Daniel Oliver, Aneeqa Fayyaz, Igor Effimov and Victor Volkov. I would also like to thank our collaborators at Tufts university and the NIH for permitting me be part of this project.

It is undeniable that without my friends this would not have been possible, so in no particular order I would like to thank; Jacob Spear, Danielle Pearson, Anna Sola Rabada and Cheryl Smith who are all wonderful people who made me laugh when I needed it and made my experience extra special by allowing me to be part of their lives.

Lastly, I would like to thank my family, specifically my cousin Kathryn Chivers who is more like a sister to me, and my mum and dad who have always believed their strange little girl would grow up to be something special, well hope I made you proud.

## Abstract

Genetic engineering has been utilised to produce a range of silk based biomaterials capable of promoting mineralisation to aid bone regeneration *via* biomimetic routes. Silk fusion proteins, where the silk domain is a derivative of the major ampullate dragline Spidroin 1 from *Nephila Clavipes*, consisting of a 15mer repeat of a 33-amino acid consensus sequence (SGRGGLGGQG AGAAAAAGGA GQGGYGGLGSQGT)<sup>15</sup>, were designed to bind to target minerals, silica and hydroxyapatite, through the incorporation of specific binding peptides.

The R5 silicifying peptide (SSKKSGSYSGSKGSKRRIL) found in diatoms, was selected for silk-silica composites, the location of the R5, N vs C terminal on the silk repeating unit, was assessed with respect to silicifying capabilities. The VTK peptide (VTKHLNQISQSY), identified *via* phage display was selected for hydroxyapatite binding, samples compared had the VTK peptide attached to the N, C and both termini of the silk repeating unit. Location and number of binding peptides was evaluated for mineralising capabilities.

Samples were primarily studied as films, it was shown that the naturally occurring beneficial physical properties of silk, high tensile strength and versatility, were not affected by the addition of binding peptides for both R5 and VTK containing samples. Further, we could manipulate the mechanical properties of the films by annealing them in the presence of methanol to increase the crystalline beta content, modifying their; hydrophobicity, stiffness and resistance to degradation.

After mineralisation studies were completed, chimeric samples were implemented as coatings on both silk and titanium scaffolds. The R5 domain silicifying capabilities were proven to be effective at silicification on the silk scaffold, however comparison to the titanium scaffold showed a more than 10-fold reduction in silica presence, a likely cause being the inert nature of the titanium being exhibited.

# Contents

<b>Chapter I: Introduction</b>	<b>1</b>
1.1 Silk as a Biomaterial	1
1.2 Biomimetic Approaches for Mineralisation	4
1.3 Overview of Hydroxyapatite and its Role as Bone Mineral	5
1.3.1 Structure Of Bone	5
1.3.2 Crystal Structure of Bone	6
1.3.3 Chemical HAP Synthesis	7
1.3.4 Biological HAP Synthesis	11
1.4 Silica	14
1.4.1 Silica in Nature	14
1.4.2 Chemistry and Synthesis of Silica	15
1.4.3 Bioinspired Silica Studies	16
1.5 Dental Implant	19
1.6 Motivations and Objectives	21
1.7 References	23
<b>Chapter II: Experimental Methods</b>	<b>31</b>
2.1 Atomic Force Microscopy	31
2.1.1 Finding the Reduced Elastic (Young's) Modulus of Silk Films	33
2.2 Scanning Electron Microscopy coupled with Energy Dispersive X-Ray Analysis	36
2.3 Powder X-ray Diffraction	37
2.3.1 The Scherrer Equation and Crystallite Size	38
2.4 Fourier Transform Attenuated Total Reflectance Infrared Spectroscopy	40
2.5 Dynamic Light Scattering and Zeta Potential	42
2.6 Wettability and Surface Energy Measurements	45
2.7 The Molybdenum Blue Assay	46
2.8 Absorption Colorimetry Plasma: The Bradford Assay	47
2.9 Inductively Couple Plasma – Optical Emission Spectroscopy	48
2.10 References	49

<b>Chapter III: Silk-Silica Composites for Biomedical Application</b>	<b>52</b>
3.1 Introduction	52
3.2 Methods and Materials	55
3.2.1 Construction of Recombinant Silk and Silk-Silica Chimeras	55
3.2.2 Expression and Purification of Recombinant Silk and Silk-Silica Chimeras	56
3.3.3 Silk Films	57
3.3.4 Solution Studies	59
3.3.5 Statistical Analysis	59
3.4 Results and Discussion	60
3.4.1 Recombinant Production of Silk-Silica Fusion Proteins	60
3.4.2 Solution Studies	61
3.4.3 Silk Films	63
3.4.4 Mechanism of Silica Particle Formation On Silk Films Made From The Genetic Constructs	68
3.4.5 Biological Response of Silk Constructs	70
3.5 Conclusion	73
3.6 References	75
<b>Chapter IV: Silk Composites Designed for Bone Regeneration</b>	<b>79</b>
4.1 Introduction	79
4.2 Materials and Methods	81
4.2.1 Construction of Recombinant and Silk-VTK Chimeras	81
4.2.2 Expression and Purification of Recombinant Silk and Silk-VTK Chimeras	82
4.2.3 Solution Studies	83
4.2.4 Silk Films	83
4.2.5 Statistical Analysis	85
4.4 Results and Discussion	85
4.4.1 Recombinant Silk Fusion Protein Design and Production	85
4.4.2 Solution Studies	86
4.4.3 Silk Films	90
4.4.4 Mechanism of Hydroxyapatite Formation in Solution Based Mineralisation	94
4.5 Conclusions	97
4.6 References	98

<b>Chapter V: Quantifying the Efficiency of Hydroxyapatite Mineralising Peptides via new Application of X-ray Diffraction Data</b>	<b>102</b>
<hr/>	
5.1 Introduction	102
5.2 Materials and Methods	103
5.2.1 Brushite Synthesis	103
5.2.2 Producing Brushite/HAP Mixtures	104
5.2.3 Assessment of Crystalline Phases Present by X-ray Diffraction	104
5.2.4 Infra-red Spectroscopy	104
5.2.5 Inductively Coupled Plasma – Optical Emission Spectroscopy	104
5.2.6 Scanning Electron Microscopy Couple to Energy Dispersive X-ray Analysis	105
5.2.7 Hydroxyapatite Synthesis Using Binding Peptides	105
5.3 Results	105
5.3.1 Conformation of Brushite Synthesis	106
5.3.2 Development of a Method to Assess Hydroxyapatite/Brushite Mixtures	106
5.3.3 Alternative Techniques	108
5.3.4 Quantitative Comparison of the Ability of Hydroxyapatite Binding Peptides to Affect Mineralisation	111
5.3.5 Quantitative Comparison of Hydroxyapatite Binding Peptide with Limited Reagents	114
5.3.6 Mechanism of Peptide Directed Mineralisation	116
5.3.7 Extension of Approach to Silk Chimeras	119
5.4 Conclusion	120
5.5 References	121
<b>Chapter VI: Response of Physical properties of Silk Films Towards Genetic Modifications, Annealing and Mineralisation</b>	<b>124</b>
<hr/>	
6.1 Introduction	124
6.2 Materials and Methods	126
6.2.1 Silk Fusion Protein Film Preparation and Mineralisation	126
6.2.2 Analysis Techniques	127
6.3 Results and Discussion	128
6.3.1 Parameter Development for Peak Deconvolution of FTIR Spectra	128
6.3.2 Method Development for Low Volume Biodegradation of Protein Films	131
6.3.3 Silk Chimeras: Incorporation of a Silicifying Domain	134
6.3.4 Silk Chimeras: Incorporation of a Hydroxyapatite Domain	138
6.4 Conclusions	142
6.5 References	144

<b>Chapter VII Silk-Silica Composites as Silk and Titanium Biomedical Scaffolds Coatings</b>	147
7.1 Introduction	147
7.2 Materials and Methods	150
7.2.1 Preparation of Silk Scaffolds	150
7.2.2 Preparation of Titanium Rods	151
7.2.3 Coating and Biosilicification of Scaffolds	151
7.2.4 Characterisation	152
7.3 Results and Discussion	153
7.3.1 Silk Scaffolds	153
7.3.2 Titanium Rods	157
7.4 Conclusion	161
7.5 References	164
<b>Conclusions and Further Work</b>	167
Future Work	171
Chimeric Silk as Scaffolds Coatings	171
Secondary Structures of Silk: Studies at the Interface	172
Appendix	174
Chapter III	174
Chapter IV	175
Chapter V	177
Chapter V1	179
Chapter VII	179
Publications:	180
Published at Times of Submission	180
Pending Reviewers Comments	180

# Chapter I

## Introduction

Provided here is a brief literature review intended to cover all background information for this investigation. Topics include discussion of silk as a biomaterial and its applicability towards forming composite biomaterials with silica and hydroxyapatite.

### 1.1 Silk as a biomaterial

Silk is a naturally occurring fibrous protein produced by epithelia cells in certain worms from the Lepidoptera order and spiders (Arachnida).<sup>1</sup> All silks have impressive qualities such as high tensile and mechanical strength rivalling high performance steel and polymeric fibres,<sup>2-12</sup> versatility towards use in different material states such as gels,<sup>13</sup> scaffolds,<sup>14-18</sup> films,<sup>19</sup> membranes<sup>20</sup> and powders<sup>21</sup> and they are bioacceptable<sup>22,23</sup> making them ideal candidates for biomedical application. Work completed here has focused on the spider silk, particularly the dragline silk from *N. clavipes* spiders. Spiders produce several diverse types of silk as shown in Figure 1.1, each having different properties tailored for specific applications.<sup>24</sup> The variance in mechanical properties arises from the differing amino acid sequences present.

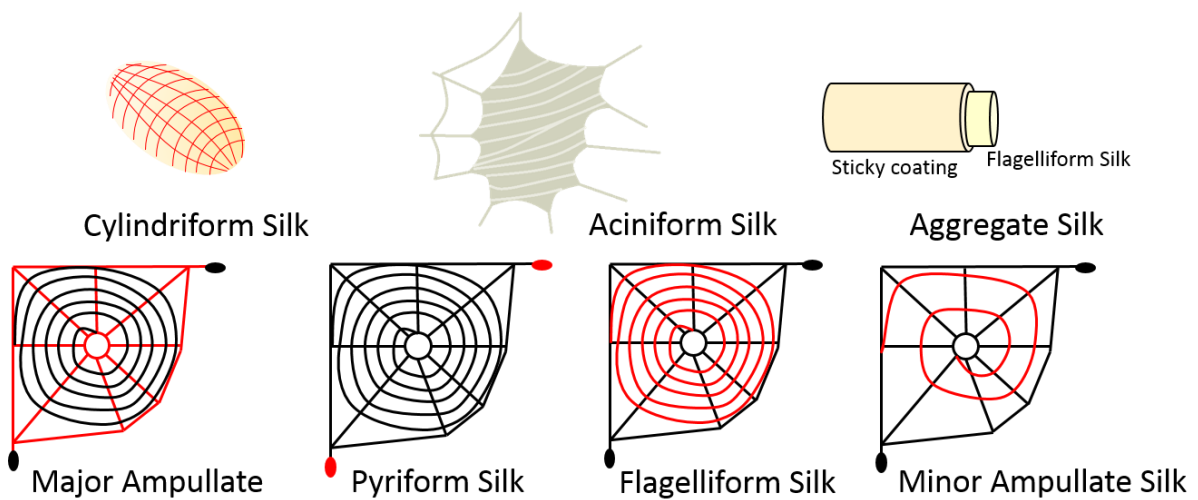


**Figure 1.1** The seven distinct types of silk spiders can produce. Each has different physical properties depending on its use, ranging from strength to support webbing and protect eggs, elasticity to produce web interiors or stickiness for anchoring points. Adapted from<sup>24</sup>

Similar to silkworm silk, the dragline silk of the *N. clavipes* is largely formed from glycine and alanine with arginine, glutamic acid and proline also present.<sup>25</sup> Dragline silk consists of two large proteins (approx. 300 KDa), spidroin 1 and spidroin 2.<sup>24</sup> Repeating units of alanine and glycine form crystalline domains (secondary  $\beta$  structures) that give silk its impressively high tensile strength. Figure 1.2 shows the production of silk in the proximal region of the glands that line a spider's lumen and the self-assembly process resulting in the formation of liquid crystals<sup>26</sup> a prerequisite to form highly ordered fibrils. Regions containing GGX termed a glycine helix, where X is likely Leucine, Tyrosine or Glutamic acid, give rise to heightened elasticity.<sup>27</sup>

In addition, the ability to manipulate the secondary structure of silk *in vitro*, to induce a higher percentage of  $\beta$  conformers, gives an added level of control most beneficial for biomedical application. The increased level of crystallinity results in increased resistance to degradation and mechanical strength. Many annealing processes have been employed to achieve greater levels of  $\beta$  secondary structure in silks such as: methanol vapour,<sup>28,29</sup> water vapour,<sup>4</sup> and high pressure/high temperatures.<sup>30,31</sup>

Dragline silk is one of the strongest naturally occurring materials, with a Young's modulus of 7.38 – 22 GPa,<sup>32</sup> it is used for safety and web construction, Figure 1.1. Despite the superior physical properties of dragline spider silk, wider use, as seen for silkworm silk, has been restricted due to the impracticality of domesticating spiders coupled with low productivity.

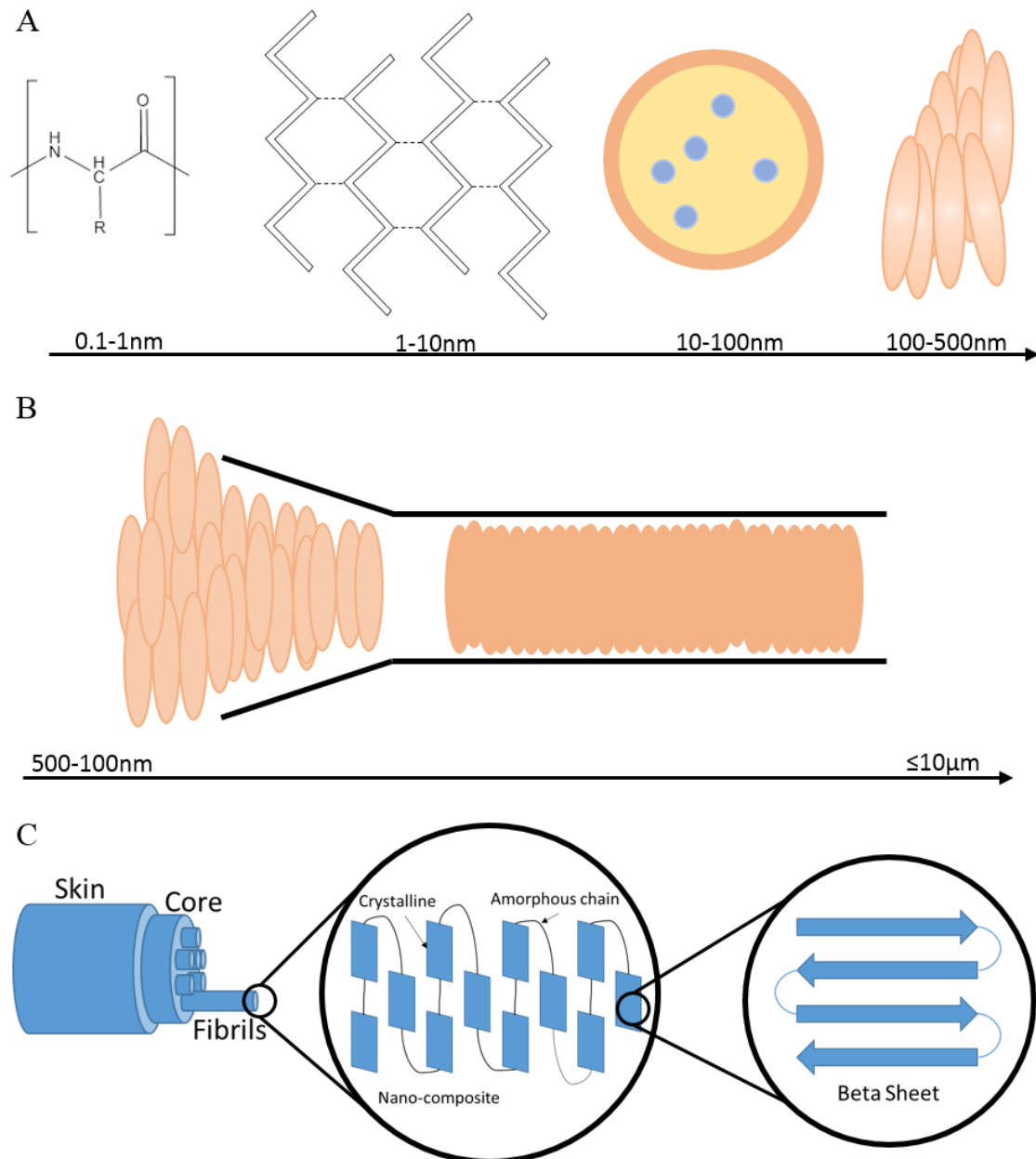


**Figure 1.2** **A)** The steps of silk self-assembly: the amino acid sequence is formed, beta sheet formation is induced *via* hydrogen bonding and hydrophobic interactions resulting in self-assembly, then inter- and intra- molecular interactions drive the formation of micelles where hydrophilic spacer groups result in small region of trapped water, finally an increase in concentration results in gelation to form liquid crystals. **B)** The liquid crystals are transformed *via* environmental factors (for example: low pH, methanol, and electric fields) into highly ordered fibrils (webbing) as they travel down the spinning ducts. **C)** Simplified diagram of the structure of silk emphasising the ordered crystalline structure embedded in a non-crystalline/amorphous matrix.<sup>33</sup> Adapted.<sup>34</sup>

Silk does have a disadvantage, in some construct forms it can be susceptible to compression, meaning added rigidity would improve the material with respect to medical application. The production of composite materials allows additional properties to be added and any negative aspects minimised.

To create composites, current research looks to nature for inspiration, the inspiration can take the form of inorganic materials that have been utilised by living organisms and the methods of production and/or incorporation.<sup>35,36</sup> For the proposed application in dental tissues, the relevant inorganic materials are the titania surface of the implant, hydroxyapatite (HAP) that bones are made from and the small amount of natural silica present in the body used in bone regrowth.<sup>37</sup> To allow the silk material to bind and promote the precipitation of these different materials, peptides identified for having high affinities for specific minerals can be attached to the silk to widen the capabilities of the material.<sup>28,29,38,39</sup>

## 1.2 Biomimetic approaches for mineralisation

Biomimetalisation is a broad term used to describe any process that results in the condensation of inorganic materials involving biological induction and/or control.<sup>40</sup> These biosynthetic routes can be specific or non-specific, it is the first that interests researchers, as there are many cases where mineralisation occurs in nature through the production of specific (both to the inorganic material and the organism) molecules that can control the shape and size of minerals produced, meaning these molecules can control the physical and chemical properties of the material being produced. By identifying these naturally occurring molecules, they can be synthesised (or a derivative can be synthesised) in order to be employed for controlled *in vitro* mineralisation, this is termed a biomimetic approach to mineralisation, the mimicking or inspiration of mineralisation from nature.<sup>41</sup>

Biomolecules for mineralisation work in three different ways; confinement, activation and templating to direct the mechanism of mineralisation.<sup>42</sup> Self-assembly approaches are now widely used for the production of minerals that are controlled on the nano- to macroscale resulting in “chemically-diverse, structurally-complex and bio-responsive materials and devices”.<sup>43-46</sup>

Hydroxyapatite (HAP) and silica binding peptides have been identified (as discussed below) for this purpose, to produce a biomedical material that can control biomineralisation to aid bone repair/regrowth. HAP mineralisation is often referred to as calcification, and the deposition of silica is known as silicification.

### **1.3 Overview of Hydroxyapatite (HAP) and its role as bone mineral**

#### **1.3.1 Structure of bone**

Every mammalian bone consists of osseous (supportive connecting) tissue, epithelium, adipose tissue and nervous tissue. Organic material, predominantly a three dimensional collagen framework (thought to provide nucleation sites for hydroxyapatite growth),<sup>47,48</sup> makes up 20-25%, up to 5% is water and the remaining 75% is inorganic materials, most of which is exclusively HAP.<sup>49</sup> Bones are used for; support, protection, mineral homeostasis (99% of the bodies' calcium is found in bone),<sup>50</sup> blood cell production and triglyceride storage.<sup>51</sup>

Bone is not at equilibrium, it is constantly undergoing 'remodelling' (the construction of new bone and the degradation of old bone tissue), in order to correct imperfections in the crystal structure, principally the presence of carbonate, sodium and other ions and the deficiency of calcium and hydroxide groups required for bone mineral to be metabolically active.<sup>49</sup> Cells responsible for bone regrowth are; osteogenic cells which are bone stem cells that develop into osteoblasts known as bone building cells. Osteoblasts synthesise and secrete collagen fibres, as they become surrounded by an extracellular matrix they morph into 'mature' bone cells responsible for maintaining the daily metabolism of the bone, the latter are known as osteocytes. Lastly, osteoclasts release enzymes and acids to digest underlying cellular bone matrix for reabsorption.

The formation of bone, ossification or osteogenesis, occurs under four conditions; as an embryo develops, bone growth, remodelling and when repair is needed from bone fractures, the forth being the focal point for this investigation. There are several types of fractures that can occur, but for the most part the natural repairing process follows these steps<sup>52</sup>:

1. Formation of a fracture hematoma, where a mass of blood builds up around the fracture site resulting in inflammation and causing the surrounding bone

cells to die, this can take up to 8 hours. Phagocytes and osteoclasts remove dead or damaged tissue over the course of several weeks.

2. Fibroblasts produce collagen fibres and chondroblasts produce fibrocartilage to bridge the ends of the broken bone together, this can take up to three weeks.
3. Osteogenic cells around the healthy bone tissues develop into osteoblasts producing spongy bone. Fibrocartilage is converted into spongy bone.
4. Bone remodelling occurs replacing spongy bone with compact bone, dead portions of the broken bone are gradually resorbed by osteoclasts.

Despite bone having a generous blood supply, healing can take several months as the calcium and phosphorous necessary to strengthen and harden new bone are only gradually deposited. The levels of calcium and phosphorus surrounding healthy bone tissue is kept at a steady concentration governed by the cells on the bone surface.<sup>53</sup> Calcification mechanisms differ between bone and cartilage as bone contains calcium binding peptides. Factors that can progress calcification include:

1. Increasing the  $\text{Ca}^{2+}$  and  $\text{HPO}_4^{2-}$  concentration in the local environment to induce spontaneous mineralisation.
2. Using substances known to act as nucleation sites.
3. Removal of mineralising inhibitors

Based on this, modern medicine now looks to incorporate methods of increasing calcium and phosphorous concentrations at breakage sites, work discussed here uses the biomimetic approach to accomplish this.

### 1.3.2 Crystal structure of bone

The inorganic calcium phosphate found in bone is hydroxyapatite (HAP), however the crystal structure present differs from that of 'pure' highly crystalline HAP. The general formula for HAP is  $\text{Ca}_{10}(\text{PO}_4)_6(\text{OH})_2$ , ions and groups are arranged in a hexagonal system  $\text{P6}_3/\text{m}$ , with some minor exceptions (only in non-calcified tissue) as monoclinic systems.<sup>54-57</sup> Cell lattice parameters;  $a=b=9.432 \text{ \AA}$  and  $c=6.884 \text{ \AA}$  with  $\gamma = 120^\circ$ , Figure 1.3. An exact stoichiometric Ca:P ratio would be 1.67.

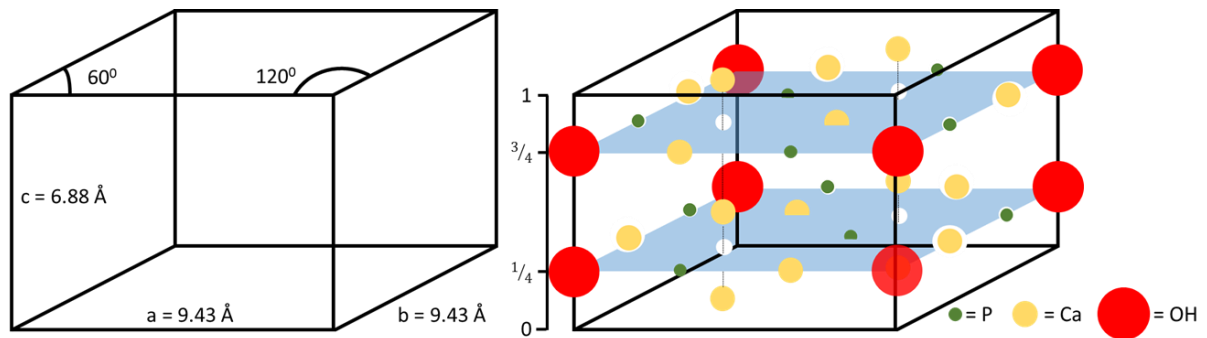


**Figure 1.3** Unit cell of HAP. Phosphate ions are found in a tetrahedral arrangement, hydroxyl groups are located on the c axis. Ca ions are found in two different sites: columns of  $\text{Ca}^{2+}$  ion and equilateral triangles. Phosphorous atoms lie in two height planes:  $\frac{1}{4}$  and  $\frac{3}{4}$ . Adapted.<sup>58,59</sup>

Naturally occurring HAP is rarely stoichiometric and the crystals formed are known to be small in size forming plates or needles, lack chemical perfection and contain many defects. These attributes are surprisingly advantageous as it results in bone being insoluble and therefore stable whilst being reactive for resorption.<sup>60</sup>

Defects can occur due to the varied chemical constituents of bone. Phosphate groups can undergo substitution by carbonates, hydroxyl groups can be replaced with fluoride, chloride or carbonate and calcium ions can be exchanged with magnesium ions. Other ions present include sodium and potassium.<sup>61</sup> The concentrations of each vary between the type of tissue with respect to its bioactivity and desired properties. The closer the Ca/P atomic ratio is to 1.67 the more biologically stable the compound is.<sup>62</sup> A decrease in the atomic ratio tends to mean the compound will be more bioactive.

### 1.3.3 Chemical HAP Synthesis

Chemical synthesis of HAP has been developed over many years using a variety of synthetic routes. Initial growth of hydroxyapatite crystals is rapid, occurring within minutes, crystals can then grow slowly over time, Figure 1.4A. In some situations, Ostwald ripening can occur where smaller crystals dissolved in solution then redeposited onto larger crystals, Figure 1.4B. However, the difficulty of the synthesis arises from the wide range of crystal phases that can be produced, Table 1.1 shows all biologically significant calcium phosphates, not including substituted variants. It is because of this that synthesis methods are intended to be as simple as possible,

often using just two reagents for sources of calcium and phosphate in a controlled environment. Additional ions present can result in a substituted HAP structure being produced or the mechanism of crystallisation being directed toward an alternate crystal phase. Table 1.2 shows a selection of chemical methods developed for *in vitro* synthesis of HAP, along with the reported atomic ratio of Ca:P.

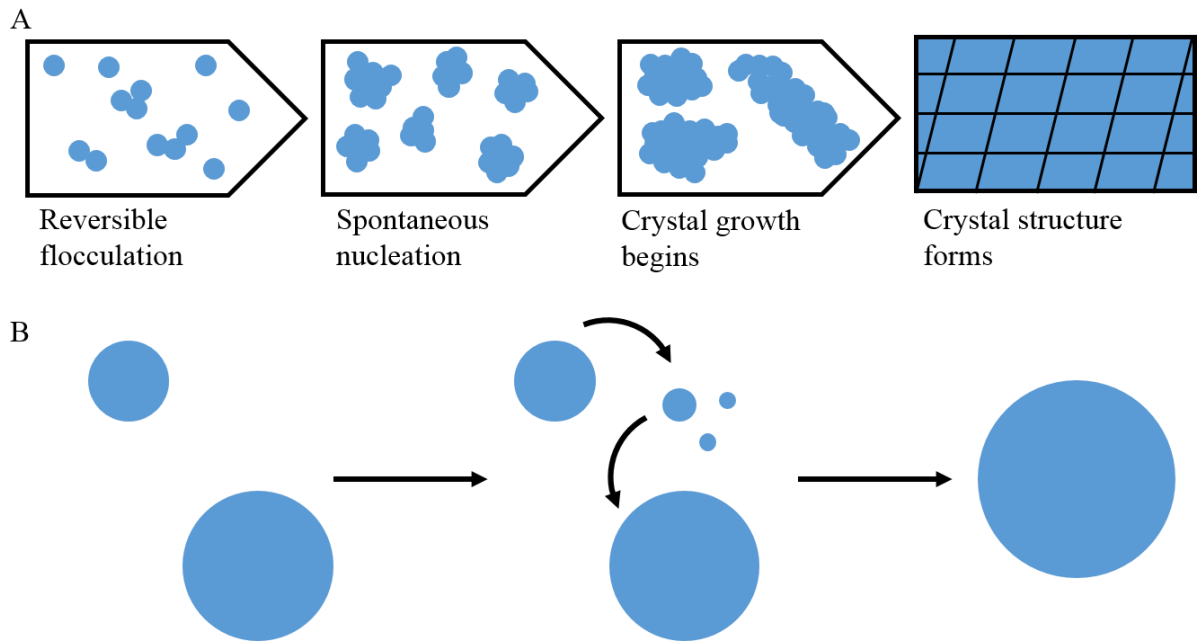


**Figure 1.4** A) Basic overview of crystal growth where flocculation results in nucleation beginning crystal growth and forming a larger crystal structure B) Ostwald ripening; dissolution of smaller crystals occurs which are then able to form part of the larger crystal.

Abbreviation	Formula	Name (mineral)	Ca/P ratio	pK <sub>sp</sub> (25°C)	pH stability	Occurrence in biological tissues
HA	Ca <sub>10</sub> (PO <sub>4</sub> ) <sub>6</sub> (OH) <sub>2</sub>	Hydroxyapatite	1.67	116.8	9.5-12	Bone, dentin, enamel, dental calcifications, urinary stones, atherosclerotic plaques
OCP	Ca <sub>8</sub> H <sub>2</sub> (PO <sub>4</sub> ) <sub>6</sub> ·5H <sub>2</sub> O	Octacalcium phosphate	1.33	96.6	5.5-7.0	Dental and urinary calculi
β-TCP	Ca <sub>3</sub> (PO <sub>4</sub> ) <sub>2</sub>	β-Tricalcium phosphate (whitlockite)	1.5	28.9		Dental and urinary calculi, soft-tissue deposits, arthritic cartilage, usually present as β-TCMP
α-TCP	Ca <sub>3</sub> (PO <sub>4</sub> ) <sub>2</sub>	α-Tricalcium phosphate	1.5	25.5		Not found
ACP	Ca <sub>3</sub> (PO <sub>4</sub> ) <sub>y</sub> ·nH <sub>2</sub> O	Amorphous calcium phosphate	1.2-2.2			Soft-tissue calcifications
MCPM	Ca(H <sub>2</sub> PO <sub>4</sub> ) <sub>2</sub> ·H <sub>2</sub> O	Monocalcium phosphate monohydrate	0.5	1.14	0-2	Not found
MCPA	Ca(H <sub>2</sub> PO <sub>4</sub> ) <sub>2</sub>	Anhydrous Monocalcium phosphate	0.5	1.14		Not found
DCPD	CaHPO <sub>4</sub> ·2H <sub>2</sub> O	Dicalcium phosphate dehydrate (brushite)	1.0	6.59	2-6	Dental calculi, urinary stones, chondrocalcinosis
DCPA	CaHPO <sub>4</sub>	Anhydrous dicalcium phosphate	1.0	6.90		Not found
TICP	Ca <sub>4</sub> (PO <sub>4</sub> ) <sub>2</sub>	Tetracalcium phosphate	2.0	38-44		Not found
CDHA	Ca <sub>10-x</sub> (HPO <sub>4</sub> ) <sub>x</sub> (PO <sub>4</sub> ) <sub>6-x</sub> (OH) <sub>2-x</sub>	Calcium deficient hydroxyapatite	1.5	85.1	6.5-9.5	Not found

**Table 1.1** Biologically significant phosphates: properties and natural presence.

Reagents		Conditions	Product Ca/P molar ratio	Ref	Comment/s	Date
0.33 M 0.2 M	Ca(NO <sub>3</sub> ) <sub>2</sub> ·4H <sub>2</sub> O (NH <sub>4</sub> ) <sub>2</sub> HPO <sub>4</sub>	Constant pH 12 (ammonia CO <sub>2</sub> free used) 25 <sup>o</sup> C Vigorous stirring 2 hours	1.67	63	Filtering may be aided by ten minutes of gentle boiling. Heating to 800 <sup>o</sup> C to dry and harden	1963
0.25 M 0.75 M	(NH <sub>4</sub> ) <sub>2</sub> HPO <sub>4</sub> CaCl <sub>2</sub> /Ca(NO <sub>3</sub> ) <sub>2</sub>	pH 10.5 (NH <sub>4</sub> OH used) 25 <sup>o</sup> C Constant stirring < 2 weeks	1.71	64	A closed system was used to avoid excessive CO <sub>2</sub> absorption	1965
1.3 x 10 <sup>-2</sup> M	CaCl <sub>2</sub> Na <sub>2</sub> HPO <sub>4</sub>	pH 7.4 (0.1 M HCl used) seeded see below	1.6 (1.2)	65	Two stage crystal growth initiated using a seed solution (see next entry)	1970
0.5 M 0.3 M	CaCl <sub>2</sub> Na <sub>2</sub> HPO <sub>4</sub>	pH 8.5 – 10 (NaOH used) 70 <sup>o</sup> C Constant stirring – seed solution produced		65	Exclusion of CO <sub>2</sub> via nitrogen pass being bubbled through	-
Equimolar	CaCl <sub>2</sub> NaH <sub>2</sub> PO <sub>4</sub>	pH 7.4 (using NaOH/H <sub>3</sub> PO <sub>4</sub> ) 25 <sup>o</sup> C / 37 <sup>o</sup> C	1	66	Not stirred Calcium chloride always added to sodium phosphate	1971
0.24 M 0.4 M	(NH <sub>4</sub> ) <sub>2</sub> HPO <sub>4</sub> Ca(OH) <sub>2</sub>	Microwave irradiated 20 minutes In air/under nitrogen	1.65	67	Equivolumes used, microwaving controlled to avoid vigorous boiling	1996
0.28 M 0.24 M	Ca(NO <sub>3</sub> ) <sub>2</sub> NH <sub>4</sub> H <sub>2</sub> PO <sub>4</sub> /(NH <sub>4</sub> ) <sub>2</sub> HP O <sub>4</sub>	pH 7.4 (using NH <sub>4</sub> OH for reagent, 1M Tris-TAM buffer post addition) 4/38 <sup>o</sup> C	1.45-1.76	68	Two different reagents used to maintain pH. Initial pH 4.5 increasing to a plateau at pH 7.5	2009
1 M 0.6 M	Ca(NO <sub>3</sub> ) <sub>2</sub> ·4H <sub>2</sub> O (NH <sub>4</sub> ) <sub>2</sub> HPO <sub>4</sub>	> pH 10 (using NH <sub>4</sub> OH) ≤10-minute reflux in microwave	1.67	69	(NH <sub>4</sub> ) <sub>2</sub> HPO <sub>4</sub> was added dropwise (2ml/min)	2012

**Table 1.2** Chemical routes previously used to produce HAP.

### 1.3.4 Biological HAP Synthesis

The biomimetic approach has been applied to further develop methods for HAP synthesis towards being more compatible for biomedical application. However, unlike other minerals such as silica (and the R5 peptide), there has been no naturally occurring peptide identified that binds and directs mineralisation towards precipitation of HAP.

To address this two different approaches have been employed by several groups, the first is the use of single amino acids (both phosphorylated and non-phosphorylated) during mineralisation. Table 1.3 shows a selection of developed methods and their success measured in terms of atomic ratio of the mineral formed. Results varied according to the amino acid used and the molar ratio of the chemical reagents and the amino acid present.

In each case, it can be argued that results were limited due to the small exclusive scale of experiments. The isolated results, focusing on one synthetic route and a handful of amino acids suggests that optimum conditions for reliable control of mineralisation using amino acids has yet to be found.

The second approach was to employ the phage display technique to identify HAP peptide binders. Briefly, phage display uses bacteriophages (viruses that infect bacteria) to categorise the binding affinities of proteins and peptides to a specific target compound. The process involves the addition of the selected protein onto the phage coat gene by inserting an encoding gene into the phage, this causing the phage to 'display' the selected protein. The displaying phages are then screened by being exposed to the target compound. A series of washing, elution and amplification steps are then performed before analysis is completed to compare binders, Figure 1.5.<sup>70</sup>

Ca Source (mM)	P Source (mM)	AAs (mM)	pH	Temp °C	Time hrs	Year	Ca:P ratio	Ref.
CaCl <sub>2</sub> (25)	(NH <sub>4</sub> ) <sub>2</sub> HPO <sub>4</sub> (15)	PSer, Glu (20-200)	9.5	37	72	2015	1.69	71
CaCl <sub>2</sub> (3.1)	NaH <sub>2</sub> PO <sub>4</sub> (1.9)	Arg, Glu (10)	7.4	37	48	2012, 2015	1.22-1.35	72
CaCl <sub>2</sub> (0.5)	KH <sub>2</sub> PO <sub>4</sub> (0.3)	Asp, Glu (0.2)	8.45	25	48-96	2011	1.61	73
(CH <sub>3</sub> COO) <sub>2</sub> Ca (75)	H <sub>3</sub> PO <sub>4</sub> (50)	Ala, Asp, Arg (150)	10	25	24	2009	1.5-1.62	74
Ca(NO <sub>3</sub> ) <sub>2</sub> ·4H <sub>2</sub> O (ns)	H <sub>3</sub> PO <sub>4</sub> (ns)	Gly, Ala, Ser, Lys, Asn (na)	9	80	18	2007	1.72-1.88	75
CaCl <sub>2</sub> (0.25-0.5)	KH <sub>2</sub> PO <sub>4</sub> (0.17-0.33)	Leu (0-1.52)	7.4	37	ns	2007	1.67	76
Ca(NO <sub>3</sub> ) <sub>2</sub> (33.4-38)	(NH <sub>4</sub> ) <sub>2</sub> HPO <sub>4</sub> (20)	Gly, Asp, Glu, Lys (4)	7.5	37	24	2006	1.58-1.67	77
Ca(NO <sub>3</sub> ) <sub>2</sub> ·4H <sub>2</sub> O (540)	(NH <sub>4</sub> ) <sub>2</sub> HPO <sub>4</sub> (320)	Asp, Glu (50-200)	ns	90	5	2006	1.68	78

**Table 1.3** Biological syntheses used for producing HAP using single amino acids. NS: not specified

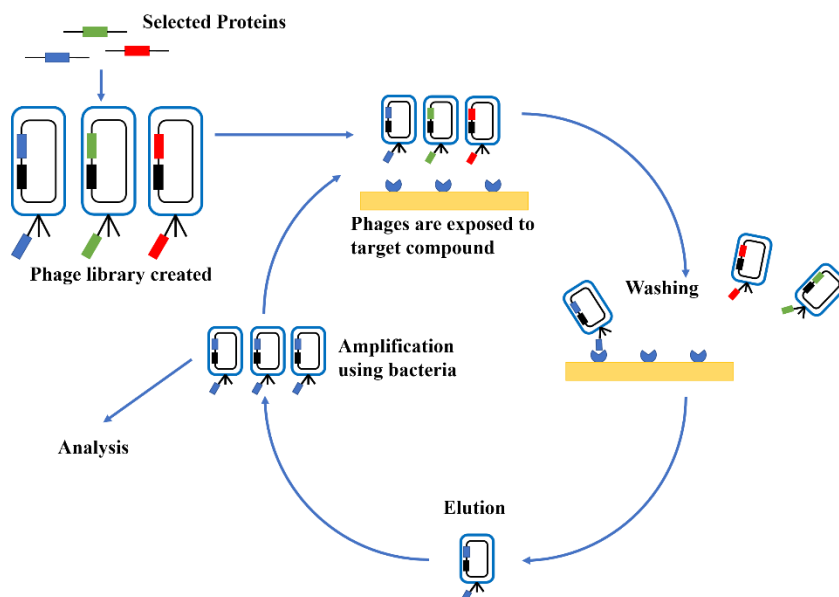


**Figure 1.5** Simplified steps of phage display to identify binding peptides and proteins.

Three peptides: CaP(S) STLPIHEFSRE,<sup>79-82</sup> CaP(V) (or VTK) VTKHLNQISQSY,<sup>81,83-86</sup> and CaP(H) SVSVG MKPSRP,<sup>79,84,87,88</sup> were all identified *via* phage display as HAP binding peptides. However, as shown in Table 1.4, the three HAP binding peptides have varying properties suggesting that mechanisms directing mineralisation also vary. CaP(H) and CaP(V) have an overall positive net charge with high isoelectric points (>pH 9.5) indicating peptides remain mostly unfolded at circumneutral pHs and direct mineralisation through electrostatic interactions with the negative phosphate ions.<sup>81,87</sup> Conversely, CaP(S) has a negative net charge with an isoelectric point of pH 5.2, suggesting that some aggregation may occur under *in vivo* conditions, with mineralisation a result on interaction with positive calcium ions.<sup>80-82,89</sup>

	Sequence	Net charge at pH 7.4	Average Hydrophobicity	pI
CaP(H)	SVSVG MKPSRP	+2	+13.87	11.71
CaP(S)	STLPIHEFSRE	-1	+16.67	5.23
CaP(V)	VTKHLNQISQSY	+1	+13.05	9.54

**Table 1.4** Properties of the HAP binding peptides Cap(S), CaP(H) and Cap(V).

Comparison of mineralisation capabilities for the three peptides is observed in Chapter V; however, HAP silk binding chimeras could only be produced using the CaP(V) sequences. Addition of CaP(S) and CaP(H) to a silk repeating unit did not produce samples that could be expressed efficiently, meaning silk-HAP chimeras discussed in Chapter IV were limited to only CaP(V) incorporated silk samples.

The inclusion of all three peptides in the study was planned as seen in Chapter V, however due to expression issues, discussed in Chapter IV, it was not possible to include all three as silk composite materials.

## 1.4 Silica

### 1.4.1 Silica in Nature

Many biomedical devices are made or incorporate silica because of its high bioactivity. However, silica's osteoinductive nature,<sup>28</sup> has proven to be not just beneficial but essential for bone growth. Animal studies completed in the 1970's showed that a silicon deficient diet resulted in defects in the connective and skeletal tissues,<sup>90,91</sup> with high levels of silicon found at bone regrowth sites.<sup>92</sup> Despite silicon being one of the most abundant elements in the body, 1-2g,<sup>37</sup> the mechanism of how it aids bone regrowth is somewhat unclear. Hench et al. showed that silicon substituted HAP and silicon containing implants had a better binding affinity for bone than their silicon free counter parts but it was Porter et al. that posed a mechanism for silicon aided bone regrowth, the use of silicon substituted HAP produced more ordered collagen fibrils with more mature bone formation than when HAP was used alone.<sup>93,94</sup> It is thought that silicon may be involved in the synthesis and/or stabilisation of collagen, and as stated previously collagen is known to provide nucleation sites for *in vivo* HAP formation.<sup>49</sup>

The wide and frequent occurrence of silica in nature is well documented.<sup>95</sup> The morphologies that biogenic silica can take are impressive in their variability, with many difficult or even impossible to replicate *in vitro*. Commonly quoted examples include the Equisetum plant that contains silica phytoliths and diatoms (eukaryotic cells) that produce shells made of silica for structural support and protection.<sup>96,97</sup> Silicification in nature often involves the utilisation of specific proteins known as silaffins that are able to promote and/or control the deposition of silica particles. In diatoms, this occurs in a silaffin rich silica deposition vesicle.<sup>35</sup> The R5 peptide

(SSKKSGSYSGSKGSKRRIL),<sup>98-101</sup> has been identified from *C. fusiformis* diatoms as the silica promoting molecule, and has further been proven to be effective with *in vitro* studies.<sup>98,99,102</sup>

The key to the R5 peptide's silicifying power is its ability to direct self-assembly using a combination of electrostatic attractions and hydrogen bonding to form supramolecular structures with areas rich in amine groups, these structures provide nucleation sites for silica deposition, working as catalysts and templates for silica formation *in vivo*.<sup>100,103</sup>

#### 1.4.2 Chemistry and Synthesis of Silica

Silica materials generally include: siloxanes ( $\equiv\text{Si-O-Si}\equiv$ ), silanols ( $\equiv\text{Si-OH}$ ), ionic siloxide ( $\text{Si-O}^-$ ) and water, figure 1.6. The proportionality of silanol to siloxane dictates the physical properties of the material, as silanols are hydrophilic and siloxanes are hydrophobic.

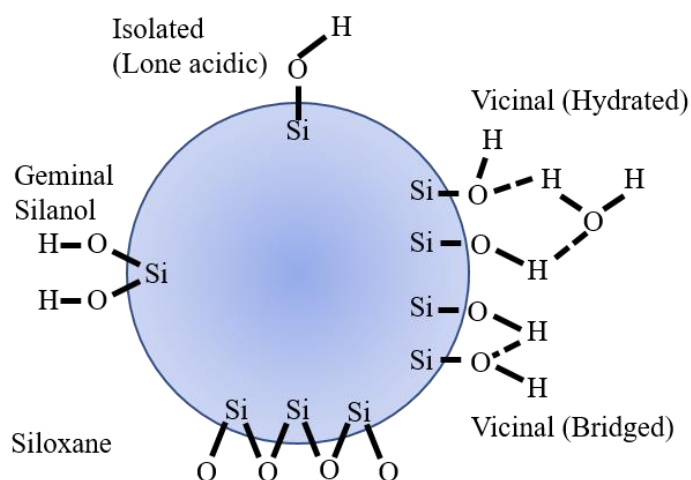


**Figure 1.6** Silanol chemistry of a silica particle showing; isolated, vicinal (hydrated and bridged), geminal, silanol and siloxane groups.

Silica is produced through the condensation of orthosilicic acid, it can occur spontaneously *in vivo* when there is an excess concentration present (100-200ppm). The process is ionic as the rate of condensation is proportional to the concentration of  $\text{OH}^-$  ions above pH 2 and  $\text{H}^+$  ions below pH 2.<sup>104</sup>

The condensation and aggregation process that results in the formation of silicas has three general steps. 1) The polymerisation of monomers producing stable nuclei 2) growth of nuclei to form spherical particles and 3) the aggregation of particles to form branched chains or motifs,<sup>104-108</sup> Figure 1.7. Further growth can occur through Ostwald ripening as discussed earlier, Figure 1.4B. This mechanism minimises uncondensed SiOH and maximises the amount of Si-O-Si bonds by favouring the formation of cyclic structures. The addition of salts and control of pH can both be used to control aggregation of silica particles during condensation.<sup>104</sup>

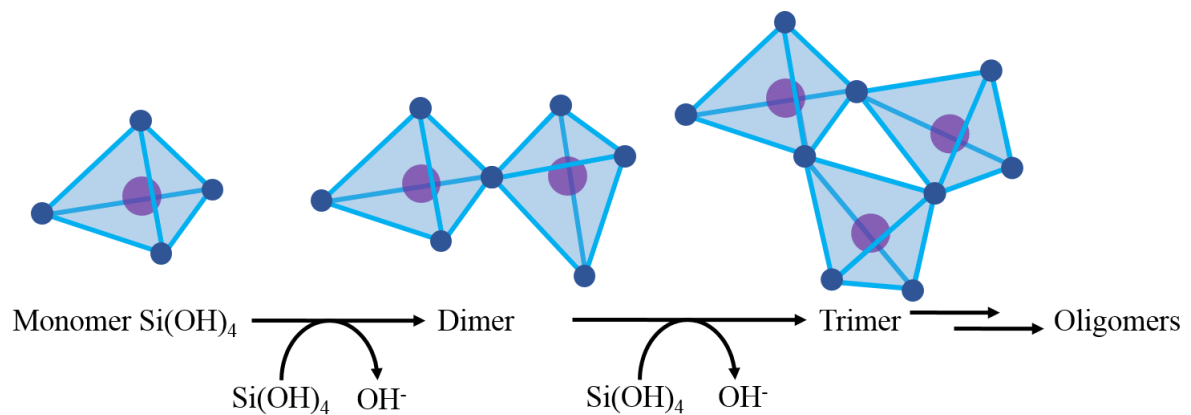


Figure 1.7 Initial stage of silica production, starting from single monomers coming together to form larger cyclic structures.

Silica nanoparticles have several beneficial properties making them appropriate for biomedical application, such as being: biocompatible, bioresorbable, permeable through biological pathways, having large surface areas and being easily functionalised. The hydroxyl groups present on the silica surface are the key to functionalising these materials, with studies into; carboxyl,<sup>109</sup> phenyl<sup>110</sup>, amine,<sup>111</sup> thiol<sup>112</sup> and methyl<sup>113</sup> functionalised silica being completed. Silica has also been proven to have immunosuppressant,<sup>114</sup> hypocholesterolemic,<sup>115</sup> anti-apoptotic<sup>116</sup> and anti-histamine<sup>117</sup> functions.

### 1.4.3 Bioinspired Silica Studies

Single amino acids, homo-polypeptides and peptides have all been used to develop *in vitro* methods of silicification with high control over the morphology of the silica

particles produced. Table 1.5 below gives an overview of biosynthetic routes that have been employed to control silicification and the main finding from each study.

Biological influence	Sequence	Result	Ref
R5	SSKKSGSYSGSKGSKRRI L	Silaffin identified	98
R5	RRIL	Essential for silicification, directing group for self- assembly	100
Diatom derivative	KASK	Nanometer scale silica particles	118
	KAEK	Grainy silica	
	KAAK	~100nm Silica particles	
Amino Acids and homo-polypeptides	S, K, P, D	Catalytic effect: Peptides > amino acids	119
Polylysine	K <sub>n</sub> n = 20 - 222	Longer chains gave hexagonal plates Smaller chains gave spherical particles	120
Range of peptides (Isolated by Phage Display)	YITPYAHLRGGN KSLSRHDHIIHH LDHSLHS MHRSDLMSAAVR MSPHPHPRHHHT RGRRRRLSCRL	Positively charged peptides strongly attracted to anionic silica  Polar groups can attach <i>via</i> silanol or siloxide groups through hydrogen bonding, ion-dipole, dipole-dipole or Van Der Waal interactions	121
Range of peptides (Isolated by Phage Display)	KLPGWSG AFILPTG LDHSLHS	Peptide binding can be controlled with subtle changes on the silica surface	97
Polylysine Polyarginine	K <sub>n</sub> (n = 25, 35, 155, 1005) R <sub>n</sub> (n = 65)	Positive groups create concentrated areas of negative silicic acids promoting silica condensation	122
Polylysine	K <sub>n</sub> n = 56, 264, 300, 400	Homo-peptide forms helical structures that induce silica plate formation	123
Amino Acids and homo-polypeptides	G, R, N, Q, S, Y, T, P, A, K K <sub>n</sub> n = 1-5 G <sub>n</sub> = 1, 4, 5	Amino acids could affect kinetics. N containing gave larger particles, hydroxyl/hydrophobic containing gave smaller particles. No. G present had no effect, increasing K presence can control porosity of silica	124

Table 1.5 Bioinspired silicification routes developed using amino acids and/or peptides and the influence the biological reagent on silica deposition.

The amorphous structures often produced by silica are brittle and lack beneficial tensile properties, making their use as the sole material for bone and dental implants impossible. By combining low levels of silica (either *in vitro* or *in vivo*) with silk to produce composite materials, a union of the best attributes of both is created. Materials produced by the Perry/Kaplan collaboration previously saw silicifying domains attached to a silk repeating units of varying lengths.<sup>29,39,125,126</sup> Table 1.6 below shows the silk and silicifying domains previously used to produce chimeric silk biomaterials.

Silk Domain	Sequence	Silicifying Domain	Sequence	Year	Ref
derived from <i>N. clavipes</i> dragline silk	(SGRGGLGGQGA GAAAAAGGAGQ GGYGGLGSQGT) <sub>6</sub>	A3	MSPHPHPRHH HT	2015	126
		A1	SGSKGSKRRI L		
		R5	SSKKSGSYSG SKGSKRRIL		
<i>N. clavipes</i> dragline silk	(SGRGGLGGQGA GAAAAAGGAGQ GGYGGLGSQG) <sub>15</sub>	A3	MSPHPHPRHH HT	2012	29
		A1	SGSKGSKRRI L		
		R5	SSKKSGSYSG SKGSKRRIL		
<i>N. clavipes</i> spider dragline silk	[SGRGGLGGQGA GAAAAAGGAGQ GGYGGLGSQG] <sub>n</sub> n = 6 or 15	Pep 1	KSLSRHDHIIH HH	2012	125
		R-Pep1	RKSLSRHDHI HHH		
		R5	SSKKSGSYSG SKGSKRRIL		
<i>B. mori</i> silkworm cocoon	-	Silica particles	-	2010	28
<i>N. clavipes</i> spider dragline silk	(SGRGGLGGQGA GAAAAGGAGQG GYGGLGSQGT) <sub>n</sub> n = 6 or 15	R5	SSKKSGSYSG SKGSKRRIL	2006	39

**Table 1.6** Previous silaffins and silk repeating units used by the Perry/Kaplan collaboration to produce silk-silica composites.

## 1.5 Dental Implants

Dental implants are a semi-permanent realistic-looking solution to missing teeth; by filling gaps with supportive materials there is a reduction in strain and an added

protection for the surrounding teeth and jaw bone.<sup>127</sup> Dental implants are unique in the sense they can be employed regardless of the cause of the missing tooth/teeth.<sup>128</sup> An implant gives a more natural feel in the mouth when compared with dentures that can often impair a person's ability to speak and eat.

The disadvantage of using dental implants is that a surgical procedure is required to insert the device, which is abrasive to the surrounding tissue and several follow up appointments are required to finish the work leading to more discomfort in the area. The process leaves a patient vulnerable to infection and requires a significant amount of healing time which can vary depending on the patient.

Dental implants tend to be made of titanium or a titanium alloy,<sup>129-133</sup> due to their low density, high strength, non-hazardous nature and high resistance to corrosion.<sup>134</sup> However the insertion process of a pure titanium/titanium alloy often results in an inflammatory response from surrounding tissues.<sup>135</sup>

The healing process must result in the acceptance of the implant with a strong complete bone-titanium interface produced. This process can take 6-12 months and is not always successful; a hindrance to this process is the inert properties of titanium alloys preventing bone from easily binding to the surface. This can be overcome by treating the implant with a coating before insertion.<sup>134-144</sup>

Previous work in the Perry group on silk composite materials for bone and dental implant coatings, has focused on the incorporation of silica *via* the use of known silicifying peptides attached to the silk, (at the C termini only), that promote condensation of silica particles onto silk materials. *In vitro* studies were conducted to assess if combining these two materials will have a significant effect on the physical and chemical properties of the silk which would allow it to be produced into feasible medical devices.<sup>29</sup>

The genetically engineered chimeric silk samples used prior to the current study always consisted of: a His<sub>6</sub> tag (for purification), a silica binding peptide such as R5, A1 or A3, see table 1.7) and a long linker connecting the His tag to the silk.<sup>39</sup> In the previous work the peptides were all coupled to the silk at the C-terminus, the genetically engineered structures containing additional charge at the N terminus (His<sub>6</sub>), a charged linker between the mineralizing peptide of interest and the silk

which makes it very difficult to understand which component binds to the mineral phase and which of the many components affects the structure/ mechanical/ biodegradation properties of the silk.

Peptide	Sequence	Specific target mineral	Reference
R5*	SSKKSGSYSGSKGSKRRIL	Silica	29
VTK	VTKHLNQISQSY	Hydroxyapatite	145
A1*	SGSKGSKRRIL	Silica	29
A3*	MSPHPHPRHHT	Silica	29
Ti-1* <sup>‡</sup>	QPYLFATDSLIIK	Titanium	146
Ti-2* <sup>‡</sup>	GHTHYHAVRTQT	Titanium	146
Ag-4*	NPSSLFRYLPSD	Silver	38
Ag-P35*	WSWRSPTPHVVT	Silver	38
Linker	SSGLVPRGSGMKETAAAK FERQHMDSPDLGTDDDDK	N/A	-
His tag	AMA HHHHHH	N/A	-

**Table 1.7** Peptides used in previous silk-silica composite studies by the Perry group.

\*denotes peptides previously used by Perry group in this study <sup>‡</sup> peptides intended to be used in the future.

## 1.6 Motivation and Objectives

The focus of the investigation was to develop a series of biomaterials suitable for coating bone and dental implants building on previous work completed by the Perry and Kaplan groups. The materials are designed to aid bone regrowth and implant binding through the induction of HAP formation and heightened silicification at the implant site, resulting in reduced healing time and limiting the chance of implant rejection.

The inspiration for this work has come from nature, utilising the natural polymer silk coupled with specific binding peptides for silica and HAP.

### Objectives

- Completion of chemical and physical analysis of genetically modified silk fusion proteins, evaluating their feasibility as a biomaterial.
- Mineralisation of chimeras, comparing each on the ability to induce and control the deposition of inorganic materials.
- Development of new methods to analyse silk chimeras.
- Biodegradability studies to estimate the *in vivo* life time of silk chimeras pre- and post-mineralisation.

## References

- 1 D. L. Kaplan and S. M. Mello, *Protein-Based Materials*, Birkhauser, Boston, 1998.
- 2 C. Fu, Z. Shao and V. Fritz, *Chemical Communications*, 2009, **43**, 6515-6529.
- 3 O. Hakimi, D. P. Knight, F. Vollrath and P. Vadgama, *Composites Part B-Engineering*, 2007, **38**, 324-337.
- 4 X. Hu, K. Shmelev, L. Sun, E. Gil, S. Park, P. Cebe and D. L. Kaplan, *Biomacromolecules*, 2011, **12**, 1686-1696.
- 5 D. Huemmerich, C. W. Helsen, S. Quedzuweit, J. Oschmann, R. Rudolph and T. Scheibel, *Biochemistry*, 2004, **43**, 13604-13612.
- 6 S. Inoue, K. Tanaka, F. Arisaka, S. Kimura, K. Ohtomo and S. Mizuno, *Journal of Biological Chemistry*, 2000, **275**, 40517-40528.
- 7 Matsumoto A, Chen J, Collette AL, Kim UJ, Altman GH, Cebe P, Kaplan DL, *The journal of physical chemistry.B*, 2006, **110**, 21630-8.
- 8 D. N. Rockwood, R. C. Preda, T. Yücel, X. Wang, M. L. Lovett and D. L. Kaplan, *Nature protocols*, 2011, **6**, 1612-31.
- 9 L. Roemer and T. Scheibel, *Prion*, 2008, **2**, 154-161.
- 10 H. Wang, Y. P. Zhang, H. L. Shao and X. C. Hu, *Journal of Materials Science*, 2005, **40**, 5359-5363.
- 11 H. Yamada, H. Nakao, Y. Takasu and K. Tsubouchi, *Materials Science & Engineering C- Biomimetic and Supramolecular Systems*, 2001, **14**, 41-46 (DOI:10.1016/S0928-4931(01)00207-7).
- 12 C. Z. Zhou, F. Confalonieri, M. Jacquet, R. Perasso, Z. G. Li and J. Janin, *Proteins-Structure Function and Genetics*, 2001, **44**, 119-122.
- 13 M. Fini, A. Motta, P. Torricelli, G. Glavaresi, N. N. Aldini, M. Tschon, R. Giardino and C. Migliaresi, *Biomaterials*, 2005, **26**, 3527-3536.
- 14 C. Acharya, B. Hinz and S. C. Kundu, *Biomaterials*, 2008, **29**, 4665-4675.
- 15 R. Nazarov, H. J. Jin and D. L. Kaplan, *Biomacromolecules*, 2004, **5**, 718-726.
- 16 J. R. Mauney, T. Nguyen, K. Gillen, C. Kirker-Head, J. M. Gimble and D. L. Kaplan, *Biomaterials*, 2007, **28**, 5280-5290.
- 17 Y. Wang, H. Kim, G. Vunjak-Novakovic and D. L. Kaplan, *Biomaterials*, 2006, **27**, 6064-6082.
- 18 K. Gellynck, P. C. Verdonk, E. Van Nimmen, K. F. Almqvist, T. Gheysens, G. Schoukens, L. Van Langenhove, P. Kiekens, J. Mertens and G. Verbruggen, *Journal of Materials Science: Materials in Medicine*, 2008, **19**, 3399-409.

- 19 N. Minoura, S. I. Aiba, M. Higuchi, Y. Gotoh, M. Tsukada and Y. Imai, *Biochemical and Biophysical Research Communications*, 1995, **208**, 511-516.
- 20 N. Minoura, M. Tsukada and M. Nagura, *Biomaterials*, 1990, **11**, 430-434.
- 21 T. Hino, M. Tanimoto and S. Shimabayashi, *Journal of colloid and interface science*, 2003, **266**, 68-73.
- 22 K. S. Mahesh, K. Arvind and K. Pramanik, *International Journal of Bioinformatics Research*, 2010, **2**, 33.
- 23 J. W. Nicholson, *The chemistry of medical and dental materials*, Royal Society of Chemistry, Cambridge, UK, 2002.
- 24 M. Xu and R. V. Lewis, *Proceedings of the National Academy of Sciences of the United States of America*, 1990, **87**, 7120-7124 (DOI:10.1073/pnas.87.18.7120).
- 25 C. Vepari and D. L. Kaplan, *Progress in Polymer Science*, 2007, **32**, 991-1007.
- 26 F. Vollrath and D. P. Knight, *Nature*, 2001, **410**, 243-249.
- 27 T. Scheibel, *Microbial Cell Factories*, 2004, **3**, 14.
- 28 A. Mieszawska, N. Fourligas, I. Georgakoudi, N. Ouhib, D. Belton, C. Perry and D. Kaplan, *Journal of Biomaterials*, 2010, **34**, 8902-8920.
- 29 D. J. Belton, A. J. Mieszawska, H. A. Currie, D. L. Kaplan and C. C. Perry, *Langmuir*, 2012, **28**, 4373-4381.
- 30 B. D. Lawrence, F. Omenetto, K. Chui and D. L. Kaplan, *Journal of Materials Science*, 2008, **43**, 6967-6985.
- 31 S. H. Park, E. S. Gil, H. Kim, K. Lee and D. L. Kaplan, *Biomaterials*, 2010, **31**, 6162-6172.
- 32 B. O. Swanson, T. A. Blackledge, J. Beltran and C. Y. Hayashi, *Applied Physics A-Materials Science & Processing*, 2006, **82**, 213-218.
- 33 F. Vollrath, *Scientific American*, 1992, **266**, 70-76.
- 34 J. A. Kluge, U. Rabotyagova, G. G. Leisk and D. L. Kaplan, *Trends in biotechnology*, 2008, **26**, 244-251.
- 35 M. Sumper and N. Kroger, *Journal of Materials Chemistry*, 2004, **14**, 2059-2065.
- 36 A. Polini, J. Wang, H. Bai, Y. Zhu, A. P. Tomsia and C. Mao, *Biomaterials Science*, 2014, **2**, 1779-1786.
- 37 R. Jugdaohsingh, *Journal of Nutrition Health & Aging*, 2007, **11**, 99-110.
- 38 H. A. Currie, O. Deschaume, R. R. Naik, C. C. Perry and D. L. Kaplan, *Advanced Functional Materials*, 2011, **21**, 2889-2895.

- 39 C. Wong Po Foo, S. V. Patwardhan, D. J. Belton, B. Kitchel, D. Anastasiades, J. Huang, R. R. Naik, C. C. Perry and D. L. Kaplan, *Proceedings of the National Academy of Sciences of the United States of America*, 2006, **103**, 9428-9433.
- 40 S. Weiner and P. Dove, *Biomaterialization*, 2003, **54**, 1-29 (DOI:10.2113/0540001).
- 41 S. Mann, *Nature*, 1993, **365**, 499-505.
- 42 E. Bauerlein, *Angewandte Chemie-International Edition*, 2003, **42**, 614-641.
- 43 F. M. Fernandes, T. Coradin and C. Aime, *Nanomaterials*, 2014, **4**, 792-812.
- 44 Dujardin, E., Mann, S., *ADEM Advanced Engineering Materials*, 2002, **4**, 461-474.
- 45 Y. Bar-Cohen, *Bioinspiration & Biomimetics*, 2006, **1**, P1-P12.
- 46 W. J. Crookes-Goodson, J. M. Slocik and R. R. Naik, *Chemical Society Reviews*, 2008, **37**, 2403-2412.
- 47 S. Weiner, *CRC critical reviews in biochemistry*, 1986, **20**, 365-408.
- 48 S. Weiner and H. D. Wagner, *Annual Review of Materials Science*, 1998, **28**, 271-298.
- 49 J. M. Vaughan, *The Physiology of bone*, Clarendon Press, Oxford, 1981.
- 50 K. Simkiss, *Bone and biomineralization.*, E. Arnold, London, 1975.
- 51 F. Bronner and M. C. Farach-Carson, *Bone Formation*, Springer-Verlag, London, 2004.
- 52 G. J. Tortora, B. H. Derrickson, B. Burkett, D. Dye, J. Cooke, T. Diversi, M. McKean, R. Mellifont, L. Samalia and G. Peoples, *Principles of anatomy & physiology*, John Wiley and Sons, Australia, 2016.
- 53 H. Rasmussen, *Clinics in Endocrinology and Metabolism*, 1972, **1**, 3-20.
- 54 Elliott, J. C., Mackie, P. E., Young, R.A., *Science*, 1973, **180**, 1055-1057.
- 55 J. C. Elliott and R. A. Young, *Nature*, 1967, **214**, 904-906.
- 56 J. W. Anthony, *Handbook of mineralogy*, Mineral Data Pub., Tucson, 1997.
- 57 G. Ma and X. Y. Liu, *Crystal growth & design*, 2009, **9**, 2991.
- 58 T. Kanazawa, *Inorganic phosphate materials*, Elsevier, Tokyo, 1989.
- 59 M. Kay, R. Young and A. Posner, *Nature*, 1964, **204**, 1050-2.
- 60 R. A. Young and J. C. Elliott, *Archives of Oral Biology*, 1966, **11**, 699-707.
- 61 E. D. Eane and A. S. Posner, in *Biological Calcification*, ed. H. Schraer, Meredith Corporation, Amsterdam, 1970, p. 1-26.

- 62 A. L. Boskey, *Elements*, 2007, **3**, 385-391.
- 63 E. Hayek and H. Newesley, *Inorganic Synthesis*, 1963, **7**, 63-65.
- 64 E. D. Eanes, I. H. Gillessen and A. S. Posner, *Nature*, 1965, **208**, 365-7.
- 65 G. Nancollas and M. Mohan, 1970, **15**, 731-745.
- 66 H. Furedimi, B. Purgaric, B. Purgaric and N. Pavkovic, *Calcified tissue research*, 1971, **8**, 142-153.
- 67 B. Vaidhyanathan and K. J. Rao, *Bulletin of Materials Science*, 1996, **19**, 1163-1165.
- 68 R. Mazze, *Periodico Di Mineralogia*, 2009, **78**, 19-43.
- 69 R. Nazir, N. Iqbal, A. S. Khan, A. Akram, A. Asif, A. A. Chaudhry, I. U. Rehman and R. Hussain, *Ceramics International*, 2012, **38**, 457-462.
- 70 W. G. Tang, R. B. Gan and K. Y. Wang, *Progress in Biochemistry and Biophysics*, 1997, **24**, 203-207.
- 71 Z. Wang, Z. Xu, W. Zhao and N. Sahai, *Journal of Materials Chemistry B*, 2015, **3**, 9157-9167.
- 72 M. T. Jahromi, G. Yao and M. Cerruti, *Journal of the Royal Society Interface*, 2013, **10**, 20120906.
- 73 X. Chu, W. Jiang, Z. Zhang, Y. Yan, H. Pan, X. Xu and R. Tang, *Journal of Physical Chemistry B*, 2011, **115**, 1151-1157.
- 74 B. Palazzo, D. Walsh, M. Iafisco, E. Foresti, L. Bertinetti, G. Martra, C. L. Bianchi, G. Cappelletti and N. Roveri, *Acta Biomaterialia*, 2009, **5**, 1241-1252.
- 75 K. S. Jack, T. G. Vizcarra and M. Trau, *Langmuir*, 2007, **23**, 12233-12242.
- 76 E. Dalas, P. Malkaj, Z. Vasileiou and D. G. Kanellopoulou, *Journal of Materials Science-Materials in Medicine*, 2008, **19**, 277-282.
- 77 E. V. Rosseeva, O. A. Golovanova and O. V. Frank-Kamenetskaya, *Glass Physics and Chemistry*, 2007, **33**, 283-286.
- 78 E. Boanini, M. Fini, M. Gazzano and A. Bigi, *European Journal of Inorganic Chemistry*, 2006, **23**, 4821-4826.
- 79 S. Segvich, S. Biswas, U. Becker and D. H. Kohn, *Cells Tissues Organs*, 2009, **189**, 245-251.
- 80 C. Chung, Y. Park, S. Rhee and J. Lee, *Peptide having the ability to regenerate bone tissue and for binding to apatite*, Seoul, South Korea, 2013.
- 81 S. J. Segvich, *Design of Peptides with Targeted Apatite and Human Bone Marrow Stromal Cell Adhesion for Bone Tissue Engineering.*, The University of Michigan, Michigan, 2009.
- 82 S. Zhang, *Biological and biomedical coatings handbook : processing and characterization*, CRC Press (Taylor & Francis Group), Boca Raton, 2011.

- 83 W. N. Addison, S. J. Miller, J. Ramaswamy, A. Mansouri, D. H. Kohn and M. D. McKee, *Biomaterials*, 2010, **31**, 9422-9430.
- 84 D. A. Puleo and R. Bizios, *Biological interactions on materials surfaces : understanding and controlling protein, cell, and tissue responses*, Springer, Dordrecht; New York, 2009.
- 85 H. Ramaraju, S. J. Miller and D. H. Kohn, *Connective tissue research*, 2014, **55**, 160-163.
- 86 G. Subramanian, *Biopharmaceutical production technology*, Wiley, 2012.
- 87 M. D. Roy, S. K. Stanley, E. J. Amis and M. L. Becker, *Advanced Materials*, 2008, **20**, 1830-1836.
- 88 F. Bronner, M. C. Farach-Carson and H. I. Roach, *Bone and development*, Springer-Verlag, London, 2010.
- 89 S. J. Segvich, H. C. Smith and D. H. Kohn, *Biomaterials*, 2009, **30**, 1287-1298 (DOI:10.1016/j.biomaterials.2008.11.008).
- 90 K. Schwarz and D. B. Milne, *Nature*, 1972, **239**, 333-4.
- 91 E. M. Carlisle, *Nutrition reviews*, 1982, **40**, 210-213.
- 92 E. M. Carlisle, *Ciba Foundation Symposia*, 1986, **121**, 123-139.
- 93 L. L. Hench, I. D. Xynos and J. M. Polak, *Journal of Biomaterials Science-Polymer Edition*, 2004, **15**, 543-562.
- 94 A. E. Porter, N. Patel, J. N. Skepper, S. M. Best and W. Bonfield, *Biomaterials*, 2004, **25**, 3303-3314.
- 95 M. Gimeno-Fabra, M. Peroglio, D. Eglin, M. Alini and C. C. Perry, *Journal of Materials Chemistry*, 2011, **21**, 4086-4089.
- 96 M. B. Dickerson, K. H. Sandhage and R. R. Naik, *Chemical Reviews*, 2008, **108**, 4935-4978.
- 97 V. Puddu and C. C. Perry, *Langmuir*, 2014, **30**, 227-233.
- 98 N. Kroger, R. Deutzmann and M. Sumper, *Science*, 1999, **286**, 1129-1132.
- 99 N. Kroger, R. Deutzmann and M. Sumper, *Journal of Biological Chemistry*, 2001, **276**, 26066-26070.
- 100 M. R. Knecht and D. W. Wright, *Chemical Communications*, 2003, **24**, 3038-3039.
- 101 J. M. Walker and R. Rapley, *Molecular biology and biotechnology*, Royal Society of Chemistry, Cambridge, 2000.
- 102 R. Plowright, N. Dinjaski, S. Zhou, D. J. Belton, C. C. Perry and D. L. Kaplan, *RSC Advances*, 2016, **6**, 21776-21788.
- 103 M. J. Pender, L. A. Sowards, J. D. Hartgerink, M. O. Stone and R. R. Naik, *Nano Letters*, 2006, **6**, 40-44.

- 104 R. K. Iler, *The Chemistry of Silica*, Wiley and Sons, 1979.
- 105 G. J. Bratton, B. R. Currell, J. R. Parsonage and M. J. K. Thomas, *Journal of Materials Chemistry*, 1993, **3**, 343-346.
- 106 S. A. Greenberg and D. Sinclair, *J.Phys.Chem.The Journal of Physical Chemistry*, 1955, **59**, 435-440.
- 107 C. C. Harrison and N. Loton, *Journal of the Chemical Society-Faraday Transactions*, 1995, **91**, 4287-4297.
- 108 R. K. Iler, *Journal of colloid and interface science*, 1980, **75**, 138-148.
- 109 Y. An, M. Chen, Q. Xue and W. Liu, *Journal of colloid and interface science*, 2007, **311**, 507-513.
- 110 Z. Wu, H. Xiang, T. Kim, M. Chun and K. Lee, *Journal of colloid and interface science*, 2006, **304**, 119-124.
- 111 E. Asenath-Smith and W. Chen, *Langmuir*, 2008, **24**, 12405-12409.
- 112 L. M. Yang, Y. J. Wang, G. S. Luo and Y. Y. Dai, *Microporous and Mesoporous Materials*, 2005, **84**, 275-282.
- 113 M. Luechinger, R. Prins and G. D. Pirngruber, *Microporous and Mesoporous Materials*, 2005, **85**, 111-118.
- 114 K. Yamamoto, D. L. Granger, W. Brehmer, I. Azuma and E. Ribí, *International journal of microbiology and hygiene*, 1981, **250**, 1-2.
- 115 M. R. Pelluso and B. O. Schineeman, *Journal of Nutrition*, 1994, **124**, 853-860.
- 116 E. Gozal, L. A. Ortiz, X. Zou, M. E. Burow, J. A. Lasky and M. Friedman, *American journal of respiratory cell and molecular biology*, 2002, **27**, 91-8.
- 117 R. Bhushan, R. S. Chauhan and R. Chauhan, *Biomedical Chromatography*, 1989, **3**, 46-47.
- 118 R. Wieneke, A. Bernecker, R. Riedel, M. Sumper, C. Steinem and A. Geyer, *Organic & Biomolecular Chemistry*, 2011, **9**, 5482-5486.
- 119 T. Coradin and J. Livage, *Colloids and Surfaces B-Biointerfaces*, 2001, **21**, 329-336.
- 120 M. M. Tomczak, D. D. Glawe, L. F. Drummy, C. G. Lawrence, M. O. Stone, C. C. Perry, D. J. Pochan, T. J. Deming and R. R. Naik, *Journal of the American Chemical Society*, 2005, **127**, 12577-12582.
- 121 S. V. Patwardhan, F. S. Emami, R. J. Berry, S. E. Jones, R. R. Naik, O. Deschaume, H. Heinz and C. C. Perry, *Journal of the American Chemical Society*, 2012, **134**, 6244-6256.
- 122 T. Coradin, O. Durupthy and J. Livage, *Langmuir*, 2002, **18**, 2331-2336.
- 123 E. G. Bellomo and T. J. Deming, *Journal of the American Chemical Society*, 2006, **128**, 2276-2279.

- 124 D. J. Belton, G. Paine, S. V. Patwardhan and C. C. Perry, *Journal of Materials Chemistry*, 2004, **14**, 2231-2241.
- 125 L. L. S. Canabady-Rochelle, D. J. Belton, O. Deschaume, H. A. Currie, D. L. Kaplan and C. C. Perry, *Biomacromolecules*, 2012, **13**, 683-690.
- 126 S. Zhou, W. Huang, D. J. Belton, L. O. Simmons, C. C. Perry, X. Wang and D. L. Kaplan, *Biomaterials*, 2015, **15**, 173-180.
- 127 S. Szmukler-Moncler, H. Salama, Y. Reingewirtz and J. H. Dubruille, *Journal of Biomedical Materials Research*, 1998, **43**, 192-203.
- 128 T. Albrektsson, G. Zard and P. Worthington, *The long-term efficacy of currently used dental implants: a review and proposed criteria of success*, Quintessence Pub. Co., Lombard, 1986.
- 129 L. Guéhenec, A. Soueidan, P. Layrolle and Y. Amouriq, *Dental Materials*, 2007, **23**, 844-854.
- 130 A. S. Assad, S. A. Hassan, Y. M. Shawky and M. M. Badawy, *Implant dentistry*, 2007, **16**, 212-223.
- 131 G. Cannizzaro, M. Leone and M. Esposito, *European Journal of Oral Implantology*, 2008, **1**, 33-43.
- 132 R. Crespi, P. Cappare, E. Gherlone and G. E. Romanos, *International Journal of Oral & Maxillofacial Implants*, 2008, **23**, 753-758.
- 133 M. Donati, V. La Scala, M. Billi, B. Di Dino, P. Torrisi and T. Berglundh, *Clinical oral implants research*, 2008, **19**, 740-748.
- 134 D. M. Brunette, *Titanium in medicine : material science, surface science, engineering, biological responses, and medical applications*, Springer, Berlin; New York, 2001.
- 135 S. Johnson, C. F. Kocha, S. Johnsona, D. Kumarb, M. Jelinekc, D. B. Chriseyd, A. Doraiswamy, C. Jine, R. J. Narayane and I. N. Mihailescuf, *Materials Science and Engineering: C*, 2005, **27**, 484-494.
- 136 W. Xia, C. Lindahl, H. Engqvist and J. Lausmaa, *Biomimetic Hydroxyapatite Deposition on Titanium Oxide Surfaces for Biomedical Application.*, INTECH Open Access Publisher, Uppsala, 2011.
- 137 O. Blind, L. H. Klein, B. Dailey and L. Jordan, *Dental Materials*, 2005, **21**, 1017-1024.
- 138 F. Barrere, Van Der Valk, C. M., G. Meijer, R. A. J. Dalmeijer, K. de Groot and P. Layrolle, *Journal of Biomedical Materials Research Part B-Applied Biomaterials*, 2003, **67B**, 655-665.
- 139 K. de Groot, J. G. C. Wolke and J. A. Jansen, *Proceedings of the Institution of Mechanical Engineers Part H-Journal of Engineering in Medicine*, 1998, **212**, 137-147.
- 140 N. C. Geurs, R. L. Jeffcoat, E. A. McGlumphy, M. S. Reddy and M. K. Jeffcoat, *International Journal of Oral & Maxillofacial Implants*, 2002, **17**, 811-815.

- 141 L. Le Guéhenec, A. Soueidan, P. Layrolle and Y. Amouriq, *Dental Materials*, 2007, **23**, 844-854.
- 142 H. F. Morris, S. Ochi, J. R. Spray and J. W. Olson, *Annals of Periodontology / The American Academy of Periodontology*, 2000, **5**, 56-67 (DOI:10.1902/annals.2000.5.1.56).
- 143 D. Tinsley, C. J. Watson and J. L. Russell, *CLR Clinical Oral Implants Research*, 2001, **12**, 159-166.
- 144 S. L. Wheeler, *The International journal of oral & maxillofacial implants*, 1996, **11**, 340-50.
- 145 H. A. Currie, O. Deschaume, R. R. Naik, C. C. Perry and D. L. Kaplan, *Advanced Functional Materials*, 2011, **21**, 2889-2895.
- 146 V. Puddu, J. M. Slocik, R. R. Naik and C. C. Perry, *Langmuir*, 2013, **29**, 9464-9472.

## Chapter II

### Experimental Methods

This chapter will briefly discuss the theory and parameters of techniques employed for analysis of samples. A basic understanding of each technique has been assumed.

#### 2.1 Atomic Force Microscopy

Atomic force microscopy (AFM) is one of several scanning probe microscopy (SPM) techniques.<sup>1</sup> In all SPM methods, a sharp probe is scanned across the sample surface producing a nanoscale image from the measured tip-surface interactions. In AFM, probes (here the term probe is used to mean a mounted cantilever with tip), are brought into close proximity of the sample to analyse the physical forces, both attractive and repulsive, between the probe and the sample surface in order to produce a topographical 3D image and acquire mechanical information about the surface by maintaining a small continual force. A piezoelectric tube scanner controls the motion of the tip in a raster pattern, interactions are observed in the reflections of a laser off the back of the cantilever by a split photodiode detector. Oscillation amplitude and cantilever deflection are determined by the change in photodetector output voltage, figure 2.1.<sup>2</sup>

Out of the three standard modes for AFM only two are frequently used, contact mode and tapping mode.<sup>3</sup> The third, non-contact mode, is designed specifically for measuring long range interactions, such as Van der Waals and electrostatic forces.<sup>4</sup>

In contact mode, the tip is brought into contact with the surface and whilst raster scanning a constant set point is maintained. Any movement of the z piezo (caused by maintaining the cantilever deflection) is then a result of sample topography that is plotted as an image. The disadvantage of this method is the risk of high lateral forces being exerted on the sample resulting in damage to the sample. Tapping mode reduces this risk by oscillating the cantilever during imaging.<sup>5</sup>

During a tapping mode scan the cantilever is oscillated at its resonance frequency achieving light periodic contact with the surface. In this case, the laser deflection allows the root mean square amplitude of the cantilever's oscillation to be found. To

keep a constant oscillation amplitude set point the scanner moves vertically providing topographical information about the surface, Figure 2.1.

PeakForce QNM (Quantitative NanoMechanics) can give high resolution ( $\approx 5\text{nm}$ ) compositional mapping of composite materials and be used for quantitative measurement of nanoscale materials for: modulus, adhesion, deformation and dissipation. PeakForce Tapping mode also avoids lateral forces by only having intermittent surface contact but differs from standard tapping mode as it functions at non-resonant frequencies. Oscillations occur far below the resonance of the cantilever eliminating the dynamics of the resonating system thereby allowing for force control and continuing avoidance of lateral forces. Information about the force involved is outputted as a force volume curve where z position data has been modulated by a sine wave not a triangular one, thus preventing resonances at the turnaround points. Individual peak force points act as triggering mechanisms that force the z piezo to retract.

There are many advantages of using AFM over typical electron microscopy techniques such as being able to scan in air or liquid as opposed to under vacuum as well as unparalleled versatility stemming from it being possible to chemically functionalise probes for quantitative measurement of specific interactions.<sup>6</sup>

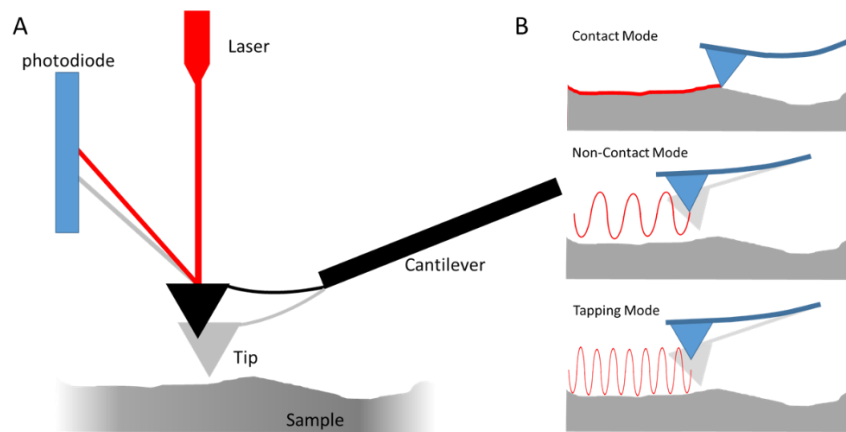


**Figure 2.1** A) General set up of an AFM showing deflection of the laser from the top surface of the tip. B) The three modes for AFM, contact mode (tip-surface contact is maintained), non-contact mode (measures long range interactions) and tapping mode (also known as semi-contact mode, intermittent tip-surface contact).

### 2.1.1 Finding the reduced elastic (Young's) Modulus of silk films

Peak force tapping mode produces a force curve at every pixel in the image. The force vs time plot, also known as the heartbeat, shows the measured force exerted on the probe as it makes contact and retracts from the sample surface. By using the z position data, a force curve can be created from the heartbeat. This in turn can be converted to a force separation curve where the proportionality of force vs deformation is given by the reduced elastic modulus, providing the correct calibration steps have been performed, figure 2.2.

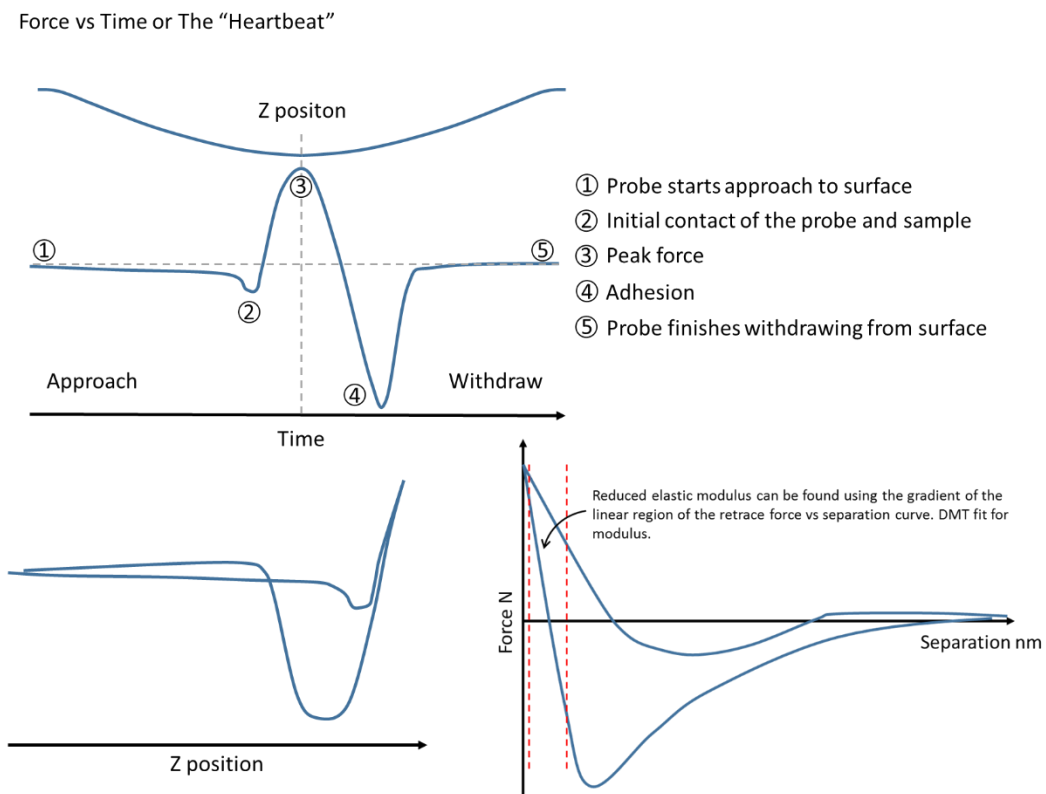


**Figure 2.2** A) Initial force vs time plot or "heartbeat" produced in PeakForce tapping mode B) Incorporation of z data into the heartbeat for data to be output as a function of z position C) Final data output form as a force vs tip-sample separation graph where the proportionality of the linear region is linked by the samples reduced elastic modulus. Adapted from<sup>7</sup>

#### Calibration Step 1: Finding deflection sensitivity, S

Force-displacement curves measured using the cantilever contain information about the applied force,  $F$ , and the sample deformation,  $(d-d_0)$ , which can be extracted using the measured cantilever deflection,  $D$ .

To separate the two parameters the deflection sensitivity,  $S$ , (response of the cantilever on an infinitely stiff surface – sapphire) is determined.

Once the deflection sensitivity is known, the applied force  $F$  and the tip position  $d$  can be calculated as follows:

$$F = kSD \quad 1$$

$$d = z - SD \quad 2$$

Where  $D$  denotes the cantilever deflection (measured in Volts),  $z$  is the vertical scanner position and  $k$  is the cantilever spring constant, which can be obtained in the second calibration step known as Thermal Tune.

### **Calibration Step 2: Thermal Tune to find the cantilever spring constant, $k$**

Self-excitation under ambient conditions, with no sample contact, measures the cantilever's mechanical response to thermal noise allowing a Power vs. Frequency plot to be obtained. This is done by measuring the fluctuations of the cantilever over time and extracting the frequency spectrum of the cantilever's mechanical response proportional to the power. The data is fitted using the Lorentzian equation and an estimation of the cantilever's spring constant found.

### **Calibration Step 3: Finding the Tip Radius**

A tip characterisation sample, e.g. a titania roughness sample, is scanned and the image processed using the tip quantification function. An estimate of the size and shape of the tip is found by assuming that the extreme physical surface properties of the sample exceed that of the tip to such an extent that any feedback from the scan is solely from the cantilever, and therefore an image of the tip is produced instead of the sample.

### **DMT Modulus**

To obtain the reduced elastic modulus from the Force vs. Separation curve, the retract curve is fitted using the DMT (Derjaguin, Muller, Toropov) model.<sup>8</sup> The DMT model looks at the theory of adhesion contact and describes the forces during tip-surface separation by:

$$F_{interaction} = \frac{4}{3}E^* \sqrt{R(d - d_0)^3} + F_{adhesion} \quad 3$$

Where  $F_{interaction}$  is the tip-sample force (also expressed as  $F_{tip}$ , force on the tip),  $E^*$  is the reduced elastic modulus of the tip and the sample,  $R$  is the tip end radius,  $d_0$  is the surface rest position,  $(d-d_0)$  is the sample deformation which can also be expressed as  $d$  for tip-sample separation and  $F_{adhesion}$  is the adhesion force.<sup>8,9</sup>

### Poisson's Ratio: Converting reduced elastic modulus to the elastic modulus

The Young's modulus of a sample,  $E_s$ , can be converted from the measured reduced modulus,  $E^*$ , using:

$$E^* = \left[ \frac{1-\nu_s^2}{E_s} + \frac{1-\nu_{tip}^2}{E_{tip}} \right]^{-1} \quad 4$$

Where  $\nu_s$  and  $\nu_{tip}$  are the Poisson's ratio of the sample and tip respectively.  $E_s$  and  $E_{tip}$  are the Young's modulus of the sample and tip respectively. It is assumed that  $E_{tip}$  is much larger than  $E_s$  to the extent it is approximated as infinite so the sample modulus is calculated using the sample's Poisson's ratio.

Poisson's Ratio applies when a material is being elastically stretched, linking the proportional decrease in a lateral measurement to the proportional increase in the length of the sample, in other words the ratio of transverse strain to axial strain.

As a general rule, the Poisson's Ratio of a sample can be assumed using data in table 2.1. As a result, the change from reduced elastic modulus to elastic modulus will be within a 4 - 25% difference. The disadvantage of using Poisson's ratio is an assumption must be made about the samples, where interpretation can produce varying values of  $E_s$ , it is for this reason that the reduced modulus of samples is often quoted instead of the Young's modulus.<sup>10</sup>

$E_s$	$\nu_s$
$E_s < 100\text{mPa}$	0.5
$0.1 < E_s < 1 \text{ GPa}$	0.4
$1 \text{ GPa} < E_s < 10 \text{ GPa}$	0.3

**Table 2.1** Accepted Poisson's values for materials<sup>10</sup>

Here a Bruker Dimension Icon with ScanAsyst was used to perform all imaging and quantum mapping. Data was collected in the Nanoscope software and processed in Nanoscope Analysis software.

## 2.2 Scanning Electron Microscopy coupled with Energy Dispersive X-ray Analysis

Surface imaging on the nano to micro scale of samples was completed using scanning electron microscopy (SEM) where high resolution images can be obtained up to  $\times 10^7$  magnification. Samples are illuminated using a beam of electrons produced by an electron gun *via* electrical heating of a tungsten filament resulting in thermionic emission. To allow electrons to escape the positively charged filament and produce a beam, a negative voltage is applied between the filament and an earthed anode disc, figure 2.4. The velocity of the electrons is then dependent upon the accelerating voltage.<sup>11</sup>

The filament is encased in a Wehnelt cylinder which manipulates the beam to have a diameter between 10-50  $\mu\text{m}$  using electrostatic forces. A disadvantage of SEM is that to avoid scattering from gas molecules scanning must be under vacuum. Positioning of the beam is controlled using a series of electrical lenses and scanning coils, firstly two condenser lenses are used to reduce the beam width to approx. 5nm, then two pairs of scanning coils, positioned perpendicular to the beam and one another, direct the beam using specific current waveforms. An objective lens then ensures the beam has the smallest diameter when striking the surface.

The electron beam hits the sample and interacts with atoms on the surface producing secondary electrons with lower kinetic energy than those in the incident beam. Emitted secondary electrons from the surface are then collected by the detector and an image generated. This image reflects the sample's surface topography as secondary electrons can only be detected from the top 10nm of the surface due to their lower energy, figure

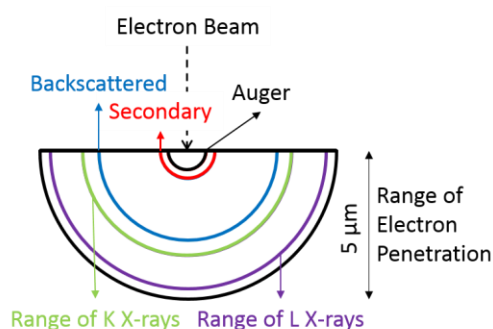


**Figure 2.3** Penetrative interactions with the sample

2.3. A portion of the electrons hitting the surface are reflected off the sample surface, known as back scattered electrons, these maintain high kinetic energy with an intensity that corresponds to specific elements, reflected electrons also emit x-rays dependant on the quantity of specific elements present in the sample.

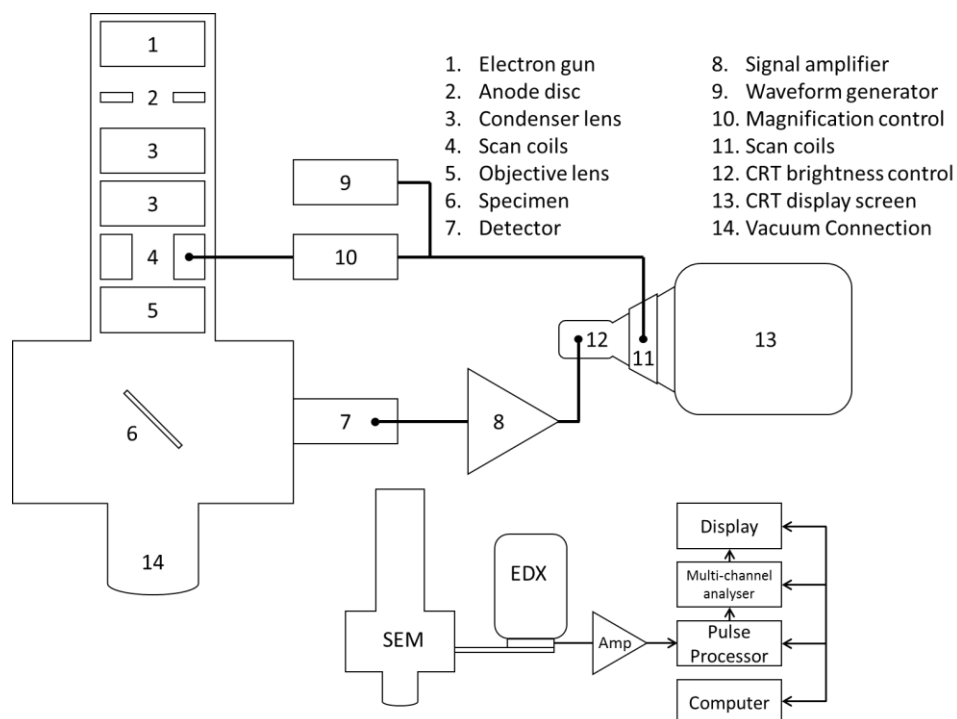


**Figure 2.4** layout of a scanning electron microscope coupled to an EDX system, adapted.<sup>12</sup>

Here a JEOL JSM-A840A scanning electron microscope, equipped with both secondary electron and back scattered electron detectors, was used with a 20 kV accelerating voltage at varying scan rates and scan sizes. Image and data processing was performed in the INCA software (Oxford Instruments). Whilst particle size measurements were taken using the ImageJ software.

### 2.3 Powder X-Ray Diffraction

All crystalline compounds have a highly ordered lattice structure comprised of atoms, ions or molecules sitting in crystal planes. Powder x-ray diffraction (XRD) can identify crystal phases by monitoring the deflection of an incident beam, as the uniform scattering of the incoming beam creates a unique diffraction pattern.

As seen in figure 2.5, when the incident x-ray beam reaches the sample surface a percentage is deflected by the initial crystal plane whilst the remainder penetrates further into the sample. At each new evenly spaced crystal plane more of the beam is deflected resulting in constructive interference as stated in Bragg's Law:

$$n\lambda = 2d\sin\theta \quad 5$$

Where the incoming beam has a wavelength  $\lambda$  and an angle of  $\theta$  (Bragg's angle) with respect to the surface of the sample. The crystal lattice plane separation known as the interplanar distance,  $d$ , links the distance travelled by scattered x-rays as  $2d\sin\theta$ . Diffracted beam intensity is plotted against  $2\theta$  to produce the XRD pattern, where each peak is a reflection from a set of crystal planes in the sample.<sup>13-15</sup>

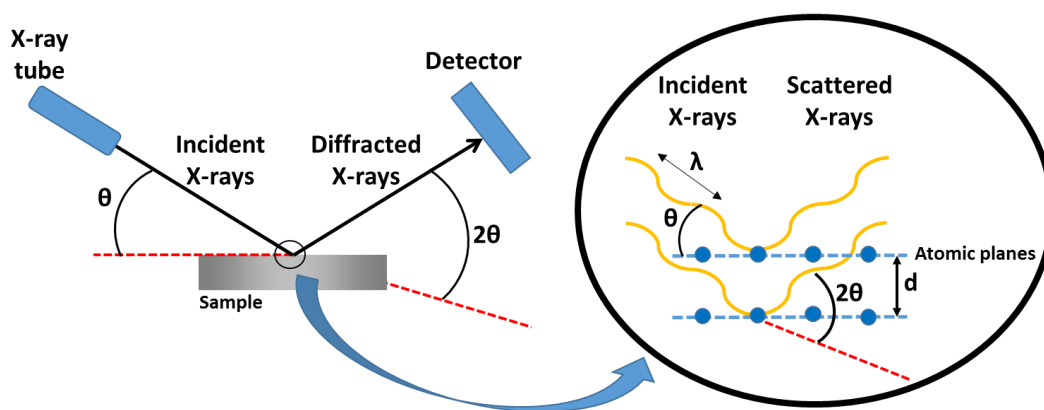


**Figure 2.5** Schematic of XRD technique for identifying crystal phases.

### 2.3.1 The Scherrer Equation and crystallite size

There is a reciprocal relationship between the crystallite size,  $D$ , and the broadening of peaks in its diffraction pattern,  $\beta$ . This can also be explained as a cumulative effect as the larger the crystallites are, the more reflections from atoms, ions or molecules occur which results in a greater averaging effect and therefore a sharper peak is produced.

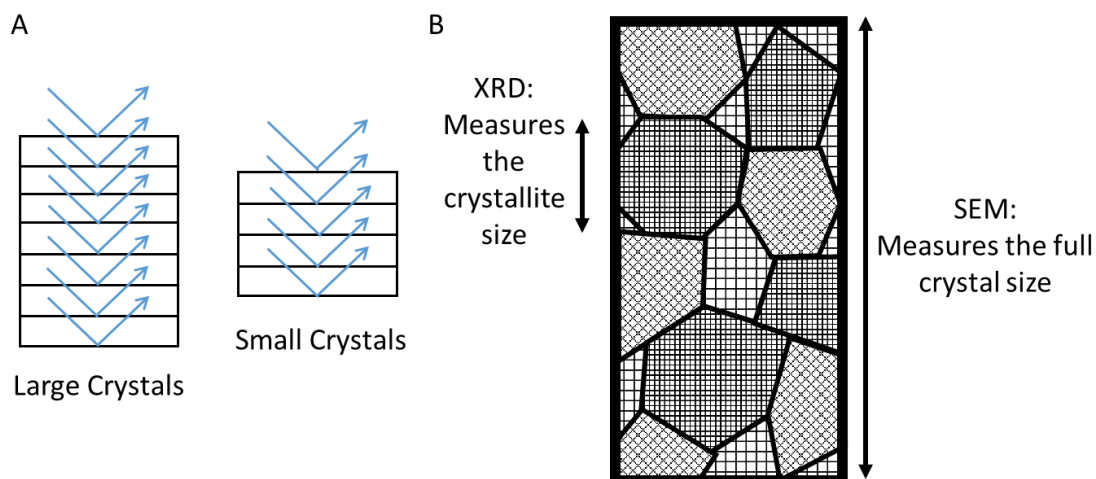


**Figure 2.6** Schematics of **A)** cumulative effect of crystallite size on peak broadening **B)** SEM crystal measurements vs XRD crystallite measurements.

The Scherrer equation, equation 6, given below links peak broadening and crystallite size,<sup>16</sup> where  $K$  is the shape factor widely accepted to be 0.9 for spherical crystals.  $D$  is the crystallite domain size,  $\lambda$  is the wavelength,  $\theta$  is the Bragg diffraction angle and  $\beta$  is the line broadening at half the maximum intensity.

$$D = \frac{K\lambda}{\beta \cos\theta} \quad 6$$

The Scherrer equation provides only a lower bound on crystal domain size due to a number of additional factors that can contribute to the width of a diffraction peak besides the instrumental effects and crystallite size. The most common influences over peak broadening are crystal lattice defects where there is lower uniformity in the overall structure and inhomogeneous strain, figure 2.7, which results in different crystallites experiencing different amounts of strain, which gives varied shifts of  $2\theta$  thus broadening the XRD peaks. Inhomogeneous strain can be caused by: Interstitials, vacancies, dislocations and layer faults.<sup>17-19</sup>

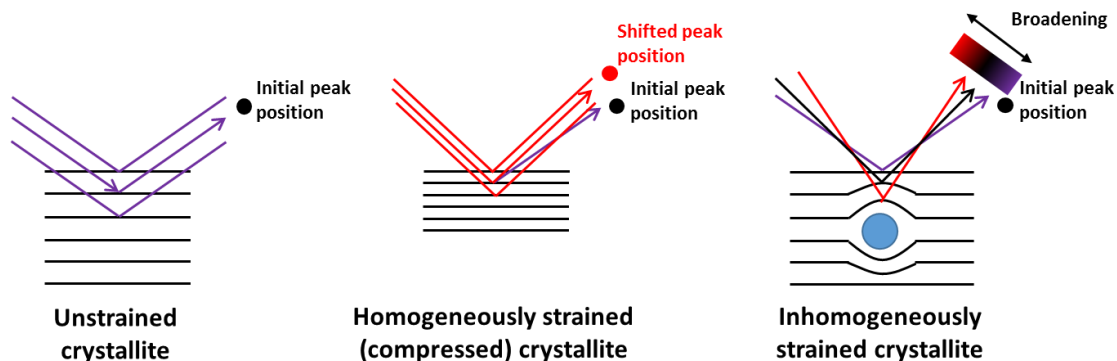


**Figure 2.7** examples on sample strain and its effect on the peak position in the XRD pattern

PANalytical X'Pert PRO x-ray diffractometer (CuK $\alpha$  radiation with wavelength 1.54060 Å) was utilised for identifying crystal phases of solid samples. Aluminium sample holders were used to hold powdered samples, multiple sample scans were taken where possible and between each scan the samples were remixed to ensure a homogenous sample was scanned that represented the bulk. Scans were performed on the spinner stage within a range of 5-90° for 2 $\theta$ , at a 45 kV accelerating voltage, 40 mA filament current, 0.08 °s<sup>-1</sup> scan speed at room temperature. Data analysis was completed using X'pert-HighScore Plus (Version 4.6.1) software, where background data was subtracted and peaks were identified. Polydimethylsiloxane (PDMS) stubs were used as spacers where limited samples quantities were produced allowing for smaller sample sizes to be analysed.

#### 2.4 Fourier Transform Attenuated Total Reflectance Infrared Spectroscopy

When infrared (IR) radiation is absorbed by samples it results in vibrational and/or rotational movement, meaning there can be fluctuations in bond length and bond angle. Samples will only absorb specific wavelengths depending on their structure. It is therefore possible to distinguish between compounds from the frequency of the radiation they absorb as it is equivalent to the vibrational frequencies of the molecules present.<sup>20,21</sup>

During attenuated total reflectance infrared spectroscopy (ATR-IR) a beam of infrared light is passed through an ATR crystal with a relatively high refractive index compared to the sample, Figure 2.8, the beam is reflected multiple times off the

internal surface creating an evanescent wave that continues into the sample, penetrating up to 2  $\mu\text{m}$ , reflected radiation is then collected by the detector.<sup>22</sup>

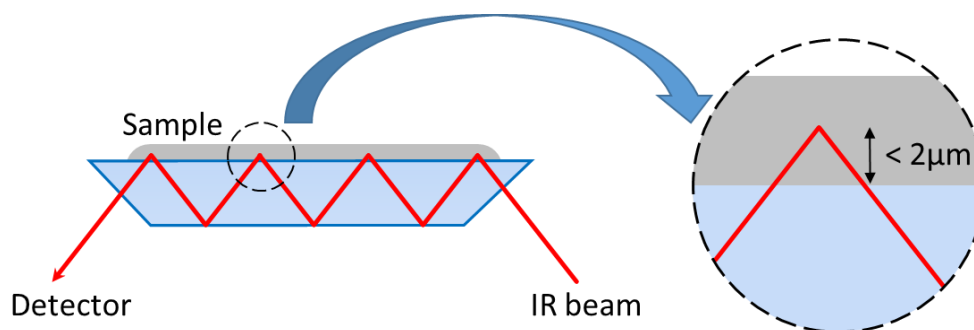


**Figure 2.8** The general structure of an ATR crystal

Analysis of infrared data obtained in the study can be separated into two parts, a general verification of functional groups present, phosphates for HAP samples,<sup>23</sup> and in depth peak deconvolution of amide bands to quantify protein conformation structure, Figure 2.9. Despite there being up to nine amide peaks present when proteins are scanned, only the amide I and amide II are widely used to assess protein structure as the others are a result of overtones and resonances of multiple functions.<sup>24-26</sup> The amide I band,  $1600 - 1700 \text{ cm}^{-1}$ , has the greatest intensity and is predominantly formed from the C=O stretching, (a smaller portion being C-N stretching), it's exact position is dependent on the backbone conformation of the sample and hydrogen bonding present.<sup>27-30</sup> The amide II band,  $1510 - 1580 \text{ cm}^{-1}$ , appears largely due to N-H bending vibrations from the C-N stretching vibration making it conformationally dependent. The amide II is also partially comprised from C-N and C-C stretching vibrations giving it a higher complexity compared with amide I.<sup>26,31-34</sup>

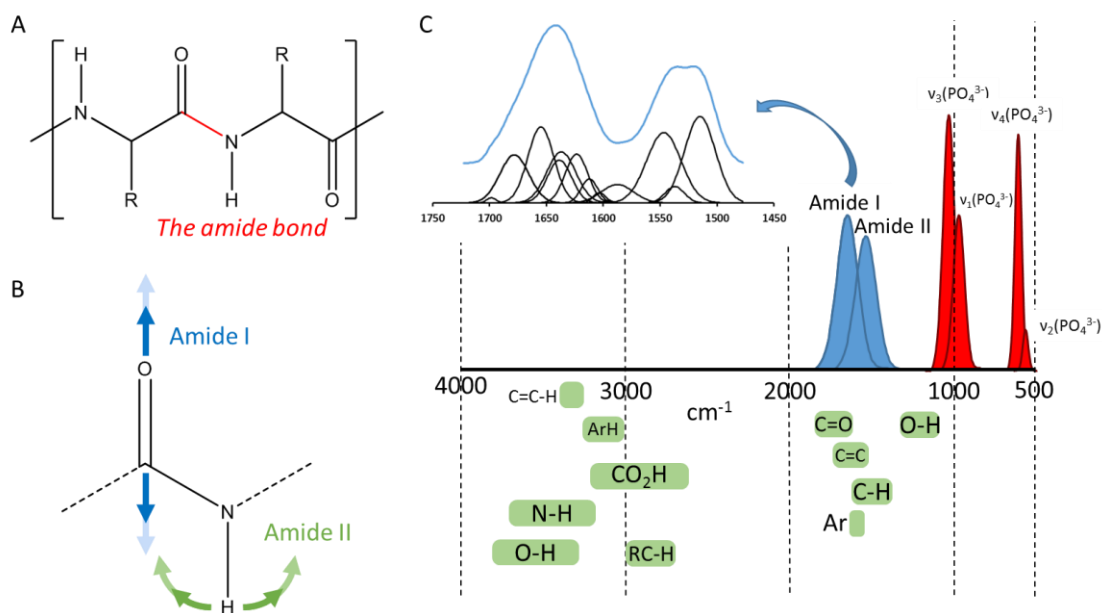


**Figure 2.9** A) The amide I bond B) The vibrations responsible for the Amide I and Amide II bands C) IR spectrum: in green general IR bands, blue shows the amide I and amide II bands used to obtain information about protein conformation and red shows phosphate bonds linking to hydroxyapatite.

Peak deconvolution assumes that a broad IR band is an accumulation of several smaller bands, in this case the amide I band is a compilation of smaller bands produced by specific elements of a protein's secondary structure. As smaller bands overlap within the amide I envelope a curve fitting process is applied to separate, analyse and identify protein structure. Method development of this curve fitting process is discussed further in Chapter 6.

Here a FTIR-ATR (Frontier, PerkinElmer, Coventry, UK) was employed with a minimum average of 32 scans performed with in the wavenumber range of 4000-650 cm<sup>-1</sup>. Grams peak fitting software was utilised for peak deconvolution.

## 2.5 Dynamic Light Scattering and Zeta Potential

Size distribution profiles of suspended particles in solution can be found using Dynamic Light Scattering (DLS). Fluctuation from Brownian motion is analysed by passing monochromatic light from a laser through a polariser and then the sample, scattered light then travels through a second polariser to reach a photomultiplier. Diffracted light from each molecule in solution is analysed over time for constructive

and destructive interference patterns by an autocorrelator and the polarisers are adjusted accordingly if necessary. The data collected for fluctuating intensities can now be used to calculate the particle size distribution using a size distribution processor (SDP), which can be output as a function of volume and number distributions, figure 2.10.<sup>35</sup> The limitations of this technique are sample specific, DLS is a relatively low resolution technique so slight changes in particle sizes may not be detected. Sample concentration is key; below the minimum concentration not enough data is acquired and above the maximum multiple scatterings can occur giving false data. Selection of dispersion medium must be considered carefully to avoid sedimentation or solvent scattering.<sup>36</sup>

The relationship between Brownian motion of particles in solution and their size is described in the Stokes-Einstein equation given below:

$$D = \frac{K_B T}{6\pi\eta r} \quad 7$$

The diffusion constant  $D$  is given as a factor relating the; dynamic viscosity  $\eta$ , particle radius (spherical)  $r$ , the Boltzmann constant  $K_B$ , absolute temperature  $T$ , and constant  $\pi$  (3.1415).

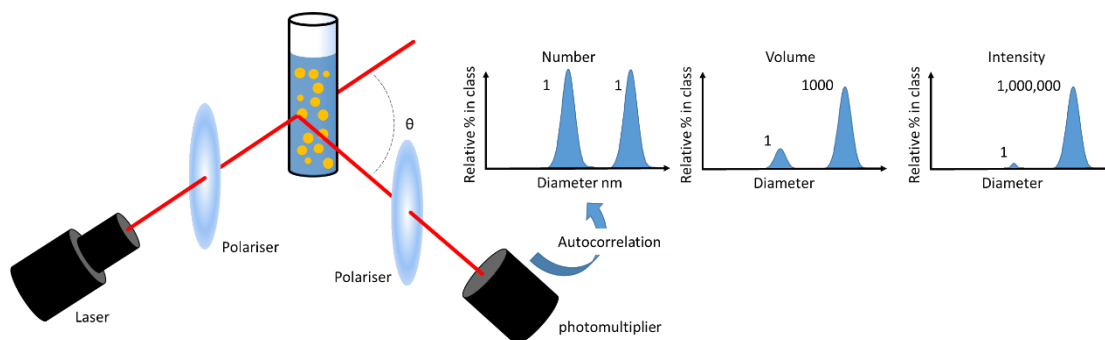


**Figure 2.10** Schematic of the light scattering experiment.

Data outputted by the DLS is a standard intensity distribution, this can be converted to a volume distribution and a number distribution. Figure 2.10 shows example data for a sample with two particle sizes ( $x$  and  $10x$ ) with the same population displayed in the three distributions. The number distribution confirms the populations are the same by producing a 1:1 ratio, the volume distribution gives a 1:1000 ratio as the data is displayed as a function of the area of a sphere,  $V = (4/3)\pi r^3$ . Conversion to intensity

includes the increased scattering from larger particles resulting in an even greater ratio between the two size distributions.

Surface charge or electrokinetic potential of particles in solution can be found by taking zeta potential measurements. Zeta potential is a known indicator for particle stability, it is generally accepted that particles with a zeta potential magnitude of  $\pm 30$  mV will be stable due to high electrostatic repulsion from like charged particles reducing the likelihood of aggregation. Small zeta potentials,  $-5 < x < 5$  mV, indicate an unstable solution where flocculation can occur as attractive intramolecular forces outweigh repulsive forces.<sup>37</sup>

The technique of zeta potential relies on the theory of an electric double layer being produced around each suspended particle in solution. Particles with a net surface charge will attract a high concentration of opposing ‘counter’ ions forming the inner Stern layer, and a less populated outer layer, the diffusion layer, together these make the electric double layer, the boundary of which is called the slipping plane. The electric potential at the slipping plane is the zeta potential of the particle, it is at this point ions are separated into those within the electric double layer/slipping plane that will migrate with the particle in solution and those outside the slipping plane where attractive forces have no significant effect over ion, figure 2.11s. Zeta potential can therefore be thought of as the potential difference between the stationary layer around the particle and the surrounding dispersion medium.

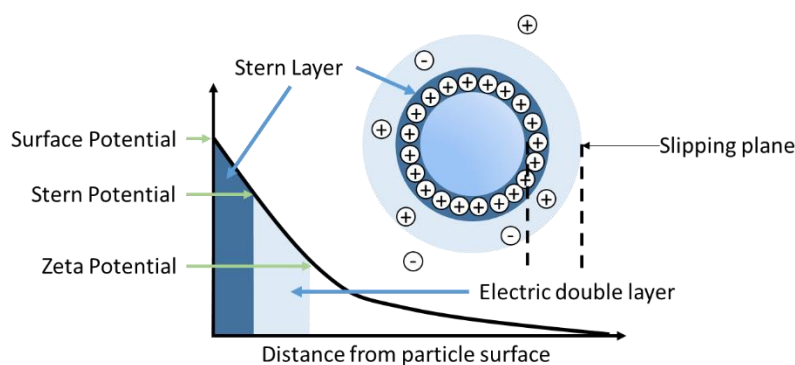


**Figure 2.11** Schematic of the electric double layer

The pH of the solution at which zeta potential measurements are taken has a significant impact on the zeta potential and allows for the isoelectric point (pI) of particles to be found, as at a particle’s pI the zeta potential will be zero.

Similarly, to DLS the disadvantages of using zeta potential measurements stem from the sample. Samples with high conductivity lead to polarisation and degradation of the electrodes, generally samples below 20 nm diameter cannot be accurately measured due to high mobility. There is a working concentration range that is unique to each sample, too high and multiple light scatterings can occur, too low and there won't be enough signal for an accurate measurement.

For DLS and zeta potential measurements a Zeta Sizer Nano Series (Malvern, UK) was employed. Measurements for both were taken together over a range of pHs, proteins were dissolved in deionised water and the pH adjusted accordingly with 1M citric acid and 1M bis tris buffer.

## 2.6 Wettability and Surface Energy Measurements

As part of a complete physical property study for biomedical materials an estimate of their hydrophobicity is required to allow *in vivo* interactions to be predicted. The desired wettability of samples is dependent on the intended application, here silk films are measured to ensure there is a significant level of hydrophobicity to withstand *in vivo* conditions whilst permitting specific interactions to take place.

Measurements were completed using a Theta Attension Instrument with OneAttention v 1.7 software (Biolin Scientific, Staffordshire, UK). The process records a water droplet being pipetted onto the silk film surface, and once stabilised measurements of the contact angle are taken at both the sides of the droplet twenty times and an average taken. These measurements give a direct comparison between samples and an indication of the wettability as it is widely accepted that contact angles over  $90^\circ$  are hydrophobic and those under are hydrophilic, figure 2.12.

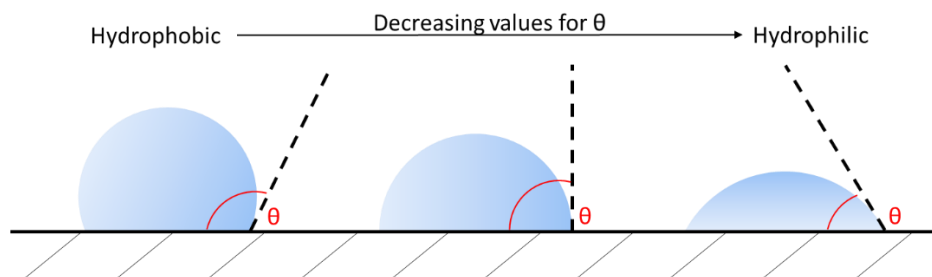


**FIGURE 2.12** Diagram of wetting of a water droplet on hydrophobic to hydrophilic surfaces.

Wettability measurements can be extended to find the surface energy of silk surfaces by incorporating the Young's equation, equation 8. The Young's equation expresses the relationship between the surface free energy of a solid  $\gamma_s$ , the contact angle  $\theta$  produced with a liquid of surface tension  $\gamma_L$  and the interfacial tension between the liquid and the surface  $\gamma_{SL}$ .

$$\gamma_s = \gamma_{SL} + \gamma_L \cos\theta \quad 8$$

Data for this is collected by repeating the experiment described above with liquids of varying surface tension, the cosine of the contact angle is plotted against surface tension in a Zisman Plot, figure 2.13. By extrapolating this graph to  $\cos\theta = 1$  ( $0^\circ$  contact angle), the surface energy can be found.<sup>38</sup>

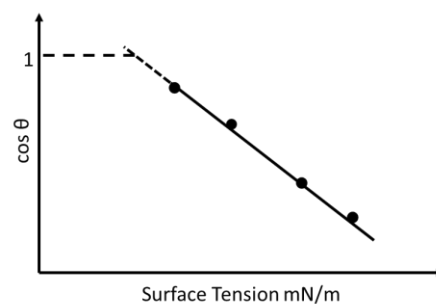


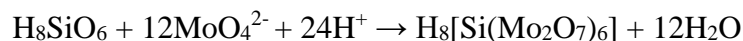
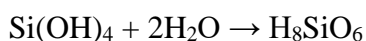
**Figure 2.13** Example of a Zisman Plot

It is noteworthy that samples measured in the study had a contact angle in excess of  $20^\circ$ , to avoid measurements being taken below the minimum accuracy level, care was taken to ensure there was a minimum variance in droplet size and to overcome the disadvantage of only a 2D plane being considered multiple droplet readings were performed.<sup>39</sup>

## 2.7 The Molybdenum Blue Assay: Quantifying Silica Presence

The molybdenum blue assay monitors the formation of polyoxometalates containing Mo(V), Mo(VI) and (in this case) silicon using absorbance shifts to find the concentration of silicon in solution.<sup>40,41</sup> Here it is used to quantify and compare the silica uptake of chimeric silk films that include a silicifying domain, the R5 peptide.

Formation of these molybdenum-silicon complexes requires a series of steps. First the monosilicic acid present in solution becomes saturated by binding to two water molecules.<sup>42</sup>



The saturated silicic acid then reacts with molybdate ions from molybdic acid forming the yellow silicon-molybdate complex, figure 2.14, with a maximum absorbance of 400nm. The structure is composed of a single central silicon atom encased in twelve MoO<sub>6</sub> octahedra (oxygen atoms are shared at the edges of these).

Reduction is then carried out to produce the blue silicomolybdous acid complex, maximum absorbance 810 nm, which has a greater extinction coefficient (the strength at which a substance absorbs light) than silicomolybdic acid. This makes silicomolybdous acid more sensitive and therefore able to detect smaller concentrations of monosilicic acid.

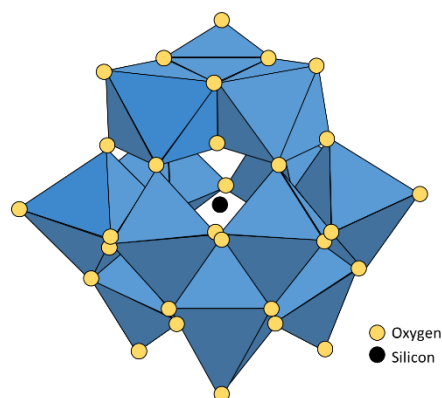


**Figure 2.14** Structure of the silicomolybdic acid cluster. The silicon atom (centre in black) surrounded by twelve MoO<sub>6</sub> octahedral structures, adapted from<sup>39</sup>

Standard absorbance spectroscopy is then performed at 810 nm, monochromatic UV light, produced using a source and a series of slits or lens, is shone through a sample of path length  $l$ . The UV-Vis spectrometer compares the intensity of the beam with  $I$  and without  $I_0$  passing through the sample, this ratio is known as transmittance and can be used to calculate the absorbance  $A$  using the Beer-Lambert Law, equation 9.<sup>43</sup> Sample absorption is then compared against suitable dilutions of 1000ppm SiO<sub>2</sub> standard. Measurements were performed here using a Varian Cary 50Bio UV-Visible Spectrometer and the Simple Reads software.

$$A = \log\left(\frac{I_0}{I}\right) \quad 9$$

## 2.8 Absorption Colorimetry: The Bradford Assay

Degradability and solubility of silk protein films under *in vivo* conditions can be estimated by monitoring the protein concentration of the solvent, in this case phosphate buffer saline (PBS), over time. The Bradford assay has been used here to measure protein concentration by observing the binding of a Coomassie Brilliant Blue Dye G-250 dye, as the dye ionically binds to acidic regions on the protein in solution as well as undergoing hydrophobic interactions. Once bound there is a metachromatic

absorbance shift in the dye, 465 to 595 nm, due to a stable anionic structure being formed.<sup>44-47</sup>

The donation of a free electron towards the protein from the red dye alters its native state resulting in exposure of hydrophobic regions that can then bind to the dye through Van der Waals interactions. This, in turn, alters the tertiary structure of the protein further to expose amine groups to the negative areas on the dye. When these ionically bind, the blue dye is stabilised and a measurement of protein dye complex can be made.

The response from different proteins can vary greatly, for example when observing a protein including arginine groups most of the signal will arise from dye-arginine interactions as opposed to other amino acids presents. It is for this reason standards and samples must be the equivalent.

Method development to optimise the parameters of the Bradford assay with the aim of reducing samples quantities required are discussed further in section 3.4.7.

## **2.9 Inductively Couple Plasma – Optical Emission Spectroscopy**

Inductively coupled plasma optical emission spectrometry (ICP-OES) is widely used for quantifying elements present in samples. ICP-OES has some limitations with respect to the elements it can detect, for example halogens have too high excitation energies and it is also not possible to quantify elements found in air.

Samples are excited by the plasma resulting in an emission of radiation, the wavelength of which is characteristic of a specific element. By measuring the intensity of emissions quantification of elements in samples can be made.<sup>48</sup>

Here a Perkin Elmer ICP-OES Optima 2100DV was used for element quantification. Samples were compared to appropriate dilution of 1000ppm stock solutions.

## 2.10 References

- 1 D. Johnson, N. Hilal and W. R. Bowen, in *Atomic Force Microscopy in Process Engineering*, ed. W. R. Bowen, , and N. Hilal, Butterworth-Heinemann, Oxford, 2009, p. 1-30.
- 2 P. J. Eaton and P. West, *Atomic force microscopy*, Oxford University Press, New York, 2014.
- 3 G. Binnig and C. F. Quate, *Physical Review Letters*, 1986, **56**, 930-933.
- 4 L. Gross, F. Mohn, N. Moll, P. Liljeroth and G. Meyer, *Science*, 2009, **325**, 1110-1114.
- 5 Q. Zhong, D. Inniss, K. Kjoller and V. B. Elings, *Surface Science*, 1993, **290**, L688-L692.
- 6 P. Russell, D. Batchelor and J. Thornton, *Scanning Electron Microscopy (SEM) and Atomic Force Microscopy (AFM): Complementary techniques for high resolution surface investigations*, ASM International, Ohio, 2002.
- 7 Introduction to Bruker's ScanAsyst and PeakForce Tapping AFM Technology, [https://www.bruker.com/fileadmin/user\\_upload/8-PDF-Docs/SurfaceAnalysis/AFM/ApplicationNotes/Introduction\\_to\\_Brukers\\_ScanAsyst\\_and\\_PeakForce\\_Tapping\\_Atomic\\_Force\\_Microscopy\\_Technology\\_AFM\\_AN133.pdf](https://www.bruker.com/fileadmin/user_upload/8-PDF-Docs/SurfaceAnalysis/AFM/ApplicationNotes/Introduction_to_Brukers_ScanAsyst_and_PeakForce_Tapping_Atomic_Force_Microscopy_Technology_AFM_AN133.pdf), (accessed 02/24 2017).
- 8 B. V. Derjaguin, V. M. Muller and Y. P. Toporov, *Effect of contact deformations on the adhesion of particles*, 1975.
- 9 V. M. Muller, B. V. Derjaguin and Y. P. Toporov, *On two methods of calculation of the force of sticking of an elastic sphere to a rigid plane*, 1983.
- 10 B. V. Derjaguin, V. M. Muller and Y. P. Toporov, *Progress in surface science.*, 1994, **45**, 131.
- 11 J. Goldstein, *Scanning electron microscopy and x-ray microanalysis.*, Springer-Verlag, New York, 2017.
- 12 G. Lawes and A. M. James, *Scanning electron microscopy and X-Ray microanalysis*, John Wiley and Sons, Chichester, 1987.
- 13 B. D. Cullity, *Elements of X-ray diffraction*, Addison-Wesley Publication Company, Reading, Mass., 1956.
- 14 W. F. de Jong, *RECL Recueil des Travaux Chimiques des Pays-Bas*, 1926, **45**, 445-448.
- 15 C. Whiston, *X-ray Methods*, Wiley and Sons, London, 1987.
- 16 A. L. Patterson, *Physical Review*, 1939, **56**, 978-982.

- 17 J. Crawford and L. Slifkin, *Point Defects in Solids General and Ionic Crystals.*, Springer, London, 2014.
- 18 W. Bollmann, *Crystal defects and crystalline interfaces.*, Springer, Berlin, 2013.
- 19 A. Kelly, G. W. Groves and P. Kidd, *Crystallography and crystal defects*, J. Wiley, West Sussex, 2012.
- 20 B. George and P. McIntyre, *Infrared Spectroscopy*, Wiley and Sons, London, 1987.
- 21 B. Stuart, W. O. George, P. S. McIntyre and D. J. Ando, *Modern infrared spectroscopy*, Wiley, Chichester, 1998.
- 22 F. M. Mirabella, *Internal reflection spectroscopy: theory and applications*, Marcel Dekker, New York, 1993.
- 23 J. Xie, C. Riley, M. Kumar and K. Chittur, *Biomaterials*, 2002, **23**, 3609-3616.
- 24 A. Barth, *Biochimica et Biophysica Acta (BBA) - Bioenergetics*, 2007, **1767**, 1073-1101.
- 25 A. Adochitei and G. Drochioiu, *Revue Roumaine De Chimie*, 2011, **56**, 783-791.
- 26 S. Krimm, *BIP Biopolymers*, 1983, **22**, 217-225.
- 27 J. L. R. Arrondo, A. Muga, J. Castresana and F. M. Goni, *Progress in Biophysics & Molecular Biology*, 1993, **59**, 23-56.
- 28 Chirgadze, Yu. N., Nevskaya, N.A., *BIP Biopolymers*, 1976, **15**, 627-636.
- 29 C. M. Li, C. Vepari, H. J. Jin, H. J. Kim and D. L. Kaplan, *Biomaterials*, 2006, **27**, 3115-3124.
- 30 H. Teramoto and M. Miyazawa, *Biomacromolecules*, 2005, **6**, 2049-2057.
- 31 J. L. R. Arrondo and F. M. Goni, *Progress in Biophysics & Molecular Biology*, 1999, **72**, 367-405.
- 32 E. Goormaghtigh, V. Cabiaux and J. M. Ruyschaert, *European Journal of Biochemistry*, 1990, **193**, 409-420.
- 33 J. Kong and S. Yu, *Acta Biochimica Et Biophysica Sinica*, 2007, **39**, 549-559.
- 34 S. H. Kim, Y. S. Nam, T. S. Lee and W. H. Park, *Polymer journal / Society of Polymer Science, Japan.*, 2003, **35**, 185-190.
- 35 B. Berne and R. Pecora, *Dynamic Light Scattering*, John Wiley, New York, 1976.
- 36 H. Fissan, S. Ristig, H. Kaminski, C. Asbach and M. Epple, *Analytical Methods*, 2014, **6**, 7324-7334.

- 37 R. J. Hunter, *Zeta potential in colloid science: principles and applications*, Academic Press, London; San Diego, 1988.
- 38 I. Gentle and G. Barnes, *Interfacial science: an introduction*, Oxford University Press, Oxford; New York, 2005.
- 39 Y. Yuan and T. Lee, in *Surface Science Techniques*, ed. G. Bracco and B. Holst, Springer, Berlin, 2013, p. 3-34.
- 40 F. A. Cotton and G. Wilkinson, *Advanced Inorganic Chemistry, 5th Edition*, Wiley and Sons, New York, 1988.
- 41 H. Yang, C. Li, C. Wei, M. Li, X. Li, Z. Deng and G. Fan, *Analytical Methods*, 2015, **7**, 5462-5467 (DOI:10.1039/c5ay01306b).
- 42 Perry CC, *Progress in molecular and subcellular biology*, 2009, **47**, 295-313.
- 43 H. Perkampus, *Uv-vis spectroscopy and its applications.*, Springer-Verlag, Berlin, 2012.
- 44 M. M. Bradford, *Analytical Biochemistry*, 1976, **72**, 248-254.
- 45 J. E. Noble and M. J. A. Bailey, in *Guide to Protein Purification, 2nd Edition*, ed. R. R. Burgess and M. P. Deutscher, 2009, p. 73-95.
- 46 J. E. Noble, *Methods in enzymology*, 2014, **536**, 17-26.
- 47 T. Zor and Z. Selinger, *Analytical Biochemistry*, 1996, **236**, 302-308.
- 48 G. W. Ewing, *Analytical instrumentation handbook*, M. Dekker, New York, 1997.

## Chapter III

### Silk-Silica Composites for Biomedical Application

Research presented in this chapter has been published - “Influence of silk-silica fusion protein design on silica condensation in vitro and cellular calcification”<sup>1</sup>

#### 3.1 Introduction

The need for foreign materials as bone and dental implants in the human body has led to the growth of research as to how to continue to improve these materials in respect of biological outcomes.

Dental implants are a semi-permanent realistic-looking solution to missing teeth; by filling gaps with supportive materials there is a reduction in strain and an added protection for the surrounding teeth and jaw bone.<sup>2</sup> Dental implants are unique in the sense they can be employed regardless of the cause of the missing tooth/teeth.<sup>3</sup> An implant gives a more natural feel in the mouth when compared with dentures that can often impair a person’s ability to speak and eat.

Dental implants tend to be made of titanium or a titanium alloy,<sup>4-8</sup> due to their low density, high strength, non-hazardous nature and high resistance to corrosion.<sup>9</sup> However the insertion process of a pure titanium/titanium alloy often results in an inflammatory response from surrounding tissues.<sup>10</sup> Another hindrance to this process is the inert properties of titanium alloys preventing bone from easily binding to the surface. This can be overcome by treating the implant with a coating before insertion.<sup>9-19</sup>

Silk materials are useful as biomedical devices due to their biocompatibility and their extraordinary physical properties.<sup>20-22</sup> High tensile strength and elasticity provide a useful basis for silk materials with medical and non-medical applications as goals.<sup>23-27</sup> Silk can be formed into gels, sponges, films, membranes and scaffolds<sup>28-32</sup> with applications from controlled release<sup>33</sup> to supportive scaffolding constructs.<sup>34,35</sup>

Dragline silk from spiders is the focus of the present study due to its support line and framing functions in orb webs.<sup>36</sup> The structure consists of protein beta sheet crystals distributed via long protein fibres, Figure 3.1.<sup>37</sup>

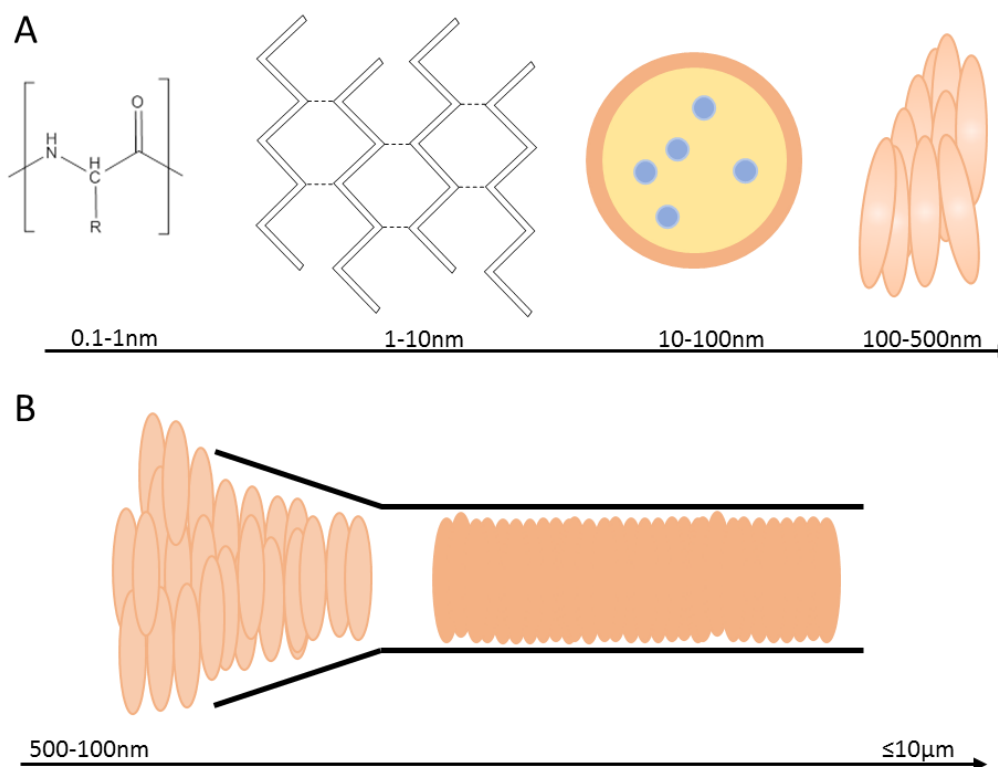


**Figure 3.1 A)** The steps of silk self-assembly: the amino acid sequence is formed, beta sheet formation is induced via hydrogen bonding and hydrophobic interactions resulting in self-assembly then inter- and intra- molecular interactions drive the formation of micelles where the provision of hydrophilic spacer groups results in small regions of trapped water, finally an increase in concentration results in gelation to form liquid crystals. **B)** The liquid crystals are transformed *via* environmental factors into highly ordered fibrils (webbing) as they travel down the spinning ducts. Adapted from <sup>37</sup>

However, to generate mechanically stiffer spider-silk biomaterials, analogies from bone composite systems can be made, whereby inorganic components are tightly integrated into collagen protein-based components, to generate unique composite features. A similar approach was taken here, building on past work completed in the Perry group,<sup>38</sup> where a range of spider silk fusion proteins were generated to study silicification. Silica has good compatibility with silk and biological systems.<sup>39</sup>

Silica is also known for its bioactivity particularly with bone tissue, as it binds strongly with bone whilst also being osteoinductive.<sup>38</sup> However, the hard crystalline structures often produced by silica are brittle and lack beneficial tensile properties. By combining the silica with silk materials the best attributes of both can be achieved,

where fully biodegradable, osteoinductive features with a mechanically robust composite system can be achieved. Additionally, the new materials would have potential to be doped with constituents such as growth factors and drugs for programmed release.<sup>40</sup>

Silica is ubiquitous in nature,<sup>41</sup> for example, diatoms are eukaryotic cells capable of producing silica minerals for structural support and protection in the form of a shell.<sup>42</sup> The processes by which these structures are made involve a specific set of proteins (silaffins) that promote the deposition of silica, in a region of the diatoms known as the silica deposition vesicle.<sup>41</sup> The R5 domain (SSKKSGSYSGSKGSKRRIL), a component of a silaffin protein, has been identified as silica promoting *in vitro* as well as in nature. The R5 peptide has been previously used to functionalize recombinant spider silk like proteins and did not disrupt the R5 silica deposition ability.<sup>43</sup> Other peptides including A1 (SGSKGSKRRIL) and the A3 peptide (MSPHPHPRHHHT), derived from the R5 peptide and phage display, respectively, showed silica deposition activity.<sup>44,45</sup> Previously composite silk-silica samples were produced *via* genetic engineering using a 15 repeating unit of a modified version of the 33 amino acid consensus sequence of the major ampullate dragline spidroin 1 (MaSp 1) from *Nephila clavipes* (SGRGGLGGQG AGAAAAAGGA GQGGYGGLGSQGT) and the three peptides mentioned above were covalently bound to the silk via a linker. In previous studies, the ability of each peptide to promote silica condensation in the context of  $\beta$ -sheet crystalline structure formation from the silk was determined.<sup>43</sup>

The work covered in this chapter is focused on further understanding the role that the position or location of the R5 sequence relative to the silk component plays in terms of silica formation. The addition of the R5 peptide was performed directly at the C- or N-terminal of the silk repeating unit by genetic engineering and the physical and chemical properties of the two protein constructs were analysed relative to the induction of silica precipitation and compared to previously published data.

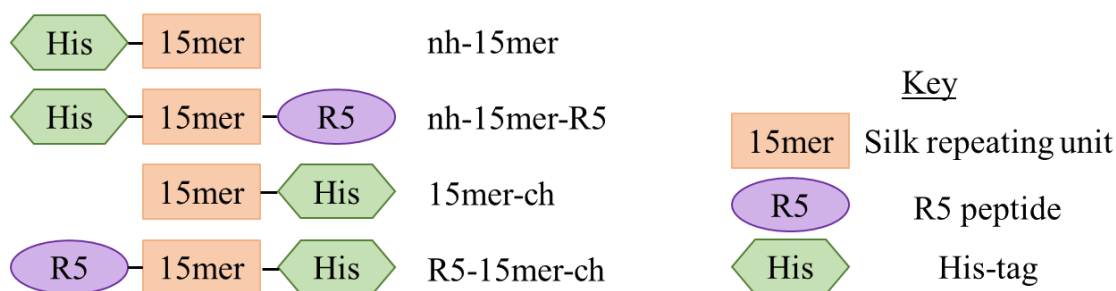


**Figure 3.2** Sample structure of the silk chimeras discussed in this chapter. A 15mer silk repeating unit with a His-tag bound at the N or C terminal, and the equivalent of these with an R5 silicifying domain occupying the vacant terminal.

### 3.2 Methods and Materials

Synthesis, expression and purification of silk chimeras was performed by collaborators at Tufts University. As part of the collaboration, a six week microbiology course was completed.

#### 3.2.1 Construction of recombinant silk and silk-silica chimeras

The following constructs were designed: 15mer-ch, nh-15mer, R5-15mer-ch and nh-15mer-R5. 15mer-ch and nh-15mer are spider silk constructs build of 15 repeating units (SGRGGLGGQG AGAAAAAGGA GGGYGGLGSQGT)<sub>15</sub> that carry a Histidine tag (His<sub>6</sub> = h) on the C-terminal and N-terminal end, respectively. R5-15mer-ch is a 15mer-ch based construct that has the R5 sequence (SSKKS GSYSGSKGSKRRIL), at N-terminal end, whereas nh-15mer-R5 is nh-15mer based construct that has the R5 sequence at C-terminal end. Plasmids pET30ch and pET30nh were used as cloning vectors, where the His-tag is located at the C- or N-terminal of the genetic constructs, respectively. Both pET-30ch and pET-30nh are pET-30a(+) (Novagen, San Diego, CA, USA) derivative vectors. The construction of the cloning vectors pET-30ch and pET-30nh was performed in a similar fashion to that described previously.<sup>46</sup> Briefly, for the construction of pET-30ch linkers 1F and 1R were used, whereas for the construction of pET-30nh linkers 2F and 2R were used. The cloning cassette linkers 5'TATGGCTAGCGGTGACCTGAATAACACTAGTC3' (linker 1F), TCGAGACTAGTGTTATTCAGGTCACCGCTAGCCA (linker 1R), 5'TATGCACCATCATCATCATCATGCTAGCGGTGACCTGAATAACACTAGTTAAAC3' (linker 2F) and TCGAGTTTAACTAGTGTTATTCAGGTCACCGCTAGCATGATGATGATGGTGCA (linker 2R) were generated with *NdeI* and *XhoI* sites and prepared by annealing two

complement synthetic nucleotides (1F-1R and 2f-2R). Annealing was accomplished by decreasing the temperature of a 20 pmol/ $\mu$ L oligonucleotide solution from 95 to 20°C at a gradient of 0.1°C/s. Mismatched double strands were denatured at 70 °C followed by a further temperature decrease to 20 °C. This cycle was repeated three times. The resulting double stranded linker was ligated into pET30a(+) previously digested with *NdeI* and *XhoI*. Both restriction sites were preserved after ligation. The resulting cloning vectors were referred to as pET30ch and pET30nh. The His-tag in the pET30nh vector was integrated as an *NdeI/NheI* fragment using pre-annealed oligonucleotides TATGCACCATCATCATCATG His-tagF and CTAGCATGATGATGATGATGGTGCA His-tagR. Next, a 1485bp DNA *NheI/SpeI* fragment containing genetic sequence coding for artificial silk protein, 15mer (SGRGGLGGQGAGAAAAAGGAGQGGYGGGLGSQGT)<sub>15</sub>, was inserted into pET30ch and pET30nh to yield pET30ch-15mer and pET30nh-15mer, respectively.<sup>47</sup> To prepare the chimeras with the R5 sequence fused at the C- and N-terminus of the 15mer, pET30ch-15mer and pET30nh-15mer were digested with *SpeI* and then treated by antarctic phosphatase (NEB, Ipswich, MA, USA) to prevent self-ligation. The nucleotide sequences of R5 were designed with restriction endonuclease sites *NheI* and *SpeI* flanked at the 5' and 3' termini, respectively. Codons were optimized for expression in *Escherichia coli* strain BL21(DE3) by using the on-line tool OPTIMIZER and were synthesized commercially (Invitrogen, Grand Island, NY, USA). The synthesized nucleotides were annealed to generate double strands and then ligated to generate the constructs pET30ch-R5-15mer and pET30nh-15mer-R5. *E. coli* DH5 $\alpha$  cells were transformed and positive clones were selected on lysogeny broth (LB) plates supplemented with kanamycin (50  $\mu$ g/mL).

### 3.2.3 Expression and purification of recombinant silk and silk-silica chimeras

The recombinant silk constructs were expressed in *E. coli* strain BL21 Star (DE3) (Invitrogen, Grand Island, NY, USA). A fermenter (Bioflo 3000, New Brunswick Scientific, Edison, NJ, USA) was used for the expression. Cells were cultivated at 37°C in LB medium with 50  $\mu$ g/mL kanamycin. Once the optical density OD<sub>600</sub> reached 0.8, the isopropyl  $\beta$ -d-1-thiogalactopyranoside, IPTG (Sigma-Aldrich, St. Louis, MO, USA) was added at a final concentration of 1 mM to induce expression. After 5 h cells were harvested by centrifugation for 20 min at 8,000 rpm. Recombinant silk protein and chimeras were purified by Ni-NTA affinity chromatography as previously described<sup>44</sup>. Once purified, proteins were dialyzed

and lyophilized<sup>44</sup>. Protein identity and purity were confirmed by SDS-PAGE (Invitrogen, Grand Island, NY, USA).

### 3.3.3 Silk Films

#### *Silk Film Production*

Polydimethylsiloxane (PDMS) discs were formed as an inert support material for silk film formation. Sylgard 184 PDMS (m/solar, Campbell, CA, USA) base and curing agent were mixed in a 10:1 ratio in a petri dish and then placed under vacuum for 1 hour so that releasing the vacuum removed the bubbles. The solution was then placed in an oven set to 57°C for 4 hours. A 6 mm diameter cork borer was used to produce discs. Next, a 2.5% solution of each recombinant protein (nh-15mer, nh-15mer-R5, 15mer-ch, R5-15mer-ch) was produced using 1,1,1,3,3,3-hexafluoroisopropanol (HFIP) (Sigma-Aldrich, Dorset, UK), the silks were allowed to dissolve overnight at room temperature. A 30 µL aliquot of the silk-HFIP solution was pipetted onto the 6 mm PDMS discs and air dried overnight. The silk films were then annealed with aqueous methanol using a vacuum oven set to 635 mbar containing 4 petri dishes: 2 containing a 60% aqueous methanol solution and 2 containing cotton wool soaked in a 60% aqueous methanol solution.

#### *Silicification of films*

For induction of silicification, the recombinant proteins (nh-15mer, nh-15mer-R5, 15mer-ch, R5-15mer-ch) mounted on a PDMS substrate were placed in a 24 well plate with 1 mL of pre-hydrolysed 30 mM tetraethyl orthosilicate in pH 7.4 buffer solution (Sigma-Aldrich, Dorset, UK) for 1 hour.<sup>44</sup> The films were then rinsed twice with water and left to dry overnight in a fume hood.

#### *Characterisation*

**Scanning Electron Microscopy and Microanalysis (SEM-EDX).** SEM-EDX at 20 kV (JEOL 840,UK with Oxford Instruments Inca X-ray microanalysis, Oxford, UK) was used to observe the morphology and size of the particles and obtain information on the elemental composition of the films. Each sample was mounted onto electrically conducting carbon tape on aluminium stubs before being gold coated using an argon gold plasma at 30mV and 1.2 kV for 2 minutes. A minimum of 50 particle diameters were measured and averaged to determine the particles size.

**Molybdenum Blue Assay.** The concentration of silicic acid remaining in solution was measured *via* a molybdenum blue assay.<sup>25</sup> In brief, 10  $\mu\text{L}$  of sample was added to 1.5 mL molybdic acid with 15 mL distilled water. After 15 minutes 8 mL of reducing agent was added, and the absorbance measured as above within 2-24 hours of reducing agent addition and compared against suitable dilutions of 1000ppm  $\text{SiO}_2$  standard treated the same way.

**Fourier Transform Infrared Attenuated Total Reflectance Spectroscopy (FTIR-ATR).**

Protein conformation was assessed using FTIR-ATR (Frontier, PerkinElmer, Coventry, UK), with an average of 40 scans over a range of 4000-650  $\text{cm}^{-1}$ . Silk films were analysed before and after annealing to observe changes in structure. Thermo Grams A1 software v8.0 was used for curve fitting, including baseline corrections. Six points were chosen from the amide I band (1700-1580  $\text{cm}^{-1}$ ), and 4 for the conformer absorbances ( $\beta$ -turn 1690–1662  $\text{cm}^{-1}$ ,  $\alpha$ -helix 1662–1645  $\text{cm}^{-1}$ , random coil 1645–1637  $\text{cm}^{-1}$ ,  $\beta$ -sheet 1637–1613  $\text{cm}^{-1}$ ).<sup>48,49</sup> The remaining 2 bands were introduced to correct for sidechain carbonyl groups and non-baseline resolution of the amide I and II bands. Absorbance bands were restricted to these parameters with the width limited to between 8 and 30  $\text{cm}^{-1}$  (at half height). An iteration was carried out forcing all peaks to have a positive area with a linear baseline and then up to a further 1,000 iterations carried out for curve fitting. The sum of the areas under the relevant peaks was found and each conformer expressed as a percentage of the total.

**Wettability and surface energy measurements.** The wettability and surface energy of each silk sample was measured using a Theta Attension Instrument with OneAttention v 1.7 software (Biolin Scientific, Staffordshire, UK). A silk film mounted on a PDMS substrate was placed on the stand, and using a syringe a 5  $\mu\text{L}$  droplet of water, dimethyl formamide or ethylene glycol was placed on the surface and the contact angle at each side of the droplet measured ten times and an average taken. It was not possible to measure contact angles of the non-annealed films with DMP and ethylene glycol as they dissolved in the solvents.

### 3.3.4 Solution Studies

#### *Zeta Potential*

The charge of each protein sample was determined by zeta potential measurements (NanoS Zetasizer, Malvern, UK) over a pH range of 5 to 9. A 1 mg/mL solution of each chimeric protein sample was prepared using 0.1 M citric acid, the solutions were then filtered using a 200 nm membrane. Five measurements were collected at each pH and an average taken. The

pH adjustment was achieved by addition of 0.1 M bis tris propane buffer and the measurements repeated.

### ***Particle Size Measurements***

The average particle size was measured using a Malvern NanoS Zetasizer (UK), over a pH range of 5 to 9 on samples prepared as above. Five measurements were collected per protein at each pH and an average taken.

### ***Silicification in aqueous media***

The effect of the chimeras on silica precipitation from a metastable monosilicic acid system was investigated. In a 96 well plate 200  $\mu\text{L}$  of 1.0  $\text{mg}/\text{cm}^3$  silk/chimera solutions buffered to pH 3–9 with 0.1 M tris bis propane/citric acid mixtures were pipetted and then 6  $\mu\text{L}$  of prehydrolyzed tetraethoxysilane (TEOS) solution added (2.23  $\text{cm}^3$  TEOS dispersed in and diluted to 9.9  $\text{cm}^3$  with 50% aqueous ethanol, 100  $\mu\text{L}$  of 1 M HCl added and allowed to hydrolyse for 10 min) to give a final  $[\text{Si}(\text{OH})_4]$  of 30 mM. The progress of the condensation process (conversion of monosilicic acid to silica) was monitored by turbidity measurement at 595 nm in a Tecan Infinite M200 pro plate reader to ensure that the process was complete before isolation of the siliceous material produced. The silica was then sedimented by centrifugation (5 minutes at 3000 RPM) and washed three times with water before freeze drying after flash freezing in liquid nitrogen. The reaction supernatant was retained for analysis of residual monosilicic acid by the molybdenum blue method described previously<sup>25</sup> and protein content by a modified Bradford assay.

### **3.3.5 Statistical Analysis**

All data provided are taken from averages with the total number of data points denoted by  $N=x$  and the error plotted as a function of standard deviation. The molybdenum blue assay data is reported for 10 replicate measurements. The protein conformation data is based on 3 separate measurements on different samples, all zeta potential measurements were repeated 5 times and contact angle measurements were performed 20 times, 10 at each of the left and right contact angle.

### 3.4 Results and Discussion

#### 3.4.1 Recombinant production of silk-silica fusion proteins

Recombinant spider silk-silica chimeras were cloned by fusing spider silk 15mers with the R5 domain at either C- or N-terminal domain of the spider silk. A similar chimeric protein was designed previously by fusing 15 repeating units of MaSp 1 and R5 peptides via a linker sequence.<sup>29</sup> The ability of this sequence to induce silica precipitation was demonstrated.<sup>43</sup> However, to improve the silicification process and to avoid possible effects of the interconnecting linker sequence a new set of chimeric proteins was designed without the linker sequence. In addition, this novel approach allowed insight to be gained on the influence of the position of the R5 domain relative to the spider silk sequence and its impact on protein structure, silicification and cell mineralisation. Figure 3.3 illustrates the successful expression and purification of the recombinant constructs nh-15mer (40 kDa), nh-15mer-R5 (43 kDa), 15mer-ch (40 kDa) and R5-15mer-ch (43 kDa).

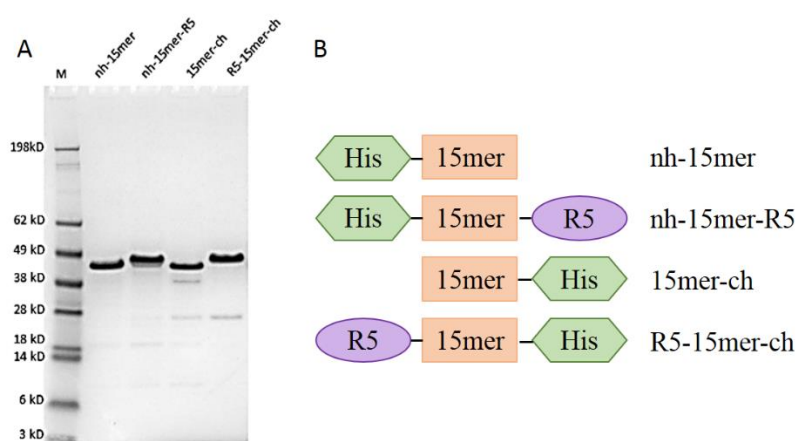


**Figure 3.3** SDS-PAGE of purified recombinant silk-silica chimeric proteins. A) nh-15mer (~40 kDa), nh-15mer-R5 (~43 kDa), 15mer-ch (~40 kDa) and R5-15mer-ch (~43 kDa), were run on the 4%-12% Bis-Tris acrylamide gel and stained with Simple Blue dye. Marker (M) sizes are indicated on the left. B) Schematic representation of silk-silica fusion proteins design strategy; His-tag (green box) has been added to spider silk 15mer at N-terminal end of nh-15mer and nh-15mer-R5 constructs, and C-terminal end of 15mer-ch and R5-15mer-ch constructs; R5 domain (purple circle) has been added to the C-terminal of nh-15mer-R5 and N-terminal of R5-15mer-ch.

### 3.4.2 Solution Studies

#### *Silicification in solution*

Using a model silicifying system, mineralising capabilities towards silica of the four silk constructs was assessed with respect to one another and a blank (no protein containing) system.

Response to pH was observed using a control construct, nh-15mer, where optimum conditions to allow the greatest control over silicification were shown to be at circumneutral pHs, pH 6.9 and pH 7.5, based on particle size uniformity measurements, Figure 3.4A. Silicification carried out under moderately basic conditions saw a decrease in particle size uniformity, whereas at acidic pH 5 two particle populations were formed (averaging approx. 200 nm and 1400 nm) well below and above the average particle sizes produced in controlled systems at circumneutral pHs, suggesting *in vivo* environments, with respect to pH, would permit control over the size of silica particles deposited by the materials. This finding is supported by previous work in the Perry group completed on a silk chimera containing a linking domain between the His-tag and the silk domain.<sup>124</sup>

The beneficial effects of the silk proteins were reflected in the much greater silica particle sizes produced compared with the blank system (2-4 nm) and the much greater monosilicic acid uptake from solution at circumneutral pHs.

All silk constructs produced spherical silica particles however there is a significant difference in size uniformity between samples with varying location of the R5 peptide when silicification was carried out at the optimum pHs discussed above, Figure 3.4B. Constructs with a ch bound His-tag produced particles with a larger size distribution than those with an nh bound His-tag, indicating poorer control over the silicification mechanism. This correlation is paralleled in measured protein concentrations at equilibrium, samples that exhibit the most control over silica deposition also saw the most protein removed from solution. The highest uniformity and therefore greatest control was seen from the nh-15mer-R5 chimera at pH 7.5 with an average particle size of approx. 400 nm, Figure 3.4B.

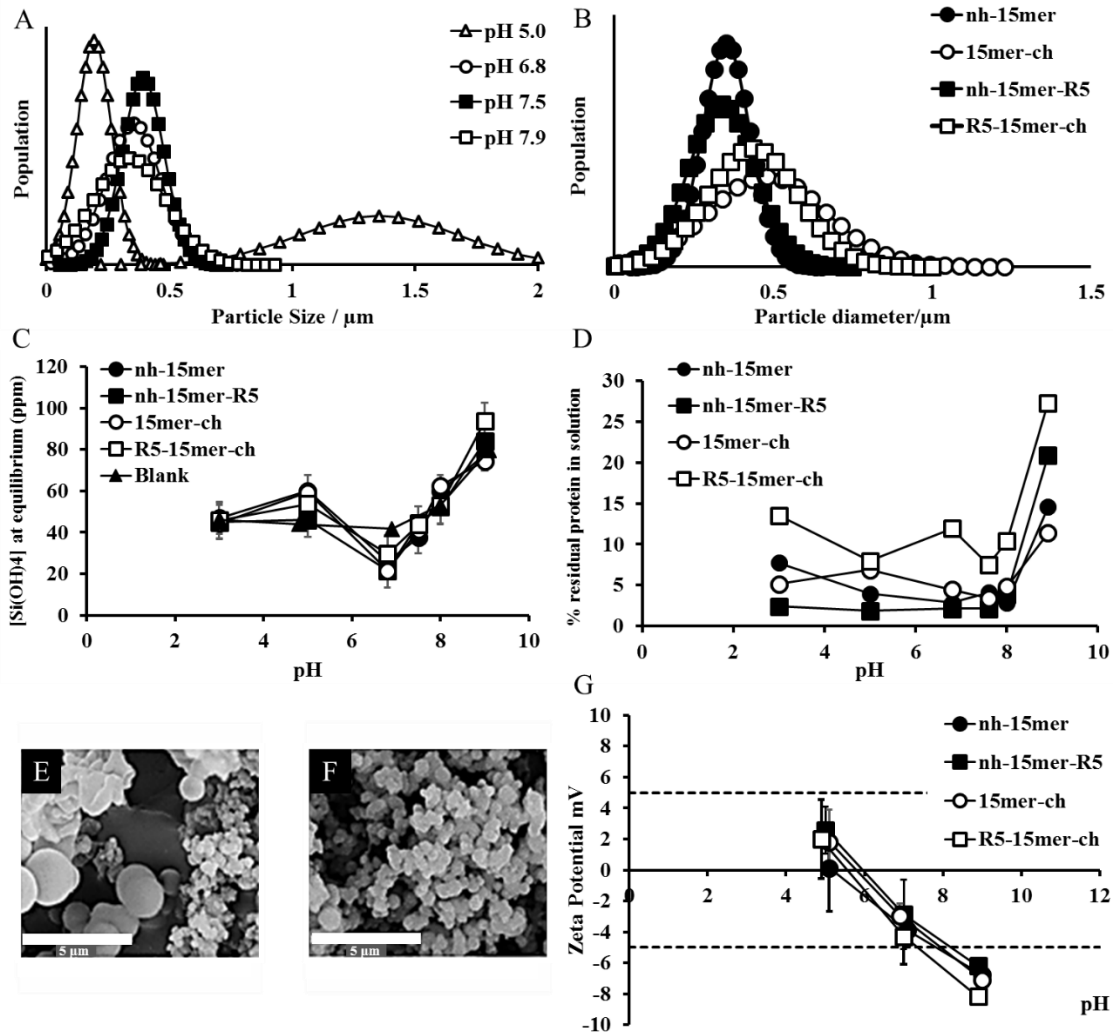


**Figure 3.4** Particle size analysis in solution of **A)** nh-15mer condensed silica pH 5.0 – 7.9 (grey scale intensity indicates level of control shown at each pH (darker scale - more control)), **B)** silica condensed at pH 7.5 in the presence of the different chimeras; solution concentration of **C)** residual monosilicic acid and **D)** silk chimeras at equilibrium. Error analysis based on standard deviation on 5 separate samples **E)** and **F)** example SEM images of nh-15mer at pH 5 and pH 6.8 respectively **G)** Zeta potential data over a range circumneutral pH's for aqueous solutions, 1mg/ml of the nh-15mer, nh-15mer-R5, 15mer-ch and R5-15mer-ch, N=5 for all methods other than particle size measurement by SEM where a minimum of 50 particles were measured.

Chimeric silk proteins are removed from solution via entrainment into condensed silica particles as part of the silicifying mechanism. Under basic conditions protein is seen to a lesser extent, it is believed this is due to the reduced positive charge on the nitrogen side

chains of the silk samples lowering silica affinity with the increased solubility of silica allowing for re-dispersion of proteins back into solution.

### ***Protein charge in solution: Zeta Potential measurements***

Aggregation of silk proteins in solution to give particles can occur due to hydrophobic interactions. A stable colloidal solution requires sufficient repulsion of particles from surface charges to prevent aggregation. With sufficient charge, proteins tend to form stable colloids of isolated molecules, but as charge is removed by changes in pH these tend to be increasingly replaced by aggregated systems. This aggregation and the forming of larger aggregates has been proposed as the mechanism by which silk chimeras have been able to influence the morphology of the silica produced when the colloidal instability and maximum silica condensation rates coincide.<sup>43</sup>

The charge on the proteins as measured via zeta potential showed that all samples, over the pH range explored, contained non-stable particles prone to aggregation with values in the  $0 \leq \pm 5$  mV region, Figure 3.4G. All samples had an isoelectric point between 5 and 6 (Figure 3.4G). The location of the R5 peptide on the silk repeating unit appeared to have negligible effect on the zeta potential at any pH. Comparable results were obtained previously for samples that contained the linking unit.<sup>25</sup> The data also suggests that lower pH offered greater stability for all silk samples with respect to particle aggregation, Figure 3.4G.

### **3.4.3 Silk films**

#### ***Silicification: Particle Size and Morphology***

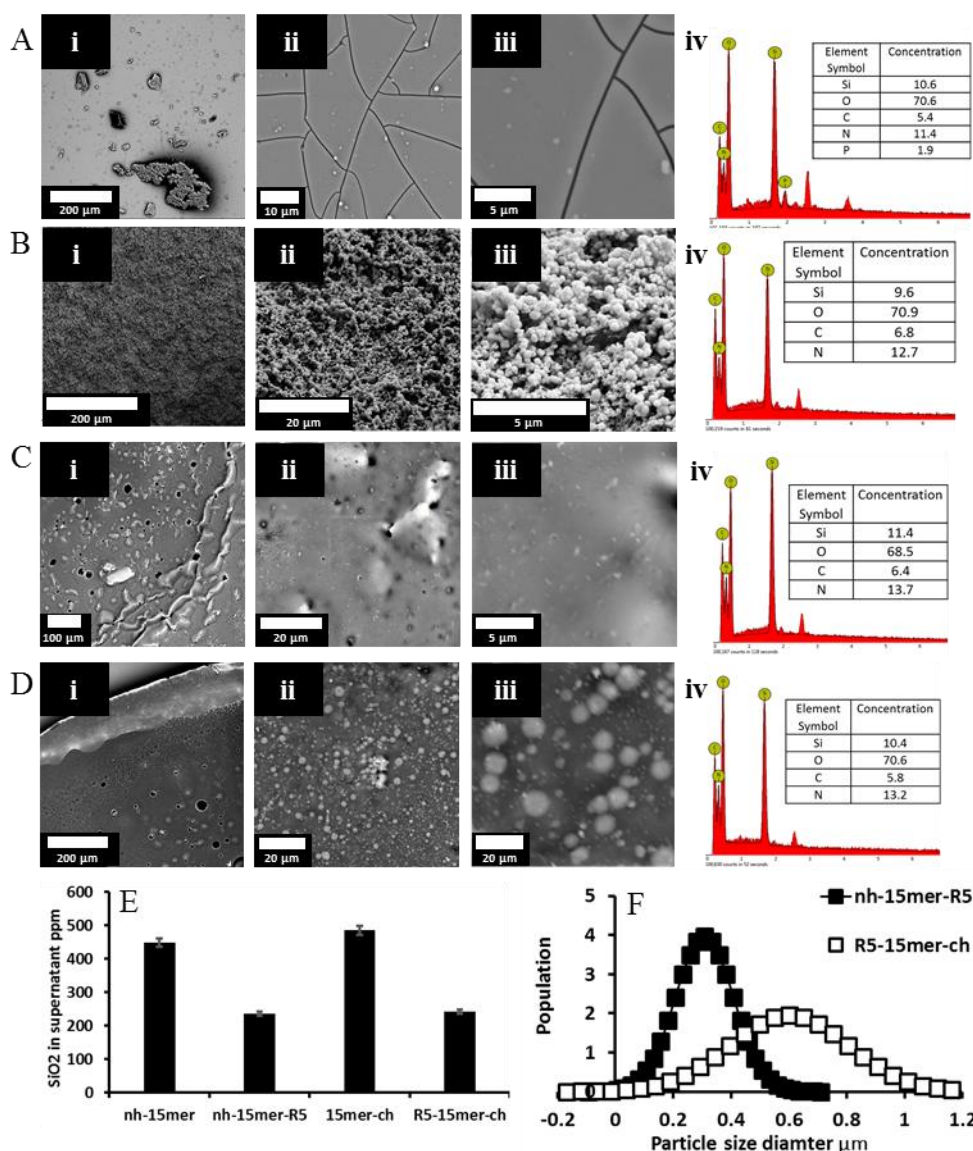
Silica particles formed with these proteins should be homogeneous within the material and large enough to strengthen the material. For practical use, a ‘good’ material will be capable of inducing accelerated silica deposition to give a high silica presence with controlled silica particle size to aid the regrowth of bone and not obstruct the formation of the bone-implant interface. These features can be exploited for bone growth and improved resilience to deformation under compression.

Figure 3.5A-D shows the effect of the presence and position of the R5 construct on the extent of silicification. EDX data for all four constructs confirm the presence of protein (*via* detection of ‘N’) and ‘Si’ on all films, Figure 3.5A-D panel iv. Only films prepared from constructs containing the R5 moiety show recognisable silica particles on the surface, with

those for nh-15mer-R5 being the surface with the highest overall coverage of particles, Figure 3.5B, D. Measurement of the particle sizes on these two surfaces, Figure 3.5D showed that particles formed on the surface of the nh-15mer-R5 chimera films were smaller (average ca. 300nm diameter) and more monodisperse than silica particles formed on the R5-15mer-ch films, Figure 3.5B (average ca. 600nm diameter). A comparison to silica formation on films containing the additional linker in addition to the nh-15mer-R5 construct presented a monolayer of small silica particles of approximately 100 nm diameter (data not shown).<sup>25</sup>

Additional support for silicification taking place on all surfaces is given from analysis of the silica remaining in solution after the films had been silicified, Figure 3.5E. All silk constructs removed silica from solution with the effect being greatest for the two constructs containing the R5 peptide. Although different sizes of silica particles were observed to form (Figure 3.5F) there was little difference in the overall levels of silica condensed for the constructs Figure 3.5F. In solution, the non-chimeric control constructs were shown to exert control over the morphology of the silicified material and this is probably due to the presence of the basic His tagged domain. This effect is clearly lost when films are formed on a PDMS substrate and subsequently annealed suggesting that the His tag may no longer be available for interaction with silica but that the R5 on the chimeras still is. An alternative view is that the R5 domain may reduce the affinity of the chimeras for the PDMS substrate and allow partial solubilisation of the protein back into solution during the silica condensation process resulting in a layer of silica particles similar to those observed during the solution chemistry study.

The presence of silica on all surfaces shows that they are not repelling the deposition of condensing silica but that the non-chimeric control films appear to be passive rather than active in the process.



**Figure 3.5** Scanning electron microscopy images of the silicified films at different magnifications (**i-iii**) with energy- dispersive X-ray spectroscopy data (**iv**) of the area represented by (**iii**). **A-D**) represent the nh-15mer, nh-15mer-R5, 15mer-ch and R5-15mer-ch respectively, with (**i**) showing areas of 100-200 µm (**ii**) 10-20 µm and (**iii**) 5 µm, **E**) Molybdenum blue assay of the supernatants after 1 hour silicification of the nh-15mer, nh-15mer-R5, 15mer-ch and R5-15mer-ch samples, N=10. **F**) Particle size data from SEM images for the nh-15mer-R5 and R5-15mer-ch samples, N=100.

### *Materials Properties of the films*

The secondary structure of silk gives rise to its high mechanical and tensile strength and thus it is instructive to know the natural levels of protein conformers present and their susceptibility to change. Using FTIR-ATR the effectiveness of the annealing

process on inducing  $\beta$ -sheet structure was evaluated by analysis (peak deconvolution) of the amide I band ( $1600\text{-}1700\text{ cm}^{-1}$ ). The amide I band arises primarily from the stretching vibrations of the C=O bond, with location dependent on the structural conformation of the backbone and the hydrogen bonding present.<sup>50,51</sup> This analysis allows quantification of structural types, distinguishing between random coil and beta type structures. Figure 3.6A depicts the  $\beta$  sheet/turn content of the samples before and after annealing, quantitative data presented in Table 3.1. Before annealing, the samples with the His tag at the N terminus exhibited higher levels of sheet/turn. As expected, once annealed, all samples showed increased  $\beta$ -sheet and  $\beta$ -turn content. This was observed in the shift of the amide I band (from approximately  $1650\text{ cm}^{-1}$  to  $1630\text{ cm}^{-1}$ ), along with the change in peak shape. Example IR spectra with peak deconvolution can be seen in Appendix Fig 3.i.

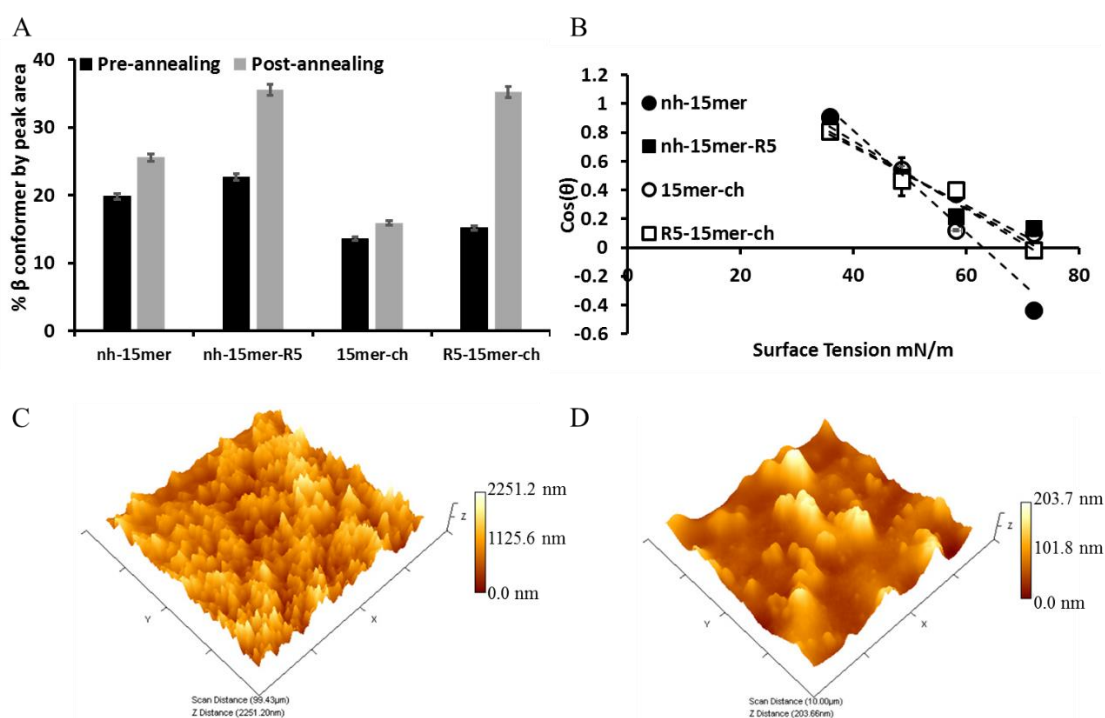


**Figure 3.6** **A)** Nature of the nh-15mer, nh-15mer-R5, 15mer-ch and R5-15mer-ch silk films before and after annealing measured as percentage area assigned as  $\beta$  sheet or turn. Error statistics are the standard deviation of 3 peak fitting results for each sample. **B)** Zisman plot of the genetic constructs. N=20. **C)** and **D)** Representative AFM 3D images for 15mer-ch sample **C)** before annealing **D)** after annealing, scanned areas  $100 \times 100\ \mu\text{m}$ .

The most dramatic change was observed for the R5-15mer-ch sample. In both cases, the presence of the R5 domain in the silk constructs enhanced the transformation to the structurally more robust beta silk structure.

The surface properties of the silk materials were assessed before and after annealing by atomic force microscopy (surface roughness) and by measurement of contact angles using a range of liquids to obtain information on wettability and 'surface' energy, Figure 3.6 and Table 3.1. These properties were measured as the surface roughness and wettability of a biomedical material can have a large effect on whether the materials are accepted or rejected in the body.

Contact angle measurements were made on the R5 peptide containing film samples (nh-15mer-R5, R5-15mer-ch) mounted on PDMS, a known hydrophobic surface, before and after annealing using water. However, it was only possible to use the annealed film surfaces with liquids having a lower surface tension than water as the pre-annealed film samples were too porous/soluble to be assessed further. Films prepared with all silk constructs were hydrophilic before annealing with increases in hydrophobicity, commensurate with the observed changes in beta sheet content (Figure 3.6A) being measured for all samples post annealing, the differences in contact angle before/after annealing was greatest for the samples without the R5 moiety (Table 3.1). The samples containing R5 were more hydrophilic than their corresponding His tagged counterparts after annealing. The surface energies of the silks containing the R5 constructs were reduced compared to the silk constructs only having a His tag, Figure 3.5B and Table 3.1, though the position of the R5 peptide had little effect on the values obtained. AFM analysis of the sample surfaces was used to measure surface roughness, Figure 3.5C and Table 3.1. All materials containing the R5 construct were smoother than their counterparts before annealing with a significant reduction in roughness being observed for both constructs containing R5 after annealing.

Sample		nh-15mer	nh-15mer-R5	15mer-ch	R5-15mer-ch
Contact Angle $\theta$	Preannealed	46.5 ± 1.7	55.0 ± 0.6	56.4 ± 1.2	43.4 ± 0.7
	Annealed	115.7 ± 0.02	74.6 ± 0.003	84.2 ± 0.02	90.9 ± 0.03
Roughness Rq*	Preannealed	348.9 ± 10.4	229.7 ± 6.8	310.2 ± 9.4	167.1 ± 5.0
	Annealed	332.3 ± 9.9	118.0 ± 3.5	-	99.2 ± 3.0
Surface Energies**	Annealed	33.9 ± 0.4	25.8 ± 2.8	30.3 ± 0.2	26.4 ± 0.9
% Beta Structure	Preannealed	19.9 ± 0.4	22.7 ± 0.5	13.6 ± 0.3	15.2 ± 0.3
	Annealed	25.6 ± 0.6	35.54 ± 0.8	15.9 ± 0.4	35.2 ± 0.8

**Table 3.1** Roughness and wettability data collected for the nh-15mer, nh-15mer-R5, 15mer-ch and R5-15mer-ch. Contact angles: N=20, surface roughness N=3, surface energies N=3. \*Root mean square \*\*2<sup>nd</sup> order standard deviation used as error.

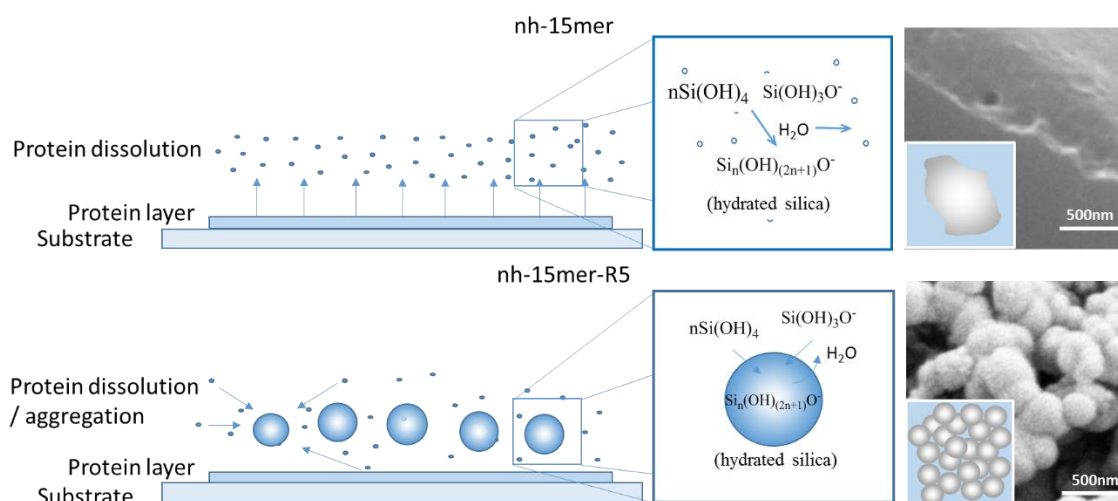
#### 3.4.4 Mechanism of silica particle formation on silk films made from the genetic constructs

It has been previously proposed that the formation of structure in silica condensation experiments performed in the presence of the silk chimeras was due to the development of silk aggregates at pH values corresponding to the natural maximum for silicic acid condensation in solution.<sup>25</sup> In this study we are additionally investigating the effect of a solid interface (silk chimera) with the silicifying medium. In the absence of the spherical structures these chimeras generate in solution, we would expect at most to see the silica deposited ‘within’ the surface if the monosilicic acid has access to it or ‘on’ the surface with electrostatic attachment if silicic acid condensation proceeds in solution in the absence of the protein. For the non-chimeric constructs this behaviour may indeed be the case as EDX analysis shows the presence of silica ‘on/within’ the films, Figure 3.5A-D. Whether this is merely a coating of the normal 2-4nm silica particles produced as for the ‘blank’ silicification reaction in the absence of protein, or a layer infused within the protein layer

could not be determined but the spheres and porosity generated by the constructs containing the silicifying R5 moiety is clearly missing.

In order to understand the differences in behaviour of the constructs containing the R5 silicifying domain positioned at either end of the repeating silk domain as well as the role of the His tag in silicification the FTIR, AFM and wettability data have to be compared (Table 3.1). The annealed silk constructs with the R5 moiety have higher  $\beta$  type content (FTIR spectroscopy) and should yield a more hydrophobic surface, however contact angle measurements do not support this with the non-chimeric nh-15mer exhibiting the highest contact angle (Table 3.1). However the surface roughness is much higher than the R5 constructs, and the scale according to the AFM data is in the correct range to invoke the Cassie-Baxter model of wetting for this surface and the Wenzel model for the R5 containing constructs.<sup>52</sup> The surface energy measurements support this hypothesis in that the annealed chimeric proteins containing the R5 silicifying domain both exhibit lower surface energies and are more hydrophobic than films made from the nh-15mer construct. Since entropic forces controlled by hydrophobic domains drive the control of aggregation in these types of protein then aggregation will be favoured for the R5 constructs.

The experimental data suggest that when these are immersed in the silicifying medium some of the layer becomes re-dispersed near the reaction interface. The R5 constructs due to their higher hydrophobic nature more readily collapse through entropic forces to aggregates whilst the non-chimeras remain largely isolated at the interfacial layer, Schematic 3.1. As a consequence, the silica condenses within the R5 chimera aggregates as for the observed solution studies but the same scale of structure does not develop in the presence of the protein constructs that only contain a His tag.



**Schematic 3.1** The mechanism for the formation of silica at the protein film surface. The none chimeric nh-15mer after dissolution remains mainly as un-associated single molecules or small clusters. The nh-15mer-R5 chimera due to its higher hydrophobic nature forms entropically favoured aggregates/droplets inside which the silicification process is activated through an electron donor/acceptor mechanism and the active elimination of water molecules.

### 3.4.5 Biological Response of Silk Constructs

In order to evaluate the silk-silica composites as potential biomaterials it is necessary to ensure they do not induce an inflammatory response and promote good mammalian cell adhesion once implanted. Assessment of cytotoxicity and cell adhesion was completed at Tufts University by observing cell growth on silk films using live/dead staining.<sup>99</sup>

Films of each R5 containing sample and their corresponding controls were compared to cells grown on a tissue culture plate (TCP) *via* fluorescent live/dead staining. It was shown that each silk film seeded with hMSCs promoted healthy cell growth, proliferation and adhesion for 2 weeks, resulting in the elongation of the hMSCs supporting the use of silk chimeras as biomaterials due to their low cytotoxicity, Figure 3.7. Each construct, silk-silica fusion protein or control, exhibited the same positive response.

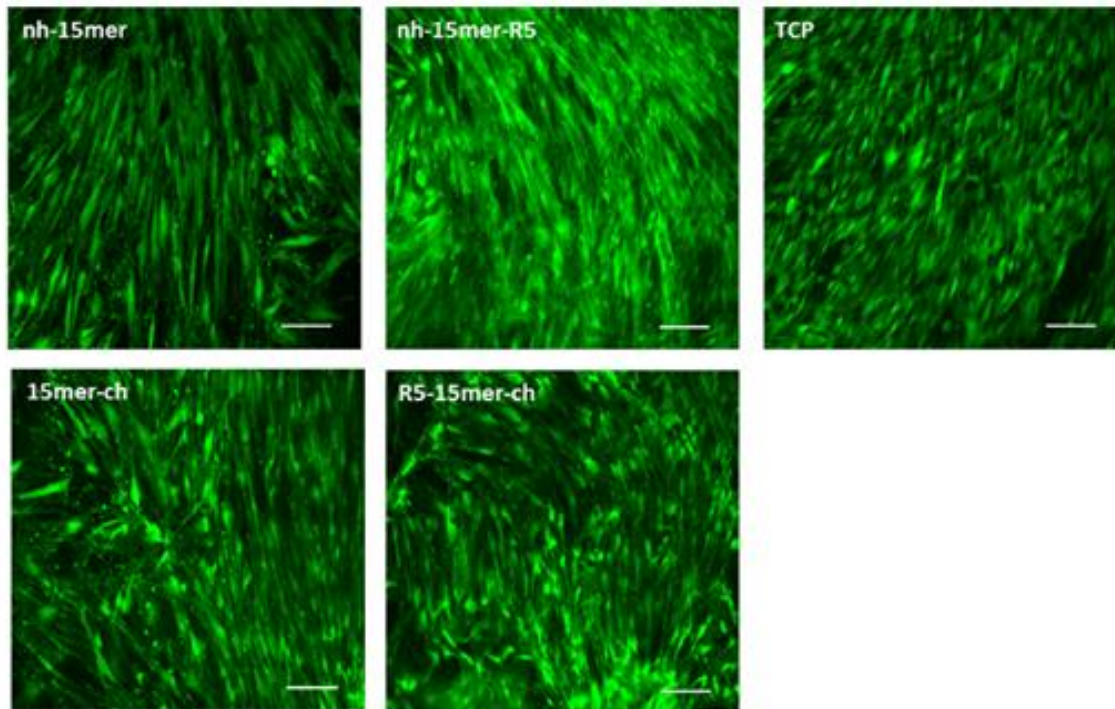


**Figure 3.7** Human mesenchymal stem cell interactions on recombinant silk and silk-silica films. Fluorescent staining was performed on hMSCs cells grown on nh-15mer, nh-15mer-R5, ch-15mer, ch-R5-15mer and tissue culture plate (TCP) two weeks post seeding. The green shows the presence of live cells on the surface, the low levels of dead cells (usually observed in red) are not visible here, Scale bars are 100  $\mu\text{m}$ .

SEM imaging over an 8 week post seeding time period showed typical cell growth over the majority of the silk surfaces, elongated hMSCs cells were visible, indicated with red arrows, Figure 3.8. There was no difference in cell response between the silk R5 chimeras and the control samples.

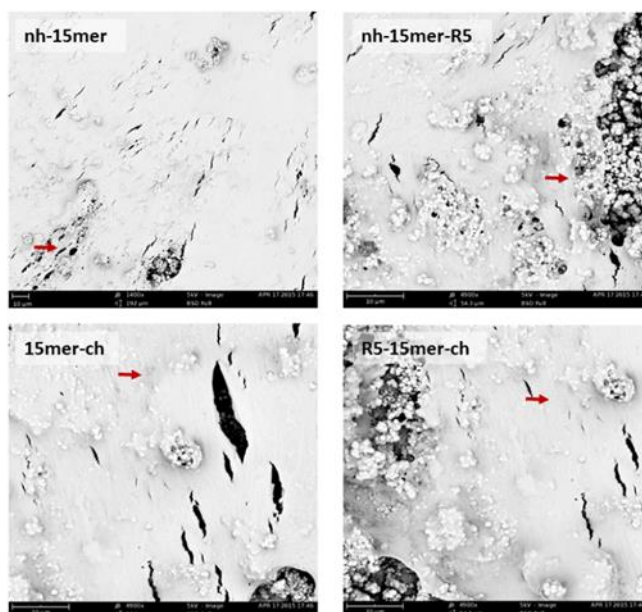


**Figure 3.8** SEM images of human mesenchymal stem cells grown on recombinant silk and silk-silica films. hMSC were grown on pre-silicified recombinant nh-15mer, nh-15mer-R5, 15mer-ch and R5-15mer-ch films. Osteogenesis was induced and cells were imaged 8 weeks post-seeding. Scale bars are 10  $\mu$ m

The potential of the silk-silica constructs to form osteoinductive biomaterials was evaluated through calcium deposition within the hMSC cultures grown on the controls, 15mer-ch and nh-15mer, and R5 constructs, R5-15mer-ch and nh-15mer-R5. Calcium deposition on the cells grown on the silk constructs were compared to TCP control samples 4 and 8 weeks post seeding. The silicifying R5 domain present in the silk chimeras showed greater potential of osteogenesis than the non-R5 containing controls or the TCP samples, Figure 3.9A, B. Both the N and C termini location of the R5 peptide on the silk backbone allowed the silicifying domain to aid calcification, however this was seen to a greater extent by the nh-15mer-R5 sample, (R5 located on the C terminal of the silk), at both 4 and 8 weeks post-seeding. Quantification of calcium present was completed at 4 weeks showing heightened levels in the nh-15mer-R5 sample, Figure 3.9 C. The silk controls used here permitted low levels of calcium deposition, three times less than the R5 samples, highlighting the importance of the R5 silicifying domain. Despite this, silk samples alone permitted more calcium deposition than the control TCP samples.

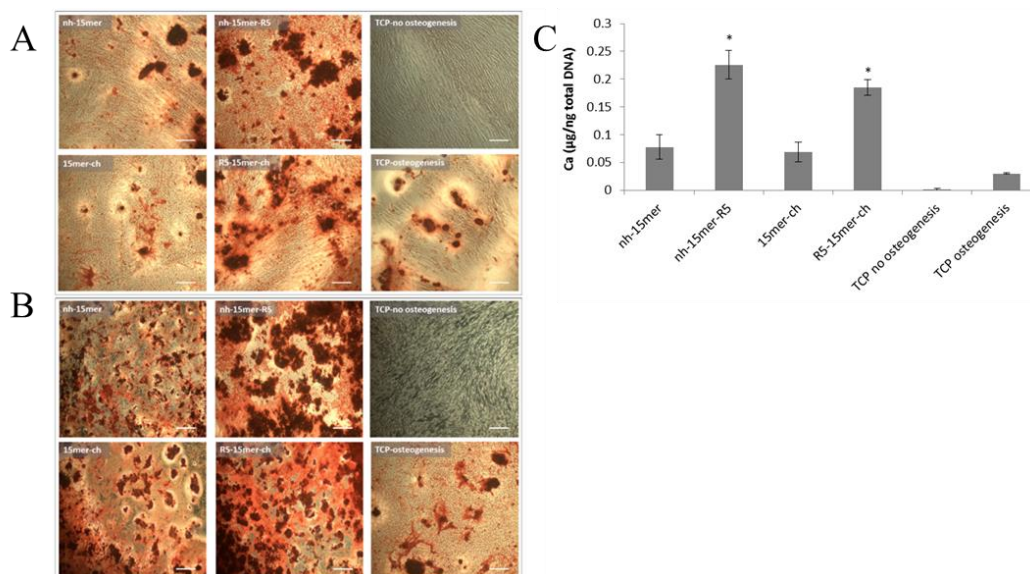


**Figure 3.9** Calcium crystal deposition by differentiating human mesenchymal stem cell on the recombinant silk and silk-silica films. Calcium crystals (red) staining by Alizarin Red S was performed on hMSCs cells grown on nh-15mer, nh-15mer-R5, 15mer-ch, R5-15mer-ch and TCP **A)** four and **B)** eight weeks post seeding. Scale bars are 300 µm. **C)** Calcium deposition of hMSCs grown on recombinant silk-silica constructs after 4 weeks in culture. Results for nh-15mer, nh-15mer-R5, 15mer-ch and R5-15mer-ch silk-silica constructs and TCP no osteogenesis and TCP osteogenesis are shown. Data are represented as the average  $\pm$  standard deviation (n=3, \*p < 0.05).

### 3.5 Conclusions

The physical properties of biomedical materials are a principal factor in the acceptance of an implant, here the location of the R5 peptide appeared to have little influence on the surface properties with respect to the wettability and surface energies of the derived spider silk domain selected here. All constructs could undergo manipulation of protein structure *via* annealing to induce a higher content of beta conformers when the R5 peptide was present.

The N-terminal location of the R5 biomineralization domain in the recombinant 15mer silk fusion proteins, R5-15mer-ch, had a higher potential to induce silica precipitation with the greatest control of silica particles deposited.

When investigated in solution, both R5 silicifying domain containing silk constructs gave reasonable control over silification. Circumneutral pHs were seen to be optimum suggesting

chimeras would have good control over the size of silica particles deposited at an implant site. Zeta potential measurements confirmed the addition of the mineralising peptide to the silk backbone had no significant effect over silk properties in solution, isoelectric points remained unchanged and therefore silks propensity to aggregate allowing heightened control over silicification remained unchanged.

The data supports the use of either of these chimeric silk samples while the chemical and physical data suggest that only minor variations occur in the relevant properties of the silk with or without the addition of the silicifying peptide in solution. The nh-15mer-R5 and R5-15mer-ch structures were both capable of controlled silica deposition on to the interface due to the control of protein particle sizes during silicification.

### 3.6 References

- 1 R. Plowright, N. Dinjaski, S. Zhou, D. J. Belton, C. C. Perry and D. L. Kaplan, *RSC Advances*, 2016, **6**, 21776-21788.
- 2 S. Szmukler-Moncler, H. Salama, Y. Reingewirtz and J. H. Dubruille, *Journal of Biomedical Materials Research*, 1998, **43**, 192-203.
- 3 T. Albrektsson, G. Zard and P. Worthington, *The long-term efficacy of currently used dental implants: a review and proposed criteria of success*, Quintessence Pub. Co., Lombard, 1986.
- 4 L. Guéhenec, A. Soueidan, P. Layrolle and Y. Amouriq, *Dental Materials*, 2007, **23**, 844-854.
- 5 A. S. Assad, S. A. Hassan, Y. M. Shawky and M. M. Badawy, *Implant dentistry*, 2007, **16**, 212-223.
- 6 G. Cannizzaro, M. Leone and M. Esposito, *European Journal of Oral Implantology*, 2008, **1**, 33-43.
- 7 R. Crespi, P. Cappare, E. Gherlone and G. E. Romanos, *International Journal of Oral & Maxillofacial Implants*, 2008, **23**, 753-758.
- 8 M. Donati, V. La Scala, M. Billi, B. Di Dino, P. Torrisi and T. Berglundh, *Clinical oral implants research*, 2008, **19**, 740-748.
- 9 D. M. Brunette, *Titanium in medicine : material science, surface science, engineering, biological responses, and medical applications*, Springer, Berlin; New York, 2001.
- 10 S. Johnson, C. F. Kocha, S. Johnsona, D. Kumarb, M. Jelinekc, D. B. Chriseyd, A. Doraiswamy, C. Jine, R. J. Narayane and I. N. Mihailescuf, *Materials Science and Engineering: C*, 2005, **27**, 484-494.
- 11 W. Xia, C. Lindahl, H. Engqvist and J. Lausmaa, *Biomimetic Hydroxyapatite Deposition on Titanium Oxide Surfaces for Biomedical Application.*, INTECH Open Access Publisher, Uppsala, 2011.
- 12 O. Blind, L. H. Klein, B. Dailey and L. Jordan, *Dental Materials*, 2005, **21**, 1017-1024.
- 13 F. Barrere, Van Der Valk, C. M., G. Meijer, R. A. J. Dalmeijer, K. de Groot and P. Layrolle, *Journal of Biomedical Materials Research Part B-Applied Biomaterials*, 2003, **67B**, 655-665.
- 14 K. de Groot, J. G. C. Wolke and J. A. Jansen, *Proceedings of the Institution of Mechanical Engineers Part H-Journal of Engineering in Medicine*, 1998, **212**, 137-147.
- 15 N. C. Geurs, R. L. Jeffcoat, E. A. McGlumphy, M. S. Reddy and M. K. Jeffcoat, *International Journal of Oral & Maxillofacial Implants*, 2002, **17**, 811-815.

- 16 L. Le Guéhenec, A. Soueidan, P. Layrolle and Y. Amouriq, *Dental Materials*, 2007, **23**, 844-854.
- 17 H. F. Morris, S. Ochi, J. R. Spray and J. W. Olson, *Annals of Periodontology / The American Academy of Periodontology*, 2000, **5**, 56-67 (DOI:10.1902/annals.2000.5.1.56).
- 18 D. Tinsley, C. J. Watson and J. L. Russell, *CLR Clinical Oral Implants Research*, 2001, **12**, 159-166.
- 19 S. L. Wheeler, *The International journal of oral & maxillofacial implants*, 1996, **11**, 340-50.
- 20 C. Vepari and D. L. Kaplan, *Progress in Polymer Science*, 2007, **32**, 991-1007.
- 21 S. Mobini, M. Solati-Hashjin, H. Peirovi, N. A. Abu Osman, M. Gholipourmalekabadi, M. Barati and A. Samadikuchaksaraei, *Journal of Medical and Biological Engineering*, 2013, **33**, 207-213.
- 22 Y. Xu, H. L. Shao, Y. P. Zhang and X. C. Hu, *Journal of Materials Science*, 2005, **40**, 5355-5358.
- 23 C. Fu, Z. Shao and V. Fritz, *Chemical Communications*, 2009, **43**, 6515-6529.
- 24 O. Hakimi, D. P. Knight, F. Vollrath and P. Vadgama, *Composites Part B-Engineering*, 2007, **38**, 324-337.
- 25 D. Huemmerich, C. W. Helsen, S. Quedzuweit, J. Oschmann, R. Rudolph and T. Scheibel, *Biochemistry*, 2004, **43**, 13604-13612.
- 26 C. Z. Zhou, F. Confalonieri, M. Jacquet, R. Perasso, Z. G. Li and J. Janin, *Proteins-Structure Function and Genetics*, 2001, **44**, 119-122.
- 27 U. Kim, J. Park, C. Li, H. Jin, R. Valluzzi and D. Kaplan, *Biomacromolecules*, 2004, **5**, 786-792.
- 28 M. Fini, A. Motta, P. Torricelli, G. Glavaresi, N. N. Aldini, M. Tschon, R. Giardino and C. Migliaresi, *Biomaterials*, 2005, **26**, 3527-3536.
- 29 M. Z. Li, M. Ogiso and N. Minoura, *Biomaterials*, 2003, **24**, 357-365.
- 30 N. Minoura, S. I. Aiba, M. Higuchi, Y. Gotoh, M. Tsukada and Y. Imai, *Biochemical and Biophysical Research Communications*, 1995, **208**, 511-516.
- 31 U. J. Kim, J. Park, H. J. Kim, M. Wada and D. L. Kaplan, *Biomaterials*, 2005, **26**, 2775-2785.
- 32 R. Nazarov, H. J. Jin and D. L. Kaplan, *Biomacromolecules*, 2004, **5**, 718-726.
- 33 E. Wenk, A. Wandrey, H. Merkle and L. Meinel, *Journal of Controlled Release*, 2008, **132**, 26-34.

- 34 L. Uebersax, H. Hagenmueller, S. Hofmann, E. Gruenblatt, R. Mueller, G. Vunjak-Novakovic, D. L. Kaplan, H. P. Merkle and L. Meinel, *Tissue Engineering*, 2006, **12**, 3417-3429.
- 35 K. Gellynck, P. C. Verdonk, E. Van Nimmen, K. F. Almqvist, T. Gheysens, G. Schoukens, L. Van Langenhove, P. Kiekens, J. Mertens and G. Verbruggen, *Journal of Materials Science: Materials in Medicine*, 2008, **19**, 3399-409.
- 36 M. Xu and R. V. Lewis, *Proceedings of the National Academy of Sciences of the United States of America*, 1990, **87**, 7120-7124 (DOI:10.1073/pnas.87.18.7120).
- 37 J. A. Kluge, U. Rabotyagova, G. G. Leisk and D. L. Kaplan, *Trends in biotechnology*, 2008, **26**, 244-251.
- 38 A. Mieszawska, N. Fourligas, I. Georgakoudi, N. Ouhib, D. Belton, C. Perry and D. Kaplan, *Journal of Biomaterials*, 2010, **34**, 8902-8920.
- 39 S. Lopez-Estebana, E. Saiza, S. Fujinob, T. Okuc, K. Sukanumac and A. Tomsia, *Journal of the European Ceramic Society*, 2003, **23**, 2921-1930.
- 40 M. Gimeno-Fabra, M. Peroglio, D. Eglin, M. Alini and C. C. Perry, *Journal of Materials Chemistry*, 2011, **21**, 4086-4089.
- 41 M. Sumper and N. Kroger, *Journal of Materials Chemistry*, 2004, **14**, 2059-2065.
- 42 M. B. Dickerson, K. H. Sandhage and R. R. Naik, *Chemical Reviews*, 2008, **108**, 4935-4978.
- 43 D. J. Belton, A. J. Mieszawska, H. A. Currie, D. L. Kaplan and C. C. Perry, *Langmuir*, 2012, **28**, 4373-4381.
- 44 S. Zhou, W. Huang, D. J. Belton, L. O. Simmons, C. C. Perry, X. Wang and D. L. Kaplan, *Biomaterials*, 2015, **15**, 173-180.
- 45 M. R. Knecht and D. W. Wright, *Chemical Communications*, 2003, **24**, 3038-3039.
- 46 O. S. Rabotyagova, P. Cebe and D. L. Kaplan, *Biomacromolecules*, 2009, **10**, 229-236 (DOI:10.1021/bm800930x).
- 47 C. Wong Po Foo, S. V. Patwardhan, D. J. Belton, B. Kitchel, D. Anastasiades, J. Huang, R. R. Naik, C. C. Perry and D. L. Kaplan, *Proceedings of the National Academy of Sciences of the United States of America*, 2006, **103**, 9428-9433.
- 48 A. Adochitei and G. Drochioiu, *Revue Roumaine De Chimie*, 2011, **56**, 783-791.
- 49 H. Teramoto and M. Miyazawa, *Biomacromolecules*, 2005, **6**, 2049-2057.
- 50 J. L. R. Arrondo and F. M. Goni, *Progress in Biophysics & Molecular Biology*, 1999, **72**, 367-405.

51 J. L. R. Arrondo, A. Muga, J. Castresana and F. M. Goni, *Progress in Biophysics & Molecular Biology*, 1993, **59**, 23-56.

52 I. Gentle and G. Barnes, *Interfacial science: an introduction*, Oxford University Press, Oxford; New York, 2005.

## Chapter IV

### Silk Composites Designed for Bone Regeneration

Results from this study have been published in “Osteoinductive recombinant silk fusion proteins for bone regeneration”.<sup>1</sup>

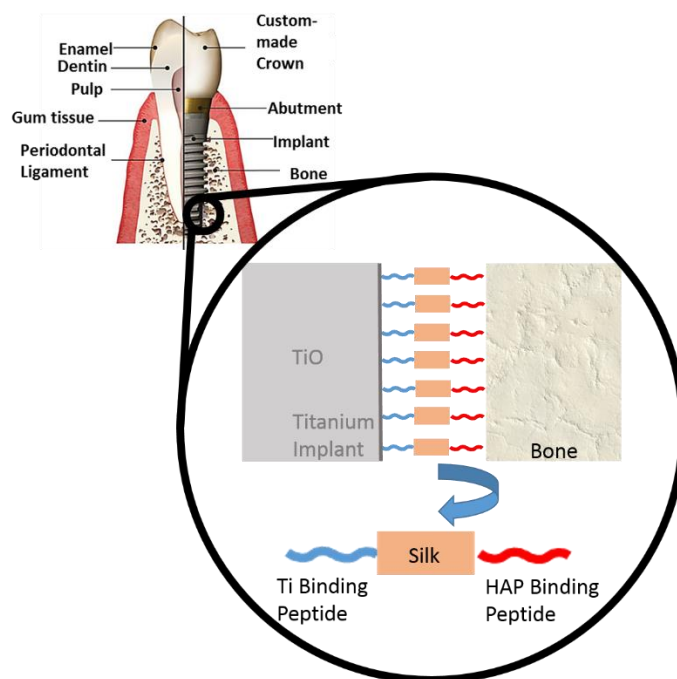
#### 4.1 Introduction

Recombinant biomaterials hold potential for the development of application-specific fine-tuned scaffolding for tissue regeneration and replacement, a major health challenge worldwide. Organic-inorganic interfaces are integral to biomaterial functions in many areas of repair and regeneration, and the surface modification of implantable biomaterial surfaces with bioactive peptides is one approach to design materials for bone formation.<sup>2,3</sup> Several fibrous proteins have been investigated for this purpose.<sup>4,5</sup> Collagens are of particular interest as scaffolds for bone tissue engineering as they are the major protein fraction of bone extracellular matrix.<sup>6,7</sup> However, collagen-based biomaterials generally lack mechanical stability and lose integrity over time.<sup>7</sup> Another unique family of fibrous proteins with impressive mechanical properties, biocompatibility and biodegradability are silks.<sup>8-12</sup> The mechanical strength of spider silk exceeds other natural polymers and most synthetic materials, rivalling even high-performance fibres such as Kevlar, making silk a suitable candidate for bone-related biomaterials.<sup>13</sup>

Biomimetic inorganic-organic hybrid systems have been explored as a route to stiffer and stronger materials.<sup>14-17</sup> To enhance osseointegration, silk has been specifically functionalized with different biological molecules.<sup>15-18</sup> Nonetheless, there is limited information on how these functional domains influence the material properties of silk.<sup>16</sup> Previously, silk-silica peptide designs were generated with studies focussing on understanding the role of the biomineralisation domain position relative to the silk component in the silk-silica fusion proteins in terms of silica formation *in vitro*.<sup>16</sup> The silica-binding peptide R5 (SSKKSGSYSGSKGSKRRIL) taken from the silaffin gene of the diatom *Cerithiopsis fusiformis* was fused to the N- or C-terminus of the silk sequence (SGRGGLGGQGAGAAAAAGGAGQGGYGGGLGSQGT)<sub>15</sub>, derived from the consensus repeat of *Nephila clavipes* dragline silk protein.<sup>16</sup> These fusion proteins were around 43 kDa. As a continuation of this approach silk based

biomaterials were designed to induce hydroxyapatite formation and enhance *in vitro* bone regeneration. Hydroxyapatite was selected as the target inorganic material due to its importance in bone tissues.<sup>19</sup>

Optimal peptide candidates for bone regeneration have been identified *via* phage display, with VTKHLNQISQSY (VTK) as a candidate with preferential interactions with both bone-like minerals and hydroxyapatite.<sup>20,21</sup> Since, the VTK peptide alone does not possess adequate mechanical properties for bone graft engineering, combination with appropriate scaffolding material is required.



**Schematic 4.1** Ideal design for a biomedical silk chimera for coating dental implants, with a titanium binding peptide and HAP binding peptide bound at opposing termini. Adapted<sup>22</sup>

In this study, an artificial silk polymer, 15mer ((SGRGGLGGQGAGAAAAGGAGQGGYGGLGSQGT)<sub>15</sub>, ~39 kDa), derived from the consensus repeat of *N. clavipes* dragline silk protein was genetically modified with the hydroxyapatite binding peptide VTK, with the aim to build a biomaterial with potential application in bone grafting, exploiting both the remarkable mechanical properties of silk and the biomineralisation properties of the VTK peptide. To identify optimal protein design with regard to mechanical performance and osteoinductive properties, the VTK peptide was fused separately to the N-, C- or

both termini of the spider silk, Figure 4.1. The influence of the designs on calcium phosphate deposition with respect to crystallinity was assessed *in vitro*, along with the impact on beta sheet content as a proxy for mechanical strength. These assessments provide insight into structure-function relationships and the effect of functional domains on silk secondary structure/folding and functionalization for bone regeneration.

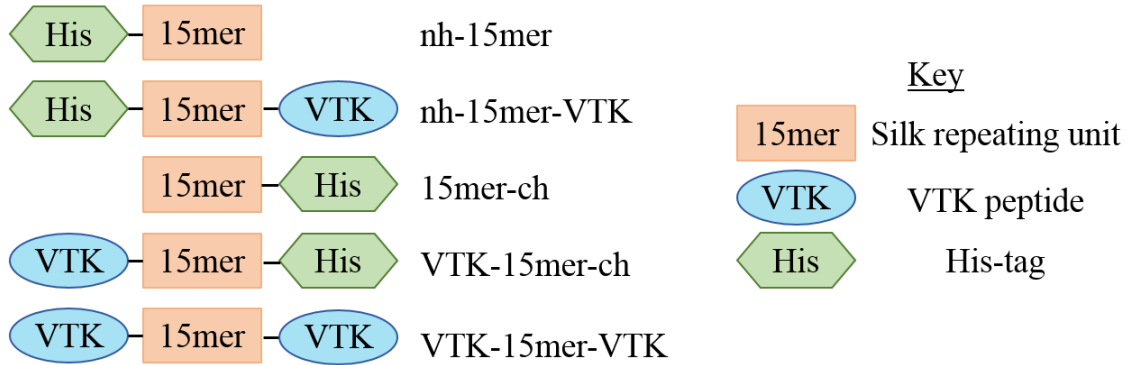


**Figure 4.1** Schematic structures of the silk chimeras discussed in this chapter. A 15mer silk repeating unit with a His-tag bound at the N or C terminal, and their equivalent with the VTK mineralising domain occupying the vacant terminal. Final sample has a VTK peptide occupying each terminal of the silk construct.

## 4.2 Materials and Methods

Synthesis, expression and purification of silk chimeras was performed by collaborators at Tufts University.

### 4.2.1 Construction of recombinant silk and silk-VTK chimeras

The following constructs were designed: 15mer-ch, nh-15mer, VTK-15mer-ch, nh-15mer-VTK and VTK-15mer-VTK, Figure 4.1. The 15mer-ch and nh-15mer are spider silk constructs built of 15 repeating units (SGRGGLGGQG AGAAAAAGGA GQGGYGGLGSQGT)<sub>15</sub> that carry a Histidine tag (His<sub>6</sub> = h) on the C-terminal and N-terminal, respectively. VTK-15mer-ch is a 15mer-ch construct that has the VTK sequence (VTKHLNQISQSY)<sup>20,21</sup> at the N-terminus, whereas nh-15mer-VTK is a nh-15mer that has the VTK sequence at the C-terminus. Plasmids pET30ch and pET30nh were used as cloning vectors, where the His-tag was located at the C- or N-termini of the genetic constructs, respectively. Both pET-30ch and pET-30nh are

pET-30a(+) (Novagen, San Diego, CA, USA) derivative vectors. The construction of the cloning vectors pET-30ch and pET-30nh was performed as described previously.<sup>17</sup> Next, a 1485bp DNA *NheI/SpeI* fragment containing genetic sequence coding for the artificial silk protein, 15mer (SGRGGLGGQGAGAAAAAGGAGQGGYGGLGSQGT)<sub>15</sub>, was inserted into pET30ch and pET30nh to yield pET30ch-15mer and pET30nh-15mer, respectively. To prepare the chimeras with the VTK sequence fused at the C-, N- or both termini of the 15mer, pET30ch-15mer and pET30nh-15mer were digested with *SpeI* and then treated with antarctic phosphatase (NEB, Ipswich, MA, USA) to prevent self-ligation. The nucleotide sequences of VTK were designed with restriction endonuclease sites *NheI* and *SpeI* flanked at the 5' and 3' termini, respectively. Codons were optimized for expression in *Escherichia coli* strain BL21(DE3) using the on-line tool OPTIMIZER and were synthesized commercially (Invitrogen, Grand Island, NY, USA). The synthesized nucleotides were annealed to generate double strands and then ligated to generate the constructs pET30ch-VTK-15mer, pET30nh-15mer-VTK and pET30-VTK-15mer-VTK. *E. coli* DH5 $\alpha$  cells were transformed and positive clones were selected with lysogeny broth (LB) plates supplemented with kanamycin (50  $\mu$ g/mL).

#### 4.2.2 Expression and purification of recombinant silk and silk-VTK chimeras

The recombinant silk constructs were expressed in *E. coli* strain BL21 Star (DE3) (Invitrogen, Grand Island, NY, USA). A fermenter (Bioflo 3000, New Brunswick Scientific, Edison, NJ, USA) was used for the expression. Cells were cultivated at 37°C in LB medium with 50  $\mu$ g/mL kanamycin. Once the optical density OD<sub>600</sub> reached 0.8, isopropyl  $\beta$ -d-1-thiogalactopyranoside, IPTG (Sigma-Aldrich, St. Louis, MO, USA) was added at a final concentration of 1 mM to induce expression. After 5 h cells were harvested by centrifugation for 20 min at 8,000 rpm. Recombinant silk protein and chimeras were purified by Ni-NTA affinity chromatography as previously described,<sup>23</sup> while the VTK-15mer-VTK protein that lacked the His-tag was purified by heat/ammonium sulphate precipitation.<sup>24,25</sup> Once purified, the proteins were dialyzed and lyophilized.<sup>25</sup> Protein identity and purity were confirmed by SDS-PAGE (Invitrogen, Grand Island, NY, USA).

### 4.2.3 Solution Studies

The charge of each protein sample was determined by zeta potential measurements (NanoS Zetasizer, Malvern, UK) over a pH range of 2 to 9. A solution of each recombinant protein was prepared at a concentration of 1 mg/mL in 0.1 M citric acid. The solutions were filtered using a 200 nm membrane and the pH was adjusted by the addition of 0.1 M bis tris propane buffer. Five measurements were collected at each pH and an average taken.

#### *Mineralisation in aqueous media*

Aqueous recombinant silk solutions (1 mg/mL) were prepared using: nh-15mer, nh-15mer-VTK, 15mer-ch, VTK-15mer-ch and VTK-15mer-VTK. For induction of mineralisation, 2 mL of 200 mM calcium chloride and 2 mL of 120 mM sodium phosphate were alternately added as 100  $\mu$ L aliquots to 1 mL of each recombinant protein solution. A pH of 7.4 was maintained using 1 M sodium hydroxide (Fisher Scientific, Loughborough, UK). The solutions were kept at 37°C for 1 hour before the precipitates were collected and washed using dd H<sub>2</sub>O.

#### *Precipitate characterization*

Powder x-ray diffraction XRD (PANalytical X'Pert PRO, Cu K $\alpha$  radiation with wavelength of 1.54056 Å) was used to characterize the crystallinity of the precipitates produced. Aluminium sample holders were used and packed with polydimethylsiloxane (PDMS) (Sylgard 184 PDMS, Mlsolar, Campbell, CA, USA), samples were scanned from 5° to 65° of 2 $\theta$ , accelerating voltage 45 kV, filament current 40 mA and scanning speed 0.02° s<sup>-1</sup>. X'PertHighScore Plus (Version 2.0a) was used for pattern manipulation (baseline correcting and smoothing) and analysis.

### 4.3.4 Silk Films

#### *Silk Film production*

The lyophilized recombinant fusion proteins (15mer-ch, nh-15mer, VTK-15mer-ch, nh-15mer-VTK, VTK-15mer-VTK) were prepared at a concentration of 2.5% (wt/vol) in ultrapure water. The proteins were allowed to dissolve overnight at 4°C. PDMS (Sylgard 184 PDMS, Mlsolar, Campbell, CA, USA) disks (R=6 mm) were used as substrates on which 30  $\mu$ L aliquots of each protein solution was deposited, ensuring a full coverage on each disk. Films were air-dried overnight and subsequently subjected to water vapour annealing using an isotemp vacuum oven for

24 h at room temperature and 635 mbar. Afterwards, films were air-dried overnight at room temperature.

#### ***Mineralisation of recombinant silk and silk-VTK films***

For induction of chemical mineralisation, the recombinant proteins (15mer-ch, nh-15mer, VTK-15mer-ch, nh-15mer-VTK, VTK-15mer-VTK) mounted on PDMS substrates and a PDMS disk with no protein film, were placed in 24 well plates with 10 mL of 1:1 solution of 12 mM NaH<sub>2</sub>PO<sub>4</sub> pH 7.4 (adjusted using NaOH) and 20 mM CaCl<sub>2</sub> (Sigma-Aldrich, Dorset, UK).<sup>26</sup> After incubation for seven days at room temperature, the films were rinsed twice with water to remove soluble salts and left to dry overnight. Data for the control PDMS disk shown in Appendix 4.ii.

#### ***Scanning electron microscopy (SEM) and energy-dispersive X-ray spectroscopy (EDX)***

SEM-EDX at 20 kV (JEOL 840, UK with Oxford Instruments Inca X-ray microanalysis, Oxford, UK) was used to observe the morphology and size of deposits post mineralisation of recombinant silk films. Elemental composition of the films was analysed. Each sample was mounted onto electrically conducting carbon tape on aluminium stubs before being gold coated using an argon gold plasma at 30 mV and 1.2 kV for 2 minutes.

#### ***Wettability and surface energy measurements***

The wettability and surface energy of each sample was measured using a Theta Attension Instrument with OneAttention v 1.7 software (Biolin Scientific, Staffordshire, UK). A silk film mounted on a PDMS substrate was placed on the stand, and using a syringe, a 10 µL droplet of water, dimethyl formamide (DMF) or ethylene glycol was placed on the surface and the contact angle at each side of the droplet measured ten times and an average taken. It was not possible to measure contact angles of the non-annealed films with DMF and ethylene glycol as the proteins dissolved in the solvents.

#### ***Fourier Transform Infrared Attenuated Total Reflectance Spectroscopy (FTIR-ATR)***

Protein conformation was assessed using FTIR-ATR (Frontier, PerkinElmer, Coventry, UK), with an average of 40 scans over the range 4000-650 cm<sup>-1</sup>. Silk films were analysed before and after annealing to observe changes in structure. Thermo Grams A1 software v8.0 was used for curve fitting including peak deconvolution and baseline corrections. Six points were chosen from the amide I band (1700-1580 cm<sup>-1</sup>

<sup>1</sup>), and 4 for the conformer absorbances ( $\beta$ -turn 1690–1662  $\text{cm}^{-1}$ ,  $\alpha$ -helix 1662–1645  $\text{cm}^{-1}$ , random coil 1645–1637  $\text{cm}^{-1}$ ,  $\beta$ -sheet 1637–1613  $\text{cm}^{-1}$ ). Absorbance bands were restricted to these parameters with the width limited to between 8 and 30  $\text{cm}^{-1}$  (at half height). An iteration was carried out forcing all peaks to have a positive area with a linear baseline. This was carried out for 1,000 iterations before curve fitting. The sum of the areas under the peaks was found and each conformer expressed as a percentage of the total.

#### **4.3.7 Statistical Analysis**

All data provided are taken from averages with the total number of data points denoted by  $N=X$  and the error plotted as a function of standard deviation. The protein conformation data is based on 3 separate measurements on different samples, all zeta potential measurements were repeated 5 times and contact angle measurements were performed 20 times, 10 at each of the left and right contact angle.

### **4.4 Results**

#### **4.4.1 Recombinant silk fusion protein design and production**

Recombinant silk fusion proteins were designed by fusing the hydroxyapatite-binding peptide VTK to the N-, C- or both termini of the artificial silk 15mer, derived from the consensus repeat of *N. clavipes* dragline silk protein. The addition of VTK domains to a spider silk resulted in recombinant silk fusion constructs with new functions for biomineralisation. The silk domain contributes to the formation of  $\beta$ -sheet structures leading to crystallinity as a proxy for mechanical strength, while the VTK domain was expected to facilitate biomineralisation. Peptide design was focused on understanding the role of the hydroxyapatite binding domain position relative to the silk component in fusion proteins in terms of protein folding and biomineralisation. Fig. 4.2 shows the successful expression and purification of these recombinant spider silk fusion proteins.

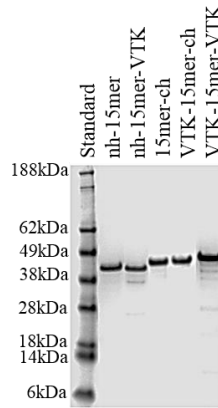


**Figure 4.2** SDS-page of purified nh-15mer (~40 kDa), 15mer-ch (~40 kDa), nh-15mer-VTK (~42 kDa), VTK-15mer-ch (~42 kDa) and VTK-15mer-VTK (~43 kDa), run on the 4% - 12% Bis-Tris acrylamide gel and stained with Simple Blue dye. Marker (M) sizes are indicated on the left.

#### 4.4.2 Solution studies

##### *Protein charge in solution: Zeta potential measurements*

Stability in solution was determined *via* zeta potential measurements, where particles with a zeta potential -5 mV to 5 mV were considered highly unstable and prone to aggregation; those with a zeta potential more/less than  $\pm 30$  mV were considered to be stable.<sup>27</sup> In order to produce a stable colloidal system using the recombinant silk samples, the balance of surface charges of the dispersed phase has to be established to inhibit hydrophobic effects and aggregation of silk in solution. Therefore, to assess the optimal surface charge that resulted in isolated chains within a solution, the pH of the solution was varied. Figure 4.3 shows that all samples had non-stable particles between pH 5–7 with isoelectric points between pH 5.5 and pH 6. However, under more acidic or more alkaline conditions (pH 3 and pH 9) all silk particles in solution could hold charge and increased in stability, Figure 4.3. The location of a single VTK peptide relative to the larger silk component had little effect on overall protein charge as assessed by zeta potential. However, constructs prepared with two VTK domains at either end of the polypeptide chain exhibited the lowest charge at ca. physiological pH.

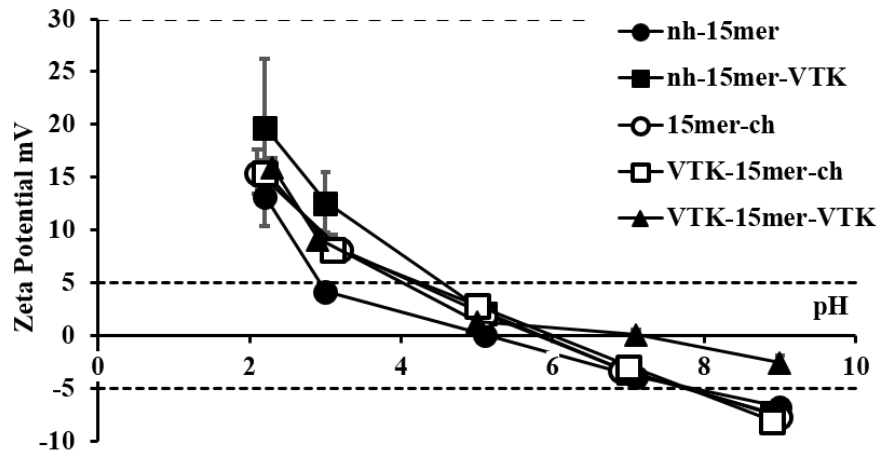


**Figure 4.3** Solution mineralisation of silk proteins. Zeta potential data over the pH range 2–9 for 1 mg/mL aqueous silk solutions, nh-15mer, nh-15mer-VTK, 15mer-ch, VTK- 15mer-ch, and VTK-15mer-VTK, (n = 5, p < 0.05).

#### *Mineralisation in solution*

The effect of each recombinant silk construct on the formation of calcium phosphate from solution was explored (Figure 4.5A), a constant pH of 7.4 was maintained throughout *via* addition of reagents in small aliquots as necessary. With no added protein, the material formed gives a dominant peak at 11.9° signifying the presence of brushite ( $\text{CaHPO}_4 \cdot 2\text{H}_2\text{O}$ ) crystals.<sup>28</sup> Addition of the nh-15mer and 15mer-ch control proteins (no VTK domain) appeared to have no effect on the precipitates formed, while addition of the nh-15mer-VTK and VTK-15mer-ch proteins had similar but limited effects on the precipitates formed producing a mixture of calcium phosphates (predominantly hydroxyapatite and brushite), Figure 4.5A. The location of the VTK peptide in relation to the silk component did affect the relative proportions of each of the mineral phases formed with increased HAP being formed when the VTK peptide was located on the C terminus of the silk. In contrast, mineralisation in the presence of VTK-15mer-VTK construct produced hydroxyapatite (HAP) alone, albeit the positions of peaks in the X-ray diffraction pattern suggested the presence of a mineral phase with defects, Figure 4.5A.<sup>29-31</sup> The absence of a peak at approximately 11.9° arising from brushite, for materials prepared in the presence of the VTK-15mer-VTK protein indicated that significant changes in the mechanism of precipitation had occurred which were not observed for the other silk-based constructs used in the study, Figure 4.5A. These results suggested that either there

was a minimum VTK peptide concentration required to induce HAP formation or that the presence of the His tag hindered the formation of the apatite materials.

To investigate this, mineralisation in the presence of varying concentrations of the VTK-15mer-VTK protein construct were performed, Figure 4.5B. At the lowest protein concentrations used both brushite and HAP were identified with the contribution from brushite disappearing as the protein concentration was increased above 1 mg/mL. A small shift of the peaks arising from the (002) and (004) planes to lower values of 2 theta were observed as the level of protein used in the precipitation experiments was increased suggesting greater control over crystal growth in the z plane of the crystal structure versus the x and y planes. Infra-red (FTIR) spectroscopy was used to compare precipitates formed in the presence of the various recombinant proteins. FTIR data shown in Figure 4.4 provided further evidence for the formation of phosphates in the presence of the silk based proteins, supporting the XRD data. There was no evidence of the presence of other organic material such as silk admixed in with the sample material though this might have been due to the limits of detection of the technique.

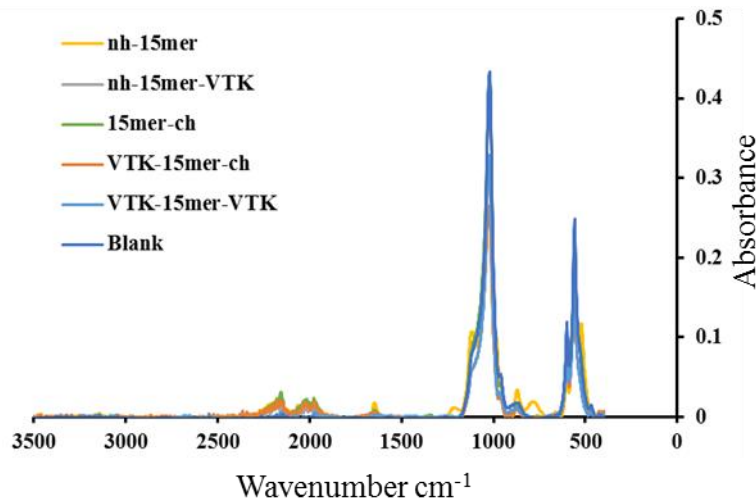


**Figure 4.4** FTIR of precipitates formed in the presence of each recombinant silk sample; nh-15mer, nh-15mer-VTK, 15merch, VTK-15mer-ch and VTK-15mer-VTK.

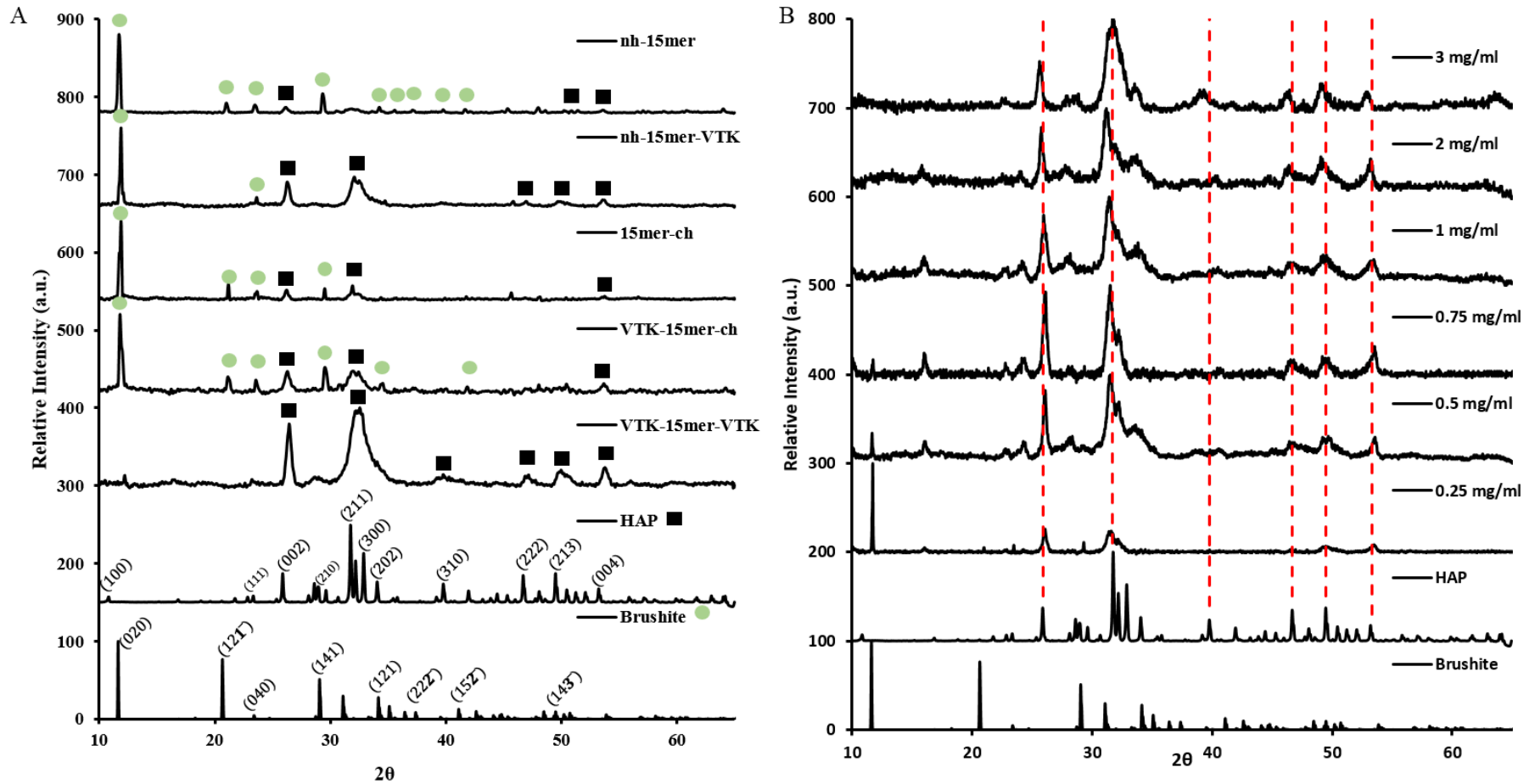


**Figure 4.5** A) XRD data for the precipitates formed in the presence of each recombinant silk sample; nh-15mer, nh-15mer-VTK, 15merch, VTK-15mer-ch and VTK-15mer-VTK. B) Solution mineralisation of silk proteins, XRD data for the precipitates formed in the presence of increasing concentrations of VTK-15mer-VTK.

### 4.4.3 Silk films

#### *In vitro hydroxyapatite mineralisation on silk fusion proteins*

Controlled mineralisation was induced by incubation of the recombinant silk fusion proteins with solutions of  $\text{CaCl}_2$  and  $\text{NaHPO}_4$ . The potential for the different constructs to induce mineralisation as annealed films *in vitro* was assessed by XRD, SEM and EDX. Figure 4.6 shows XRD data for the precipitates formed on each silk film. All samples containing the VTK peptide; nh-15mer-VTK, VTK-15mer-ch and VTK-15mer-VTK, induced the formation of HAP as shown by the broad peak at approx.  $32^\circ$  2 theta, while mineralisation in the presence of films prepared from the constructs without the VTK peptide (nh-15mer and 15mer-ch) did not generate crystalline calcium phosphates. The position of the VTK peptide in relation to the silk construct did show an effect. When bound to the C terminal of the silk, the VTK domain had a greater ability to induce hydroxyapatite formation and, as for the mineralisation studies using the protein in solution, films made from the VTK-15merVTK silk construct were better still, Figure 4.6. FTIR data of the precipitates confirmed the presence of phosphates for the nh-15mer-VTK, VTK-15mer-ch and VTK-15mer-VTK films (phosphate peaks:  $550\text{ cm}^{-1}$   $\nu_4(\text{PO}_4^{3-})$ ,  $960\text{ cm}^{-1}$   $\nu_2(\text{PO}_4^{3-})$ ,  $1010\text{ cm}^{-1}$   $\nu_3(\text{PO}_4^{3-})$ ) and with mixtures of phosphates and carbonates being observed for the control samples nh-15mer and 15mer-ch (carbonate peaks:  $850\text{ cm}^{-1}$   $\nu_2(\text{CO}_3^{2-})$ ,  $1530\text{ cm}^{-1}$   $\nu_3(\text{CO}_3^{2-})$ ). These results suggest that the VTK containing constructs are still able to direct mineralisation when present as part of a solid construct. SEM images coupled with EDX of the recombinant silk films post mineralisation (Figure 4.6B-F) provide further supporting evidence for Ca/P mineralisation on the nh-15mer-VTK, ch-15mer-VTK and VTK-15mer-VTK films. Traces of sodium chloride were present on all analysed films arising from the solutions used in the mineralisation studies. The nh-15mer control sample showed minimal salt deposition, likely sodium chloride, while the 15mer-ch film promoted substantial deposition of a mixture of precipitates, containing calcium, chlorine and phosphorous. Figure 4.6 B,D respectively. Spherical calcium phosphate particles can be seen on films produced with a VTK domain containing chimera, Figure 4.6 C, E, F.

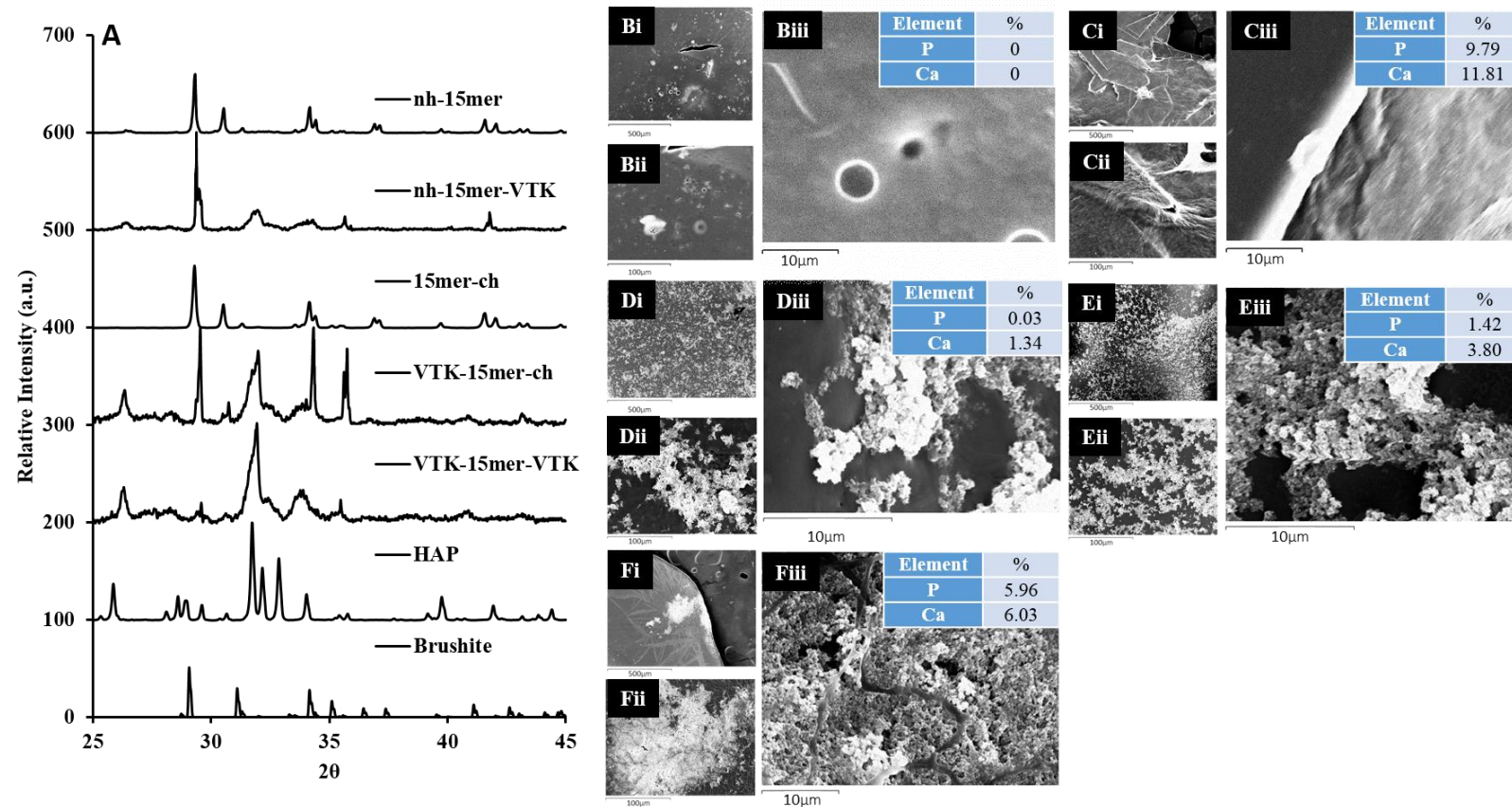


**Figure 4.6** A) XRD patterns of the precipitates formed in the presence of: nh-15mer, nh-15mer-VTK, 15mer-ch, VTK-15mer-ch and VTK-15mer-VTK. B, C, D, E, and F) SEM and EDX; nh-15mer and nh-15mer-VTK, 15mer-ch, VTK-15mer-ch and VTK-15mer-VTK films respectively after 7 day mineralisation. Scale bars are 500  $\mu\text{m}$ , 100  $\mu\text{m}$  and 10  $\mu\text{m}$ .

Similarly, to what was found for solution based mineralisation, the position and the number of hydroxyapatite binding VTK domains in the recombinant silk fusions had an impact on the level of mineralisation on the film surfaces. The constructs harbouring VTK domains on both the N- and C-termini induced the highest level of calcification when compared to all other constructs. This is possibly due to the difference in protein folding and exposure of the VTK domains that are the key factor in catalysing the process. The effect of peptide location on mineralisation (where the VTK domain being attached to the C terminal of silk allows easier access to a greater density of hydroxyl groups) was greater for the solid films than the proteins in solution, probably due to hindered peptide motion restricting contact with mineralizing ions in the immediate environment of the film itself.

### ***Materials properties of the films***

Silk materials possess high tensile strength due to the naturally occurring beta sheet features of the proteins when formed into fibres or other materials.<sup>32,33</sup> The percentage of beta conformers, both sheet and turn, are directly related to the physical properties exhibited by the silk, therefore it is important to measure and explore the ability to customise the beta content of such materials.

The secondary structure of recombinant protein films (nh-15mer, nh-15mer-VTK, 15mer-ch, VTK-15mer-ch, VTK- 15mer-VTK) was analysed by FTIR-ATR. The quantification of protein secondary structure was performed by peak deconvolution analysis of the amide I band. The position and shape of the amide I band changed with varying beta sheet content as the C=O stretching vibrations are influenced by alterations to the conformation of the backbone of the structure and the pattern of hydrogen bonding present.<sup>34,35</sup> Figure 4.7A shows the changes in structural conformation of the silk films before and after annealing. Before annealing the control and VTK containing samples exhibited similar percentages of beta sheet with the exception of the nh-15mer control sample, which contained more beta sheet initially, but showed the smallest structural transformation upon annealing. All samples were susceptible to induced beta structure formation, suggesting these samples have the potential to be tailored in terms of their physical properties. These changes were seen in the shift of the amide I band from  $1650\text{ cm}^{-1}$  to  $1630\text{ cm}^{-1}$ . Example deconvoluted spectra are shown in Appendix Fig 4.i. The wettability and surface energetics of the

films was assessed by contact angle measurements on the silk films before and after methanol annealing. Surface energy calculations were only possible for the annealed films as the non-annealed films were not stable. Each prepared silk film was hydrophilic becoming more hydrophobic after annealing. Non-annealed films produced from the VTK containing samples were more hydrophobic than the control samples, but exhibited less structural change upon annealing, Figure 4.7B. The presence of the VTK peptide at the N terminus of the silk resulted in no significant change in surface energy, in direct contrast to the addition of the VTK domain at the C-terminus of the silk which resulted in a significant decrease in surface energy (from approx. 30–23 Jm<sup>-2</sup>).

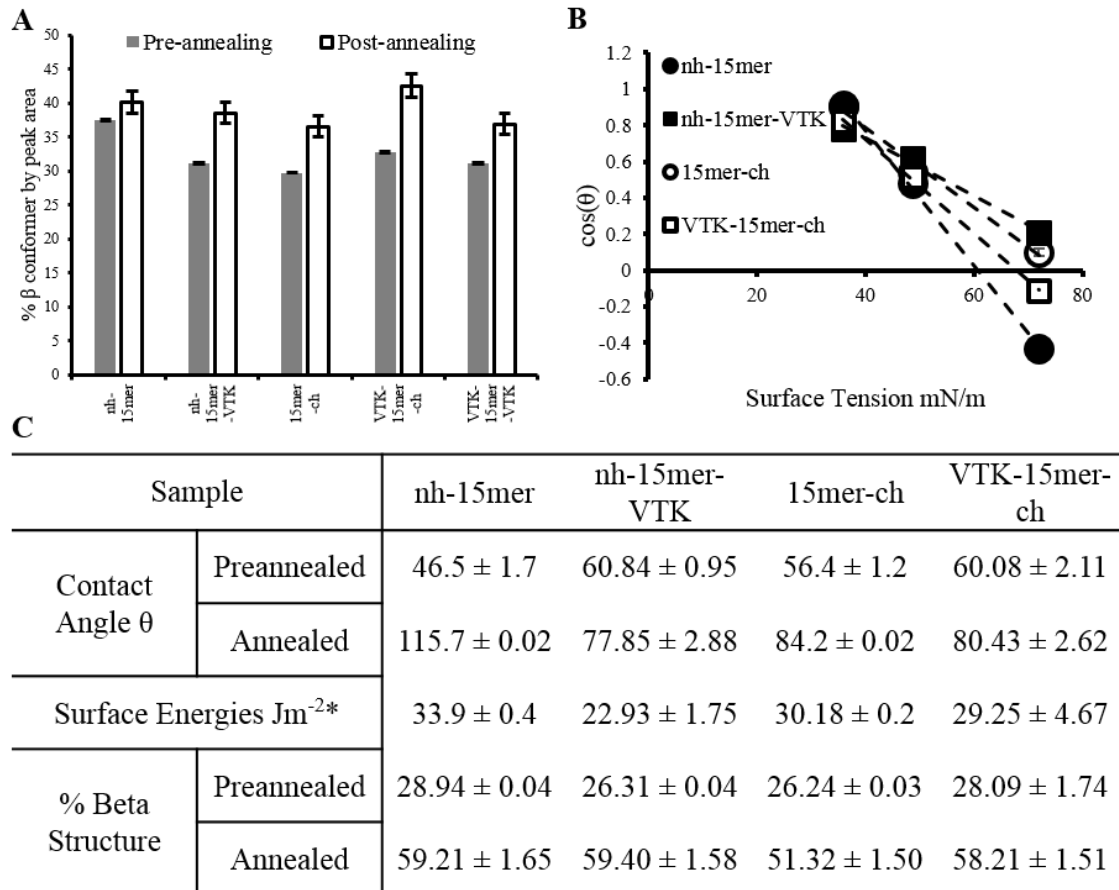


**Figure 4.7** Physical properties of chimeric silk films. A) Beta-sheet content of each silk film before and after annealing ( $n = 5$ ,  $p < 0.05$ ). B) Zisman plots for each silk sample ( $n = 5$ ,  $p < 0.05$ ). C) Table compiling the physical property data to observe any changes occurring from the addition of the VTK peptide.

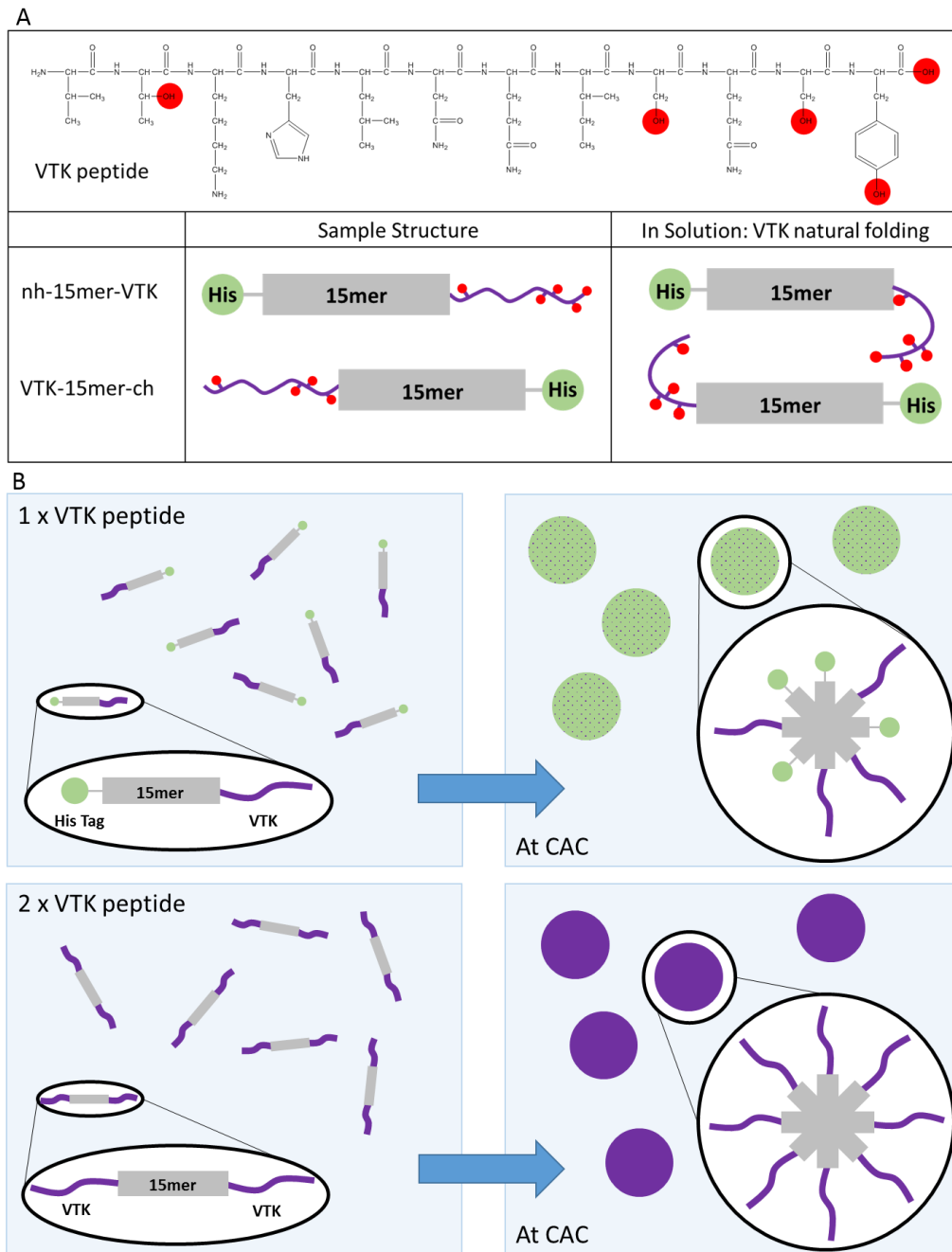
#### 4.4.4 Mechanism of Hydroxyapatite formation in solution based mineralisation

Key parameters for the induction of biomineralisation catalysed by VTK functionalized silk in solution was the number of VTK domains alongside the position of the VTK domain, Scheme 4.2.

Addition of nh-15mer-VTK and VTK-15mer-ch chimeras to mineralisation solutions resulted in a mixture of HAP and Brushite being formed. A comparison of the XRD patterns for materials generated in the presence of these two constructs suggested that the nh-15mer-VTK chimera was more effective at directing the formation of HAP as the intensities of peaks arising from brushite in comparison to those arising from HAP were lower. When the VTK peptide was bound to the C-terminus of the silk, a larger density of hydroxyl groups are available for interaction with mineralizing ions, and this combined with a greater flexibility of the hydroxyl rich end of the peptide leads to a greater effect on mineralisation, Scheme 4.2. The opposite is true for VTK-15mer-ch, as the end of the VTK peptide with the greater density of hydroxyl groups is anchored to the silk domain, likely resulting in limited interactions with the reagents in solution and hence the peptide component is less able to affect the formation of mineralized precipitates, Scheme 4.2. When the same experiment was repeated using the VTK-15mer-VTK chimera, the precipitate formed was solely HAP, highlighting the fact that at either terminus the VTK peptide can be effective. This outcome is probably caused by the assembly of the proteins into micelle-like structures, where the VTK domain is located on the outer surface of the micelle and is therefore more exposed to the solution. This effect is exhibited to a lesser extent with samples containing only one VTK domain, because as the proteins align to form the micelles there is a non-specific arrangement causing peripheral localization of some VTK domains and central localization of others. This results in the shielding of the VTK domains and exposure of the His-tag. This non-specific arrangement does not affect the VTK-15mer-VTK molecules due to either terminus holding the hydroxyapatite binding domain, Scheme 4.2.

In addition, protein concentration was a critical factor to induce biomineralisation. The protein concentration required to optimize physical properties to permit the VTK peptide to influence the formation of precipitates was defined using the VTK-15mer-VTK construct. By increasing the concentration of the VTK-15mer-VTK protein a

narrowing of the peaks in the XRD pattern was observed, suggesting an increase in crystallite domain size. Therefore, modification of protein concentration may be used to tailor the size of crystallites that form in the system. In addition, with increasing VTK-15mer-VTK concentration a significant shift in the XRD peaks with miller indices (002) and (004) towards apatite-like structure was observed, indicating that increased protein concentration leads to a reduction in homogenous strain in the z plane.



(Caption overleaf)

**Scheme 4.2** Structural schematic of the assumed VTK peptide folding in solution when bound to the recombinant silk (A) and solution based mineralization comparing samples with one or two VTK peptides attached to the 15mer silk repeating unit (B). (A) When bound to the C termini of the silk, nh-15mer-VTK, the majority of the hydroxyl groups on the VTK peptide are at the opposite end to the silk where there will be greater mobility and therefore solution interaction allowing heightened control over the precipitates formed. The opposite can be said of ch-15mer-VTK, where most hydroxyl groups will experience shielding and steric hindrance limiting solution interactions and control over mineralization. (B) With one terminus of the silk occupied with the HAP binding domain and the other the His Tag when protein aggregation occurs the two ends will organise in a non-uniform manner. When both ends of the silk are occupied by the VTK peptide non-uniform aggregation has no effect, as one HAP domain will always be exposed to the solution regardless of the orientation of the chimeric protein. CAC: critical aggregation concentration.

#### **4.4.5 Biological Response of Silk Chimeras**

Assessment of cytotoxicity and cell adhesion was completed at Tufts University by observing cell growth on silk films using live/dead staining. Due to the level of similarity to data obtained in the section 3.4.5, the biological results are discussed briefly here with figures omitted.

The ability of the silk-HAP fusion proteins to support cell growth and proliferation whilst inducing osteogenesis was assessed by using human mesenchymal stem cells (hMSCs) cultured (after being cultured in control, chondrogenic or osteogenic medium) on the surface of each film. Culture-expanded hMSCs maintained the ability to selectively undergo chondrogenic and osteogenic differentiation, as assessed histologically. Live/dead staining was used to investigate the ability of the recombinant silk fusion proteins to support hMSC growth and promote differentiation, the cells were grown on the various mineralised film surfaces and compared to those cells grown on a control tissue culture plate (TCP). After 2 weeks the mineralised films were shown to support good cell growth and proliferation with clear elongation of the hMSCs indicating a low cytotoxicity. Strong cell viability and metabolic activity of the hMSCs grown on the control silk films and the VTK containing constructs was verified using an Alamar blue assay 2 weeks post seeding.

Osteogenic parameters were evaluated in the hMSC cultures 8 weeks post seeding. A higher bone sialoprotein production was observed for all the VTK containing samples when compared to the corresponding His-tagged controls. Despite the single VTK bound samples, VTK-15mer-ch and nh-15mer-VTK, showing increased sialoprotein levels, it was the VTK-15mer-VTK silk films that showed the highest potential for influencing bone regrowth. Calcium deposition on the films was assessed using Alizarin Red staining where the importance the HAP binding domain, VTK, was proven. Samples containing a single VTK domain showed a higher calcium deposition than their control counter parts, whilst the VTK-15mer-VTK sample showed the most potential as an osteoinductive biomaterial, permitting 3 times more calcium deposition than the control silk films.

#### **4.5 Conclusions**

Silk materials have been identified for possible biomedical application due to their impressive physical properties, here the genetic modification of the spider silk derived domain to incorporate the HAP binding peptide, VTK, proved to have no detrimental effect on these desired beneficial properties. It was possible to increase the beta conformer content in both the control and chimeric silk films, measured as a percentage of the secondary protein structure, indicating that the mechanical strength of these films can be adapted as required.

HAP mineralisation performed on chimeras in solution (pH 7.4) showed the VTK binding domain to be effective whilst bound to the silk backbone. Samples with a single VTK present both exhibited a limited control over HAP mineralisation with nh-15mer-VTK having greater control over mineralisation compared with VTK-15mer-ch, both produced mixtures of HAP and Brushite. The VTK-15mer-VTK sample, containing a VTK peptide on both termini was shown to have greater control over mineralisation than the singular VTK containing samples. This lead to further experiments proving that chimeric sample concentrations are also a key parameter in mineralisation as well as number of VTK peptides.

Solid state mineralisation also showed the same trend, the presence of control samples produced Brushite such as that found in a blank system, VTK-15mer-ch and nh-15mer-VTK had some control over mineralisation, with the latter being moderately

better, however it was the VTK-15mer-VTK sample that gave a more complete control for inducing HAP formation.

All the data in this study supports the use of the silk-VTK chimeric samples as biomedical materials. Physical and chemical property data showed insignificant variation with the addition of VTK peptide to the silk backbone. The VTK peptide maintained mineralising capabilities once anchored to the silk and under *in vivo* mimicking conditions.

## 4.6 References

- 1 N. Dinjaski, R. Plowright, S. Zhou, D. J. Belton, C. C. Perry and D. L. Kaplan, *Acta Biomaterialia*, 2017, **49**, 127-139.
- 2 H. Shin, S. Jo and A. Mikos, *Biomaterials*, 2003, **24**, 4353-4364 (DOI:10.1016/S0142-9612(03)00339-9).
- 3 J. A. Hubbell, *Current Opinion in Biotechnology*, 1999, **10**, 123-129.
- 4 Geiger, M, Li, R.H,Friess, W, *Advanced Drug Delivery Reviews*, 2003, **55**, 1613-1629.
- 5 L. Meinel, R. Fajardo, S. Hofmann, R. Langer, J. Chen, B. Snyder, G. Vunjak-Novakovic and D. Kaplan, *Bone*, 2008, **43**, 1122-1122.
- 6 A. H. Reddi, *Biochemical Society transactions*, 2000, **28**, 345-349.
- 7 J. Riesle, A. Hollander, R. Langer, L. Freed and G. Vunjak-Novakovic, *Journal of cellular biochemistry*, 1998, **71**, 313-327.
- 8 Wang Y, Kim UJ, Blasioli DJ, Kim HJ,Kaplan DL, *Biomaterials*, 2005, **26**, 7082-94.
- 9 G. H. Altman, F. Diaz, C. Jakuba, T. Calabro, R. L. Horan, J. Chen, H. Lu, J. Richmond and D. L. Kaplan, *Biomaterials*, 2003, **24**, 401-416 (DOI:[http://dx.doi.org/10.1016/S0142-9612\(02\)00353-8](http://dx.doi.org/10.1016/S0142-9612(02)00353-8)).
- 10 U. J. Kim, J. Park, H. J. Kim, M. Wada and D. L. Kaplan, *Biomaterials*, 2005, **26**, 2775-2785.
- 11 B. Panilaitis, G. Altman, J. Chen, H. Jin, V. Karageorgiou and D. Kaplan, *Biomaterials*, 2003, **24**, 3079-3085.
- 12 S. Sofia, M. B. McCarthy, G. Gronowicz and D. L. Kaplan, *Journal of Biomedical Materials Research*, 2001, **54**, 139-148.
- 13 T. Scheibel, *Microbial Cell Factories*, 2004, **3**, 14.
- 14 S. Gomes, I. B. Leonor, J. F. Mano, R. L. Reis and D. L. Kaplan, *Soft Matter*, 2011, **7**, 4964-4973.

- 15 C. Wong Po Foo, S. V. Patwardhan, D. J. Belton, B. Kitchel, D. Anastasiades, J. Huang, R. R. Naik, C. C. Perry and D. L. Kaplan, *Proceedings of the National Academy of Sciences of the United States of America*, 2006, **103**, 9428-9433.
- 16 R. Plowright, N. Dinjaski, S. Zhou, D. J. Belton, C. C. Perry and D. L. Kaplan, *RSC Advances*, 2016, **6**, 21776-21788.
- 17 J. Huang, C. Wong, A. George and D. L. Kaplan, *Biomaterials*, 2007, **28**, 2358-2367.
- 18 Gomes, S., Leonor, I. B., Mano, J. F., Reis, R. L., Kaplan, D.L., *Progress in Polymer Science*, 2012, **37**, 1-17.
- 19 B. Stevens, Y. Yang, A. Mohandas, B. Stucker and K. T. Nguyen, *Journal of Biomedical Materials Research Part B-Applied Biomaterials*, 2008, **85B**, 573-582.
- 20 W. N. Addison, S. J. Miller, J. Ramaswamy, A. Mansouri, D. H. Kohn and M. D. McKee, *Biomaterials*, 2010, **31**, 9422-9430.
- 21 S. J. Segvich, H. C. Smith and D. H. Kohn, *Biomaterials*, 2009, **30**, 1287-1298.
- 22 Association of Dental Implantology: Dental Implants Introduction, <http://consideringdentalimplants.co.uk/considering-dental-implants/introduction1.html>, (accessed 04/26 2017).
- 23 H. Dams-Kozłowska, A. Majer, P. Tomasiewicz, J. Lozinska, D. L. Kaplan and A. Mackiewicz, *Journal of Biomedical Materials Research Part a*, 2013, **101**, 456-464.
- 24 S. Fahnestock and S. Irwin, *Applied Microbiology and Biotechnology*, 1997, **47**, 23-32.
- 25 D. Huemmerich, C. W. Helsen, S. Quedzuweit, J. Oschmann, R. Rudolph and T. Scheibel, *Biochemistry*, 2004, **43**, 13604-13612.
- 26 T. Tsuji, K. Onuma, A. Yamamoto, M. Iijima and K. Shiba, *Journal of Crystal Growth*, 2011, **314**, 190-195.
- 27 D. J. Belton, A. J. Mieszawska, H. A. Currie, D. L. Kaplan and C. C. Perry, *Langmuir*, 2012, **28**, 4373-4381.

- 28 G. Walsh, *Proteins : biochemistry and biotechnology*, Wiley-Blackwell, Chichester, 2014.
- 29 D. S. Bocciarelli, *Calcified tissue research*, 1970, **5**, 261-+.
- 30 D. Carlström and J. B. Finean, *Biochimica et biophysica acta*, 1954, **13**, 183-91.
- 31 H. H. Roseberry, *X-ray analysis of bone and teeth.*, University of Chicago, Chicago, 1931.
- 32 F. Chengjie, S. Zhengzhong and F. Vollrath, *Chemical Communications*, 2009, , 6515-6529.
- 33 O. Hakimi, D. P. Knight, F. Vollrath and P. Vadgama, *Composites Part B-Engineering*, 2007, **38**, 324-337.
- 34 J. L. R. Arrondo, A. Muga, J. Castresana and F. M. Goni, *Progress in Biophysics & Molecular Biology*, 1993, **59**, 23-56.
- 35 J. L. R. Arrondo and F. M. Goni, *Progress in Biophysics & Molecular Biology*, 1999, **72**, 367-405.

## Chapter V

### Quantifying the efficiency of Hydroxyapatite Mineralising Peptides *via* new application of X-ray Diffraction Data

Work discussed in this chapter resulted in the publication “Quantifying the efficiency of Hydroxyapatite Mineralising Peptides”<sup>1</sup>

#### 5.1 Introduction

The mineralising potential of specific binding peptides has been studied for a wide range of materials and reaction conditions.<sup>2,3</sup> Methods that allow accurate quantification of the mineralised products tend to have one of two distinguishing features; either only one product is formed (or not formed) or the by-products of the experiment are easily separated from the target compound.

In peptide driven hydroxyapatite (HAP) synthesis it is often the case that inseparable mixtures of various calcium phosphate crystalline materials are produced.<sup>4</sup> The range of crystal phases produced varies with the method of mineralisation employed, however the more commonly used methods tend to be the simplest, and result in two significant phases forming, namely HAP and brushite. Analysis of the efficiency of peptide directed mineralisation that generates impure products / mixtures is then limited to a qualitative discussion of products, for example ‘products produced in the presence of sample 1 appears to contain a greater fraction of HAP than sample 2’.

X-ray diffraction is the most widely used technique for identifying HAP as each pattern produced is unique to a mineral’s crystalline structure. Hydroxyapatite exists as a hexagonal space group,  $P6_3/m$ , with some minor exceptions (none in calcified tissue) as monoclinic systems.<sup>5-8</sup> (Specific cell lattice parameters;  $a=b=9.432 \text{ \AA}$  and  $c=6.884 \text{ \AA}$  with  $\gamma = 120^\circ$ , Figure 5.1). In nature, HAP is rarely stoichiometric as described above, the Ca to P atomic ratio varies around the stoichiometric 1.67. There are trace amounts of the ions;  $\text{CO}_3^{2-}$ ,  $\text{Mg}^{2+}$ ,  $\text{Na}^+$ ,  $\text{F}^-$  and  $\text{Cl}^-$  in naturally occurring HAP, the concentrations of each vary between the type of tissue with respect to its bioactivity and desired properties. The closer the Ca/P atomic ratio is to 1.67 the more biologically stable the compound is.<sup>9</sup> A decrease in the atomic ratio tends to mean the compound will be more bioactive.

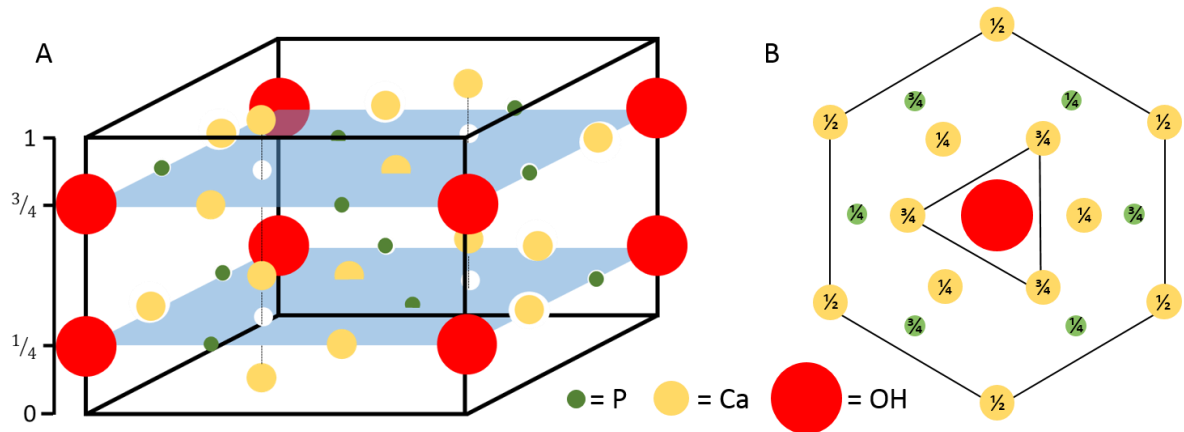


**Figure 5.1 A and B)** HAP unit cell and hexagonal system layout of HAP respectively. Phosphate ions are found in a tetrahedral arrangement, hydroxyl groups are located on the c axis. Ca ions are found in two different sites: columns of  $\text{Ca}^+$  ion and equilateral triangles. Phosphorous atoms lie in two height planes:  $\frac{1}{4}$  and  $\frac{3}{4}$ . Adapted from <sup>10,11</sup>

To explore the possibility of quantifying the amount present of these phases in a mixture, a series of HAP/brushite mixtures with increasing molar ratios of HAP to brushite (the most commonly formed calcium phosphate without mineralising directing influences present)<sup>12-15</sup> have been analysed *via* XRD with the intention of creating an analytical method applicable to the quantifiable estimation of, in this case, peptides that promote HAP mineralisation.

Three HAP binding peptides, all of which were previously identified *via* phage display: CaP(S) STLPIPEFSRE,<sup>16-19</sup> CaP(V) VTKHLNQISQSY<sup>18,20-23</sup> and CaP(H) SVSVGMKPSRP,<sup>16,21,24,25</sup> have used in this study. An extension of the approach to quantify the effect on mineralisation of larger proteins such as silk chimeras built from mimics of spider silk MASP1 protein and the CaP(V) peptide is also included.<sup>26</sup>

## 5.2 Methods and Materials

### 5.2.1 Brushite Synthesis.

Equal volumes of saturated aqueous solutions of 200 mM calcium chloride (Sigma-Aldrich, Dorset UK) and 120 mM dibasic sodium phosphate (Sigma-Aldrich, Dorset UK) were added together and the solution stirred for 1 hour. The precipitate was collected and washed *via* centrifugation and sonication using dd water. A total of 5

washes were performed. Precipitates were dried by lyophilisation for 24 hours (Virtis, Biopharma Process Systems, Winchester UK).

### **5.2.2 Producing Mixtures Brushite/HAP Mixtures**

Hydroxyapatite (Sigma-Aldrich, Dorset, UK) and brushite (synthesised for this study) were mixed according to percentage weight of each: 0, 20, 40, 50, 60, 70, 80, 90 and 100% and the molar ratio calculated. The full range was produced to allow use in the study of mineralisation with increasing concentrations of known HAP binding peptides and non-directed (control) mineralisation. A total of 10 XRD patterns were collected for each mixture with thorough stirring of each mixture between each scan.

### **5.2.3 Assessment of crystalline phases present by powder x-ray diffraction.**

XRD (PANalytical X'Pert PRO, Cu K $\alpha$  radiation with wavelength of 1.54056 Å) was used to characterise the crystallinity of the brushite precipitates produced and mixtures formed from brushite and HAP. Aluminium sample holders were packed with polydimethylsiloxane (PDMS) (Sylgard 184 PDMS, MIsolar, Campbell, CA, USA), and samples scanned from 5° to 65° of 2 $\theta$ , accelerating voltage 45 kV, filament current 40 mA and scanning speed 0.02° s<sup>-1</sup>. X'PertHighScore Plus (Version 2.0a) was used for pattern manipulation (baseline correcting and smoothing) and analysis. Artificially generated mixtures were analysed 10x and materials generated in the presence of peptides were analysed 3 times with mixing of the precipitate between each scan with samples being kept in the lyophilising chamber until analysis.

### **5.2.4 Infra-red Spectroscopy.**

FTIR-ATR (Frontier, PerkinElmer, Coventry, UK), was performed to identify the presence of phosphate groups in initial materials, mixtures and mineralised products generated in the presence of peptides. For each sample, an average of 40 scans were performed over the range 4000-650 cm<sup>-1</sup> at 2 cm<sup>-1</sup> resolution.

### **5.2.5 Inductively Coupled Plasma – Optical Emission Spectroscopy**

The molar ratio of HAP to Brushite was assessed *via* the Ca:P ratio determined from ICP, with data normalised with respect to 100% HAP and 100% Brushite. Approximately 5mg of each HAP/Brushite standard (the same standards as used in XRD analysis), was digested in 1mL aqua regia overnight then diluted 10 fold using dd. water. Measurements are stated as an average of 3 readings per sample.

### **5.2.6 Scanning Electron Microscopy Coupled to Energy Dispersive X-ray Analysis.**

SEM-EDX at 20 kV (JEOL 840,UK with Oxford Instruments Inca X-ray microanalysis, Oxford, UK) was used to observe the morphology of crystals and obtain information on the elemental composition of the HAP/Brushite mixtures. Each standard was mounted onto electrically conducting carbon tape on aluminium stubs before being gold coated using an argon gold plasma at 30mV and 1.2 kV for 2 minutes. A minimum of 3 100 $\mu$ m<sup>2</sup> areas were scanned and the Ca:P ratio measured as an average of these.

### **5.2.7 Hydroxyapatite synthesis using binding peptides.**

1mL aqueous solutions of each peptide; CaP(S) STLPIPHEFSRE, CaP(V) VTKHLNQISQSY and CaP(H) SVSVGMKPSRP (Pepceuticals Limited, Leicester, UK - >95% purity), were produced at concentrations of: 0.1 mg/mL, 0.25 mg/mL, 0.5 mg/mL, 1 mg/mL, and 2 mg/mL. Each solution had equal volumes (4 mL) of calcium chloride 200 mM (Sigma-Aldrich, Dorset, UK) and dibasic sodium phosphate 120 mM (Sigma-Aldrich, Dorset, UK) added in 200  $\mu$ L aliquots and solutions were kept at circumneutral pH, Appendix Fig 5.iii. After addition of all reagents, solutions were left to stir for 1 hour before washing the solid product 3 times with dd water. Synthesis of mineralised products was then repeated using lower reagent concentrations, namely 20mM calcium chloride and 12mM dibasic sodium phosphate.<sup>27-31</sup>

## **5.3 Results**

XRD was selected for this study as it is a well-established non-destructive technique for the identification of HAP. Patterns produced from highly crystalline materials require little processing so there is a minimal risk of loss of information.<sup>32</sup> IR and Raman spectroscopy were excluded as both require a higher level of processing (baseline correction followed by peak deconvolution of phosphate peaks) on the spectra is required to gain quantifiable data. The peaks present in the IR spectra of HAP and Brushite are phosphate groups and cannot be easily classified as HAP or Brushite in nature. ICP, as a destructive technique, can measure total ion concentrations but cannot quantify ions arising from the specific phases, though the possibility of normalising measured Ca:P ratios from ICP data is explored here, assuming 100% HAP is 1.67 and 100% Brushite is 1.

### 5.3.1 Confirmation of Brushite synthesis

X-ray diffraction (XRD) and infra-red spectroscopy (IR) were used to confirm the formation of Brushite. The XRD pattern showed the distinctive Brushite pattern whilst IR confirmed the presence of phosphate groups with minimal water content in the sample, Figure 5.2.

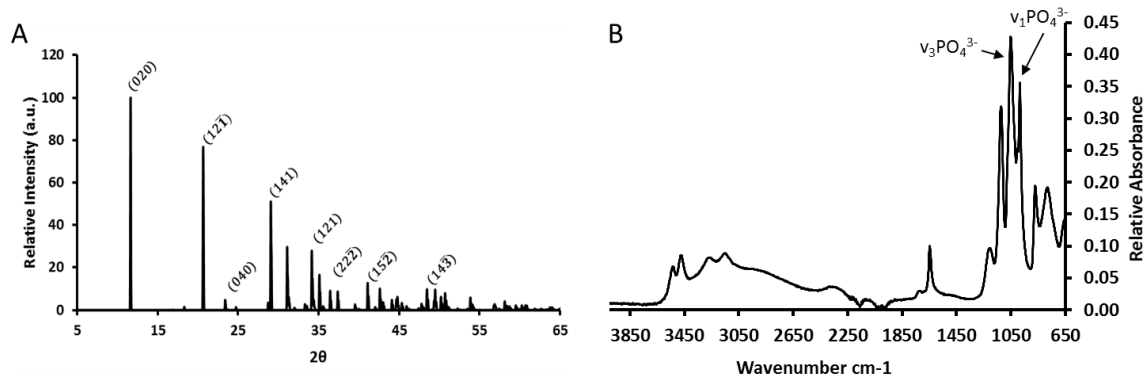


**Figure 5.2** XRD pattern of the bulk Brushite powder produced for this study.

### 5.3.2 Development of a method to assess Hydroxyapatite/Brushite mixtures

Powder x-ray diffraction has been extensively used for HAP identification since Dejong first observed the difference between bone powder and standard highly crystalline HAP.<sup>33</sup> [The crystal structure of HAP is an hexagonal system, space group is  $P6_3/m$  with lattice parameters  $a=b=9.432 \text{ \AA}$  and  $c=6.884 \text{ \AA}$  with  $\gamma = 120^\circ$ .] This gives a complex and distinct XRD pattern that allows in depth analysis where defects in structure can be determined.<sup>34,35</sup> For quantification of the relative amounts of each phase present in mixed samples, a single intense peak was selected from each pattern; the (020) peak at approximately  $12^\circ$  for Brushite and initially the (211) peak for HAP at approximately  $32^\circ$  to allow smaller quantities of either material to be detected more easily, Figure 5.3. Once a trend was established the (002) peak at  $25^\circ$  two theta was then used for HAP as there is no risk of peak merging, a common occurrence in naturally produced (non-heat treated) HAP XRD patterns due to the smaller crystallite sizes present and/or the non-stoichiometric nature of the sample.<sup>36</sup>

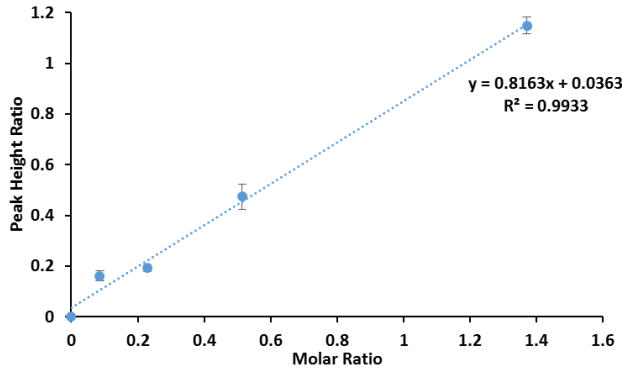


**Figure 5.3** Average peak height ratio of the (020) Brushite peak and the (211) HAP peak versus the molar ratio of HAP : Brushite.

Mixtures of HAP and Brushite at pre-defined ratios were produced and studied by XRD to establish whether a relationship exists between information extractable from the XRD patterns and the molar ratio of the two calcium phosphates present in an individual sample. Relationships between concentration and peak height or peak area for the two phases were compared Figure 5.4 A and B. Analysis using peak height ratios gave the clearer relationship with a clear linear trend between the average peak height ratio for the (020) Brushite peak vs the (002) HAP peak and the molar ratio of HAP to Brushite for each sample being observed, Figure 5.4. The trend can be visualised in example XRD patterns for each mixture in Figure 5.4C, which shows that (i) the Brushite (020) peak at  $12^\circ$  decreases in intensity with increasing HAP concentration, and (ii) the most intense HAP peak at  $32^\circ$  (211) increases in intensity with increasing HAP concentration. Additional confidence in the approach arises from the very small variations in the values obtained from multiple independent (N = 10) sample measurements.

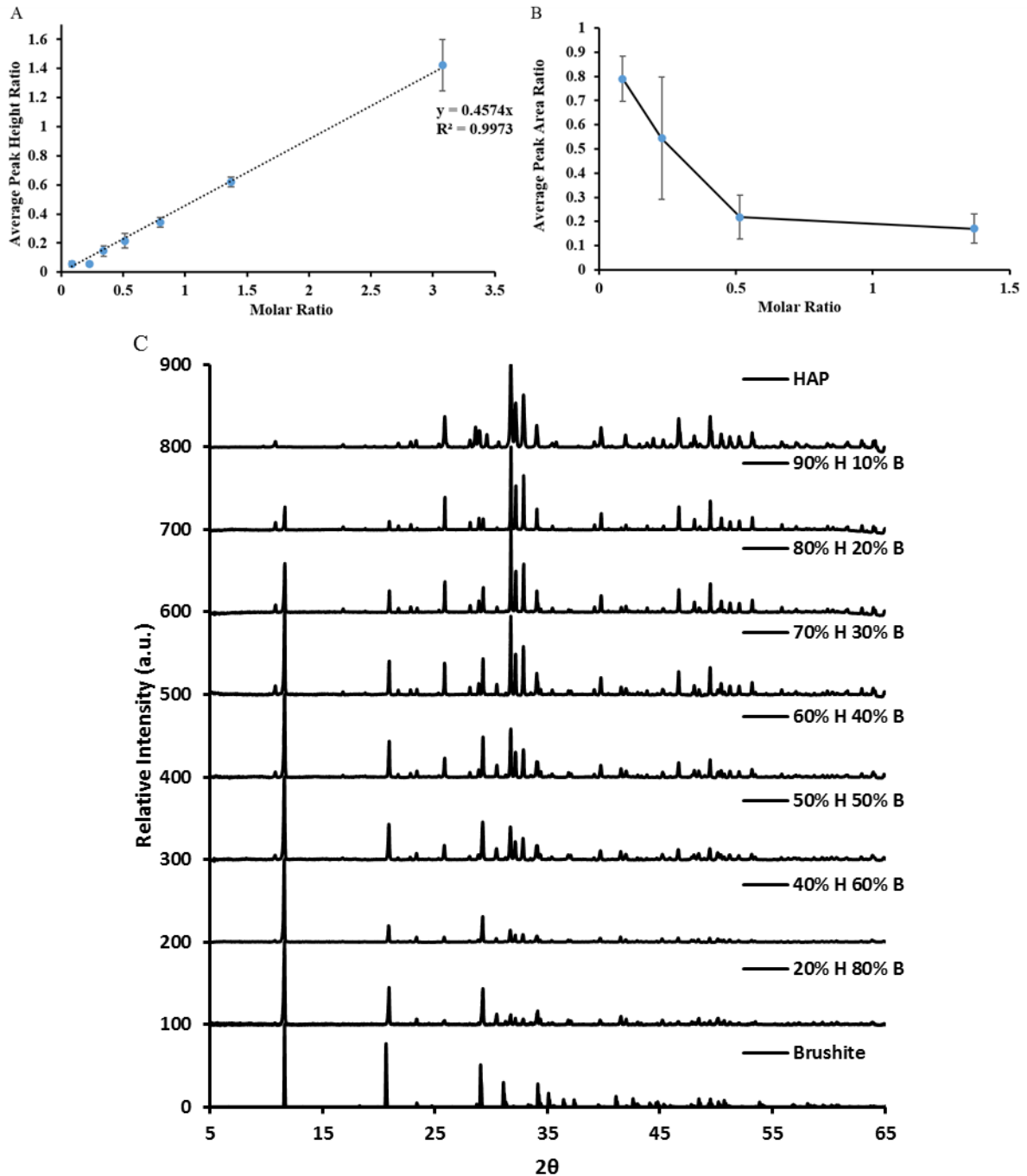


**Figure 5.4** **A**) Average peak height ratio of the (020) Brushite peak and the (002) HAP peak versus the molar ratio of HAP : Brushite **B**) Average peak area ratio of the (020) Brushite peak and the (002) HAP peak vs molar ratio of HAP : Brushite. n=10 **C**) Example XRD patterns for the HAP and brushite %/wt mixtures.

### 5.3.3 Alternative Techniques

The method developed here is unique in that it is non-destructive and is a quantitative technique solely for comparing crystalline phases present as opposed to

concentrations of elements, ions or compounds. However, data from alternative techniques have been provided here for the HAP/Brushite mixtures as a form of method verification.

### *Infrared Spectroscopy*

FTIR spectra was used to confirm the presence of phosphates for the mixtures and precipitates formed in the presence of a mineralising peptides, Figure 5.5, phosphate peaks:  $950\text{ cm}^{-1}$   $\nu_1(\text{PO}_4^{3-})$ ,  $1010\text{ cm}^{-1}$   $\nu_3(\text{PO}_4^{3-})$ . However, this data cannot be readily used quantitatively due to; the effect of water presence on the spectra, the difficulty of measuring peak heights from a baseline that fluctuates significantly more than that of XRD, and problems due to significant overlap between peaks making deconvolution difficult.

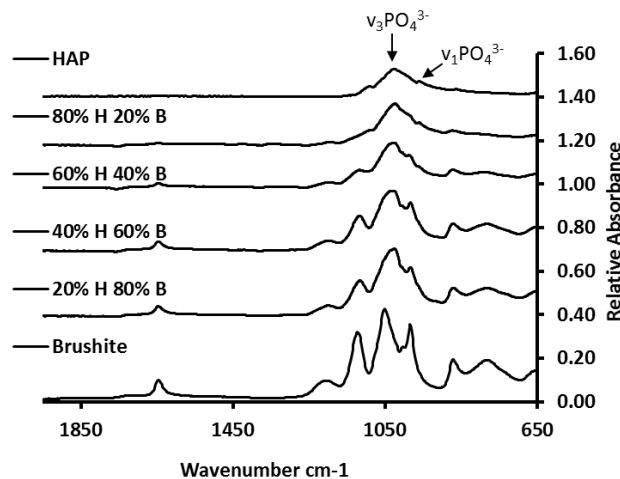


**Figure 5.5** Example FTIR (ATR) spectra for a selection of the HAP/Brushite mixtures, phosphate peaks:  $950\text{ cm}^{-1}$   $\nu_1(\text{PO}_4^{3-})$ ,  $1010\text{ cm}^{-1}$   $\nu_3(\text{PO}_4^{3-})$ .

### *Inductively Coupled Plasma-Optical Emission Spectrometry*

Measurement of the same standards used in this study were also carried out *via* ICP-OES to find the Ca:P ratio of samples. Once normalised to the 0 and 100% HAP sample values, (assuming a 1:1 ratio for Brushite presence and a 1:1.67 for HAP presence), there was a clear increase in the molar ratio with increased HAP percentage, Figure 5.6, and Table 5.1.

However, calculated values for HAP percentage in the standards was both over and underestimated. Normalisation carried out on the Ca:P ratio data for the standards is not possible for sample data as it requires the knowledge of phases present, making sample data and standard data not directly comparable. Additionally, ICP-OES used in this manner relies on two assumptions; that the calcium to phosphorus ratio is based on defect free structures and that there are only two crystal phases present in the

samples, HAP and Brushite. While XRD highlights all phases present, ICP-OES cannot, and when multiple phases are present in samples there is no interference in the XRD data for the ratio of HAP to Brushite.

### *Scanning Electron Microscopy coupled with Energy Dispersive X-ray Analysis*

Each standard mixture was scanned in multiple areas, EDX analysis was performed to find the Ca:P ratio. There was no correlation in the data found here and the actual molar ratio and therefore %/wt HAP present in the samples, Figure 5.6 and Table 5.1.

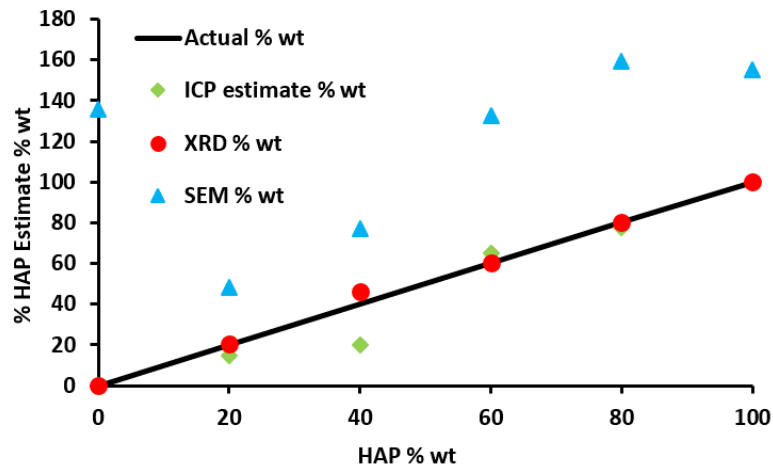


**Figure 5.6** Exact percentage of HAP present in standards plotted against the measured percentage from the different analytical techniques employed: ICP-OES data calculated from the Ca:P ratio and normalised to 0% HAP as a 1:1 ratio and 100% HAP as a 1.67:1 ratio. SEM coupled with EDX data from the measured Ca:P ratio from element percentages present. XRD estimation was found using the method described above.

Actual % wt	XRD % wt	ICP % wt	EDX % wt
0.00	0.00	0.00	135.75
20.27	20.73	14.83	48.28
40.62	43.36	19.98	77.28
61.87	60.18	64.80	132.33
80.21	79.96	77.73	159.22
100.00	100.00	99.38	155.09

**Table 5.1** Tabulated data for the HAP/Brushite mixtures. The actual (%/wt) based on masses of the two characterised phases when the mixtures were produced, the XRD estimation was found using the method described in this chapter, ICP-OES data was calculated from the Ca:P ratio and the data normalised to 0% HAP as a 1:1 ratio and 100% HAP as a 1.67:1 ratio. SEM coupled with EDX data is from the measured Ca:P ratio from element percentages present.

### 5.3.4 Quantitative comparison of the ability of hydroxyapatite binding peptides to affect mineralisation

Three known HAP binding peptides, previously identified by phage display were included in the study to see if the mineralising capabilities of each could be measured quantitatively. The effect of peptide concentration and reagent concentrations were both explored. The three peptides, (CaP(S) STLPIPHEFSRE, CaP(V) VTKHLNQISQSY and CaP(H) SVSVGMMKPSRP)<sup>16,24</sup> had all previously been identified as HAP binding peptides. Initial experiments were carried out using the same concentrations of calcium chloride (200mM) and dibasic sodium phosphate (120 mM) as used to generate brushite for the development of the approach.

All three peptides were able to direct mineralisation towards HAP formation. Figure 5.7 A-C shows the XRD patterns produced from precipitates formed in the presence of each peptide at initial concentrations; 0.1 mg/mL, 0.25 mg/mL, 0.5 mg/mL, 1 mg/mL and 2 mg/mL. Table 5.2 shows the estimated percentages of HAP present in each precipitate formed. There is a clear increase in the percentage of HAP produced with increasing concentration of all peptides. In the XRD patterns this can be visualised by the decrease in intensity of the (020) Brushite peak and an increase in the (002) peak (and (211) peaks of HAP).

As the percentage of HAP increases with initial peptide concentration it suggests that the concentration of peptide used is a key parameter in HAP mineralisation. This will

reach a limit, however, when all precipitated material is present as the HAP phase as seen in this study for CaP(V) and CaP(H) when added to the initial reaction at a level above 1 mg/ml and for additions of CaP(s) at 2 mg/ml. From this data it suggests that for all such peptides a maximum limit on the amount of peptide required for HAP mineralisation can be ascertained using XRD as a quantitative tool. The efficacy of the peptides in promoting mineralisation can be readily compared, with data on CaP(S) and CaP(V) supporting earlier literature studies where more CaP(V) was found to bind to HA than CaP(S).<sup>20,21,37</sup>

Addition of either CaP(V) and Cap(H) led to a greater degree of control over mineralisation at the lower concentrations used, (at 1 mg/mL 99% and 100% HAP was produced respectively compared with CaP(S) at 62%). CaP(V) was shown to have more influence at the lowest concentrations explored at 0.1 mg/mL and 0.25 mg/mL. An argument could be made that CaP(V) has greater influence and is therefore better at inducing HAP formation, however, all of these peptides could be used providing an appropriate concentration level is selected for each, information which may be useful for peptide selection if charge or hydrophobicity are important factors.

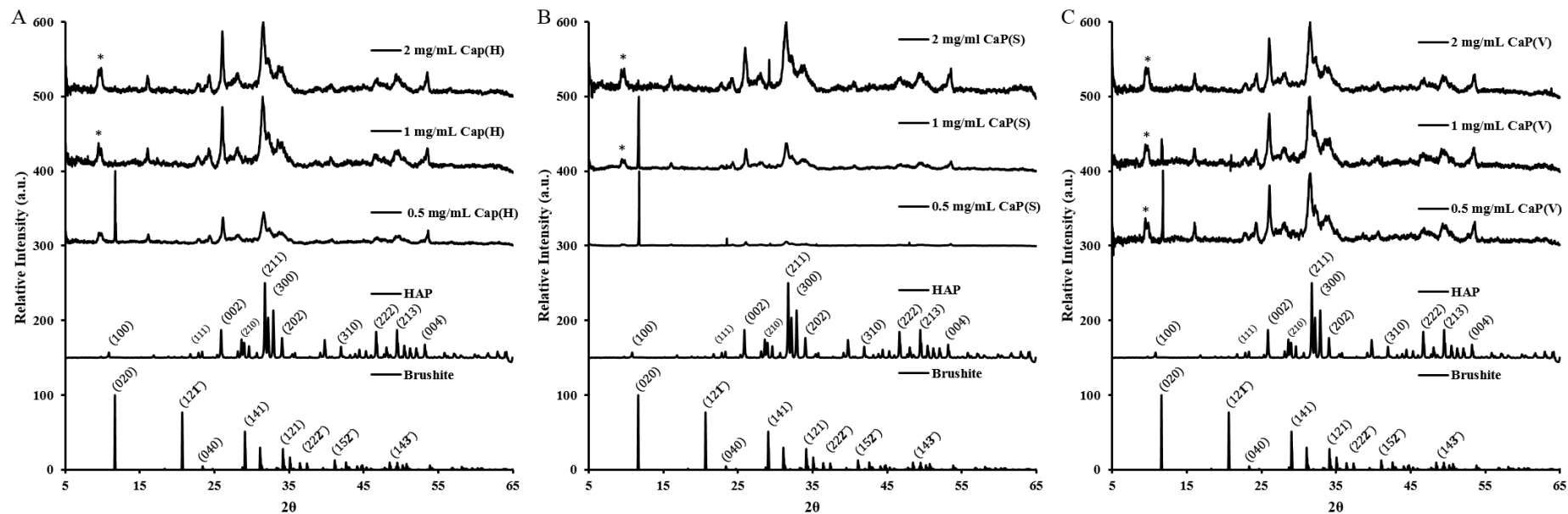


**Figure 5.7 A-C)** XRD patterns of precipitates formed from reaction of 200mM calcium chloride and 120mM sodium phosphate dibasic in the presence of CaP(H) SVSVGMPSPRP, CaP(S) STLPPIHEFSRE and CaP(V) VTKHLNQISQSY at initial concentrations: 0.1, 0.25, 0.5, 1 and 2 mg/mL.

Concentration of peptide used	Estimated Percentage HAP Produced		
	CaP(H)	CaP(S)	CaP(V)
0.1 mg/mL	39.11 ± 1.13	33.11 ± 0.96	43.40 ± 1.26
0.25 mg/mL	47.14 ± 1.36	27.21 ± 0.79	58.84 ± 1.70
0.5 mg/mL	67.19 ± 1.95	26.39 ± 0.77	82.80 ± 2.40
1 mg/mL	100 ± 0	62.09 ± 1.80	99.30 ± 0.54
2 mg/mL	100 ± 0	100 ± 0	100 ± 0

**Table 5.2** Calculated percentage mass of HAP in each precipitate. \*Peak from sample holder, n=3.

### 5.3.5 Quantitative comparison of hydroxyapatite binding peptide with limited reagents

Once each peptide was shown to be capable of inducing HAP formation, the concentration of each reagent was reduced tenfold and the experiments repeated as above to determine if the three selected HAP binding peptides could still influence mineralisation under much reduced ion concentrations. The peptide concentrations were chosen to replicate effects (differences in mineralisation activity for the various peptides) observed at the lower end of the of peptide concentration range used in the initial experiments. Figure 5.8 A-C shows the XRD patterns for precipitates produced in the presence of the peptides; CaP(H), CaP(S) and CaP(V) at a range of initial concentrations (0.5-2 mg/ml) and Table 5.3 shows the estimated percentages of HAP present in the precipitates. All of the peptides influenced precipitation particularly as the initial concentration of peptide was increased. Under these conditions, the maximum level of HAP formation in the precipitates was of the order of 50%. In contrast to results obtained for the effect of peptide on HAP formation at ‘high’ reagent concentrations, Figure 5.7, here CaP(S) was the most effective HAP ‘promoter’ at the lowest reagent concentration level used. The reasons for different behaviour of the CaP(H), CaP(S) and CaP(V) probably relate to the specific properties of the peptides themselves and will be discussed later in this chapter.

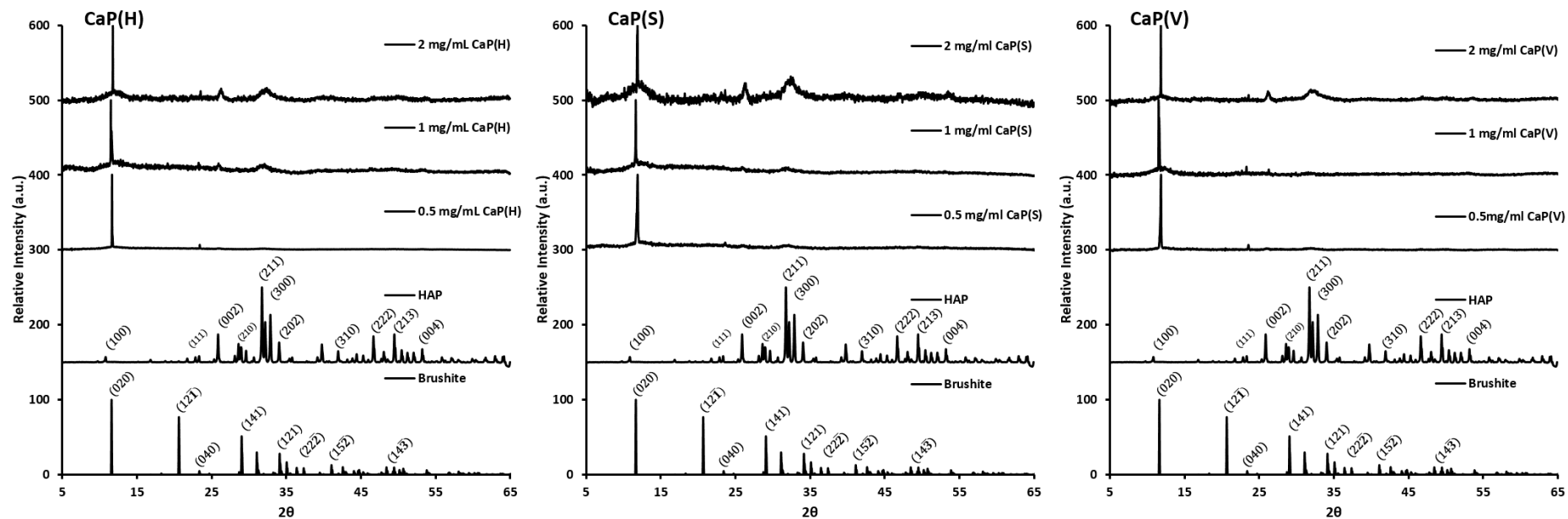


**Figure 5.8** A-C) XRD patterns of the precipitates formed from the reaction of 20mM calcium chloride and 12mM sodium phosphate dibasic in the presence of CaP(S) STLPIPHEFSRE, CaP(V) VTKHLNQISQSY and CaP(H) SVSVGMKPSRP at initial concentrations: 0.5, 1 and 2 mg/mL.

Concentration of peptide used	Estimated Percentage HAP Produced		
	CaP(H)	CaP(S)	CaP(V)
0.5 mg/mL	5	3	6
1 mg/mL	41	41	21
2 mg/mL	49	57	44

**Table 5.3** Calculated percentage mass of HAP in each precipitate (it was not possible to obtain data from multiple samples owing to the very small amount of sample generated).

### 5.3.6 Mechanism of peptide directed mineralisation

The role of the individual peptides in their response during mineralisation has been theorised here based on chemical information on the peptide themselves, Scheme 5.1. Note, prior research has shown that scrambling of the sequence of CaP(V) had little effect on peptide binding to a range of synthetic bone-like and apatitic materials.<sup>20</sup> At higher reagent concentrations (200 mM CaCl<sub>2</sub> and 120 mM NaHPO<sub>4</sub>), additions of CaP(H) and CaP(V) showed greater control over mineralisation, and as both peptides have a net positive charge it is suggested that their addition drives mineralisation through phosphate ion attraction. Under the conditions of the mineralisation experiments, despite CaP(H) having a +2 charge and CaP(V) only +1 charge, Table 5.4 and Figure 5.9, it is likely that CaP(V) is able to rival the mineralising capabilities of CaP(H) as the positively charged lysine group resides at the amino terminal of the peptide, thereby creating an area of high charge density; this coupled with the large number of hydroxyl groups at the carboxyl terminal, gives the peptide a polar quality. CaP(V) would be able to attract both cations and anions thereby providing a site for crystal growth, Scheme 5.1.

	Sequence	Net charge at pH 7.4	Average Hydrophobicity	pI
CaP(H)	SVSVGMKPSRP	+2	+13.87	11.71
CaP(S)	STLPIPHFSRE	-1	+16.67	5.23
CaP(V)	VTKHLNQISQSY	+1	+13.05	9.54

**Table 5.4** Properties of the peptides CaP(H), CaP(S) and CaP(V) used in the study.

CaP(S) had less of an effect over mineralisation compared to CaP(H) and CaP(V) at high ion concentrations, which we suggest is due to the overall negative charge of CaP(S) and small changes in pH away from neutral during the mineralisation reaction preventing organisation of cations and anions in proximity to the peptide or protein. At lower ion concentrations, this effect is felt less and mineralisation where cation organisation is key most likely dominates, with CaP(S) becoming a good mineralisation promoter. It is possible that the differing physical properties of CaP(S) (negative overall charge with an acidic calculated isoelectric point) compared with CaP(H) and CaP(V) may allow for a more stable unfolded protein structure in solution which would allow for greater exposure of amine groups and therefore greater promotion of mineralisation.

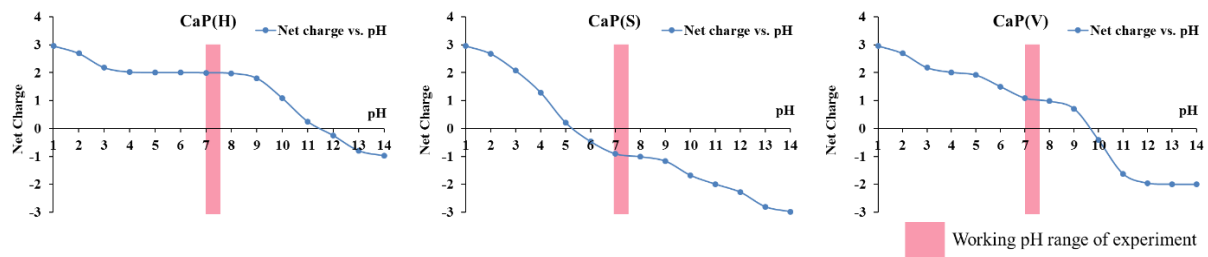
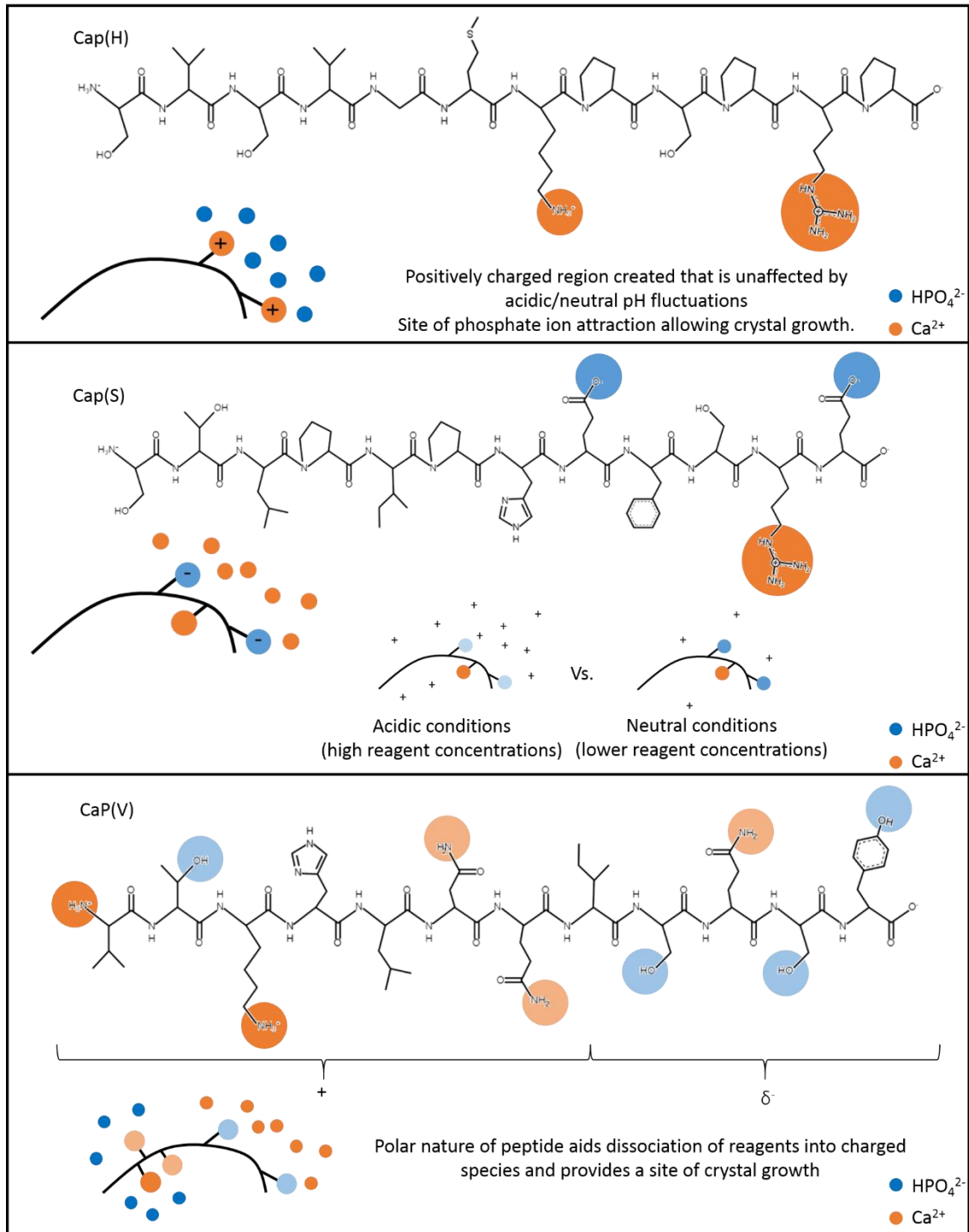


**Figure 5.9** Net charge of the CaP(H), CaP(S) and CaP(V) peptides in response to the change in environmental pH.



**Schematic 5.1** influences of each peptide over mineralisation with respect to charged species and pH.

### 5.3.7 Extension of approach to silk chimeras

Previous published work has focused on one of the mineralising peptides, CaP(V) (also referred to as VTK), as part of a genetically engineered silk material.<sup>26</sup> The prior study showed that increased number of peptides attached to the silk backbone resulted in greater control over mineralisation. However, discussion of the diffraction data was limited to statements of ‘increase or reduction’ in HAP and brushite peaks respectively. Using the analytical method described in this chapter, we can show that silk constructs based on spider silk MASP1 with a His tag are able to promote HAP formation, Table 5.5. The location of the peptide at either the N or C terminus had little effect on the extent of mineralisation but the presence of peptide at both ends of the fusion protein leads to enhanced mineralisation. What is particularly impressive is the low concentration of peptide, when attached to the silk construct required to generate pure HAP samples, at 0.033mg/ml as compared to when the peptide is used alone when a 1mg/ml solution is required, Table 5.6.

Sample 1 mg/mL	%/wt HAP
nh-15mer	32
nh-15mer-VTK	63
15mer-ch	44
VTK-15mer-ch	62
VTK-15mer-VTK	100

**Table 5.5** Previously published data<sup>26</sup> on silk-fusion proteins containing the CaP(V) (or VTK) binding peptide with new quantification method applied. %/wt of HAP in the precipitates produced from previous samples at 1 mg/mL stating concentrations, nh refers to His tag at N-terminus of protein; ch refers to His tag at C-terminus of protein; 15mer refers to 15 repeats of the spider silk modified MASP1 33 amino acid sequence.

Concentration VTK-15mer-VTK mg/mL	%/wt HAP
0.25	59
0.5	87
0.75	92
1	100
2	100
3	100

**Table 5.6** Calculated effect of sample concentration of %/wt of HAP produced for the VTK-15mer-VTK sample.<sup>18</sup>

## 5.4 Conclusions

An analytical calibration tool to quantitatively estimate the % HAP in mixed phase precipitates was successfully developed from the previously solely qualitative technique XRD. The production of mixtures of HAP and Brushite (known concentrations) allowed a direct correlation between average peak height (XRD) and molar ratio to be found, which can then be expressed as a % wt HAP presence when the absence of additional phases has been established. Other techniques were utilised; ICP-OES, IR and SEM/EDX, to authenticate the method and further prove that quantifying crystal phases can exclusively be accomplished *via* this new method.

It was proven that this method can be applied to compare the mineralisation efficiency of peptides and fusion proteins. Using this calibration method, it was possible to compare the activity of three known HAP binding peptides. Although it was found that CaP(V) showed better control over mineralisation at lower concentrations of peptide, it is believed all peptides included in the study would be a suitable choice as a HAP binder providing an appropriate concentration is used, meaning other aspects such as physical properties of the biomolecules themselves could also be considered.

It is believed that the general approach should be applicable to other mineralisation systems where mixed phases are commonly produced and the assessment of the role(s) of additives in mineralisation control is required.

## 5.5 References

- 1 R. Plowright, D. J. Belton, D. L. Kaplan and C. C. Perry, *Nature Scientific Reports*, 2017, **7**, 7681.
- 2 A. Sigel, H. Sigel and R. Sigel, *Biomineralisation: From Nature to Application*, John Wiley and Sons Ltd, Chichester, 2010.
- 3 S. Mann, *Biomineralization: Principles and Concepts in Bioinorganic Materials Chemistry*, Oxford University Press, Oxford, 2001.
- 4 H. Furedimi, B. Purgaric, B. Purgaric and N. Pavkovic, *Calcified tissue research*, 1971, **8**, 142-153.
- 5 J. C. Elliott, P. E. Mackie and R. A. Young, *Science*, 1973, **180**, 1055-1057.
- 6 J. C. Elliott and R. A. Young, *Nature*, 1967, **214**, 904-906.
- 7 J. W. Anthony, *Handbook of mineralogy*, Mineral Data Pub., Tucson, 1997.
- 8 G. Ma and X. Y. Liu, *Crystal growth & design*, 2009, **9**, 2991.
- 9 A. L. Boskey, *Elements*, 2007, **3**, 385-391.
- 10 T. Kanazawa, *Inorganic phosphate materials*, Elsevier, Tokyo;, 1989.
- 11 M. Kay, R. Young and A. Posner, *Nature*, 1964, **204**, 1050-2.
- 12 E. D. Eanes, I. H. Gillessen and A. S. Posner, *Nature*, 1965, **208**, 365-7.
- 13 G. Walsh, *Proteins Biochemistry and Biotechnology.*, Wiley, Hoboken, 2002.
- 14 M. Shiryayev, T. Safronova and V. Putlyayev, *J Therm Anal Calorim*, 2010, **101**, 707-713.
- 15 T. V. Safronova, A. V. Kuznetsov, S. A. Korneychuk, V. I. Putlyayev and M. A. Shekhirev, *Cent Eur J Chem*, 2009, **7**, 184-191.
- 16 S. Segvich, S. Biswas, U. Becker and D. H. Kohn, *Cells Tissues Organs*, 2009, **189**, 245-251.

17 C. Chung, Y. Park, S. Rhee and J. Lee, *Peptide having the ability to regenerate bone tissue and for binding to apatite*, Seoul, South Korea, 2013.

18 S. J. Segvich, *Design of Peptides with Targeted Apatite and Human Bone Marrow Stromal Cell Adhesion for Bone Tissue Engineering.*, The University of Michigan, Michigan, 2009.

19 S. Zhang, *Biological and biomedical coatings handbook : processing and characterization*, CRC Press (Taylor & Francis Group), Boca Raton, 2011.

20 W. N. Addison, S. J. Miller, J. Ramaswamy, A. Mansouri, D. H. Kohn and M. D. McKee, *Biomaterials*, 2010, **31**, 9422-9430.

21 D. A. Puleo and R. Bizios, *Biological interactions on materials surfaces : understanding and controlling protein, cell, and tissue responses*, Springer, Dordrecht; New York, 2009.

22 H. Ramaraju, S. J. Miller and D. H. Kohn, *Connective tissue research*, 2014, **55**, 160-163.

23 G. Subramanian, *Biopharmaceutical production technology*, Wiley, 2012.

24 M. D. Roy, S. K. Stanley, E. J. Amis and M. L. Becker, *Advanced Materials*, 2008, **20**, 1830-1836.

25 F. Bronner, M. C. Farach-Carson and H. I. Roach, *Bone and development*, Springer-Verlag, London, 2010.

26 N. Dinjaski, R. Plowright, S. Zhou, D. J. Belton, C. C. Perry and D. L. Kaplan, *Acta Biomaterialia*, 2017, **49**, 127-139.

27 M. T. Jahromi, G. Yao and M. Cerruti, *Journal of the Royal Society Interface*, 2013, **10**, 20120906.

28 M. T. Jahromi and M. Cerruti, *Crystal Growth & Design*, 2015, **15**, 1096-1104.

29 H. Pan, J. Tao, X. Xu and R. Tang, *Langmuir*, 2007, **23**, 8972-8981.

- 30 N. Spanos, P. Klepetsanis and P. Koutsoukos, *Journal of colloid and interface science*, 2001, **236**, 260-265.
- 31 J. Tao, H. Pan, Y. Zeng, X. Xu and R. Tang, *Journal of Physical Chemistry B*, 2007, **111**, 13410-13418.
- 32 K. A. Selvig, *J. Ultrastruct. Res.*, 1972, **41**, 369-375.
- 33 W. F. de Jong, *RECL Recueil des Travaux Chimiques des Pays-Bas*, 1926, **45**, 445-448.
- 34 A. A. Chaudhry, J. Goodall, M. Vickers, J. K. Cockcroft, I. Rehman, J. C. Knowles and J. A. Darr, *J Mater Chem*, 2008, **18**, 5900-5908.
- 35 R. Panda, M. Hsieh, R. Chung and T. Chin, *Journal of Physics and Chemistry of Solids*, 2003, **64**, 193-199.
- 36 I. Mobasherpour, M. S. Heshajin, A. Kazemzadeh and M. Zakeri, *J Alloy Compd*, 2007, **430**, 330-333.
- 37 S. J. Segvich, H. C. Smith and D. H. Kohn, *Biomaterials*, 2009, **30**, 1287-1298.

## Chapter VI

### **Silica and Hydroxyapatite Silk Composites: Material Studies for Biomedical Application**

Results discussed in this chapter form part of the publication “Intracellular Pathways Involved in Bone Regeneration Triggered by Recombinant Silk-silica Chimeras” Published pending print in *Advanced Functional Materials*.

#### **6.1 Introduction**

Mineralised polymeric based biomaterials provide cell-instructive surfaces with value towards tissue repair and regeneration, it is therefore beneficial to gain a comprehensive knowledge of the key features of these biomaterials that modulate the biological outcomes.

Silk materials have become increasingly popular as biomedical devices because they possess impressive physical properties whilst being biocompatible and bioacceptable.<sup>1-3</sup> Silk can be processed in many ways that allow it to keep its naturally high tensile strength, high mechanical strength and extraordinary elasticity making it useful for a wide variety of medical and non-medical applications.<sup>4-8</sup> The structure of silk makes it possible to produce different material forms such as gels, sponges, films, membranes and scaffolds<sup>9-13</sup> which can then in turn be adapted to a variety of medical applications from controlled release<sup>14</sup> to supportive constructs.<sup>15,16</sup> Further, silk fibroin has the potential for fine-tuning properties through bioengineered sequence modification to incorporate diverse functional domains.<sup>17-20</sup>

Organic-inorganic biomaterial systems, such as silk-silica and silk-hydroxyapatite materials, have shown high potential and worthy of study for tissue regeneration. In this study we initially focused on silk-silica chimeras,<sup>20-23</sup> these are comprised by a core census repeat [(SGRGGLGGQGAGAAAAAGGAGQGGYGGGLGSQGT)x15] derived from the spider *Nephila clavipes* major ampullate dragline silk, with a MW of ~40 KDa, which serves as an organic scaffold that controls material stability, fused with the silica-promoting peptide R5 (SSKKSGSYSGSKGSKRRIL) derived from the *Cylindrotheca fusiformis* silaffin gene, Figure 6.1.<sup>24</sup> The R5 peptide has been previously used to functionalise recombinant spider silk-like proteins, demonstrating

that it did not disrupt the mineral deposition ability of the R5 domain.<sup>22,23</sup> In previous studies we determined that the N-terminal location of the R5 peptide promoted improved control of silica precipitation.<sup>23</sup> Computational simulation studies showed that the location of the charged biomineralization domain had only a minor effect on protein folding and did not alter the surface exposure of charged amino acids, in agreement with experimental data. Moreover, cell compatibility and the ability to promote hMSC differentiation were demonstrated for variants of these fusion proteins.<sup>23</sup>

Similar studies were completed using silk-hydroxyapatite chimeras, the same spider silk derivative was selected for the backbone repeating unit and paired to the HAP binding peptide VTK (VTKHLNQISQSY), identified *via* phage display,<sup>25,26</sup> VTK domains were present on the; N, C or both termini of the silk backbone, Figure 6.1. Studies showed the VTK domain was capable of controlling HAP deposition independent of location on the silk but the number of peptides present dramatically increased the material's mineralising directing capabilities. Genetic modification of the silk to incorporate the HAP binding domain showed no adverse effect on the desired chemical and physical properties of the silk.<sup>27</sup> Strong cell compatibility with the ability to promote hMSC differentiation were demonstrated for variants of these fusion proteins.

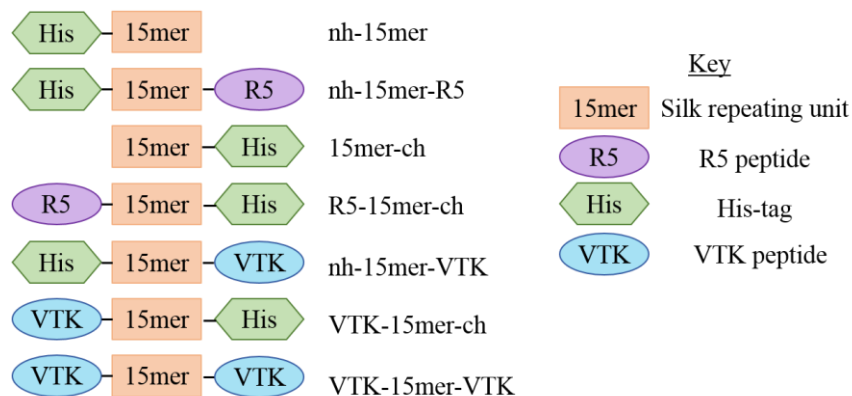


**Figure 6.1** Schematic representation of silk fusion proteins design strategy; His-tag (green box) has been added to spider silk 15mer at N-terminal end of nh-15mer, nh-15mer-R5 and nh-15mer-VTK constructs, and C-terminal end of 15mer-ch, R5-15mer-ch and VTK-15mer-ch constructs; R5 domain (purple circle) has been added to the C-terminal of nh-15mer-R5 and N-terminal of R5-15mer-ch; VTK domain (blue circle) has been added to the C-terminal of the nh-15mer-VTK sample, the N-terminal of the VTK-15mer-ch and both termini of the VTK-15mer-VTK sample.

This chapter offers the final stage of *in vitro* study for these silk chimeras designed for biomedical application, Figure 6.2. A full material study has been completed to highlight the impact of genetic modification to incorporate mineralising domains on a repeating unit, further the implication of mineralisation on the chimeric silk films is explored with respect to; Young's modulus, protein structure and biodegradability, all key parameters that must be considered when designing biomaterials.

Material Studies: Biomedical application appropriate?	All Chimeras	<ul style="list-style-type: none"> <li>• Young's modulus: AFM</li> <li>• Biodegradability: Bradford Assay</li> <li>• Protein Structure: FTIR</li> </ul>	This Chapter
Initial studies: Sample feasibility	Silk-HAP Chimeras	<ul style="list-style-type: none"> <li>• HAP mineralisation: XRD, SEM/EDX</li> <li>• General physical and chemical properties</li> <li>• Good biocompatibility: Live/Dead staining</li> <li>• High bioactivity: hMSC differentiation</li> </ul>	Chapter IV
Initial studies: Sample feasibility	Silk-Silica Chimeras	<ul style="list-style-type: none"> <li>• Silica mineralisation: SEM/EDX, ICP-OES, molybdenum blue assay</li> <li>• General physical and chemical properties</li> <li>• Good biocompatibility: Live/Dead staining</li> <li>• High bioactivity: hMSC differentiation</li> </ul>	Chapter III

**Figure 6.2** Tiers of study using the chimeric silk films for biomedical application

## 6.2 Materials and Methods

### 6.2.1 Silk fusion protein film preparation and mineralisation

#### *Silk Film Production*

The lyophilized recombinant fusion proteins (15mer-ch, nh-15mer, nh-15mer-R5, R5-15mer-ch, VTK-15mer-ch, nh-15mer-VTK, VTK-15mer-VTK) were prepared at a concentration of 2% (wt/vol) in dd water. The proteins were left to dissolve overnight at 4°C. PDMS (Sylgard 184 PDMS, Milsolar, Campbell, CA, USA) disks (R=6 mm) were used as substrates on which 30 µL aliquots of each protein solution was deposited. Films were air-dried overnight in a fume hood and subsequently subjected to methanol vapour annealing using an isotemp vacuum oven for 24 h at room temperature and 635 mbar. Afterwards, films were air-dried overnight at room temperature.

#### *Silicification of silk films*

To induce silicification, the recombinant proteins (nh-15mer, nh-15mer-R5, 15mer-ch, R5-15mer-ch) mounted on a PDMS substrate were placed in a 24 well plate with

1 mL of 30 mM tetraethyl orthosilicate-phosphate buffer solution (Sigma-Aldrich, Dorset, UK) for 1 hour.<sup>28</sup> The films were then rinsed twice with water and left to dry overnight in a fume hood.<sup>23</sup>

### ***Hydroxyapatite Mineralisation of Silk Films***

For induction of chemical HAP mineralisation, the recombinant proteins (15mer-ch, nh-15mer, VTK-15mer-ch, nh-15mer-VTK, VTK-15mer-VTK) mounted on PDMS substrates and a PDMS disk with no protein film, were placed in 24 well plates with 10 mL of 1:1 solution of 12 mM NaH<sub>2</sub>PO<sub>4</sub> pH 7.4 (adjusted using NaOH) and 20 mM CaCl<sub>2</sub> (Sigma-Aldrich, Dorset, UK). After incubation for seven days at room temperature, the films were rinsed twice with water to remove soluble salts and left to dry overnight. Data for the control PDMS disk did not show due to no influence on mineralisation occurring.

### **6.2.2 Analysis techniques for: pre-annealed, annealed and mineralised films**

#### ***Fourier Transform Infrared Attenuated Total Reflectance Spectroscopy (FTIR-ATR)***

Protein conformation was assessed using FTIR-ATR (Frontier, PerkinElmer, Coventry, UK), with an average of 40 scans over the range 1750-1450 cm<sup>-1</sup>. Thermo Grams A1 software v8.0 was used for curve fitting (including peak deconvolution), and baseline corrections. Eight points were chosen from the amide I band (1700-1580 cm<sup>-1</sup>); 4 points corresponding to  $\beta$  conformers: 1693, 1680, 1633 and 1615 cm<sup>-1</sup>, 2 points for non- $\beta$  conformers at 1656 and 1644 cm<sup>-1</sup>, and 2 at 1712 and 1592 cm<sup>-1</sup> to allow for peak shifting and amide II band overlap respectively. An iteration was carried out forcing all peaks to have a positive area with a linear baseline. This was carried out for 1,000 iterations before curve fitting. The sum of the areas under the peaks was found and each conformer expressed as a percentage of the total.

#### ***Wettability and surface energy measurements***

The wettability and surface energy of each sample was measured using a Theta Attension Instrument with OneAttention v1.7 software (Biolin Scientific, Staffordshire, UK). A silk film mounted on a PDMS substrate was placed on the stand, and using a syringe, a 10  $\mu$ L droplet of water, dimethyl formamide (DMF) or ethylene glycol was placed on the surface and the contact angle at each side of the droplet measured ten times and an average taken. It was not possible to measure

contact angles of the non-annealed films with DMF and ethylene glycol as the proteins dissolved in the solvents.<sup>23</sup>

### ***Atomic Force Microscopy***

A Bruker Dimension Icon with ScanAsyst was used to perform all imaging and nanoquantum mapping. Data was collected in PeakForce Tapping mode and processed using Nanoscope Analysis software. Young's modulus values are stated as an average of 20 measurements taken across a 20  $\mu\text{m}^2$  area with an assumed Poisson's ratio of 0.3.<sup>29</sup>

### ***Biodegradability/Solubility***

Chimeric silk films prepared as above were submerged in 2mL 100mM PBS pH 7.4 at 37°C, degradation was measured by periodically taking 10  $\mu\text{L}$  aliquots of the PBS supernatant and measuring protein concentration by adding 90  $\mu\text{L}$  Coomassie stock solution (200mg Brilliant blue dye (Sigma-Aldrich, Dorset, UK), 100 mL methanol, 20 mL 85% orthophosphoric acid, 200 mL dd water), then measuring the absorbance ratio at a wavelengths 590nm and 450 nm.<sup>30</sup>

## **6.3 Results and Discussion**

### **6.3.1 Parameter Development for Peak Deconvolution of FTIR Spectra**

Previous use of peak fitting on the infrared spectra of protein films across the amide I band by the Perry group was reliable but limited, with the use of only six peaks across the amide I and amide II bands.<sup>20-23,27,28,31</sup> Therefore, development of a new method where peak fitting reveals in depth information about protein structure, such as specific changes in conformers, was completed.

Table 6.1 shows the initial literature values considered for secondary structure conformer locations within the amide I band. From these, a parameter set was established, Table 6.2.

Region $\text{cm}^{-1}$	A) Adochitei et al 2010		B) Jilie Kong and Shaoning Yu 2007		C) Susi and Byler 1986		D) Goormaghtigh et al 1990							
	Value $\text{cm}^{-1}$	Assignment	Value $\text{cm}^{-1}$	Assignment	Value $\text{cm}^{-1}$	Assignment	Value $\text{cm}^{-1}$	Assignment						
<b>1682+</b> <b><math>\beta</math>-Sheet</b>	1680-1691	$\beta$ Sheet or $\beta$ Turn	1696	$\beta$ -Sheet	1694	$\beta$ -Turn	1685	$\beta$ -Sheet						
			1691	$\beta$ -Sheet	1688	$\beta$ -Turn								
			1685	$\beta$ -Turn	1683	$\beta$ -Turn								
<b>1662-1682</b> <b>Turn</b>	1677 1673 1667 1661	$\beta$ -Turn $\beta$ -Turn $\beta$ -Turn $\beta$ -Turn	1680	$\beta$ -Turn	1675	$\beta$ -Sheet	1678	$\beta$ -Turn						
			1675	$\beta$ -Turn	1670	turns	1670	$\beta$ -Turn						
			1667	$\beta$ -Turn	1663	turns	1664	$\beta$ -Turn						
			1663	Helix										
<b>1645-1662</b> <b>Unordered</b> <b>Helix</b>	1653-1657 1655 1654 1642-1657 1647-1648 1648 1649	Helix Helix Random Coil Random Coil $\beta$ -Sheet Random Coil Helix	1656 1648	Helix Random	1654 1645	alpha-helix unordered	1656 1648	alpha-helix alpha-helix						
									1642	$\beta$ -Sheet				
									1634-1639	$\beta$ -Sheet	1637	$\beta$ -Sheet	1641	unordered
									1630	$\beta$ -Sheet	1631	$\beta$ -Sheet	1633	$\beta$ -Sheet
									1621-1623	$\beta$ -Sheet	1627	$\beta$ -Sheet	1624	$\beta$ -Sheet
		1624	$\beta$ -Sheet											
<1620	1615-1620	Aggregated protein												

**Table 6.1** Literature IR peak values for secondary protein structures within the amide I and amide II band.

Value $\text{cm}^{-1}$	Assignment
1712	Side Chain
1693	intermolecular $\beta$ sheet
1680	$\beta$ turn
1656	random coil
1644	$\alpha$ helix
1628	intramolecular $\beta$ sheet
1615	intermolecular $\beta$ sheet
1592	non-baseline amide I and II separation compensation
1568	Amide II
1546	Amide II
1526	Amide II
1511	Amide II
1497	Amide II

**Table 6.2** Selected values for peak deconvolution of the amide I and amide II band.

Iterations of the method development saw various parameters explored such as Gaussian vs Lorentzian, and fixed vs non-fixed peak: height, width, position and area. The final peak parameter settings have peaks limited to a half height width of 10-30  $\text{cm}^{-1}$  allowing for any positive height/area. Peak are solely based on the Gaussian fit. The conformer composition was calculated as the area of the relevant peaks expressed as a percentage of the total amide I peak area, (peaks 1615 through 1693  $\text{cm}^{-1}$ ).

The new method allows for trends to be more reliably monitored, each conformer is monitored with high repeatability displayed. The high statistical merit of this method is shown in Figure 6.3, where errors bars represent 1 standard deviation, there are no enveloping regions between error bars.

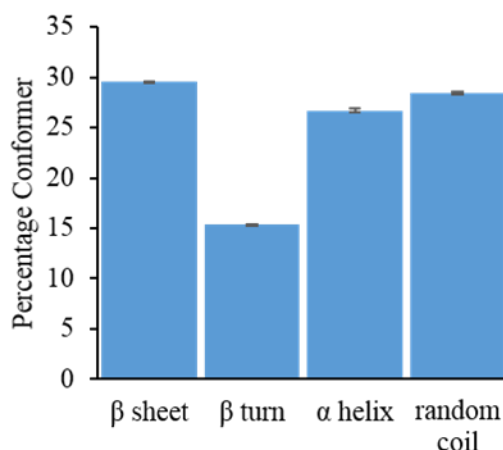


**Figure 6.3** Estimation of secondary structure of protein for the nh-15mer pre-annealed film using the new peak fitting parameters discussed above.

### 6.3.2 Method Development for Low Volume Biodegradation of Protein Films

To estimate and observe the effects of annealing and mineralisation on the *in vivo* lifetime of silk chimeric films as biomaterials, the Bradford assay was employed to monitor dissolution of protein films over time under *in vivo* mimicking conditions. A new method was developed here to overcome the small quantity of sample material available for this study.

Previous methods for the Bradford protein assay in the Perry group are as follows:

60  $\mu$ L Bradford reagent (100 mg Coomassie Blue/Brilliant Blue G250 dissolved in 50 mL methanol with 100 mL 85% orthophosphoric acid and 100 mL deionised water), was added to a well of a 96 well plate with 130  $\mu$ L deionised water and 10  $\mu$ L sample. Shifts in colour from protein-dye binding were measured at 595 nm and 450 nm, the ratio found, and results compared to appropriate standards.

Results varied with proteins analysed but this method continually produced a good correlation of standards with reliable measurements made when there is an abundance of sample. Here the limits of this assay are explored to allow for a degradation study of the chimeric silk proteins as films, where 0.6 mg of sample is initially present and sampling to monitor degradation can be sustained over a two month period.

Tabulated in Table 6.3 are the results of the trial studies, briefly Trial 1: two sets of standards were prepared using the 15mer spider silk repeating unit; one as described above, and the second to explore if a known volume of protein can be preloaded into

samples to ensure measurements are performed within the working range. It was observed that the solutions were non-homogenous and it was decided that the Bradford reagent must first be prediluted with water to ensure a homogenous solution, samples can then be added with additional stirring. Trial 2: Samples were prepared as in Trial 1 with a Bradford/water stock ready to use. There was no correlation seen for the calibration range of 0.001-0.01 mg protein added, which questioned if the Bradford assay is suitable for silk proteins or if saturation from the dye had occurred. Trial 3: standards were prepared as in Trial 2 using BSA instead of silk proteins, no correlation was seen again indicating that the ratio of dye to protein present was too high. Trials 4 and 5, the dilution factor of Bradford stock was varied along with the total volume of each standard solution prepared, a 3:1 water to Bradford ratio was proven optimum and a lower sample volume of 10  $\mu\text{L}$  was proven feasible within a total sampling volume of 100  $\mu\text{L}$ . Trial 6 proved that smaller sample volumes ( $<10\mu\text{L}$ ) were beyond the lower limit of this method and Trial 7 demonstrated that at lower volumes no preloading of proteins was necessary.

Final experimental parameters were selected that require 60% less sample (protein/silk) than the previous method employed, making a timed study of chimeric silk films degradation under *in vivo* mimicking conditions now possible. The method selected is listed in Table 6.3 and labelled trial 5biii, where the optimum stock solution ratio (Bradford : Water) was found to be 1:3, and detection was possible with 0.001mg sample present. This method was proven compatible with silk.

Trial	Protein	Water : Bradford	Diluted Bradford $\mu\text{L}$	Calibration standard $\mu\text{L}$	Preload 10 $\mu\text{L}$	Prediluted	Calibration range by mass mg	Total $\mu\text{L}$	Results				
1a	15mer	13:6	190	10	no	No	0.001-0.01	200	Little to no correlation. Observation: samples appeared non-homogeneous. Action: Pre-dilution of Bradford dye with water				
1b		2:1	180		0.5 mg/ml								
2a	15mer	13:6	190	10	no	Yes	0.001-0.01	200	Homogenous samples produced. No correlation. Not suitable for silk? Bradford Saturation?				
2b		2:1	180		0.5 mg/ml								
3a	BSA	13:6	190	10	no	Yes	0.001-0.01	200	No correlation: Bradford Saturation				
3b		2:1	180		0.5 mg/ml								
4ai	15mer	13:6	190	10	no	Yes	0.001-0.01	200	Lower Bradford concentrations saw a poor correlation present and poor repeatability. Increase sample conc, add another Bradford dilution. Pre-load gave better correlation				
4aii			180		0.5 mg/ml								
4bi		13:3	190		no								
4bii			180		0.5 mg/ml								
5ai	15mer	13:3	175	25	No	Yes	0.001-0.01	200	Correlations from most were reasonable ( $R^2 > 0.9$ ), reduced volumes proved successful meaning lower sample concentrations can now be used. 3:1 Bradford dilute showed to be optimum.				
5aii			165	0.5 mg/ml									
5aiii			90	10	No			100					
5aiv			80	0.5 mg/ml									
5bi			175	25	No			200					
5bii			3:1	165	0.5 mg/ml								
5biii		90		10	No			100					
5biv		80	0.5 mg/ml										
5ci		2:1	175	25	No			200					
5cii			165	0.5 mg/ml									
5ciii			90	10	No			100					
5civ			80	0.5 mg/ml									
6			15mer	3:1	95			5		No	Yes	0.0005-0.005	100
7a		15mer	3:1	90	10			No		Yes	0.001-0.01	100	No pre-load gave optimum correlation $R^2 > 0.99$
7b	80			0.5 mg/ml									
7c	80			0.8 mg/ml									
7d	80			1 mg/mL									

**Table 6.3** Variations to Bradford Assay method with observations and conclusions at each step.  
\*Shaded areas indicate variable being explored.

### 6.3.3 Silk Chimeras: Incorporation of a silicifying domain

The secondary protein structure of each chimeric silk film was quantified using a peak fitting method developed in (Belton et al, 2017 – Publication pending in Biomacromolecules) applied to FTIR-ATR spectra over the amide I and amide II region. The profile of the amide I peak depends largely on the stretching vibrations of the C=O groups which is dictated by the samples protein structure.

As seen previously (Plowright et al, 2016, Chapter III),<sup>23</sup> annealing of silk films resulted in an increase in the beta conformers with no significant difference between R5 bound silk films and their control counter parts, (R5-15mer-ch compared with 15mer-ch and nh-15mer-R5 compared to nh-15mer). Here, in depth analysis showed that the increased level of  $\beta$  conformer in each silk film arises solely from an increase in  $\beta$  sheet at the expense of  $\alpha$  helical structures, Figure 6.4. Similar results to this was seen by Izutsu et al for near IR spectroscopy of proteins.<sup>32</sup> Further, silicification carried out on fully annealed films had no significant effect on the protein structure of the silk films, with no change in any conformer quantities from annealed to silicified films. These results suggest that *in vivo*, the presence of silica particles would also not affect protein structure meaning a predetermined  $\beta$  percentage of biomaterial silk can be selected by the surgeon/scientist and assumed stable prior to implantation. The level of random coil regions appears unchanged regardless of any process the silk films underwent suggesting that initial random coil regions may define the maximum  $\beta$  conformer level that can be induced in silk films, Figure 6.4.

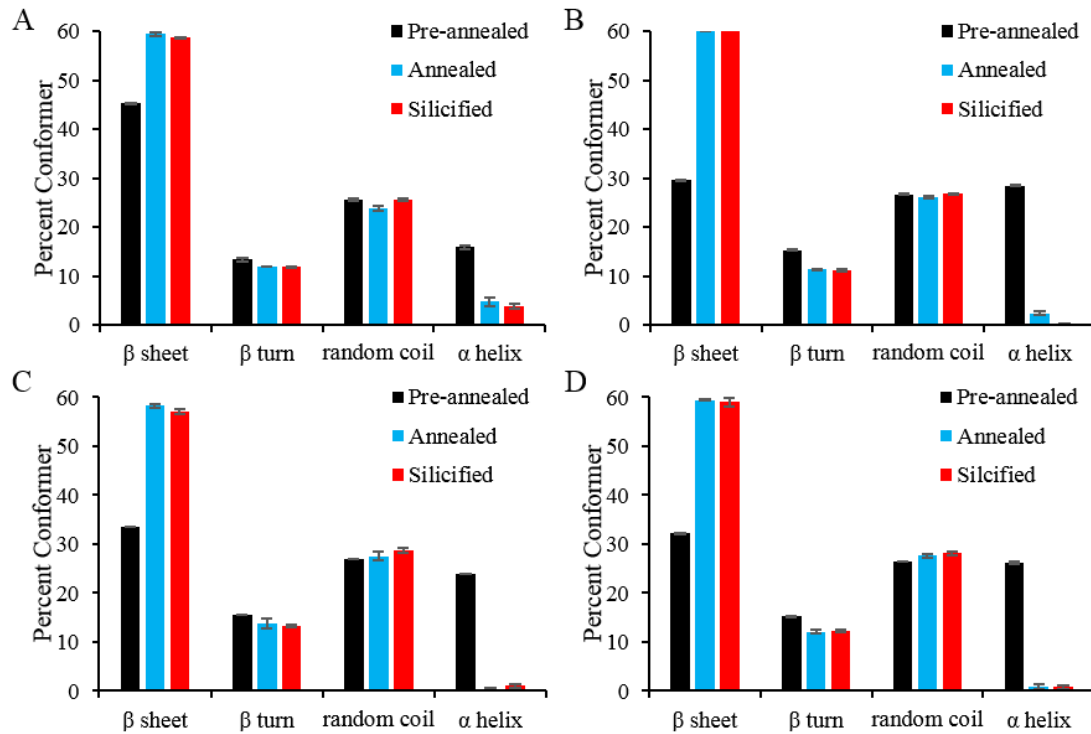


**Figure 6.4** Percentage of secondary protein conformers present in R5 and control silk films; pre-annealed, annealed and silicified A) 15mer-ch B) nh-15mer C) R5-15mer-ch and D) nh-15mer-R5. N=5

Mechanical properties of biomaterials were estimated from the measurement of the Young's modulus. Appendix Fig 6.i gives an example of the force separation graphs used for this. One aim of incorporating silica into silk to form composites was to produce a silk material with heightened resilience to deformation at implant sites. Figure 6.5C shows the measured Young's modulus for the preannealed, annealed and silicified silk films. Addition of the R5 binding domain appears to lower the stiffness of the raw state silk films. However once annealed, the R5 bound chimeras rivalled the modulus' of the two controls used in the study. Furthermore, a substantially larger increase was seen in the Young's modulus after silicification for the R5-15mer-ch sample compared with the control and nh-15mer-R5 samples. The R5-15mer-ch chimera has previously been shown to have the greatest control over silicification confirming that the binding of silica particles to produce silk composites aids in stiffening the material, particularly as there is no change in protein structure (percent  $\beta$  conformer) during the silicification process, Figure 6.5D.

Topography of the silk surfaces was observed using the images obtained from AFM. Figure 6.5 Ai-iii is the nh-15mer control preannealed, annealed and silicified respectively. Each process results in further roughening of the surface as the protein film undergoes structural changes when annealed and then silica deposition during mineralisation. Figure 6.5 Bi and Bii are the R5-15mer-ch and nh-15mer-R5 silicified films. The R5-15mer-ch film is a uniform surface with peaks due to uniform silica particle presence and nh-15mer-R5 surface has two populations of peak sizes present, supporting previous findings of a lesser controlled silicification mechanism occurring.<sup>23</sup>

Estimation of *in vivo* lifetime of biomaterials and the effect of sample processing on this life time is an essential parameter that needs to be known prior to *in vivo* use. Silk composites are intended for temporary use in the body, the material is designed to aid bone regeneration and then naturally and harmlessly degrade over a designated time frame. Figure 6.5E show the solubility of silk films under *in vivo* mimicking conditions, the black lines are preannealed films which are comparatively more soluble (for all samples) in PBS than annealed films (blue lines), showing solubility and therefore biodegradability of silk biomaterials can be tailored *via* the annealing process. Silicification appears to offer some slight gain in resilience to degradation, however this is not to the extent that degradation will be hindered, as previous data suggested that silica particle sizes induced to form in the presence of the chimeras were still on a bio-absorbable scale.<sup>31</sup>

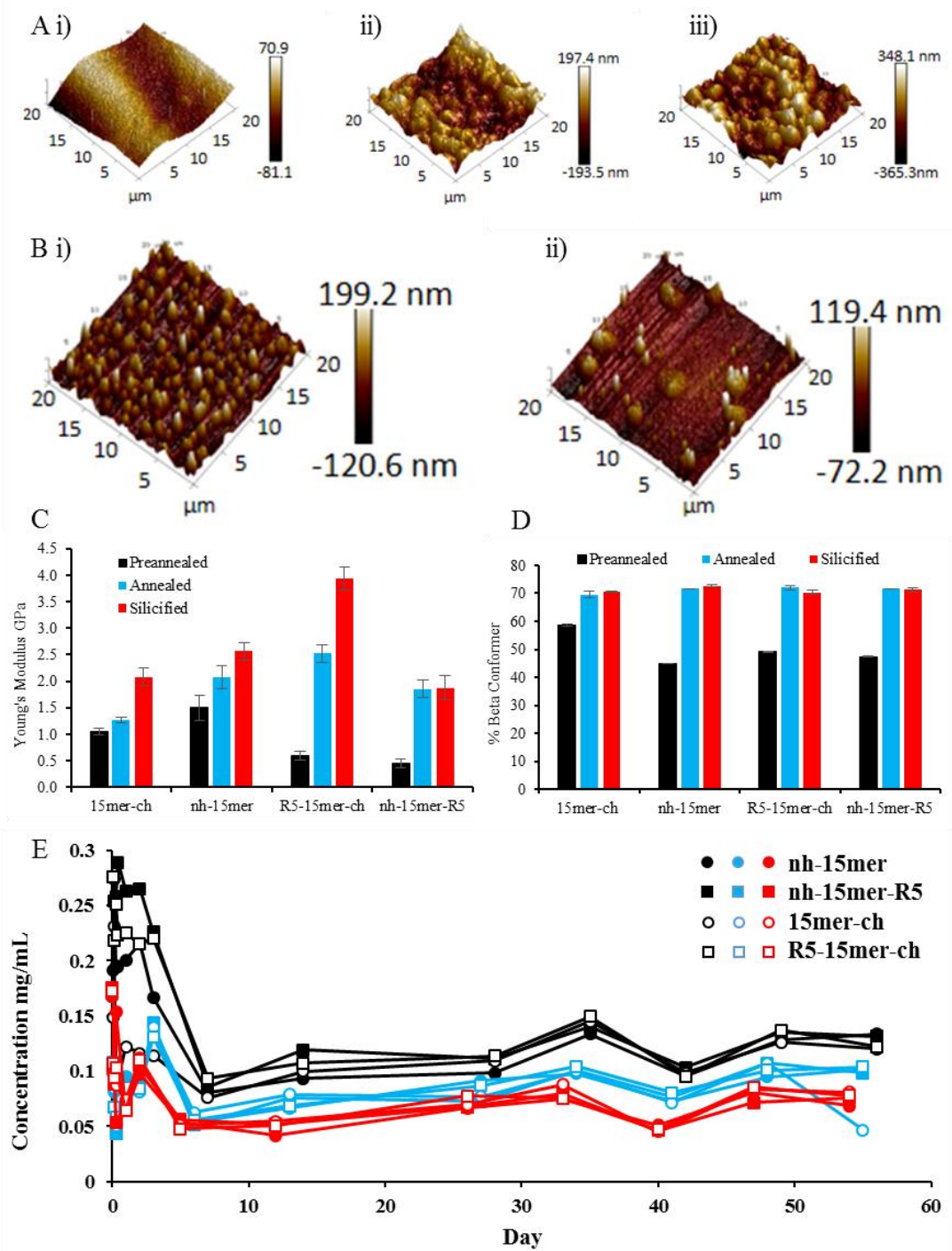


**Figure 6.5** A) AFM images for the nh-15mer control silk film i) preannealed ii) annealed and iii) silicified B) Silicified films i) R5-15mer-ch ii) nh-15mer-R5 C) Young's modulus measurements for the silk fusion proteins with an assumed Poisson's ratio of 0.3, N=20 D) Beta sheet content of preannealed, annealed and silicified silk chimeras and controls, N=3 E) Protein concentration of PBS supernatant in the presence of 0.6mg silk films; preannealed (black), annealed (blue) and silicified (red) over time

Table 6.4 shows mechanical property data for the silicified chimeras and control silk samples. There is a clear correlation between the increasing percentage  $\beta$  conformer and the increasing Young's modulus of the samples, this is also reflected in the heightened tolerance towards dissolution in PBS, Figure 6.5E.

	15mer-ch	nh-15mer	R5-15mer-ch	nh-15mer-R5
Percent Beta Structure:				
Preannealed	58.59 $\pm$ 0.42	44.87 $\pm$ 0.04	49.11 $\pm$ 0.11	47.36 $\pm$ 0.16
Annealed	69.41 $\pm$ 1.17	71.56 $\pm$ 0.15	72.06 $\pm$ 0.83	71.55 $\pm$ 0.08
Silicified	70.52 $\pm$ 0.18	72.70 $\pm$ 0.43	70.32 $\pm$ 0.85	71.16 $\pm$ 0.85
Young's Modulus GPa:				
Preannealed	1.04 $\pm$ 0.06	1.50 $\pm$ 0.23	0.60 $\pm$ 0.08	0.45 $\pm$ 0.08
Annealed	1.26 $\pm$ 0.05	2.07 $\pm$ 0.22	2.52 $\pm$ 0.17	1.86 $\pm$ 0.16
Silicified	2.08 $\pm$ 0.17	2.56 $\pm$ 0.16	3.94 $\pm$ 0.21	1.87 $\pm$ 0.23

**Table 6.4** Percent beta conformer and Young's modulus data collected for the 15mer-ch, nh-15mer, R5-15mer-ch and nh-15mer-R5. Surface energies: N=3, Young's modulus N=20.

### 6.3.4 Silk Chimeras: Incorporation of a Hydroxyapatite Binding Domain

The effect of the addition of the VTK peptide to the silk backbone on protein secondary structure was assessed using peak deconvolution of the amide I band as described above. Unlike the incorporation of the R5 silicifying domain, addition of the VTK peptide at either termini of the silk repeating unit had no significant effect on the protein secondary structure of raw state silk films, Figure 6.6. Silk constructs containing VTK domains were able to undergo annealing to induce higher  $\beta$  conformer content to the same extent as that observed in their control counter parts, additional  $\beta$  content coming from increased  $\beta$  sheet structures with a negative correlation to  $\alpha$  helix structures, Figure 6.6. At this stage the effect of HAP mineralisation on protein conformers present was to be considered, however it was not possible to achieve IR data for the amide I band, it is believed this is due to the layer of mineral present being too thick for the IR beam to penetrate into the silk, or for minimal beam penetration to occur producing low intensity amide peaks that are within background noise levels compared to high intensity phosphate peaks present.

Similarly to the R5 constructs, the measured quantity of random coil conformers present in the VTK and control silk films remained unchanged after annealing, suggesting these regions are unaffected by the annealing process and limit the amount of  $\beta$  sheet that can be induced using this method.

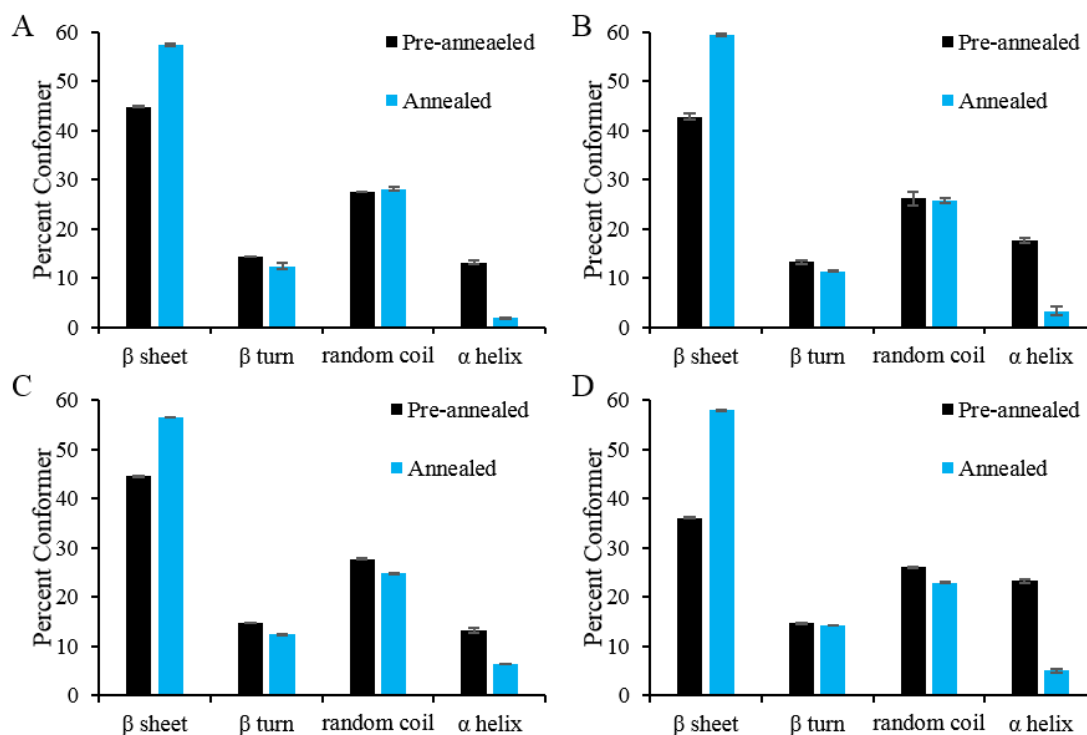


**Figure 6.6** Secondary protein structure of pre-annealed and annealed VTK containing silk chimeras with their control counterparts A) 15mer-ch B) nh-15mer C) VTK-15mer-ch and D) nh-15mer-VTK. N = 5

The mineralising capabilities of the VTK chimeras was explored previously in Chapter IV,<sup>27</sup> here a comparison of the silk films mechanical properties is presented to evaluate the potential of these samples as biomaterials. Annealing of the control and the VTK domain containing constructs resulted in a stiffening of the silk films, to between 1-4 GPa, Figure 6.7B, correlating with the increased levels of the  $\beta$  conformer, Figure 6.7 C. Once mineralised the control samples showed no further improvement with respect to mechanical properties (Young's modulus measurements), however the VTK samples had varied responses to mineralisation; the nh-15mer-VTK construct had a marked increase in Young's modulus after mineralisation but this was seen to a lesser extent compared with the VTK-15mer-ch and VTK-15mer-VTK samples. Young's modulus data for the samples suggests that the crystalline precipitates produced in the presence

of the samples is the result of different mineralising mechanism by the VTK peptide to produce HAP which is dictated by the location of the VTK domain on the silk backbone. Further, stiffness measurements support XRD data shown in Chapter IV (Section 4.4.3), where the nh-15mer-VTK sample was seen to have less control over HAP mineralisation than the VTK-15mer-ch and VTK-15mer-VTK samples, with a less intense HAP pattern being produced, conversely, it is the film/precipitate material produced by the nh-15mer-VTK sample that fits best to the Young's modulus of bone, 6-30 GPa,<sup>33,34</sup> at 18.43 GPa. An argument can be made that precipitates produced by the VTK-15mer-ch and VTK-15mer-VTK samples would not integrate neatly into the surrounding bone due to much higher Young's moduli of 148.39 and 168.71 GPa respectively.

Protein dissolution over time in PBS was measured using a Bradford assay to estimate *in vivo* lifetime of the silk films; pre-annealed, annealed and HAP mineralised. Similar to what was observed for the R5 constructs, annealing to produce films with higher  $\beta$  conformer content provided the control and VTK samples with resilience to degradation under *in vivo* mimicking conditions, suggesting a degree of control over biodegradation of silk films can be obtained. Data presented in Figure 6.7 D shows that less protein was released into solution from the mineralised films (likely due to protein-solvent interactions being reduced by the mineral creating a barrier), however it is believed that there was protein loss during the mineralisation of silk films so potentially the maximum concentrations presented for mineralised films are likely to be overestimates. Given this, HAP mineralisation of VTK-silk chimeras appears to not interfere with the natural break down of the silk material, suggesting that if applied *in vivo*, these films would be appropriate for use as temporary biomaterials.

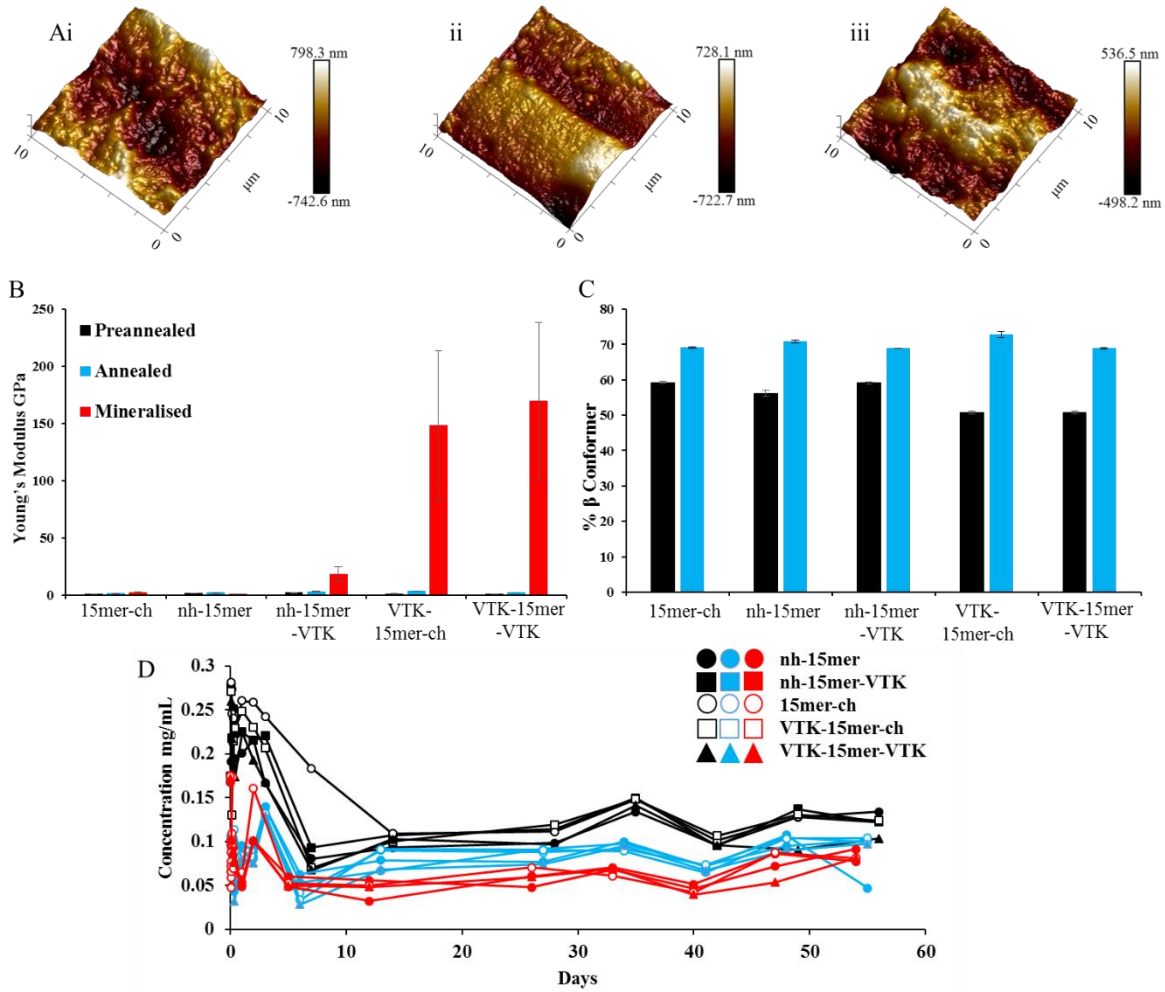


**Figure 6.7** A) AFM images of HAP mineralised films i) nh-15mer-VTK ii) VTK-15mer-VTK iii) VTK-15mer-VTK B) Young's modulus measurements for the silk fusion proteins with an assumed Poisson's ratio of 0.3, N=20 C) Beta sheet content of preannealed and annealed films N=3 D) and E) Protein concentration of PBS supernatant in the presence of 0.6 mg silk films; preannealed (black), annealed (blue) and hydroxyapatite mineralised (red) over time

	15mer-ch	nh-15mer	nh-15mer-VTK	VTK-15mer-ch	VTK-15mer-VTK
Percent Beta Structure:					
Preannealed	59.3 ± 0.31	56.14 ± 0.89	50.8 ± 0.42	59.1 ± 0.35	50.8 ± 0.24
Annealed	69.1 ± 0.24	70.85 ± 0.43	72.82 ± 0.87	68.9 ± 0.06	68.9 ± 0.16
Young's Modulus GPa:					
Preannealed	1.04 ± 0.06	1.50 ± 0.23	2.05 ± 0.32	1.21 ± 0.03	0.73 ± 0.05
Annealed	1.26 ± 0.05	2.07 ± 0.22	3.04 ± 0.41	3.51 ± 0.23	2.25 ± 0.11
HAP Mineralised	2.49 ± 0.26	0.85 ± 0.6	18.43 ± 6.38	148.39 ± 65.34	169.71 ± 68.45

**Table 6.5** Percent  $\beta$  conformer and Young's modulus data collected for the 15mer-ch, nh-15mer, VTK-15mer-ch, nh-15mer-VTK and VTK-15mer-VTK. Surface energies: N=3, Young's modulus N=20.

## 6.4 Conclusions

A full *in vitro* study of silk chimeras for use as biomaterials (films) to coat dental and bone implants has been performed. The theorised link between  $\beta$  content of a chimeric silk film and its stiffness has been proven *via* Young's modulus measurements of pre-annealed and annealed films, where an increase in  $\beta$  sheet structure (reduction in  $\alpha$  helical structures), saw a correlated increase in sample stiffness. Silk films with a greater percent  $\beta$  conformer also showed increased resilience towards degradation under *in vivo* mimicking conditions.

The effect of genetic modification of silk to incorporate mineralising domains was evaluated to ensure that the biocompatibility and beneficial physical properties of the silk remained unchanged. Addition of the R5 peptide (at either terminus of the silk backbone) lowered the rigidity of samples as raw silk films with a reduction of overall  $\beta$  structures present, however this could be compensated by annealing the R5 constructs proving that these films can be manipulated to have a similar secondary protein structure to that of their control counter parts.

Presence of the R5 peptide promoted binding of uniform silica particles that further enhanced the material stiffness of the composites generated. However silicification had little influence on solubility or protein structure of the films indicating the desired physical properties of the silk film can be modified *via* an annealing process prior to *in vivo* insertion. Further development of silk as a biomaterial can be performed by the use of varying annealing methods to give predetermined physical properties.

Unlike the R5 peptide, incorporation of the VTK peptide had no significant effect on the raw state films and allowed for induction of  $\beta$  conformers *via* methanol annealing to the same degree as the control samples used. HAP mineralisation was thought to not interfere with the breakdown of films in the body, but the location of the VTK peptide on the silk backbone of proteins used to make the mineralised films was shown to be a key parameter in determining the physical properties of the samples, with dramatic differences in Young's modulus of the precipitates formed during mineralisation by the nh-15mer-VTK sample compared with the VTK-15mer-ch and VTK-15mer-VTK samples being observed. Comparison with literature values for the Young's modulus of bone suggests that the less stiff material produced by the nh-15mer-VTK may be more compatible with bone as it falls within the generally accepted range of Young's moduli for bone. The Young's modulus of the more crystalline materials produced in the presence of the VTK-15mer-ch and VTK-15mer-VTK was measured to be up to ten times greater than that of bone.

All physical property data suggests that the chimeras are good candidates for biomedical use, particularly the R5-15mer-ch given its exceptional silicifying capabilities and the nh-15mer-VTK as the crystalline HAP precipitates produced by this sample are the most likely to be readily incorporated into surrounding bone tissue due to similar physical properties of the materials themselves.

## 6.5 References

- 1 C. Vepari and D. L. Kaplan, *Progress in Polymer Science*, 2007, **32**, 991-1007.
- 2 S. Mobini, M. Solati-Hashjin, H. Peirovi, N. A. Abu Osman, M. Gholipourmalekabadi, M. Barati and A. Samadikuchaksaraei, *Journal of Medical and Biological Engineering*, 2013, **33**, 207-213.
- 3 Y. Xu, H. L. Shao, Y. P. Zhang and X. C. Hu, *Journal of Materials Science*, 2005, **40**, 5355-5358.
- 4 C. Fu, Z. Shao and V. Fritz, *Chemical Communications*, 2009, **43**, 6515-6529.
- 5 O. Hakimi, D. P. Knight, F. Vollrath and P. Vadgama, *Composites Part B-Engineering*, 2007, **38**, 324-337.
- 6 D. Huemmerich, C. W. Helsen, S. Quedzuweit, J. Oschmann, R. Rudolph and T. Scheibel, *Biochemistry*, 2004, **43**, 13604-13612.
- 7 C. Z. Zhou, F. Confalonieri, M. Jacquet, R. Perasso, Z. G. Li and J. Janin, *Proteins-Structure Function and Genetics*, 2001, **44**, 119-122.
- 8 U. Kim, J. Park, C. Li, H. Jin, R. Valluzzi and D. Kaplan, *Biomacromolecules*, 2004, **5**, 786-792.
- 9 M. Fini, A. Motta, P. Torricelli, G. Glavaresi, N. N. Aldini, M. Tschon, R. Giardino and C. Migliaresi, *Biomaterials*, 2005, **26**, 3527-3536.
- 10 M. Z. Li, M. Ogiso and N. Minoura, *Biomaterials*, 2003, **24**, 357-365.
- 11 N. Minoura, S. I. Aiba, M. Higuchi, Y. Gotoh, M. Tsukada and Y. Imai, *Biochemical and Biophysical Research Communications*, 1995, **208**, 511-516.
- 12 U. J. Kim, J. Park, H. J. Kim, M. Wada and D. L. Kaplan, *Biomaterials*, 2005, **26**, 2775-2785.
- 13 R. Nazarov, H. J. Jin and D. L. Kaplan, *Biomacromolecules*, 2004, **5**, 718-726.
- 14 E. Wenk, A. Wandrey, H. Merkle and L. Meinel, *Journal of Controlled Release*, 2008, **132**, 26-34.
- 15 L. Uebersax, H. Hagenmueller, S. Hofmann, E. Gruenblatt, R. Mueller, G. Vunjak-Novakovic, D. L. Kaplan, H. P. Merkle and L. Meinel, *Tissue Engineering*, 2006, **12**, 3417-3429.
- 16 K. Gellynck, P. C. Verdonk, E. Van Nimmen, K. F. Almqvist, T. Gheysens, G. Schoukens, L. Van Langenhove, P. Kiekens, J. Mertens and G. Verbruggen, *Journal of Materials Science: Materials in Medicine*, 2008, **19**, 3399-409.

- 17 B. An, M. D. Tang-Schomer, W. Huang, J. He, J. A. Jones, R. V. Lewis and D. L. Kaplan, *Biomaterials*, 2015, **48**, 137-146.
- 18 S. C. Gomes, I. B. Leonor, J. F. Mano, R. L. Reis and D. L. Kaplan, *Biomaterials*, 2011, **32**, 4255-4266.
- 19 K. Numata, B. Subramanian, H. A. Currie and D. L. Kaplan, *Biomaterials*, 2009, **30**, 5775-5784.
- 20 C. Wong Po Foo, S. V. Patwardhan, D. J. Belton, B. Kitchel, D. Anastasiades, J. Huang, R. R. Naik, C. C. Perry and D. L. Kaplan, *Proceedings of the National Academy of Sciences of the United States of America*, 2006, **103**, 9428-9433.
- 21 L. L. S. Canabady-Rochelle, D. J. Belton, O. Deschaume, H. A. Currie, D. L. Kaplan and C. C. Perry, *Biomacromolecules*, 2012, **13**, 683-690.
- 22 D. J. Belton, A. J. Mieszawska, H. A. Currie, D. L. Kaplan and C. C. Perry, *Langmuir*, 2012, **28**, 4373-4381.
- 23 R. Plowright, N. Dinjaski, S. Zhou, D. J. Belton, C. C. Perry and D. L. Kaplan, *RSC Advances*, 2016, **6**, 21776-21788.
- 24 M. R. Knecht and D. W. Wright, *Chemical Communications*, 2003, **24**, 3038-3039.
- 25 M. D. Roy, S. K. Stanley, E. J. Amis and M. L. Becker, *Advanced Materials*, 2008, **20**, 1830-1836.
- 26 W. N. Addison, S. J. Miller, J. Ramaswamy, A. Mansouri, D. H. Kohn and M. D. McKee, *Biomaterials*, 2010, **31**, 9422-9430.
- 27 N. Dinjaski, R. Plowright, S. Zhou, D. J. Belton, C. C. Perry and D. L. Kaplan, *Acta Biomaterialia*, 2017, **49**, 127-139.
- 28 S. Zhou, W. Huang, D. J. Belton, L. O. Simmons, C. C. Perry, X. Wang and D. L. Kaplan, *Biomaterials*, 2015, **15**, 173-180.
- 29 B. V. Derjaguin, V. M. Muller and Y. P. Toporov, *Progress in surface science.*, 1994, **45**, 131.
- 30 J. E. Noble and M. J. A. Bailey, in *Guide to Protein Purification, 2nd Edition*, ed. R. R. Burgess and M. P. Deutscher, 2009, p. 73-95.
- 31 A. Mieszawska, N. Fourligas, I. Georgakoudi, N. Ouhib, D. Belton, C. Perry and D. Kaplan, *Journal of Biomaterials*, 2010, **34**, 8902-8920.
- 32 K. I. Izutsu, Y. Fujimaki, A. Kuwabara, Y. Hiyama, C. Yomota and N. Aoyagi, *Journal of pharmaceutical sciences*, 2006, **95**, 781-789.
- 33 L. L. Hench, *Journal of the American Ceramic Society*, 1998, **81**, 1705-1728.

34 A. Ravaglioli and A. Krajewski, *Bioceramics : Materials · Properties · Applications.*, Springer Netherlands, Dordrecht, 2012.

## Chapter VII

# Silk-Silica Composites as Coatings for Silk Scaffolds and Titanium Rods

### 7.1 Introduction

The production of implantable biomedical devices began in 1931 for dentistry, when Greenfield produced an iridioplatinum basket implant attached to a gold crown.<sup>1</sup> There was unmistakable evidence of osseointegration of these implants and they often lasted several years. Bothe et al. were the first to use titanium as the implant material, where notably elevated levels of osseointegration<sup>2</sup> saw this become that preferred material of choice for bone and dental implants. Over the years numerous animal studies have proven the close proximity a titanium surface can achieve with bone, some studies reporting the bone effectively adhering to the implant.<sup>3</sup>

The vast majority of modern implants now consist of a titanium screw that is affixed to the jaw bone, Figure 7.1, the surface of the implant is treated prior to insertion to produce a roughened surface on the macro, micro or nanoscale.<sup>4</sup> Texturizing of the surface can be done by etching, anodic oxidation or blasting to increase the surface area for heightened osseointegration. The macroscale of an implant surface refers to the overall geometry of the implant ( $\mu\text{m}$ -mm), high levels of roughening on this level has proven increased stability of the implant, both in the long and short term.<sup>5-7</sup> Studies have shown limiting the roughness to between 1-2  $\mu\text{m}$  will lower the risk of infection and ionic leakage, this is referred to as roughening on the mesoscale, between 1-10  $\mu\text{m}$ . The nanoscale properties of a surface define interactions of proteins with the surface and the adhesion of osteoblastic cells.<sup>8</sup>



Figure 7.1 X-ray showing a titanium dental implant in the lower jaw bone upon completion of permanent crown fixture. Picture taken at Charles Clifford Dental Hospital.

Despite treating the titanium implant surface, it is still comparably inert, osseointegration occurs effectively but slowly, and this has led to new research into potential coatings for implants. As the composition of the titanium implants surface directly effects protein adsorption and cell attachment, careful consideration into the design of an implant coating is necessary. Hydrophilic surfaces can be beneficial for interactions with biological fluids, cells and tissues<sup>9,10</sup> resulting in greater bone-implant contact.<sup>9</sup> Conversely, reports of *in vivo* studies on hydrophilic dental implant surfaces showed no improvement on osseointegration compared with more hydrophobic samples.<sup>11</sup>

Coatings of hydroxyapatite on titanium surfaces prior to insertion have been developed. Once implanted the coating dissociates from the surface creating a region of high calcium and phosphate ion presence. Saturation around the site results in biological apatite precipitation containing endogenous proteins aiding cell growth and attachment.<sup>12-14</sup> This mechanism results in biological implant-bone fixation occurring much faster than without HAP coatings,<sup>15,16</sup> leading to improved long term success rates due to superior osseointegration.<sup>17</sup>

Methods for adding HAP coatings to implant surfaces vary widely, there is a growing interest in using biomimetic approaches as these avoid the drawbacks of the more industrial coating processes, (for example; plasma spraying can cause changes in the implant porosity, changes in crystallinity of the HAP, added stress to the bulk material and even run the risk of delamination of the coating from the surface). Accelerated precipitation from SBF buffer solutions to HAP coated implants has been studied using electrodeposition,<sup>18,19</sup> hydroxylation of the titanium surface and increased ion concentrations.<sup>20</sup>

Hydroxyapatite is not the only mineral identified as useful for bone regrowth, there have also been many biomimetic studies looking to induce silica deposition for biomedical applications. Silica binds strongly with bone whilst also being osteoinductive, it is acknowledged that silica plays a fundamental role in the natural formation of bones.<sup>21,22</sup>

Previous work by the Perry and Kaplan group has identified the possibility to genetically modify spider silk in order to incorporate silica to produce biomaterials. By combining silica with the numerous advantages of silk, a material was produced that was versatile<sup>23</sup>

yet hard, fully biodegradable/bioabsorbable over a long time period and osteoinductive at the bone interface.<sup>24-29</sup> In the study, a derivative of the major ampullate dragline silk of the *N. clavipes*, was modified to incorporate specific binding peptides. Repeating units of the silk, [(SGRGGLGGQGAGAAAAAGGAGQGGYGGLGSQGT)<sub>15</sub>], were used as a backbone to which the R5 silica binding peptide, (SSKKSGSYSGSKGSKRRIL), was attached at the N or C termini of the silk. It was proven the R5-15mer-ch sample, (ch representing a Hig-tag) had good potential for biomedical use with strong silicifying capabilities.<sup>24</sup>

Complimentary studies by the Perry and Kaplan groups observed silk-silver recombinant proteins, where a silver binding peptide (NPSSLFRYLPSD or WSWRSPTPHVVT) was added to the C terminal of the spider silk repeating unit (SGRGGLGGQGAGAAAAAGGAGQGGYGGLGSQGT). Chimeric proteins studied both in solution and as films resulted in silver nanostructural growth, which were proven to be effective antimicrobials.<sup>30</sup>

Despite a successful study, the disadvantage of these chimeric silks was the overall cost of production, suggesting that the larger quantities needed to produce biological scaffolds, would not be cost effective. In this study, the use of chimeric silk as a thin coating for biologically inert scaffolds and rods has been explored. Two materials have been selected for the bulk of the structures; (the standard) titanium and the *Bombyx mori* (*B. mori*) silk.

*B. mori* silkworm silk has been widely explored as a candidate for biological scaffolds, but its use as a biomaterial is not limited to scaffolds, silk biomaterials also include: gels,<sup>31</sup> membranes<sup>32</sup> and films.<sup>24,33,34</sup> Silks demonstrate biocompatibility, good resilience to degradation and impressive yet tailorable physical properties.<sup>35,36</sup>

Silk's beneficial properties for biomedical application are from the  $\beta$  structures formed on expulsion of the protein from the silkworm's glands.<sup>37</sup>  $\beta$  sheet structure consists of long strands of protein horizontally connected to one another *via* hydrogen bonding (C=O---H-N) resulting in the formation of a pleated sheet. The strands can be arranged either parallel or antiparallel and are interlinked with regions of  $\beta$  turn structures. The induction of  $\beta$  conformers *in vitro* can be achieved through one of several annealing processes, allowing control of the samples physical properties.<sup>24</sup>

Porous silk scaffolds for bone regrowth have proven good suitability allowing the transport of nutrients and waste as well as cell attachment, proliferation and migration.<sup>38</sup> Silks ability to be functionalised for purpose has resulted in a variety of structural, chemical and biomechanical modifications being produced.<sup>39</sup> Despite good biocompatibility, silk is not bioactive in the sense it does not promote bone regrowth. It is hoped a silicifying coating will change this.

Figure 7.2 shows the samples produced for this study. *B. mori* silk scaffolds and titanium rods were produced then coated in the R5-15mer-ch silicifying silk chimera. Controls for the study included uncoated silk scaffolds and titanium rods to assess the inert underlying surface of the bulk materials, and a coating made of non-R5 containing spider silk protein in order to evaluate the silicifying capabilities of the R5 domain when used as part of a thin layer coating.

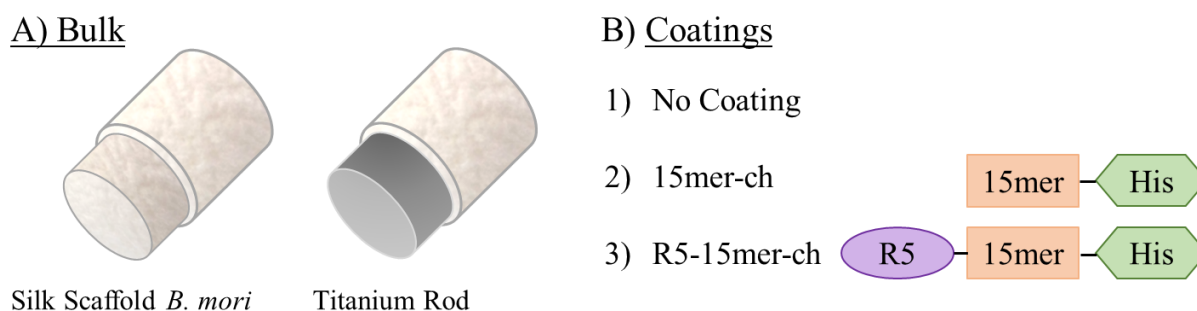


**Figure 7.2** Sample structures included in this study. **A)** The bulk material made from silkworm silk (*B. mori*) or titanium, typical size: 2mm (D) x 5mm (L). **B)** Coatings for each material: no coating, 15mer-ch (spider silk derivative) and R5-15mer-ch (silicifying spider silk derivative). All samples were characterised after silicification.

## 7.2 Methods and Materials

Preparation of scaffold materials was carried out by Tufts University, Boston.

### 7.2.1 Preparation of silk scaffolds

Aqueous silk solutions were prepared using previously established methods.<sup>40</sup> Briefly, sericin protein was removed from *Bombyx mori* silkworm cocoons by placing 5 g of cut cocoons (Tajima Shoji, Yokohama, Japan) in 2 L of a boiling 0.02 M sodium carbonate solution (Sigma-Aldrich, St. Louis, MO) for 30 min. After rinsing in deionised (DI) water three times, the degummed fibres were dried overnight and solubilized in 9.3 M

lithium bromide (Sigma-Aldrich, St. Louis, MO) for 4 h at 60°C. The resulting silk solution was then dialyzed against DI water using standard grade regenerated cellulose dialysis cassettes (3.5 kD MWCO; Pierce, Rockford, IL). After 6 changes over 3 days, insoluble silk particulates were removed by centrifugation (two times at 9000 RPM, 5°C, 20 min). Silk concentration was determined by weighing a dried sample of a known volume. The silk was then diluted in DI water to a final concentration of 5% and this solution poured into cylindrical-shaped containers with 4 mm in diameter and 6 mm in height. The containers were then frozen at -80°C and subsequently lyophilized for 2 days. The scaffolds were then autoclaved and cut in two equal pieces to final size (2 mm in width and 6 mm in height).

### **7.2.2 Preparation of titanium rods.**

Medical grade titanium wires with a 2 mm diameter were purchased (Sigma-Aldrich, St. Louis, MO) and cut by sawing to final size (2 mm in diameter and 5 mm in height).

### **7.2.3 Coating and biosilicification of scaffolds and rods.**

For coating, the lyophilized recombinant fusion proteins (15mer-ch and R5-15mer-ch) were prepared at a concentration of 2% (wt/vol) in ultrapure water. The proteins were allowed to dissolve overnight at 4°C. Then, titanium rods and silk scaffolds were placed in a 24 well plate with 1 mL of 2% silk solution for 5 min. Samples were then subjected to water vapour annealing using an isotemp vacuum oven for 24 h at room temperature and 635 mbar. Afterwards, samples were air-dried overnight at room temperature.

For inducing silicification, the silk and titanium coated with recombinant proteins (15mer-ch, R5-15mer-ch) were placed in a 24 well plate with 1 mL of 30 mM tetraethyl orthosilicate-phosphate buffer solution (Sigma-Aldrich, Dorset, UK) for 1 hour as described previously.<sup>27</sup> Scaffolds and rods were then rinsed three times with water and left to dry overnight in a fume hood.<sup>24</sup>

### **7.2.4 Characterisation Techniques**

#### ***Atomic Force Microscopy***

A Bruker Dimension Icon with ScanAsyst was used to perform all imaging, topographical measurements and nanoquantum mapping. Data was collected in PeakForce Tapping mode and processed using Nanoscope Analysis software. Elastic modulus values are stated as an average of 20 measurements taken across a 20  $\mu\text{m}^2$  area.

### ***Fourier Transform Infrared Attenuated Total Reflectance Spectroscopy (FTIR-ATR)***

Protein secondary structure of the coatings was assessed using FTIR-ATR (Frontier, PerkinElmer, Coventry, UK), with an average of 64 scans over the range 1750-1450  $\text{cm}^{-1}$ . Thermo Grams A1 software v8.0 was used for curve fitting (including peak deconvolution), and baseline corrections. Eight points were chosen from the amide I band (1700-1580  $\text{cm}^{-1}$ ); 4 points corresponding to  $\beta$  conformers: 1693, 1680, 1633 and 1615  $\text{cm}^{-1}$ , 2 points for non- $\beta$  conformers at 1656 and 1644  $\text{cm}^{-1}$ , and 2 at 1712 and 1592  $\text{cm}^{-1}$  to allow for peak shifting and amide II band overlap respectively. An iteration was carried out forcing all peaks to have a positive area with a linear baseline. This was carried out for 1,000 iterations before curve fitting. The sum of the areas under the peaks was found and each conformer expressed as a percentage of the total.

### ***Scanning Electron Microscopy and Microanalysis (SEM-EDX).***

SEM-EDX at 20 kV (JEOL 840, UK with Oxford Instruments Inca X-ray microanalysis, Oxford, UK) was used to observe the morphology and size of the silica particles and obtain information on the elemental composition of the scaffolds and rods. Each sample was mounted onto electrically conducting carbon tape on aluminium stubs before being gold coated using an argon gold plasma at 30mV and 1.2 kV for 2 minutes. A minimum of 50 particle diameters were measured and averaged to determine the particles size.

### ***Inductively Coupled Plasma – Optical Emission Spectroscopy***

The quantity of silicon present on sample surfaces was assessed *via* ICP (Perkin Elmer ICP-OES Optima 2100DV). One scaffold or rod was digested in 10M sodium hydroxide overnight then diluted 10 fold using dd. water. Measurements are stated as an average of 3 readings per sample compared against appropriate dilutions of 1000 ppm silicon stock solution (BDH Laboratory Supplies).

### ***Wettability Measurements***

The wettability and surface energy of the titanium rods was measured using a Theta Attension Instrument with OneAttention v1.7 software (Biolin Scientific, Staffordshire, UK). Samples were placed on the stand, and using a syringe, a 10  $\mu\text{L}$  droplet of water was placed on the surface and the contact angle at each side of the droplet measured ten times and an average taken.<sup>24</sup> Silk scaffolds prepared from *B.mori* could not be measured in this way due to their porous nature.

### ***Biodegradability/Solubility***

Scaffolds/rods prepared as above were submerged in 2mL 100mM PBS pH 7.4 at 37°C, degradation was measured by periodically taking 10 µL aliquots of the PBS supernatant and measuring protein concentration by adding 90 µL Coomassie stock solution (200mg Brilliant blue dye (Sigma-Aldrich, Dorset, UK), 100 mL methanol, 20 mL 85% orthophosphoric acid, 200 mL dd water), then measuring the absorbance ratio at a wavelengths 590nm and 450 nm.<sup>41</sup>

## **7.3 Results and Discussion**

### **7.3.1 Silk Scaffolds**

The three *B. mori* silk scaffolds were synthesised using well established methods for silkworm silk processing.<sup>40</sup> Coatings of chimeric spider silk proteins were then added through submersion, finally the scaffolds were silicified using pre-hydrolysed TEOS as previously described.<sup>24</sup>

Silk scaffolds were designed with the intended application of aiding bone regrowth when repair is needed. The bulk material, *B. mori* silk, has been widely discussed and explored as it is bioacceptable, malleable and impressively strong. The genetically synthesised spider silk coatings containing the R5 silica binding domain, (R5-15mer-ch), was selected based on previous studies highlighting this samples high control over silicification under *in vivo* mimicking conditions. Further, the addition of the R5 peptide had been shown to have no effect on the physical or chemical properties of the spider silk derivative, suggesting its high biocompatibility and resistance to biodegradation remained uncompromised.<sup>24</sup>

A silk scaffold has been produced here, where the bulk material is the cheaper *B. mori* silk with a coating of the R5-15mer-ch fusion protein. Control samples for comparison included in the study are an uncoated *B. mori* silk scaffold and a *B. mori* scaffold coated in a spider silk derivative that does not contain the R5 binding domain (15mer-ch). These will allow accurate analysis of how chimeric silk coatings of a bulk silk scaffold effect its  $\beta$  structures and therefore physical properties and the silicifying capabilities of the R5 peptide when used as a coating.

To observe silica particulate growth on the silk scaffold surface SEM coupled with EDX was used. Figure 7.3, showed that there was silica present on the surface of all three

samples. Only trace (non-particulate) amounts were present on the non-coated silk scaffold suggesting that whilst there is no obvious repulsion of silica particles, the *B. mori* silk surface does not provide nucleation sites for silicification. Both the 15mer-ch and R5-15mer-ch coated silk scaffolds promoted silica particle deposition, with particles of a similar size and size range, however ICP data, Figure 7.3 D showed the R5 peptide containing sample was able to promote more silica deposition per unit surface area ( $\sim 1.3 \mu\text{gmm}^{-2}$ ) than the 15mer-ch coated sample ( $\sim 1 \mu\text{gmm}^{-2}$ ), the uncoated scaffold had no measurable volume of silica present.

Unsurprising, as in nature, the uncoated *B. mori* silk scaffold had the greatest percentage of  $\beta$  conformer present, proving that the annealing process is still affective on silk when produced in scaffolds form. However, there was little difference in  $\beta$  content between the three scaffolds suggesting the derivative of the dragline spider silk was capable of reaching high levels of  $\beta$  conformer,  $>50\%$ . Proving that the thin layer of chimeric silk on the surface is still able to undergo structural reordering even when bound to a different silk material *via* the annealing process.

Figure 7.3 F shows the measured reduced elastic modulus of the scaffolds, the naturally beneficial properties of silk can be seen in the uncoated silk scaffold, where it was shown little to no silica binding had occurred but the stiffness was measured at  $\sim 6\text{GPa}$ . In this case there is an inverse relationship between increase in  $\beta$  content and the measured modulus of each sample, the 15mer-ch sample having greater stiffness than the uncoated silk scaffold, and the R5-15mer-ch silk scaffold exhibited a greater stiffness than both yet had the lowest level of  $\beta$  conformers present. Thus, it can be assumed that the production of the silica-silk composite has created a stiffer material, as there is a direct relationship between the mass of silica in a scaffold and the measured reduced modulus.

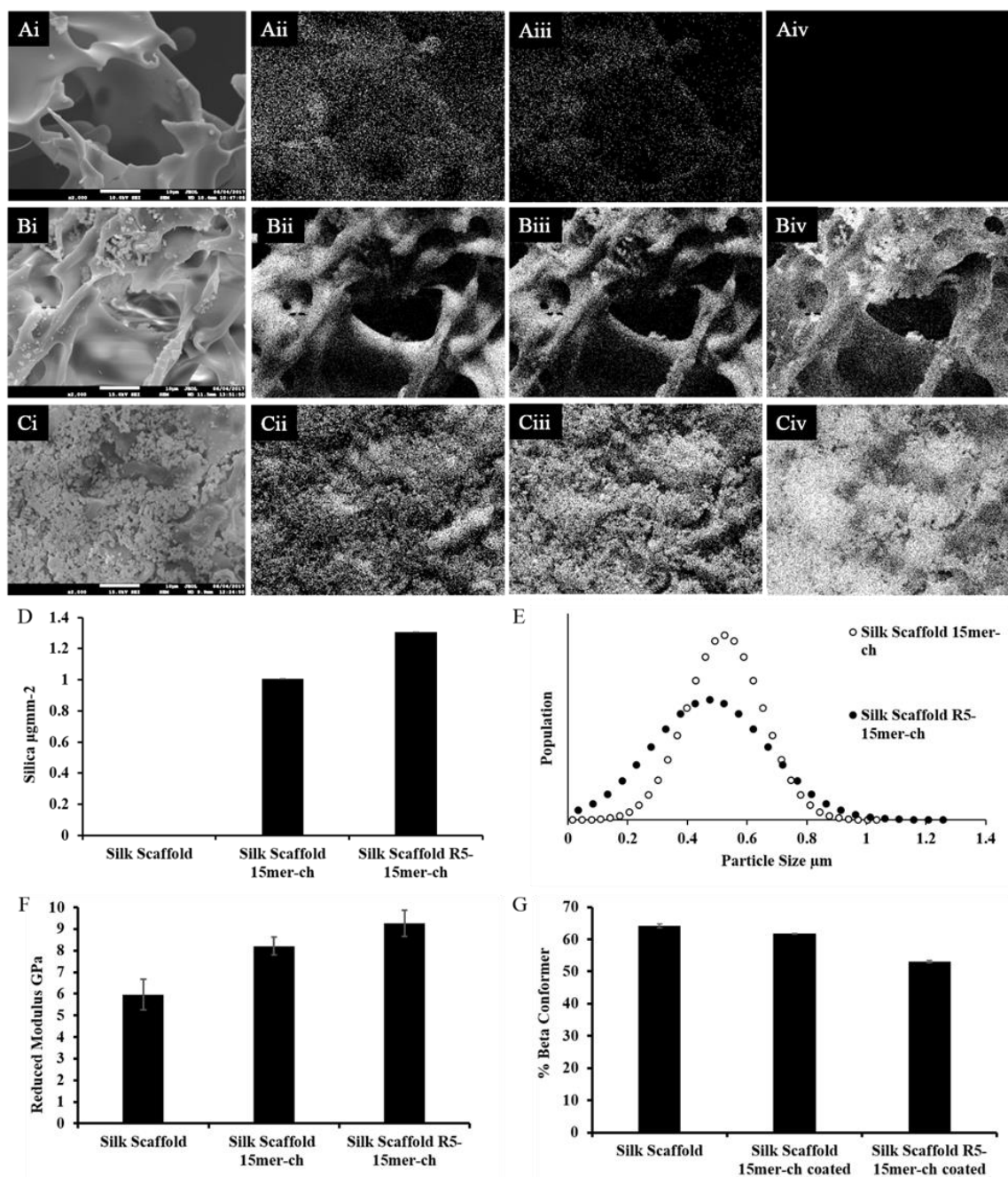


**Figure 7.3** Imaging and characterisation of the three silicified silk scaffolds: silk scaffold, silk scaffold coated in 15mer-ch and silk scaffold coated in R5-15mer-ch. A-C) SEM with EDX mapping, A, B and C are the silk scaffolds as listed above, i, ii, iii, iv are the image and mapping for carbon, oxygen and silicon respectively. Scale bar: 10  $\mu\text{m}$ . D) ICP data for the volume of silica present represented as  $\mu\text{g}$  of silica per  $\text{mm}^{-2}$  of scaffold surface  $n = 3$  E) Population of silica particle sizes on the scaffold surfaces plotted as a function of particles size  $n = 50$  F) Measured reduced elastic modulus of the silk scaffold from AFM data  $n = 20$  G) Total  $\beta$  conformer present as a percentage of secondary structures measured by IR,  $n = 3$ .

To assess the porosity of the samples nitrogen gas absorption was performed on each scaffold with negligible measurements given suggesting the actual surface area of the scaffolds does not differ significantly from that of a flat material of the same shape. The implication of the data being these samples do not have pores on the meso scale (2-50 nm), this is advantageous for biomaterials as mesoporous surfaces are not able to bind to cells well and tend to result in the binding of unwanted materials. To further support to the gas absorption data, surface area measurements were performed using AFM, where the surface area of a material is measured and then compared to that of a flat material, Appendix Fig 7.i shows a schematic of this approach. All scaffolds had a less than 3% surface area increase per distance measured suggesting no mesopores were present on the surface. The percentage increase was highest for the R5-15mer-ch coated scaffold likely due to the high volume of silica particles present, Table 7.1.

	No Coating	15mer-ch	R5-15mer-ch
Gas Absorption $\frac{m^2}{m \cdot g}$	$1/\infty$	$1/\infty$	$1/\infty$
Percent surface area increase*	$0.083 \pm 0.035$	$1.226 \pm 0.467$	$2.826 \pm 0.792$
Reduced Modulus GPa	$5.968 \pm 0.722$	$8.214 \pm 0.433$	$9.262 \pm 0.607$
% Beta Conformer	$64.184 \pm 0.523$	$61.703 \pm 0.090$	$53.090 \pm 0.434$
Silica $\mu\text{gmm}^{-2}$	0	$1.009 \pm 0.000$	$1.308 \pm 0.000$
Silica Particle Size $\mu\text{m}$	-	$0.524 \pm 0.128$	$0.474 \pm 0.196$

**Table 7.1** All data collected for the silk scaffold materials. \*The additional surface area increase as a percent when compared to a flat surface.

Degradation of the silk scaffolds was measured as protein loss to an *in vivo* mimicking solution. Figure 7.4B shows only minimal fluctuation of absorbance readings for the solutes of the scaffolds indicating a high resilience to degradation. Figure 7.4A displays the secondary structures present in the silk scaffolds, all have high  $\beta$  sheet and  $\beta$  turn levels known to give resilience to protein break down.

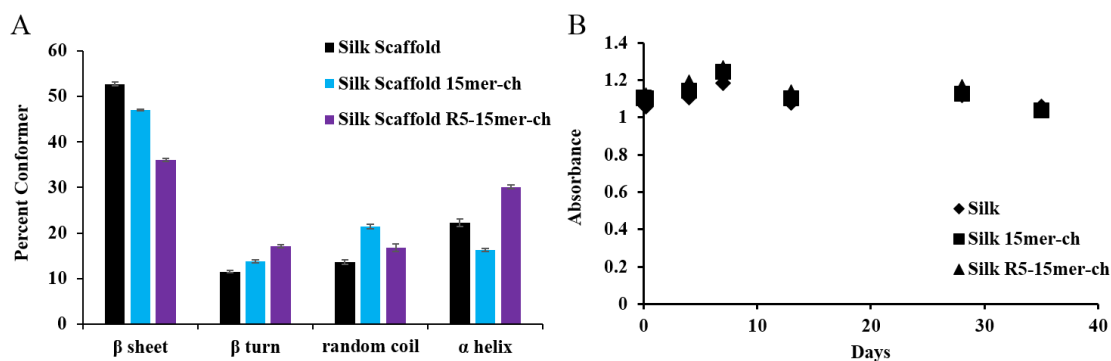


**Figure 7.4** A) In depth peak deconvolution results showing the exact percentage of each  $\beta$  conformer present in each silk scaffold  $n = 3$  B) Degradation study using protein absorbance to compare the silk scaffolds protein release,  $n = 10$ .

Chimeric silica binding silk proteins have proven effective as a coating for a semi-permanent silk scaffolds for biomedical use. The ability of these proteins to undergo structural reordering *via* annealing provides a degree of tailorability with respect to stiffness and degradation in an *in vivo* mimicking environment. Incorporation of nanoscale bioabsorbable silica aided mechanical strength whilst providing a known osteogenic material. This additional mineral phase exhibited no effect on the protein structures present meaning increased stiffness was a direct result of silica presence.

### 7.3.2 Titanium Rods

Titanium rods have been evaluated to observe if coating the inert titanium surface with a silk material will result in silicification on the surface of the material creating a more bioactive surface that will heighten bone regrowth around a fracture site. The silk fusion protein, R5-15mer-ch, was selected from previous studies as a known silk material with silicifying capabilities stemming from the addition of the R5 silica binding peptide; two control samples were also included in the study; an uncoated titanium rods and a titanium rod coated in the 15mer-ch sample, a non-R5 containing counterpart. All rods underwent silicification as previously described and the results shown here were collected on the post-silicified rods.<sup>24</sup>

The extent of silicification on the titanium implant surfaces was assessed *via* SEM imaging, the uncoated titanium rod displayed no silica particulates deposited on the surface suggesting the inert titanium surface did not provide a site for nucleation to occur, Figure 7.5 A. Both chimeric coated titanium rods permitted silica deposition on

the rod surface with the R5 containing rod inducing a greater coverage of silica across the surface, Figure 7.5 B and C.

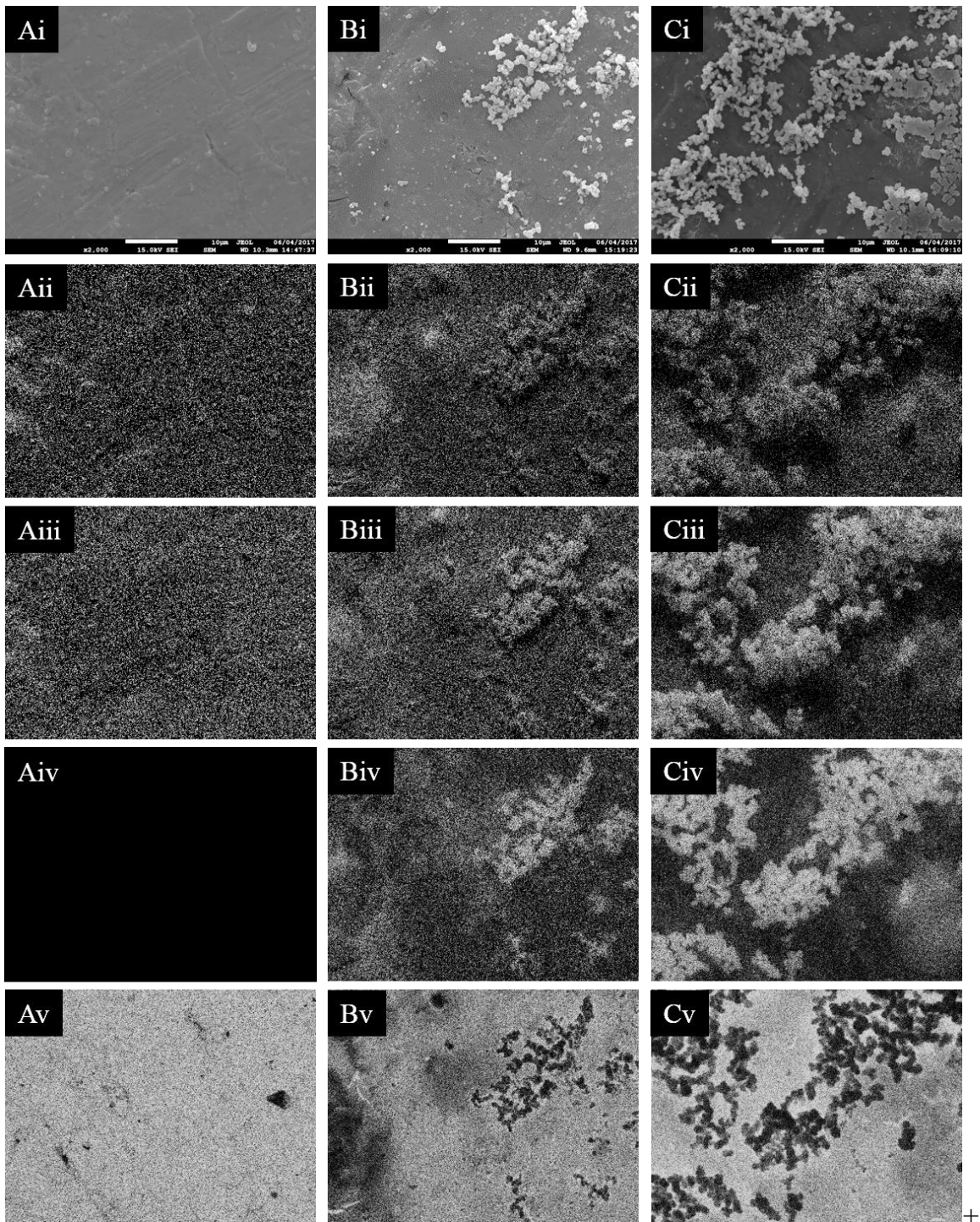
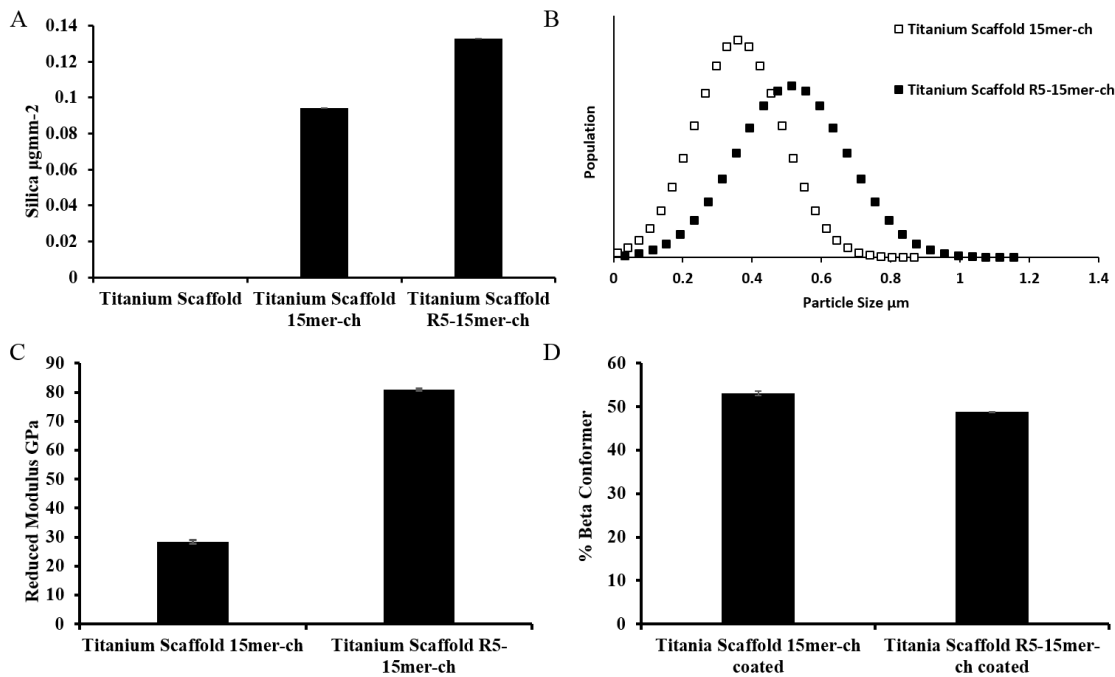


**Figure 7.5** A-C) SEM with EDX mapping for the uncoated titanium rod, the 15mer-ch coated titanium rod and the R5-15mer-ch rod respectively, i, ii, iii, iv and v are the image and mapping for carbon, oxygen, silicon and titanium respectively. Scale bar: 10 µm.

ICP was employed to find the mass of silica bound to each rod, the uncoated titanium rod had no measurable silica present when measured by ICP, validating the images seen by SEM with EDX analysis, the 15mer-ch and R5-15mer-ch coatings allowed the binding of silica particles to the rod surface with a greater concentration, and larger particles, forming on the R5 containing rod as might be expected, Figure 7.6 A and B. However, direct comparison to the silk rod coated in the same R5-15mer-ch chimera reveals a tenfold less silica presence on the titanium implant surface.

Measurements to find the reduced elastic modulus for the uncoated titanium rod proved impossible due to the hard nature of the titanium surface. Analysis of the 15mer-ch and R5-15mer-ch coated titanium rods showed, similarly to the *B. mori* silk rod counterparts, that the greater silica presence on the R5 coated rod surface resulted in an increase in the sample's elastic modulus when compared with the non-R5 silk coated rod, Table 7.2.

The secondary structure of the chimera coatings saw similar results to the silk rods of ~50%  $\beta$  conformer for the 15mer-ch and R5-15mer-ch samples when coating titanium rods, Table 7.2, Figure 7.6. This confirms that the chimeras can still undergo  $\beta$  conformer induction even as a thin coating layer on a titanium surface.



(Caption overleaf)

**Figure 7.6** A) volume of silica present on the titanium rods measured by ICP B) the average particle size and distribution of silica particles on the surface the titanium rods n = 50 C) AFM measured reduced elastic modulus of the 15mer-ch and R5-15mer-ch titanium rods (uncoated sample was too stiff to be measured) n = 20 D) Total percentage  $\beta$  conformer of the 15mer-ch and R5-15mer-ch coated titanium rods n = 3.

Sample porosity was assessed *via* nitrogen gas absorption, and similarly to the silk rods, the titanium rod surfaces were not mesoporous, lessening the risk of implant rejection from cells being unable to bind, Table 7.2. Point to point measurements however suggested that the multi-layering of silica particles as seen in the SEM image for R5-15mer-ch, Figure 7.4 Ci, resulted in a much larger increase in surface area when compared to the two control titanium rods and all *B. mori* silk rods produced in the study. Contact angle measurements were performed on the three rods with data further supporting silk coated titanium rods use as biomaterials as addition of the chimeras had no significant effect on the wettability of the rod surface, Table 7.2.

	No Coating	15mer-ch	R5-15mer-ch
Gas Absorption $\text{m}^2\text{g}^{-1}$	$1/\infty$	$1/\infty$	$1/\infty$
Percent surface area increase*	$1.868 \pm 0.535$	$6.115 \pm 1.515$	$52.663 \pm 7.193$
Reduced Modulus GPa	$\infty$	$28.370 \pm 2.617$	$80.954 \pm 5.997$
% Beta Conformer	-	$53.016 \pm 0.267$	$48.767 \pm 0.958$
Silica $\mu\text{gmm}^{-2}$	0	$0.094 \pm 0.000$	$0.132 \pm 0.000$
Silica Particle Size $\mu\text{m}$	-	$0.360 \pm 0.127$	$0.514 \pm 0.160$
Contact Angle	$129.304 \pm 3.45$	$117.553 \pm 2.85$	$125.002 \pm 6.68$

**Table 7.2** All data collected for the titanium rod materials. \*The addition surface area increased as a percent when compared to a flat surface.

Despite titanium implants intending to be for use as permanent implants, the silk coatings employed here are intended to be semi-permanent, slowly degrading over time, preferably when no longer needed for bone regrowth. The breakdown of this protein film was monitored as protein released into an *in vivo* mimicking solution. Figure 7.7 shows that after 5 weeks in *in vivo* conditions there was no loss of protein to solution indicating a high resilience to degradation from these samples.

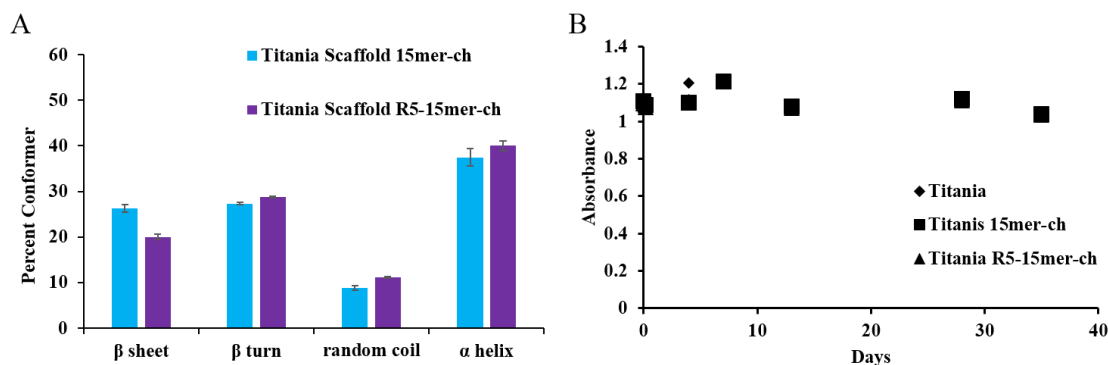


**Figure 7.7** A) In depth protein secondary structure analysis of the two protein coated titanium rod using IR data,  $n = 3$  B) Measured protein release from the surfaces of the titanium rods: titanium, titanium 15mer-ch and titanium R5-15mer-ch,  $n = 10$

Material study of titanium rods with and without chimeric silk coatings was performed to judge applicability towards biomedical use. The inert surface of the titanium was highlighted when silica deposition on the uncoated titanium surface was inhibited, silk coatings provided a barrier to overcome this and limited silica was permitted to bind to the surface. Use of silk as a thin coating on the surface of a titanium rod had no adverse effect on the protein, reordering of secondary protein structure *via* annealing was successful at inducing  $\beta$  conformers. Despite positive results indicating the high potential for silk coated titanium rods for use as biomaterials, further improvements targeted towards increasing silica deposition would expand the capability of these materials to result in successful implantation.

## 7.4 Conclusions

Silk materials have been widely used as biomaterials thanks to their highly beneficial physical properties. Here work from several previous studies were built on to produce biomedical silk scaffolds that combine the genetically modified spider silk derivative

containing the silicifying domain R5, and *B. mori* (silkworm) silk as a cheaper bulk material or medical grade titanium as a sturdy but inert scaffold bulk.

Use of the R5-15mer-ch and 15mer-ch fusion proteins as scaffold and rod coatings proved that these materials were unaltered in their ability to undergo annealing for reordering of secondary protein structure to achieve formation of more  $\beta$  conformers when used as thin layer coatings. This was true for coatings on both the silk scaffold and the titanium rod. It was also seen that the *B. mori* silk when produced into a scaffold behaved as normal, reaching high levels of  $\beta$  conformers required for mechanical strength and degradation resilience.

When used as a coating the R5-15mer-ch silicifying chimera gave reasonable control over silification. Particulates were seen on all silk scaffolds and titanium rods that were coated in spider silk when compared to their naked counterpart, suggesting that the *B. mori* silk scaffold and titanium rod surfaces do not support silification. Despite the 15mer-ch coating permitting silica deposition on the samples surfaces, it was shown, for both the titanium rods and silk scaffolds, that the presence of the R5 peptide actively promoted silification on to the surfaces. As silification was performed under circumneutral pHs this suggests the R5 containing coating would be able to replicate these results *in vivo*.

A major difference between the R5-15mer-ch coated titanium rod and silk scaffold, was silification was seen to a much lesser degree. The trend of R5 presence aiding silification was observed, however silica presence on the *B. mori* silk scaffold was seen to be tenfold greater than on the titanium coated rod. It is possible this is due to the thin nature of the coating allowing the inert nature of the underlying titanium surface to be displayed either discouraging silification or inhibiting strong binding of silica particles meaning there is silica loss in transit.

The incorporation of silica nanoparticles into the silk scaffolds resulted in a stiffening of the material shown through measurements of the reduced elastic modulus of the scaffolds after silification. These data suggest that the presence of silica is multifunctional, aiding bone regrowth through collagen ordering and strengthening the implantable scaffolds.

All data collected supports the use of chimeric coated scaffolds as biomedical devices. All scaffolds exhibited no significant loss of protein into solution after 5 weeks of *in vivo* mimicking incubation indicating biological stability over this time frame. The chemical and physical data suggest that only minor variations occur in the relevant properties of the silk and titanium surfaces, and the R5-15mer-ch was able to function as a biomedical silicifying coating on both a silk scaffold and titanium rod. This has potential for use as an osteoinductive implantable device.

It is noteworthy that these samples are currently being used in animal studies to give further information on their use as a biomaterial.

## 7.5 References

- 1 E. J. Greenfield, *Dental Cosmos*, 1931, **55**, 364-369.
- 2 R. T. Bothe, K. E. Beaton and H. A. Davenport, *Surgery Gynecology and Obstetrics*, 1940, **71**, 598-602.
- 3 P. I. Brånemark, G. A. Zarb and T. Albrektsson, *Tissue-integrated prostheses osseointegration in clinical dentistry*, Quintessence, Chicago, 1992.
- 4 L. Guéhenec, A. Soueidan, P. Layrolle and Y. Amouriq, *Dental Materials*, 2007, **23**, 844-854.
- 5 D. Buser, R. K. Schenk, S. Steinemann, J. P. Fiorellini, C. H. Fox and H. Stich, *Journal of Biomedical Materials Research*, 1991, **25**, 889-902.
- 6 K. Gotfredsen, A. Wennerberg, C. Johansson, L. T. Skovgaard and E. Hjorting-Hansen, *Journal of Biomedical Materials Research*, 1995, **29**, 1223-1231.
- 7 A. Wennerberg, T. Albrektsson, B. Andersson and J. J. Krol, *Clinical oral implants research*, 1995, **6**, 24-30.
- 8 W. Becker, B. E. Becker, A. Ricci, O. Bahat, E. Rosenberg, L. F. Rose, M. Handelsman and H. Israelson, *Clinical Implant Dentistry and Related Research*, 2000, **2**, 159-165.
- 9 D. Buser, N. Brogini, M. Wieland, R. Schenk, A. Denzer, D. Cochran, B. Hoffmann, A. Lussi and S. Steinemann, *Journal of dental research*, 2004, **83**, 529-533.
- 10 G. Zhao, Z. Schwartz, M. Wieland, F. Rupp, J. Geis-Gerstorfer, D. Cochran and B. Boyan, *Journal of Biomedical Materials Research Part a*, 2005, **74A**, 49-58.
- 11 L. V. Carlsson, T. Albrektsson and C. Berman, *The International journal of oral & maxillofacial implants*, 1989, **4**, 199-204.
- 12 K. de Groot, J. Wolke and J. Jansen, *Proceedings of the Institution of Mechanical Engineers Part H-Journal of Engineering in Medicine*, 1998, **212**, 137-147.
- 13 G. Daculsi, O. Laboux, O. Malard and P. Weiss, *Journal of Materials Science-Materials in Medicine*, 2003, **14**, 195-200.
- 14 J. E. Davies, *Journal of dental education*, 2003, **67**, 932-49.
- 15 H. F. Morris, S. Ochi, J. R. Spray and J. W. Olson, *Annals of Periodontology Annals of Periodontology*, 2000, **5**, 56-67.

- 16 F. Barrere, C. van der Valk, G. Meijer, R. Dalmeijer, K. de Groot and P. Layrolle, *Journal of Biomedical Materials Research Part B-Applied Biomaterials*, 2003, **67B**, 655-665.
- 17 N. Geurs, R. Jeffcoat, E. McGlumphy, M. Reddy and M. Jeffcoat, *International Journal of Oral & Maxillofacial Implants*, 2002, **17**, 811-815.
- 18 B. Yang, M. Uchida, H. Kim, X. Zhang and T. Kokubo, *Biomaterials*, 2004, **25**, 1003-1010.
- 19 X. Wang, W. Yan, S. Hayakawa, K. Tsuru and A. Osaka, *Biomaterials*, 2003, **24**, 4631-4637.
- 20 Habibovic, Pamela, Barrère, Florence, Blitterswijk, Clemens A., Groot, Klaas, Layrolle, Pierre, *Journal of the American Ceramic Society*, 2004, **85**, 517-522.
- 21 S. Lopez-Estebana, E. Saiza, S. Fujinob, T. Okuc, K. Suganumac and A. Tomsia, *Journal of the European Ceramic Society*, 2003, **23**, 2921-1930.
- 22 M. Sumper and N. Kroger, *Journal of Materials Chemistry*, 2004, **14**, 2059-2065.
- 23 S. Szmukler-Moncler, H. Salama, Y. Reingewirtz and J. H. Dubruille, *Journal of Biomedical Materials Research*, 1998, **43**, 192-203.
- 24 R. Plowright, N. Dinjaski, S. Zhou, D. J. Belton, C. C. Perry and D. L. Kaplan, *RSC Advances*, 2016, **6**, 21776-21788.
- 25 A. Mieszawska, N. Fournaligas, I. Georgakoudi, N. Ouhib, D. Belton, C. Perry and D. Kaplan, *Journal of Biomaterials*, 2010, **34**, 8902-8920.
- 26 L. L. S. Canabady-Rochelle, D. J. Belton, O. Deschaume, H. A. Currie, D. L. Kaplan and C. C. Perry, *Biomacromolecules*, 2012, **13**, 683-690.
- 27 S. Zhou, W. Huang, D. J. Belton, L. O. Simmons, C. C. Perry, X. Wang and D. L. Kaplan, *Biomaterials*, 2015, **15**, 173-180.
- 28 C. Wong Po Foo, S. V. Patwardhan, D. J. Belton, B. Kitchel, D. Anastasiades, J. Huang, R. R. Naik, C. C. Perry and D. L. Kaplan, *Proceedings of the National Academy of Sciences of the United States of America*, 2006, **103**, 9428-9433.
- 29 D. J. Belton, A. J. Mieszawska, H. A. Currie, D. L. Kaplan and C. C. Perry, *Langmuir*, 2012, **28**, 4373-4381.
- 30 H. A. Currie, O. Deschaume, R. R. Naik, C. C. Perry and D. L. Kaplan, *Advanced Functional Materials*, 2011, **21**, 2889-2895.

- 31 M. Fini, A. Motta, P. Torricelli, G. Glavaresi, N. N. Aldini, M. Tschon, R. Giardino and C. Migliaresi, *Biomaterials*, 2005, **26**, 3527-3536.
- 32 N. Minoura, M. Tsukada and M. Nagura, *Biomaterials*, 1990, **11**, 430-434.
- 33 N. Minoura, S. I. Aiba, M. Higuchi, Y. Gotoh, M. Tsukada and Y. Imai, *Biochemical and Biophysical Research Communications*, 1995, **208**, 511-516.
- 34 N. Dinjaski, R. Plowright, S. Zhou, D. J. Belton, C. C. Perry and D. L. Kaplan, *Acta Biomaterialia*, 2017, **49**, 127-139.
- 35 X. Chen, Z. Shao, D. P. Knight and F. Vollrath, *Proteins-Structure Function and Bioinformatics*, 2007, **68**, 223-231.
- 36 U. Kim, J. Park, C. Li, H. Jin, R. Valluzzi and D. Kaplan, *Biomacromolecules*, 2004, **5**, 786-792.
- 37 C. Vepari and D. L. Kaplan, *Progress in Polymer Science*, 2007, **32**, 991-1007.
- 38 C. Correia, S. Bhumiratana, L. Yan, A. L. Oliveira, J. M. Gimble, D. Rockwood, D. L. Kaplan, R. A. Sousa, R. L. Reis and G. Vunjak-Novakovic, *Acta Biomaterialia*, 2012, **8**, 2483-2492.
- 39 A. R. Murphy and D. L. Kaplan, *Journal of Materials Chemistry*, 2009, **19**, 6443-6450.
- 40 D. N. Rockwood, R. C. Preda, T. Yücel, X. Wang, M. L. Lovett and D. L. Kaplan, *Nature protocols*, 2011, **6**, 1612-31.
- 41 J. E. Noble and M. J. A. Bailey, in *Guide to Protein Purification, 2nd Edition*, ed. R. R. Burgess and M. P. Deutscher, 2009, p. 73-95.

## Conclusions and Further Work

The biomimetic approach has been successfully utilised here to build on previous work by the Perry/Kaplan collaboration on genetically modified spider silk to produce mineralising biomaterials. Previous work had explored using different lengths of the 33 amino acid consensus sequence of the major ampullate dragline spidroin 1 (MaSp 1) from *Nephila clavipes* (SGRGGLGGQG AGAAAAAGGA GQGGYGGLGSQGT), specifically a 6mer and 15mer, with a known silicifying domain attached at the C terminal of the silk; R5 (SSKKS<sub>5</sub>SGSKGSKRRIL), a component of a silaffin protein, and the A1 (SGSKGSKRRIL) and A3 (MSPHPHPRHHHT) peptides, both derivatives of the R5 peptide. The aim of these studies was to combine silk and silica to produce a biomaterial for implant coatings that was as versatile and strong as silk with added rigidity from the silica particles as well as improved osseointegration from the silica interactions with collagen. It was found that the 15mer silk backbone and the R5 silicifying domain showed the most promise to be continued in the study.

Here two samples were produced using the 15mer repeating unit of the spider silk modified with an R5 peptide bound at either the C or N termini of the silk to observe if the location of the R5 domain affected the overall material properties of silk and the silicifying capabilities of the R5 domain. The samples also contained a His-tag for purification located at the opposite termini and were compared against non-R5 containing control counterparts. The major findings here highlighted the use of genetically modified silk chimeras as biomaterials, the addition of the peptide still allowed the annealing of the silk to achieve higher levels of beta conformer known to stiffen the material. Samples observed in solution had the same properties as their counterparts in term of charging and isoelectric point. The potential of each material to induce silica deposition under *in vivo* mimicking conditions was evaluated in solution and solid state; in solution both R5 silk chimeras exhibited good control of the size and volume of silica particles produced however as a film it was the R5-15mer-ch sample that showed greater potential to induce silica precipitation with the greatest control of silica particles deposited.

Work on chimeras then progressed into hydroxyapatite binding silk fusion proteins. Again, three peptides were identified as mineralising domains but only one, the VTK peptide (VTKHLNQISQSY), was able to be expressed under the methods used for sample synthesis here. Similar to before, samples were produced with a binding peptide at either the C or the N terminal of the silk with a His-tag on the opposing termini, non-VTK samples produced as controls, however in addition to these, a sample was produced with a VTK domain at both termini to allow the effect of both location of the peptide and number of peptides present on the silk on hydroxyapatite mineralisation to be measured. Once again, the genetic modification of the 15mer silk derivative to incorporate the binding peptide did not alter the physical or chemical properties of the silk and more importantly, samples could be successfully annealed for beta conformer induction. The hydroxyapatite mineralising capabilities of the single VTK samples were reasonable but limited, the location of the VTK on the silk backbone influencing the crystallinity of the precipitates formed only slightly for both solid state and solution mineralisation. The VTK-15mer-VTK sample, had greater control over mineralisation than the singular VTK containing samples. This led to further experiments proving that chimeric sample concentrations are also a key parameter in mineralisation as well as number of VTK peptides. Table 8 shows publications by the group, including the two new papers from this work, on the chimeric silk samples.

Silk Domain	Sequence	Silicifying Domain	Sequence	Year	Ref
derived from <i>N. clavipes</i> dragline silk	(SGRGGLGGQGAGA AAAAGGAGQGGYG GLGSQGT) <sub>15</sub>	VTK	VTKHLNQISQSY	2017	202
derived from <i>N. clavipes</i> dragline silk	(SGRGGLGGQGAGA AAAAGGAGQGGYG GLGSQGT) <sub>15</sub>	R5	SSKKSGSYSGSK GSKRRIL	2016	99
		A3	MSPHPHPRHHHT		
derived from <i>N. clavipes</i> dragline silk	(SGRGGLGGQGAGA AAAAGGAGQGGYG GLGSQGT) <sub>6</sub>	A1	SGSKGSKRRIL	2015	124
		R5	SSKKSGSYSGSK GSKRRIL		
		A3	MSPHPHPRHHHT		
<i>N. clavipes</i> dragline silk	(SGRGGLGGQGAGA AAAAGGAGQGGYG GLGSQGT) <sub>15</sub>	A1	SGSKGSKRRIL	2012	29
		R5	SSKKSGSYSGSK GSKRRIL		
		Pep 1	KSLSRHDHIIHH		
<i>N. clavipes</i> spider dragline silk	[SGRGGLGGQGAGA AAAAGGAGQGGYG GLGSQGT] <sub>n</sub> n = 6 or 15	R-Pep1	RKSLSRHDHIIH H	2012	123
		R5	SSKKSGSYSGSK GSKRRIL		
<i>B. mori</i> silkworm cocoons	-	Silica particles	-	2010	28
<i>N. clavipes</i> spider dragline silk	(SGRGGLGGQGAGA AAAAGGAGQGGYG GLGSQGT) <sub>n</sub> n = 6 or 15*	R5	SSKKSGSYSGSK GSKRRIL	2006	39

**Table 8** Previous silaffins and silk repeating units used by the Perry/Kaplan collaboration to produce silk-silica composites. \*a derivative also was produced with the cell building domain RGD. Linking section were included between the silk and peptide in all publications prior to 2016, sequence: SSGLVPRGSGMKETA AAKFERQHMDSPDLGTDDDDKAMA

During characterisation of the VTK chimeras it was noted that evaluation of mineralising capabilities were limited to a qualitative comparison of XRD data, whereas for the R5 chimeras there were several methods for quantifying the amount of silica precipitated. This led to method development of a novel way to use XRD data. Through the use of calibration samples containing a known mixture of all crystal phases being produced, in this case brushite and hydroxyapatite, a calibration curve was produced displaying specific peak height ratios against the molar ratio of the mixture. This method was proven effective for comparing efficiency of different binding peptides and fusion proteins. It is believed that this method may be translatable to other crystalline materials where quantification of phases through well-established means is not possible.

To conclude work on silk film chimeras as biomaterials, further studies were completed on both the R5 samples and VTK samples. At this stage no sample was disregarded as all were shown to be reasonable at mineralisation and likely to be biocompatible. Here the theorised proportional link between  $\beta$  content of a chimeric silk film and its stiffness was proven *via* Young's modulus measurements for all samples, regardless of the mineralising domain present. Higher  $\beta$  conformer percentage additionally resulted in increased resilience towards degradation under *in vivo* mimicking conditions. Silicification performed on the R5 samples, previously shown to achieve binding of uniform silica particles, enhanced the material stiffness of composites further as desired, particularly for the R5-15mer-ch sample. Silica presence will therefore aid material endurance and likely increase osseointegration. HAP mineralisation carried out on the VTK samples highlighted the location of the VTK peptide as a key parameter influencing the physical properties of the samples. Young's modulus data showed that despite the highly crystalline precipitates produced by the VTK-15mer-ch and VTK-15mer-VTK samples, these may not be the most compatible with bone, as modulus values were tenfold that of literature values for bone. The nh-15mer-VTK sample however, produced a less crystalline material that was within the range of stated values for the Young's modulus of bone. All physical property data would suggest the chimeras are good candidates for biomedical use, particularly the R5-15mer-ch given its exceptional silicifying capabilities and the nh-15mer-VTK as the crystalline HAP precipitates produced by

this sample are the most likely to be readily incorporated into surrounding bone tissue due to similar physical properties.

The final part of the study was to begin use of chimeras as implant coatings. Based on the conclusions so far, the R5-15mer-ch sample was selected to be taken forward. Here both *B. mori* silk and titanium scaffolds were coated with the chimera silk sample. Use of the chimera as a scaffold coating did not change the physical properties of the silk and still allowed structural reordering to occur through annealing. No protein loss under *in vivo* mimicking incubation proved the chimeras show resilience to degradation was also unaffected. The R5 domain silicifying capabilities were shown to be effective at inducing and controlling the size of silica particles deposited for the silk scaffold, however comparison to the titanium scaffold showed a more than tenfold reduction in silica presence, a likely cause being the inert nature of the titanium material itself being exhibited. Incorporation of silica onto the silk scaffolds led to a stiffening of the material, suggesting the presence of silica is multifunction, aiding bone regrowth through collagen ordering and strengthening the implantable scaffolds.

## **Future work**

### **Chimeric silk as scaffold coatings**

The titanium scaffolds included in the study were not able to match the successful results produced by the *B. mori* silk scaffolds. It is likely that the chimeric silk coatings used here may have been too thin, to address this different surface processing techniques will be explored:

- Electrospinning the chimeras onto the titanium surface, this process produces nanofibers that collect on target surfaces. It is thought, providing there is no change in the behaviour of the chimera, this can be used to build up a thicker coating.
- Double layer coatings. The titanium can be first coated in the cheaper *B. mori* silk and once annealed, a chimeric coating can then be applied.
- Roughening of the titanium surface to give a larger surface to increase chance of chimeric silk adhering to the surface.

Once a method for improving titanium scaffold coating has been found, the project will move on to using the VTK containing chimeras as scaffold coating of both silk and titanium scaffolds.

Prior to this, it is desired that further study into the VTK chimeras can be completed to look at the lower concentration limits with respect to mineralisation. It was shown that the VTK-15mer-ch produced highly crystalline HAP precipitates with an elastic modulus much greater than that of bone. It is believed that if the mass of sample used is reduced, by producing films of the same surface area but from a solution mixture of chimera and either a control sample or *B. mori* silk, a more compatible HAP precipitate may be produced. This would reduce the overall cost of the coating if a mixture can be used in place of a pure chimera solution. The results of this would determine which VTK chimera would be taken forward to be studied as a scaffold coating.

As a conclusion to this work, a mixture of the two selected chimeras, R5 and VTK containing, would be produced for scaffold coatings. The goal being to premineralise the surface of the scaffold with both silica and HAP, or to produce a scaffold coated in silica and HAP binding peptides, to increase osseointegration at the implant site.

### **Secondary structure of silk: studies at the interface**

The aim of this work would be to fully understand how the annealing process induces  $\beta$  conformers. An in depth study would hope to provide answers to questions such as: can the annealing process offer control over the  $\beta$  sheet/ $\beta$  turn content induced? What variables for the annealing process can be altered to achieve this? Is there a uniform affect from annealing across the width and depth of the film? Does the substrate the film is mounted on determine protein structures? Is there a correlation between film thickness and protein structure?

To study this, silk films of varying thickness would be produced using dip coating of substrates in varying concentrations of aqueous silk solutions at a set withdrawal rate. AFM and IR would be used to measure film thickness and the protein structure of the films.

Additionally to this, methods would be developed aiming to reduce the amount of helical structures produced when films are first produced. This would build on the

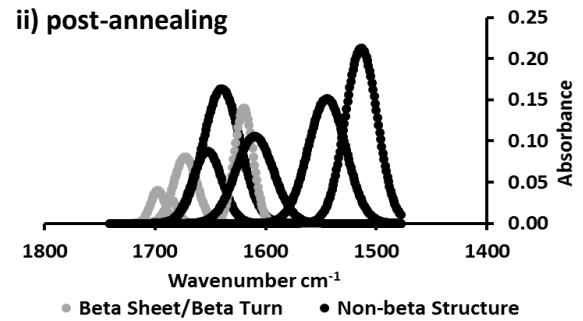
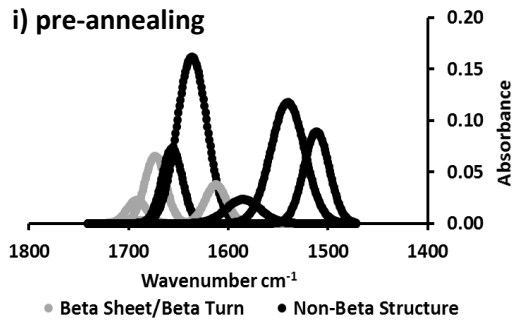
observation that structural changes occurring during annealing are the reorganisation of random coil regions whilst  $\alpha$  helical regions remained unchanged. It is believed that the initial percentage of random coil structures present dictates the maximum amount of  $\beta$  conformers that can be induced, it is hoped by reducing the initial amount of random coil there will be greater control over the final percentage of  $\beta$  conformer present.

Knowledge gained from this work would allow for more varied but specialised silk materials to be produced, increasing the possible applications of silk in, but not limited to, the biomedical field.

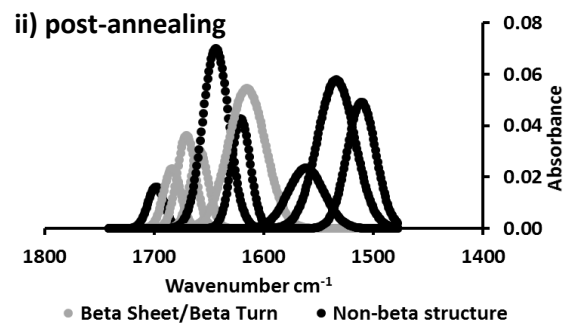
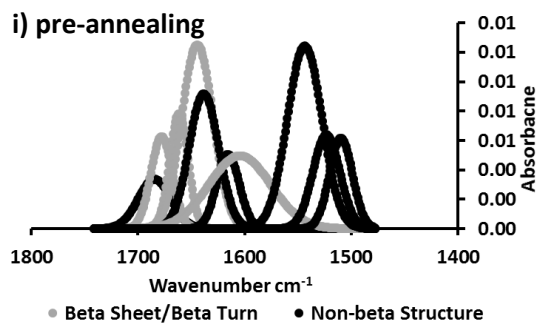
## Appendix

### Chapter III

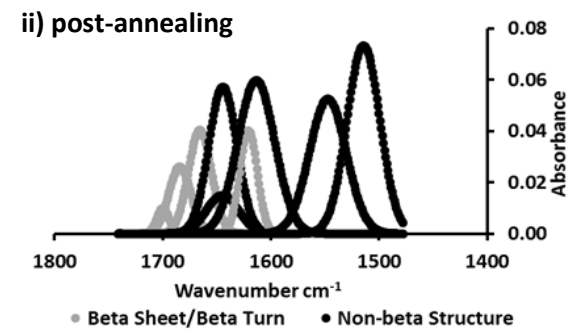
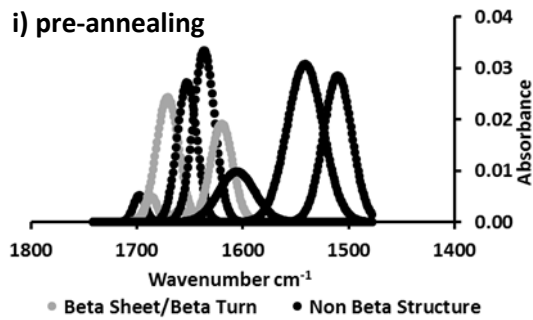
#### a) nh-15mer



#### b) nh-15mer-R5



#### c) 15mer-ch



#### d) R5-15mer-ch

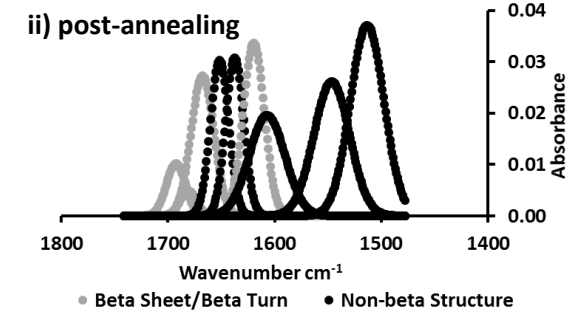
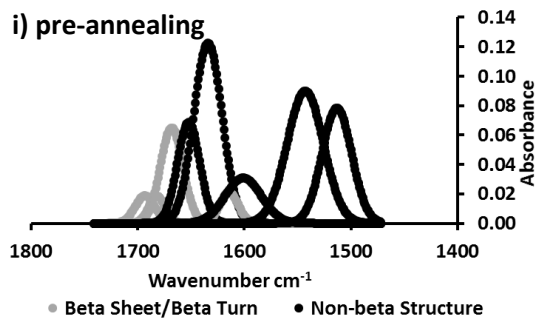


**Fig 3i** Peak deconvolution of chimeric silk films pre and post annealing.

## Chapter IV

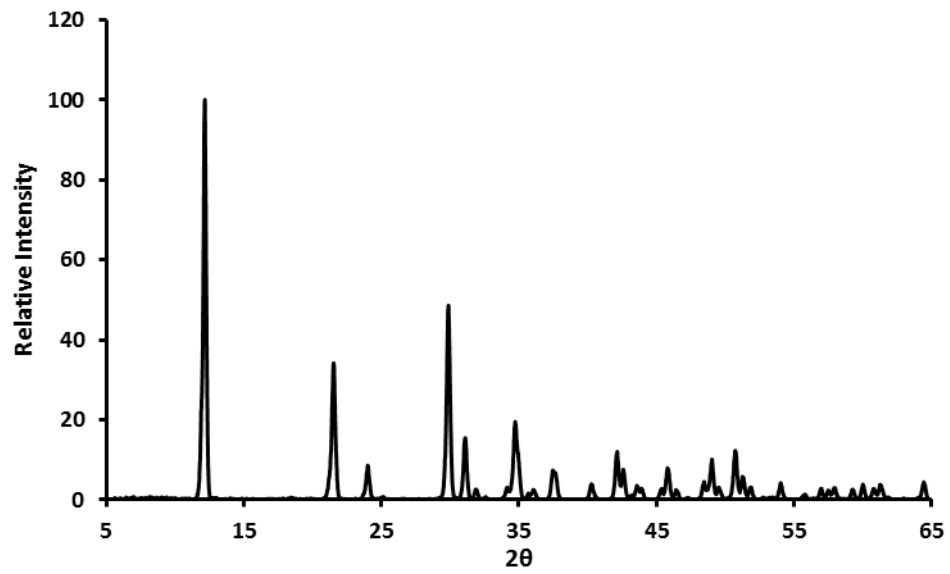
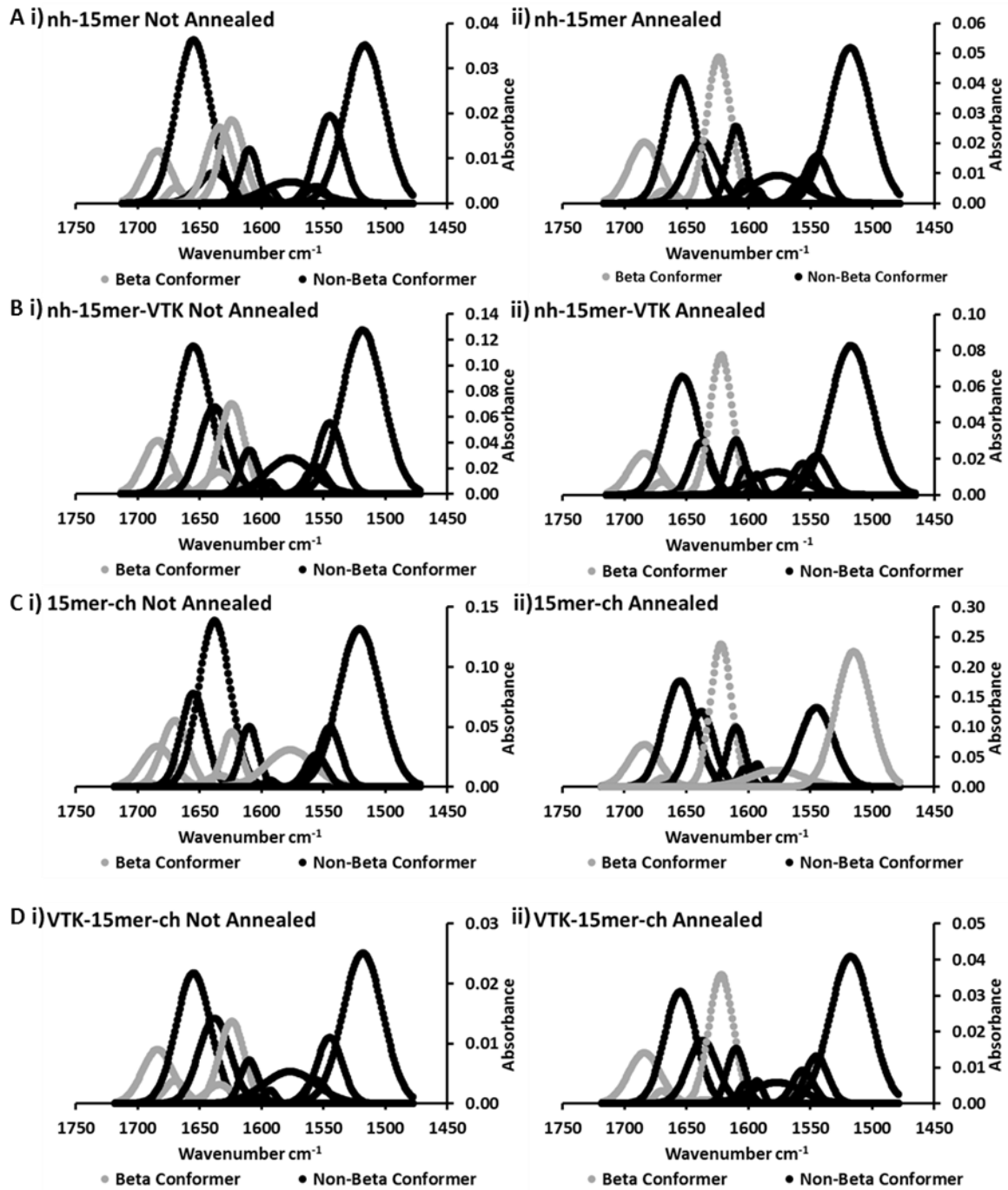
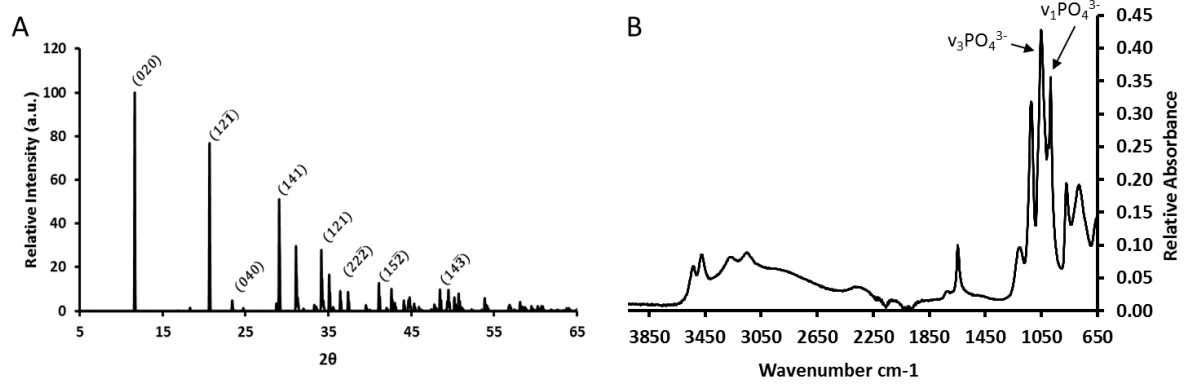


Figure 4.i XRD pattern of calcium phosphate precipitate produced after mineralisation in the presence of the control PDMS (no sample).



**Fig 4.ii** Comparison of recombinant silk films, nh-15mer, nh-15mer-VTK, 15mer-ch, VTK-15mer-ch, before and after the methanol annealing process with respect to the changes in protein secondary structure.

Chapter V

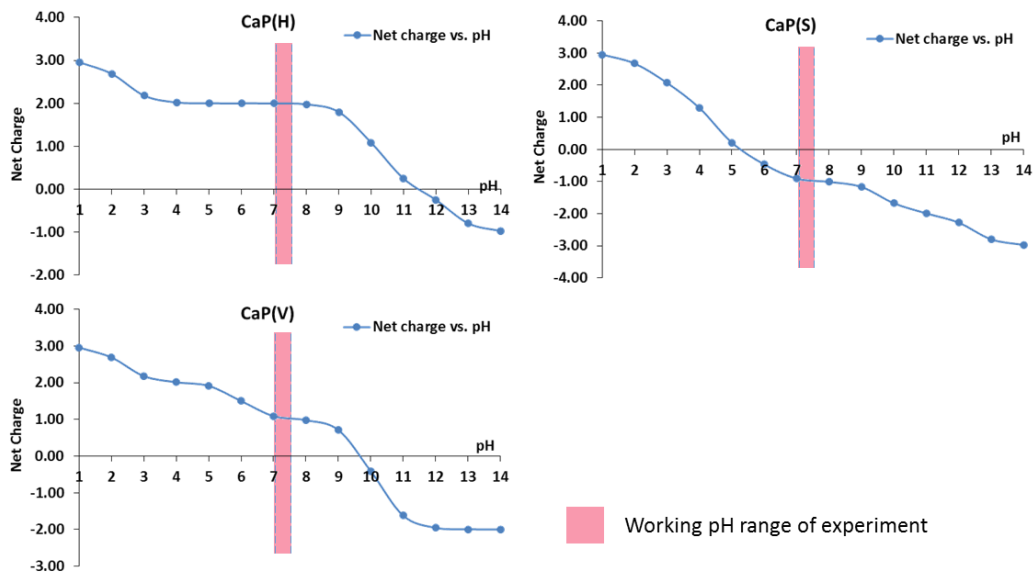


**Fig 5.i** Confirmation of the presence of brushite A) XRD B) FTIR (ATR).

A

	Sequence	Net charge at pH 7.4	Average Hydrophobicity	pI
CaP(H)	SVSVGMKPSRP	+2	+13.87	11.71
CaP(S)	STLPIPHFSRE	-1	+16.67	5.23
CaP(V)	VTKHLNQISQSY	+1	+13.05	9.54

B



C

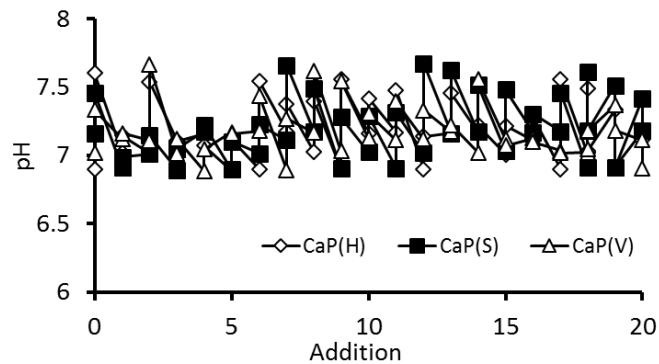


**Fig 5.ii** Calculated peptide properties for the three HAP binding peptides included in the study. A) Tabulated physical property data for each peptide B) Graphical representations of peptide net charges with response to pH. C) pH of the peptide mineralising solution after each addition of 200 μL 120 mM sodium phosphate dibasic and 200 μL 200 mM calcium chloride.

**Chapter VI**

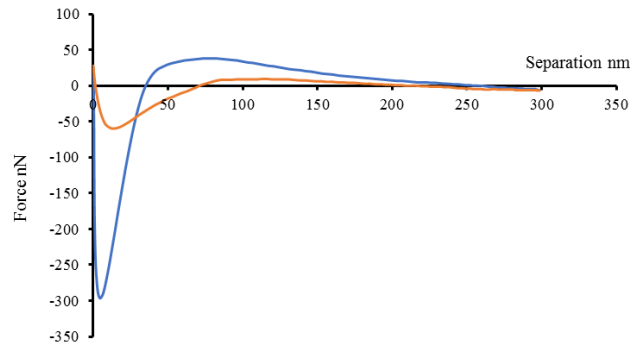


**Fig 6.i** Example of a force separation curve from PeakForce tapping mode AFM scanning of a chimeric silk film.

**Chapter VII**

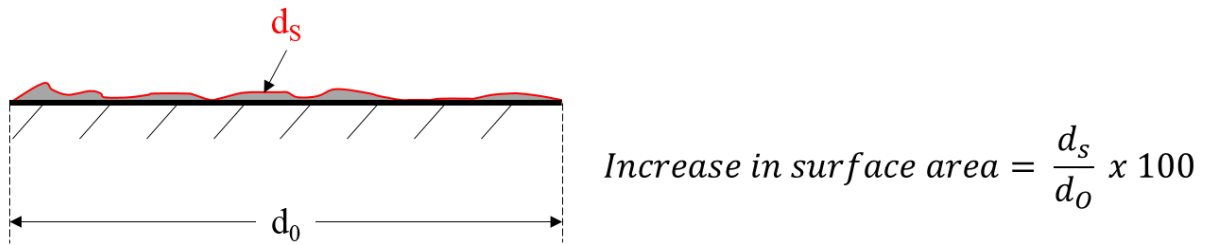


**Fig 7.i** Schematic of how percentage surface area increase has been calculated.

## Publications

### Published at time of submission

Plowright, R.\*, Dinjaski, N.\*, Zhou, S., Belton, D. J., Perry, C. C., & Kaplan, D. L. (2016). Influence of silk–silica fusion protein design on silica condensation in vitro and cellular calcification. *RSC Advances*, 6(26), 21776-21788.

Dinjaski, N.\*, Plowright, R.\*, Zhou, S., Belton, D. J., Perry, C. C., & Kaplan, D. L. (2017). Osteoinductive recombinant silk fusion proteins for bone regeneration. *Acta Biomaterialia*, 49, 127-139.

Plowright, R., Belton, D. J., Kaplan, D. L., Perry, C. C. (2017) Quantifying the efficiency of Hydroxyapatite Mineralising Peptides, *Nature Scientific Reports*, 7, 7681

“Intracellular Pathways Involved in Bone Regeneration Triggered by Recombinant Silk-silica Chimeras” Z. Martín-Moldes, D. Ebrahimi, R. Plowright, N. Dinjaski, C. C. Perry, M. J. Buehler, D. L. Kaplan, *Advanced Functional Materials*

### Pending reviewers comments:

“A Robust Spectroscopic Method for the Determination of Protein Conformational Composition- Application to the Annealing of Silk” D. J. Belton, R. Plowright, D. L. Kaplan, C. C. Perry, *Biomacromolecules*

\*Joint lead Authors

Cite this: *RSC Adv.*, 2016, 6, 21776

## Influence of silk–silica fusion protein design on silica condensation *in vitro* and cellular calcification†

Robyn Plowright,<sup>‡</sup> Nina Dinjaski,<sup>‡</sup> Shun Zhou,<sup>b</sup> David J. Belton,<sup>a</sup> David L. Kaplan<sup>\*b</sup> and Carole C. Perry<sup>\*a</sup>

Biomaterial design via genetic engineering can be utilized for the rational functionalization of proteins to promote biomaterial integration and tissue regeneration. Spider silk has been extensively studied for its biocompatibility, biodegradability and extraordinary material properties. As a protein-based biomaterial, recombinant DNA derived derivatives of spider silks have been modified with biomimetic domains which lead to silica deposition and potentially accelerated bone regeneration. However, the influence of the location of the R5 (SSKKS<sub>2</sub>SGSYSGSKGSKRRIL) silicifying domain fused with the spider silk protein sequence on the biosilicification process remains to be determined. Here we designed two silk–R5 fusion proteins that differed in the location of the R5 peptide, C- vs. N-terminus, where the spider silk domain consisted of a 15mer repeat of a 33 amino acid consensus sequence of the major ampullate dragline spidroin 1 from *Nephila clavipes* (SGRGGLGGQG AGAAAAAGGA GQGGYGGLSQGT). The chemical, physical and silica deposition properties of these recombinant proteins were assessed and compared to a silk 15mer control without the R5 present. The location of the R5 peptide did not have a significant effect on wettability and surface energies, while the C-terminal location of the R5 promoted more controlled silica precipitation, suggesting differences in protein folding and possibly different access to charged amino acids that drive the silicification process. Further, cell compatibility *in vitro*, as well as the ability to promote human bone marrow derived mesenchymal stem cell (hMSC) differentiation were demonstrated for both variants of the fusion proteins.

Received 6th January 2016  
Accepted 16th February 2016

DOI: 10.1039/c6ra03706b  
www.rsc.org/advances

### 1. Introduction

The need for foreign material implants in the human body has led to the growth in research of how to continue to improve these materials related to biological outcomes. Silk materials are useful as biomedical devices due to their biocompatibility and their extraordinary physical properties.<sup>1–3</sup> High tensile strength and elasticity provide a useful basis for silk materials with medical and non-medical applications as goals.<sup>4–6</sup> Silk can be formed into gels, sponges, films, membranes and scaffolds<sup>9–13</sup> with applications from controlled release<sup>14</sup> to supportive scaffolding constructs.<sup>15,16</sup>

Dragline silk from spiders is the focus of the present study due to its support line and framing functions in orb webs.<sup>17</sup> The structure consists of protein beta sheet crystals distributed *via* long protein fibers.<sup>18</sup> However, to generate mechanically stiffer spider-silk biomaterials, analogies from bone composite systems can be made, whereby inorganic components are tightly integrated into collagen protein-based components, to generate unique composite features. A similar approach was taken here, building on our past work where we generated a range of spider silk fusion proteins to study silicification. Silica has good compatibility with silk and biological systems.<sup>19</sup> Silica is also known for its bioactivity particularly with bone tissue, as it binds strongly with bone whilst also being osteoinductive.<sup>20</sup> However, the hard crystalline structures often produced by silica are brittle and lack beneficial tensile properties. By combining silica with silk, materials that combine the best attributes of both can be achieved. The composite materials formed can be fully biodegradable, exhibit osteoinductive features and retain mechanical robustness. Additionally, the new materials would have potential to be doped with constituents such as growth factors and drugs for programmed release.<sup>21</sup>

<sup>a</sup>Biomolecular and Materials Interface Research Group, Interdisciplinary Biomedical Research Centre, School of Science and Technology, Nottingham Trent University, Clifton Lane, Nottingham, UK NG11 8NS. E-mail: carole.perry@ntu.ac.uk; Tel: +44 (0)115 84 86695

<sup>b</sup>Department of Biomedical Engineering, Tufts University, 4 Colby Street, Medford, Massachusetts, 02155, USA. E-mail: David.Kaplan@Tufts.edu; Fax: +1 617 627 3231; Tel: +1 617 626 3251

† Electronic supplementary information (ESI) available. See DOI: 10.1039/c6ra03706b

‡ These authors contributed equally to this work.



Contents lists available at ScienceDirect

Acta Biomaterialia

journal homepage: [www.elsevier.com/locate/actabiomat](http://www.elsevier.com/locate/actabiomat)

Full length article

## Osteoinductive recombinant silk fusion proteins for bone regeneration

Nina Dinjaski<sup>a,1</sup>, Robyn Plowright<sup>b,1</sup>, Shun Zhou<sup>a</sup>, David J. Belton<sup>b</sup>, Carole C. Perry<sup>b,\*</sup>, David L. Kaplan<sup>a,\*</sup><sup>a</sup> Department of Biomedical Engineering, Tufts University, 4 Colby Street, Medford, MA 02155, United States<sup>b</sup> Biomolecular and Materials Interface Research Group, Interdisciplinary Biomedical Research Centre, School of Science and Technology, Nottingham Trent University, Clifton Lane, Nottingham NG11 8NS, UK

## ARTICLE INFO

## Article history:

Received 31 July 2016

Received in revised form 3 November 2016

Accepted 2 December 2016

Available online 8 December 2016

## Keywords:

Silk

Spider silk

Hydroxyapatite

Fusion proteins

Biomaterials

Calcification

## ABSTRACT

Protein polymers provide a unique opportunity for tunable designs of material systems due to the genetic basis of sequence control. To address the challenge of biomineralization interfaces with protein based materials, we genetically engineered spider silks to design organic-inorganic hybrid systems. The spider silk inspired domain (SGRGGGGGAGAAAAAGGA GQG GYGGLGSQGT)<sub>15</sub> served as an organic scaffold to control material stability and to allow multiple modes of processing, whereas the hydroxyapatite binding domain VTKHLNQISQSY (VTK), provided control over osteogenesis. The VTK domain was fused either to the N-, C- or both terminals of the spider silk domain to understand the effect of position on material properties and mineralization. The addition of the VTK domain to silk did not affect the physical properties of the silk recombinant constructs, but it had a critical role in the induction of biomineralization. When the VTK domain was placed on both the C- and N-termini the formation of crystalline hydroxyapatite was significantly increased. In addition, all of the recombinant proteins in film format supported the growth and proliferation of human mesenchymal stem cells (hMSCs). Importantly, the presence of the VTK domain enhanced osteoinductive properties up to 3-fold compared to the control (silk alone without VTK). Therefore, silk-VTK fusion proteins have been shown suitable for mineralization and functionalization for specific biomedical applications.

## Statement of Significance

Organic-inorganic interfaces are integral to biomaterial functions in many areas of repair and regeneration. Several protein polymers have been investigated for this purpose. Despite their success the limited options to fine-tune their material properties, degradation patterns and functionalize them for each specific biomedical application limits their application. Various studies have shown that the biological performance of such proteins can be improved by genetic engineering. The present study provides data relating protein design parameters and functional outcome quantified by biomineralization and human mesenchymal stem cell differentiation. As such, it helps the design of osteoinductive recombinant biomaterials for bone regeneration.

© 2016 Acta Materialia Inc. Published by Elsevier Ltd. All rights reserved.

## 1. Introduction

Recombinant biomaterials hold potential for the development of application-specific fine-tuned scaffolding for tissue regeneration and replacement, a major health challenge worldwide [1]. Organic-inorganic interfaces are integral to biomaterial functions in many areas of repair and regeneration, therefore the surface modification of implantable biomaterial surfaces with bioactive

peptides is one approach to design materials for bone formation [2,3]. Several fibrous proteins have been investigated for this purpose [4,5]. Collagens are of particular interest as scaffolds for bone tissue engineering as they represent the major protein fraction of bone extracellular matrix [6]. However, collagen-based biomaterials generally lack mechanical stability and lose integrity over time [7]. Another unique family of fibrous proteins with impressive mechanical properties, biocompatibility and biodegradability are silks [8–12]. The mechanical properties of spider silk exceed other natural polymers and most synthetic materials, rivalling even high-performance fibers such as Kevlar, making silk a suitable candidate for bone-related biomaterials [13].

\* Corresponding authors.

E-mail addresses: [Carole.Perry@ntu.ac.uk](mailto:Carole.Perry@ntu.ac.uk) (C.C. Perry), [David.Kaplan@tufts.edu](mailto:David.Kaplan@tufts.edu) (D.L. Kaplan).<sup>1</sup> These authors contributed equally to this work.<http://dx.doi.org/10.1016/j.actbio.2016.12.002>

1742-7061/© 2016 Acta Materialia Inc. Published by Elsevier Ltd. All rights reserved.

# SCIENTIFIC REPORTS

## OPEN Quantifying the efficiency of Hydroxyapatite Mineralising Peptides

Received: 16 February 2017  
Accepted: 19 June 2017  
Published online: 09 August 2017

Robyn Plowright<sup>1</sup>, David J. Belton<sup>2</sup>, David L. Kaplan<sup>2</sup> & Carole C. Perry<sup>1</sup>

We present a non-destructive analytical calibration tool to allow quantitative assessment of individual calcium phosphates such as hydroxyapatite (HAP) from mixtures including brushite. Many experimental approaches are used to evaluate the mineralising capabilities of biomolecules including peptides. However, it is difficult to quantitatively compare the efficacy of peptides in the promotion of mineralisation when inseparable mixtures of different minerals are produced. To address this challenge, a series of hydroxyapatite and brushite mixtures were produced as a percent/weight (0–100%) from pure components and multiple ( $N=10$ ) XRD patterns were collected for each mixture. A linear relationship between the ratio of selected peak heights and the molar ratio was found. Using this method, the mineralising capabilities of three known hydroxyapatite binding peptides, CaP(S) STLPIPHFSRE, CaP(V) VTKHLNQISQSY and CaP(H) SVSVGMPKSPRP, was compared. All three directed mineralisation towards hydroxyapatite in a peptide concentration dependent manner. CaP(V) was most effective at inducing hydroxyapatite formation at higher reagent levels ( $\text{Ca}^{2+} = 200$  mM), as also seen with peptide-silk chimeric materials, whereas CaP(S) was most effective when lower concentrations of calcium (20 mM) and phosphate were used. The approach can be extended to investigate HAP mineralisation in the presence of any number of mineralisation promoters or inhibitors.

The mineralising potential of specific binding peptides has been studied for a wide range of materials and reaction conditions<sup>1,2</sup>. Methods that allow accurate quantification of the mineralised products tend to have one of two distinguishing features; either only one product is formed (or not formed) or the by-products of the experiment are easily separated from the target compound.

In peptide driven hydroxyapatite (HAP) synthesis it is often the case that inseparable mixtures of various calcium phosphate crystalline materials are produced<sup>3</sup>. The range of crystal phases produced varies with the method of mineralisation employed, however the more commonly used methods tend to be the simplest, and result in two significant phases forming, namely HAP and brushite. Analysis of the efficiency of peptide directed mineralisation that generates impure products/mixtures is then limited to a qualitative discussion of products, for example 'products produced in the presence of sample 1 appears to contain a greater fraction of HAP than sample 2'.

In this study a series of HAP/brushite mixtures with increasing molar ratios of HAP to brushite (the most commonly formed calcium phosphate without mineralising directing influences present)<sup>4,7</sup> have been analysed with the intention of creating an analytical method applicable to the quantifiable estimation of, in this case, peptides that promote HAP mineralisation. Three HAP binding peptides, all of which were previously identified via phage display: CaP(S) STLPIPHFSRE<sup>8–11</sup>, CaP(V) VTKHLNQISQSY<sup>12–15</sup> and CaP(H) SVSVGMPKSPRP<sup>8, 13, 16, 17</sup>, have been used in this study. An extension of the approach to quantify the effect on mineralisation of larger proteins such as silk chimeras built from mimics of spider silk MASPI protein and the CaP(V) peptide is also included<sup>18</sup>.

### Method

**Brushite Synthesis.** Equal volumes of saturated aqueous solutions of 200 mM calcium chloride (Sigma-Aldrich, Dorset UK) and 120 mM dibasic sodium phosphate (Sigma-Aldrich, Dorset UK) were added together

<sup>1</sup>Biomolecular and Materials Interface Research Group, Interdisciplinary Biomedical Research Centre, School of Science and Technology, Nottingham Trent University, Clifton Lane, Nottingham, NG11 8NS, UK. <sup>2</sup>Department of Biomedical Engineering, Tufts University, 4 Colby Street, Medford, Massachusetts, 02155, United States. Correspondence and requests for materials should be addressed to C.C.P. (email: [carole.perry@ntu.ac.uk](mailto:carole.perry@ntu.ac.uk))